Simulation en dynamique moléculaire des modificateurs de frottement aminés : comportement en diffusion, adsorption et frottement

Rafael Pereira de Matos

N° ordre : 2019LYSEC013 Année 2019

Thèse de doctorat de l'Université de Lyon
délivrée par l'École Centrale de Lyon

Spécialité : Génie des Matériaux de l'École Doctorale EDML (34)

préparée au Laboratoire de Tribologie et Dynamique des Systèmes
en collaboration avec Total Marketing & Services

Soutenue le 19 avril 2019 à Lyon

par

Rafael PEREIRA DE MATOS

Molecular dynamics simulations of amine-based friction modifiers: diffusion, adsorption and friction behaviors

Simulation en dynamique moléculaire des modificateurs de frottement aminés : comportement en diffusion, adsorption et frottement

Composition du jury :

MDC HDR	Nicolas FILLOT	LaMCoS (France)	Rapporteur
Prof.	Michael MOSELER	Fraunhofer IWM (Allemagne)	Rapporteur
MDC	Tristan ALBARET	iLM (France)	Examinateur
Prof.	Charlotte BECQUART	UMET (France)	Examinatrice
Dr.	Sophie LOEHLE	Total M&S (France)	Membre Invité
Prof. Emérite	Akira MIYAMOTO	Tohoku University (Japon)	Membre Invité
MDC	Manuel COBIAN	LTDS (France)	Co-encadrant
MDC HDR	Clotilde MINFRAY	LTDS (France)	Directrice de thèse

Contents

Abstract

Fatty amines and their derivatives are employed as organic friction modifiers (OFM) in lubricant oils in order to mitigate the negative effects of friction and wear, both induced by the moving and rubbing components of an internal combustion engine that are subjected to boundary lubrication conditions (*i.e.*, high contact pressure and low sliding velocity). In addition to their tribological performance, these additives exhibit the benefit of being compatible with exhaust aftertreatment systems that equip the current light-duty vehicles, owing to their sulfur- and phosphorus-free chemical composition. For these reasons, we have developed a computational protocol, composed of equilibrium and non-equilibrium (classical) molecular dynamics simulations, in order to gain a deeper understanding into their mechanisms of action at nanoscale, and in particular into their *diffusion*, *adsorption* and *friction behaviors*. In this context, the influence of different molecular structure factors — related to lubricant constituents — on OFM working performance were investigated. The obtained results have shown that: *(i) Diffusion* — OFM diffusivity is substantially affected by the base oil structure and chemistry (*e.g.*, polarity and molar mass), where solvents with relatively larger and higher polar groups tend to slow down their diffusive rate; besides, the OFM dynamics in liquid phase is also impacted by their own composition, where the molecules with relatively smaller and less polar structure are the most mobile additives. *(ii) Adsorption* — primary alkyl amines do chemisorb onto iron-oxide substrates, thereby forming molecular films whose packing order and thickness increase with increasing surface coverage. *(iii) Friction* — adsorbed layers containing primary amines with linear, saturated, C_{18} hydrocarbon tails are able to reduce friction in a single-asperity, boundary nano-contact model, where their efficiency is dependent on their molecular ordering under confinement and shear; in addition, the organic films allowing the formation of well-defined slippage interface(s) with little molecular interdigitation are more prone to diminish the sliding resistance of solid substrates in relative motion. Therefore, those findings are expected to foster the exploration and development of computational simulation approaches, as a complement of experimental techniques, to investigate the fundamental phenomena present in tribological-relevant engineering systems.

Keywords: *organic friction modifiers, fatty amines, iron oxide surfaces, boundary lubrication regime, classical molecular dynamics, diffusion, adsorption, friction.*

Résumé

Les amines grasses sont présentes dans la formulation de lubrifiants automobiles, en tant que modificateurs de frottement organiques (MFO), afin d'atténuer les effets négatifs entraînés par le frottement et l'usure induits au sein des pièces sujettes aux conditions limites (c'est-à-dire, sous haute pression et basse vitesse de glissement). Outre leurs propriétés de lubrification, ces additifs présentent l'avantage d'être compatibles avec les systèmes de dépollution des gaz d'échappement, puisque leur composition organique est exempte d'éléments nocifs, tels que le soufre, le phosphore et certains métaux. Ainsi, un protocole de calcul de simulation en dynamique moléculaire classique a été mis en place et utilisé pour étudier, à l'échelle moléculaire, les propriétés des surfactants. En particulier, trois mécanismes d'action ont été considérés, à savoir : leur *diffusion* dans un milieu liquide, leur *adsorption* sur des substrats solides, et leur comportement en *frottement*. Dans ce contexte, différents facteurs associés à la structure des constituants des lubrifiants ont été analysés, notamment leur effet sur la performance des MFO. Les simulations révèlent que : *(i) Diffusion* — le coefficient de diffusion des composés aminés sont considérablement impactées par les caractéristiques de l'huile de base (exemple : leur polarité et masse moléculaire), sachant que les modèles de solvant les plus polaires et les plus lourds provoquent le ralentissement du flux diffusif des MFO ; par ailleurs, la structure des additifs jouent également un rôle dans leur diffusion, où les molécules les plus petites et les moins polaires s'avèrent relativement les plus mobiles. *(ii) Adsorption* — les amines primaires réagissent chimiquement avec une surface d'oxyde de fer, en formant des monocouches auto-assemblées, dont l'organisation et l'épaisseur augmentent avec leur taux de recouvrement. *(iii) Frottement* — les films adsorbés contenant d'amines constituées d'une chaîne hydrocarbonée C_{18} linéaire et saturée sont capables de réduire le frottement d'un système modèle représentant un nano-contact en régime limite ; en plus, leur efficacité dépend de la microstructure développée par les amines adsorbées sur les substrats sous compression et cisaillement ; d'ailleurs, les films permettant la formation de(s) plan(s) de glissement bien défini(s) entre les molécules organiques confinées sont davantage disposés à diminuer la résistance de glissement. Par conséquent, ces études ont permis de confirmer l'intérêt de l'apport d'une approche numérique complémentaire aux techniques expérimentales dans le but de comprendre les phénomènes élémentaires des systèmes tribologiques.

Mots-clés : *amines, oxyde de fer, dynamique moléculaire, diffusion, adsorption, frottement.*

Preface

The accomplishments made in this PhD thesis are the result of a fruitful collaborative project conducted by a large team involving academic and industrial partners. I am deeply grateful to all of them, for their countless efforts and valuable cooperation. Besides, I acknowledge the financial support of the *French National Association of Research and Technology* (ANRT), via a CIFRE agreement. For that, I thank every person that pays taxes in France.

In particular, I thank my academical supervisors: Manuel Cobián, for his meaningful computational expertise and for performing complementary DFT calculations, and Clotilde Minfray, for her considerable experimental knowledge and for managing the entire project. Despite some "high-friction" episodes encountered during this four-years journey, it was a great pleasure working with them and I really appreciated their guidance and mentoring.

I would like to thank Sophie Loehlé, my industrial supervisor, for her commitment and helpful support throughout this project. I am likewise thankful to Benoît Thiebaut, for his contribution to constructive discussions, and to Denis Lançon for his wake-up calls and project managing advice. Also, I thank other members of *Total* team, notably Eric Lacroix, Dominique Faure, Ghislaine Teillon, Catherine Bosson-Azzopardi and Jean-Yves Lacharte.

I will always be grateful to Toni Massoud — whose strength and life experience are genuinely admirable — for his experimental contribution and friendship. Additionally, I express my sincere appreciation to my colleagues: Deepthi Jose, Stéphane Tromp, David Souchon, Nicolas Scremin, Joana Pereira, Mariem Fall, Yuta Muratomo, Haohao Ding, Mariana de Souza, Mayssa Al kharboutly, Vilayvone Saisnith, Takeshi Kunishima and Amaury Guillermin. Special thanks to Hélène Schoch, who have always helped me with administrative tasks. I also extend my thanks to other members of *ECL*, *INSA Lyon* and *UCLB - Lyon I*, namely: Franck Dahlem, Thierry Le-Mogne, Michel Belin, Laurent Pouilloux, Dan-Gabriel Calugaru, Sandrine Bec, Vincent Fridrici, Maria-Isabel de Barros Bouchet, Fabrice Dassenoy, Christophe Pera and Jean-Yves Buffière. Moreover, I would like to take this opportunity to thank Prof. Akira Miyamoto and his team, for their warm welcome in Sendai and interesting discussions.

Finally, I grateful to my esteemed friends: Amanda, Marina, Rosiane, André, Estefânia, Hamilton, Raiana, Roberto, Charlotte, Olívia, Guilherme, Nicolas, Beto, Cátia, Paula, Anne-Cat', Audrey, Gayou, Stéph', Natacha, Vincent and Anna Luiza. Last but not least, I express my deep gratitude to my precious Brazilian and French families, which are the rock of my foundation!

"A vida é um soco no estômago."

(Clarice Lispector, in *A hora da estrela*)

"O que dá o verdadeiro sentido ao encontro é a busca, e é preciso andar muito para se alcançar o que está perto."

(José Saramago)

"Life is a text that we learn to read too late."

(Iván Capote)

"Mintam, mintam por misericórdia!"

(Nelson Rodrigues)

"I am certain of nothing but the holiness of the Heart's affections and the truth of the Imagination."

(John Keats)

To my beloved brother, Ricardo Pereira de Matos,
who has always spurred me on to eagerly fight for my dreams.

Rafael Pereira de Matos, Écully, April 19th 2019

Abbreviations & Acronyms

ACEA European Automobile Manufacturers' Association

AFM Atomic force microscopy

API American Petroleum Institute

AW Anti-wear additive

BL Boundary lubrication (regime)

BO Base oil(s)

CAFE Corporate Average Fuel Economy standards

CIFRE Conventions Industrielles de Formation par la Recherche

DFT Density functional theory

EC European Commission

EMD Equilibrium molecular dynamics

EPA (U.S.) Environmental Protection Agency

EU European Union

FM Friction modifier(s)

GGA Generalized gradient approximation

GHG Greenhouse gas(es)

HL Hydrodynamic lubrication (regime)

ICE Internal combustion engine(s)

ILSAC International Lubricants Standardization and Approval Committee

LAMMPS Large-scale atomic/molecular massively parallel simulator

LFM Lateral force microscopy

LJ Lennard Jones (potential)

MD Molecular dynamics

MFO Modificateur(s) de frottement organique

ML Mixed lubrication (regime)

MoDTC Molybdenum dithiocarbamate

MS Maxwell-Stefan theory

MSD Mean-squared displacement

MY Methyl yellow (4- dimethylaminoazobenzene)

NEDC New European Driving Cycle

NEMD Non-equilibrium molecular dynamics

NHTSA National Highway Traffic Safety Administration

NMR Nuclear magnetic resonance

NPT Isothermal-isobaric ensemble

NVE Microcanonical ensemble

NVT Canonical ensemble

OFM Organic friction modifier(s)

OPLS-AA All-atom optimized potentials for liquid simulations

PAG Polyalkylene glycol

PAO Poly-alpha-olefin

PBC Periodic boundary conditions

PBE Perdew-Burke-Ernzerhof functional

PFG Pulsed-field gradient

PM-IRRAS Polarization modulation-infrared reflection-adsorption spectroscopy

PPPM Particle-particle particle-mesh solver

QCM Quartz crystal microbalance

RDF Radial distribution function

RMS Root-mean-square (roughness)

SAM Self-assembled monolayer(s)

SC Surface coverage

SFA Surface force apparatus

SFG Sum frequency generation spectroscopy

SFM Scanning force microscopy

TBQC-MD Tight-binding quantum chemical molecular dynamics

VACF Velocity autocorrelation function

VASP Vienna *ab initio* simulation package

vdW van der Waals (forces / interactions)

VII Viscosity index improvers

WLTP World-Harmonized Light-duty vehicle Test Procedure

XPS X-ray photoelectron spectrometry

ZDDP Zinc dialkyldithiophosphate(s)

1

Introduction

1.1 Context

It is undeniable that automobiles offer diverse benefits in terms of mobility for people, and as a practical option to deliver goods and services considered essential in our modern lives. However, they impose adverse costs to society, harming the air quality in urban areas and contributing to global climate change, which has been associated with anthropogenic *greenhouse gas* (GHG) emissions.[1–3]

As a matter of fact, conventional vehicles equipped with *internal combustion engines* (ICE) generate several tailpipe pollutants as byproducts of the petroleum-based fuel combustion, such as *carbon dioxide* (CO_2, a GHG), nitrogen oxides (NO_x) and particulates.[3] In addition, the mechanical moving parts composing these engines induce unwanted *friction*, which leads in turn to energy dissipation — usually in the form of heat —, thereby reducing powertrain efficiency, increasing fuel consumption, and raising exhaust gas emissions.[4–7]

To illustrate that issue, it is worth noting that, in the European Union (EU), passenger cars, light-commercial and heavy-duty vehicles equipped with ICE technology are responsible for the largest portion of CO_2 emissions produced by the transport sector, which approximately represent 23% of the total amount of GHG emitted in these countries.[8–10] Besides, CO_2 emis-

sions from activities related to the transportation sector have recorded a significant increase at the European level since 1990, as can be seen from figure 1.1.[8] Despite a recent reduction in test-cycle emissions for new vehicles, the observed increase in CO_2 emissions comes from a growth in vehicle fleet and in number of kilometers driven, from a shift toward larger vehicles, as well as from a widening gap between test-cycle findings and real-world emissions.[8]

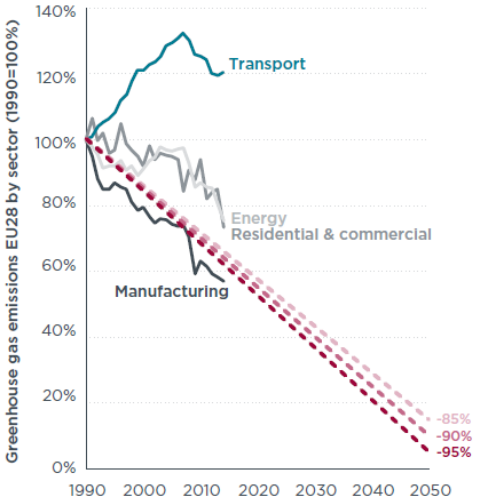

Figure 1.1 – GHG emissions in the EU by activity sector, including an aspirational target range (dashed lines) representing the EU's goals for reducing emission levels by 2050, from all sources and by 85-95% compared to 1990 baseline.[8,11]

Therefore, there is an urgent need to reduce the carbon footprint of road transport.[12] In that perspective, governments worldwide have recently adopted or strengthened GHG emissions and fuel economy standards in order to reduce fossil fuel consumption and limit the amount of CO_2 emitted by new vehicles (cf. figure 1.2, p. 3).[10,13] For instance, the European Commission (EC) set in 2013 a second mandatory regulation[1] that establishes an average CO_2 emission target of 95 g/km for new passenger cars, which must be met by 2021.[9,10] More recently, in 2018, the EC has updated its transport GHG regulation, targeting a further ambitious decrease in CO_2 emissions of light vehicles by 15% by 2030, and by 37.5% by 2050.[15,16] In the United States, current fuel economy regulation[2] for passenger vehicles and light trucks requires, by 2025, a performance of 54.5 miles per gallon of gasoline, or equivalently,[3] a CO_2 emission target of 99 g/km.[3,10]

[1] Regulation (EC) n° 333/2014. A summary of the mentioned legislation can be found in the indicated reference.[14]

[2] *Corporate average fuel economy* standards (CAFE), regulated by the *National Highway Traffic Safety Administration* (NHTSA), which works in collaboration with the *U.S. Environmental Protection Agency* (EPA), responsible for the measurement control of vehicle fuel efficiency in the USA.

[3] The reduction of CO_2 *emissions* implies a reduction in *fuel consumption*, as they are effectively proportional.[17]

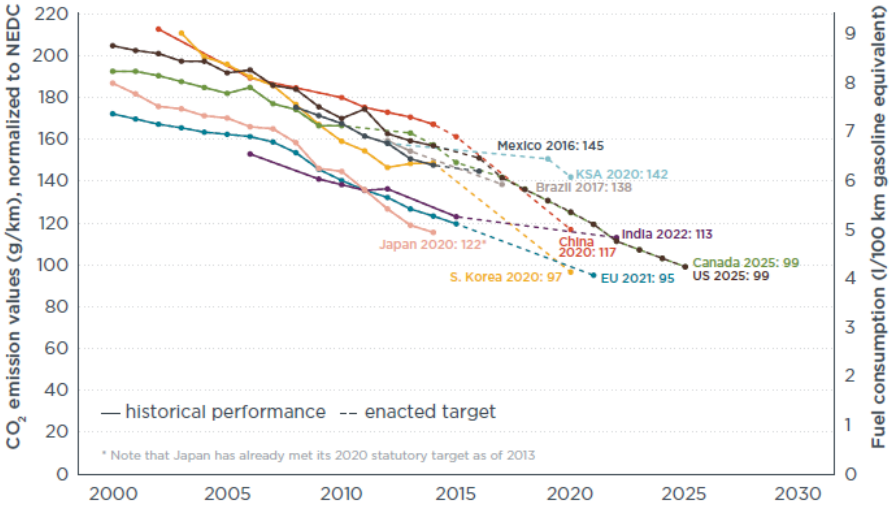

Figure 1.2 – Historical fleet CO_2 emissions performance and current standards (gCO_2/km normalized to *New European Driving Cycle*, NEDC) for passenger cars. Notice that NEDC is the old European testing procedure used to measure vehicles' fuel consumption and CO_2 emissions. It was replaced in 2017 by a new test methodology named *World-Harmonized Light-duty vehicle Test Procedure* (WLTP), which better represents everyday driving profiles, and consequently, real-world CO_2 emissions.[10] Further information can be found on: `http://wltpfacts.eu/`.

In order to comply with these stringent vehicle efficiency regulations, automotive related industries have been seeking innovative solutions to improve ICE performance, to promote fuel economy, and eventually, to minimize tailpipe emissions.[4] In that way, vehicle manufacturers have redesigned *powertrain hardware* (*e.g.*, downsizing of engine components combined with turbocharging, addition of fuel direct injection, cam-profile switching, and variable valve-lift and timing), adopted *load-reduction solutions* (*e.g.*, lightweighting, improved aerodynamics, and lower tyre rolling resistance) and developed *off-cycle*[5] *technologies* (*e.g.*, engine idle stop, powertrain-warm up, and electric heater circulation pump), among other technological innovations.[13, 18, 19]

Besides, *engine lubricants* have become an essential component for the successful development and application of these emerging fuel-efficient technologies.[20–26] Indeed, with modern engines getting smaller and power output densities going up, lubricants must ensure overall vehicle protection and operability in much more complex and severe conditions. Also, it is expected that lubricants offer a greater contribution to fuel economy by means of lower vis-

[4] For information, *electric*, *fuel cell electric*, *hydrogen* and *all hybrid vehicle* technologies were not targeted and treated in this work.

[5] *Off-cycle technologies* comprise design features or equipments that improve fuel efficiency but whose effects cannot be directly measured through laboratory-based test procedures used to certify new vehicles against fuel-economy and GHC emission requirements.[18]

cosity *base oils* (BO) blended with an optimized balance of suitable *additives*, such as *viscosity index improvers* (VII), *friction modifiers* (FM) and *anti-wear* (AW) agents, among others.[6] The FM and AW additives are specially adapted to maintain a reliable operation in *boundary lubrication* (BL) regime, where the lubricating film thickness between the two opposing surfaces is lower than their root-mean-square roughness (cf. figure 1.3).[27,30] In these circumstances, there is not enough liquid lubricant within the rubbing surfaces and their asperities can come into direct contact, which may lead to higher friction, wear and even adhesion.[6,31]

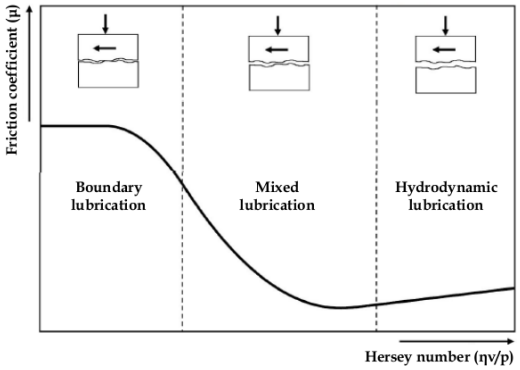

Figure 1.3 – *Stribeck curve* describing the evolution of the *friction coefficient* (μ) as a function of the *Hersey number* ($\eta v/p$; where η is the lubrication viscosity, v is the surface velocity and p is the normal load), along with the different *lubrication modes*: *hydrodynamic* (HL), *mixed* (ML) and *boundary regimes* (BL).[27,32] Actually, when Hersey number is high, the opposing surfaces are separated by a sufficiently thick liquid film and low friction and wear are achieved, defining the *hydrodynamic regime*. When the Hersey number is small, the lubrication mode changes to *boundary regime*: the surfaces come into contact with each other and high friction and wear are observed. A *mixed lubrication regime* is an intermediate mode between hydrodynamic and boundary regimes. (figure adapted from the indicated reference)[32]

For these reasons, advanced lubricant formulations must be tailored to obtain an improved oil robustness, to effectively control wear, deposits and oxidation, as well as to provide higher fuel economy throughout the oil change interval, all while being compatible with exhaust gas treatment systems.[7] Concerning the additives required for these higher performance engine oils, there are four main classes of materials used as friction modifiers: (oil-soluble) organomolybdenum compounds, *organic friction modifiers* (OFM), functionalized polymers and dis-

[6] With respect to the chemical composition of a *fully formulated engine lubricant*, it contains between 80% and 95% of a (mineral or synthetic) *base stock*, and the remainder is represented by an *additive package*, comprising *tribo-improvers* (*e.g.*, extreme pressure agent, anti-wear agent, friction modifier), *maintainers* (*e.g.*, anti-oxidant, detergent, corrosion inhibitor, dispersant, anti-foam agent, demulsifier), and *rheo-improvers* (*e.g.*, pour point depressant, viscosity modifier).[27–29]

[7] All of those performance requirements are addressed by the *new generation engine oil specifications*, such as the ACEA 2016 oil sequence and the forthcoming ILSAC GF-6. For detailed information on these lubricant standards, the interested reader is referred to some specific references.[20–26]

persed nanoparticles.[33,34] Nevertheless, this PhD thesis has focused exclusively on OFM additives, which have regained interest in recent years as a promising candidate to meet new generation lubricant specifications, particularly for criteria related to fuel economy improvement, engine protection and compatibility with aftertreatment systems.[6,30,31,33–66] For additional information about the other mentioned FM classes, comprehensive reviews are available in recent literature.[33,34]

Actually, OFM are surfactant compounds having predominately organic elements, namely *carbon*, *hydrogen*, *nitrogen* and *oxygen* atoms.[34] Their amphiphilic molecular structure comprises a long nonpolar hydrocarbon tail functionalized — at one end of their backbone chain — with one or more polar groups possessing affinity for metal surfaces.[34] Commercial OFM typically have a straight alkyl chain — whether saturated or unsaturated — containing from 12 to 20 carbon atoms (C_{12}-C_{20}), which ensures their solubility within the lubricant BO.[34,57] Incidentally, it is known from the specialized literature that the hydrocarbon tail must have at least 14 carbons in order to yield a low and stable friction coefficient.[67,68] Moreover, possible polar heads include *carboxyl*, *hydroxyl*, *ester*, *amine*, *carboxyamide* and their derivatives, as well as other functional groups.[6,33,34] Therefore, since their chemical composition does not exhibit any sulfur, phosphorus or metal atom, these additives are compatible with catalytic converters present in modern post-combustion control devices.

In practice, OFM are *surface-active molecules* adapted to act under BL conditions, by forming a *thin low-shear-strength film*, adsorbed on the sliding surfaces, thereby reducing friction and preventing their rubbing asperities from a direct contact, which may eventually lead to damaging wear (cf. figure 1.4).[27,33,34]

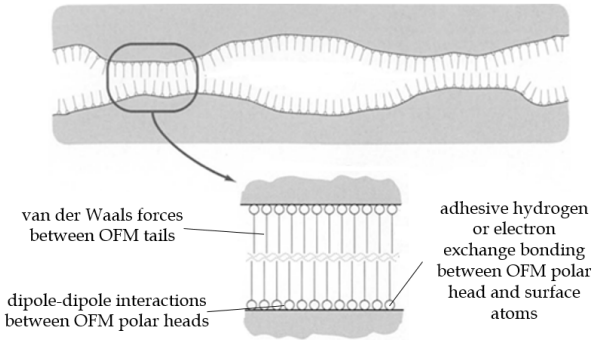

Figure 1.4 – Schematic illustration of a model lubricated contact describing highly orientated, close-packed monolayers of OFM molecules adsorbed on rubbing substrates. The polar head groups are represented by circles and nonpolar tail groups are represented by lines. (figure adapted from the indicated reference)[27]

The prevalent lubrication models proposed in the literature to explain the friction-reducing properties of OFM rely on the hypothesis that these additives adsorb and self-assemble on surfaces to form *vertically oriented, close-packed monolayers*[8] (cf. figure 1.4, p. 5), especially when their alkyl tail structure permits a linear configuration.[27,28,33,34,60,70–72] In fact, adsorption occurs through physical and/or chemical interactions between the OFM polar group and the solid substrate.[31,34] Then, as a result of the attractive forces between the anchored head groups and between proximal hydrocarbon chains, the molecules align themselves and form multimolecular clusters, covering the surface with an incompressible protective film.[28] In particular, the *interchain van der Waals (vdW) bonding* confers strength and robustness to the adsorbed monolayers that support the applied load, while the opposing alkyl tails provide a plane of low shear strength, which eventually mitigates friction during rubbing processes.[34]

It is thus important to highlight that the effectiveness of OFM additives strongly depends on their *molecular structure* and *chemistry*, which define their ability to form an adsorbed and close-packed film on the engine component surfaces. Besides, their friction and wear control behavior observed at macroscopic scale is driven and governed by molecular-level events. Therefore, an in-depth understanding of the mechanisms occurring at the liquid/substrate interface and involving the different lubricant constituents is needed to point out innovative ways of enhancing their low friction and fuel-economy properties.

In this context, *Total Marketing & Services* and *LTDS*[9] laboratory have been working together in order to better understand the OFM mechanisms of action, through computational and experimental techniques. The major target is to discern the *key structural factors* and *performance indicators* likely to improve their tribological behavior, and to identify *structure-property relationships* between them. Beyond that, the long-term industrial objective is to develop predictive tools, based on a *molecular engineering approach*, allowing the design of novel and more efficient additives to be done, which are capable of meeting the needs of the evolving automotive industry and environmental legislation. To achieve these ambitious aims, it is thus crucial to elucidate the links existing between OFM molecular structure and their friction-reducing properties. That is why molecular-level simulations are employed to supplement conventional experiments (*e.g.*, surface analyses and friction tests), as well as to obtain insights from the nanoscale behavior of lubricant constituents.

[8] Even though multilayer OFM films have also been observed in macroscopic experiments,[64,69] their role in lubrication still remains a subject of debate and they are not considered in our computational studies.

[9] LTDS: *Laboratoire de Tribologie et Dynamique des Systèmes* (Écully, France).

In previous works of Dr. Sophie Loehlé and Dr. Christine Matta (2011-2014),[31,46,55,56] fatty acids containing a straight C_{18} aliphatic tail group were studied by means of molecular simulations (*e.g., tight-binding quantum chemical molecular dynamics*, TBQC-MD) and experimental techniques (*e.g., X-ray photoelectron spectroscopy*, XPS; *polarization modulation-infrared reflection-adsorption spectroscopy*, PM-IRRAS; *tribo-tests*). Their adsorption mechanisms on ferrous surfaces, along with their tribological properties, were investigated as a function of unsaturation degree of their hydrocarbon chain, considering saturated, mono- and diunsaturated molecules (cf. figure 1.5). The employed coupling methods have confirmed that these fatty acids do react with iron-based surfaces, mainly under sliding conditions, forming strongly bonded monolayers that adeptly control friction and wear.[55] The obtained results have also shown that the unsaturation present in the nonpolar tail leads to steric effects that inhibit the organization of close-packed films, decreasing their lubricating efficiency.[46,56]

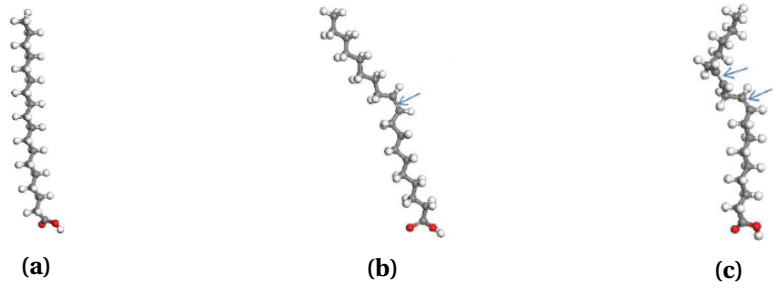

Figure 1.5 – C_{18} fatty acids: **(a)** *stearic acid* ($C_{18}H_{36}O_2$); **(b)** *cis-9-oleic acid* ($C_{18}H_{34}O_2$); **(c)** *cis-9-cis-12-linoleic acid* ($C_{18}H_{32}O_2$). Note that the double carbon bonds are indicated by blue arrows. (figures retrieved from the indicated reference)[31]
Atomic color code: white - hydrogen, *gray* - carbon, *red* - oxygen.

In the framework of this PhD thesis, research efforts were concentrated on other OFM structural factors and chemistry, notably on *nitrogen-containing molecules*, such as the *saturated C_{18} primary amine* showed in figure 1.6. In the next section, the chief aims of the current work are described, as well as the methodology used to carry out the simulation studies covered in this manuscript.

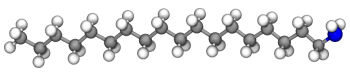

Figure 1.6 – Fatty amine investigated in this thesis as OFM model ($C_{18}H_{39}N$).
For information, the molecular images depicted in this manuscript were rendered using visualization tools such as *OVITO*[73] and *VMD*.[74]
Atomic color code: white - hydrogen, *gray* - carbon, *blue* - nitrogen.

1.2 Aims of the work and methodology

The main objective of this thesis was to establish a *simulation protocol* enabling the investigation and screening of OFM additives at the atomic scale. In particular, the simulations must cover and represent different (isolated) aspects of their *mechanisms of action*, namely: *(i)* molecular diffusion within the bulk of a liquid BO; *(ii)* structural organization of an OFM-based self-assembled monolayer (SAM) adsorbed on a ferrous substrate; *(iii)* friction-reducing behavior of a thin lubricating layer, containing OFM and BO molecules, subjected to confinement and shear. To do so, the C_{18} primary amine ($C_{18}H_{39}N$; cf. figure 1.6, p. 7) was selected as the additive model for the development and the validation of those computational procedures.

Different molecular simulation methods and interaction potentials were evaluated during the first part of this PhD project, in order to select the most relevant technique(s) and force field(s) able to address the considered OFM mechanisms (*i.e.*, diffusion, adsorption and friction processes). As a result of that preliminary assessment, *classical molecular dynamics* (MD) was chosen and then used to set up the desired protocol employed in the simulation studies that are described hereafter. Further details about MD method are provided in chapter 2 (cf. § 2.2, p. 23), along with the description of the interatomic potentials selected to mimic the lubricant and substrate interactions. Besides, since classical MD cannot represent the electronic structure of a molecule and thus cannot provide reactivity information, supplementary calculations based on the *density functional theory* (DFT)[75] were employed to investigate the adsorption mechanism of fatty amines at the quantum level (cf. chapter 4, § 4.1.1, p. 67). The *ab initio* analysis was carried out by Dr. Manuel Cobián (member of LTDS laboratory and co-advisor of this thesis), and its results were used to derive an interfacial potential adapted to reproduce the interactions between the investigated OFM and the surface models.

Furthermore, it is important to stress that particular care was taken to obtain a reliable set of MD simulations that provides a reasonable balance between the *atomic-level description* of the modeled systems, the *accuracy* related to their calculations, and the *computing resources* required to perform the numerical studies. Because of the inherent limitations imposed by the computational methods, in terms of time and length scales that can be simulated in practice, these "*computer experiments*" were designed taking into account relatively *ideal conditions* (*e.g.*, OFM-based SAM adsorbed on flat and smooth surfaces; high shear rates), *small system models* (*e.g.*, dimensions less than 1 μm) and *short periods of time* (*e.g.*, duration of a few nanoseconds).

Therefore, in proposing this simulation protocol, there is no ambition to accurately describe all of the complex, macroscopic tribological phenomena occurring in real engineering systems (*e.g.*, an ICE). Instead, we have rather aligned our simulation models with the well-controlled conditions that characterize the nanoscale experiments used to probe interfacial materials employed in boundary lubrication (*e.g.*, XPS and *atomic/lateral force microscopy*, AFM/LFM).

It should also be noted that, simultaneously with this simulation-based PhD thesis, Dr. Toni Massoud (postdoctoral researcher), Dr. Franck Dahlem (associate professor in ECL) and other LTDS members have performed a series of experimental studies related to the adsorption and the lubricating properties of different fatty amines in steel-steel sliding contacts, using different techniques such as friction tribo-tests, *in-situ* XPS and liquid cell *scanning force microscopy* (SFM).[61] Their valuable results have guided the simulation models adopted in our numerical studies and they will be described later.

In what follows, the three MD simulation studies composing this work are outlined, covering the *diffusion*, *adsorption* and *friction-reducing behavior of OFM*, and mainly focusing on the action mechanisms of an amine-based molecule ($C_{18}H_{39}N$).

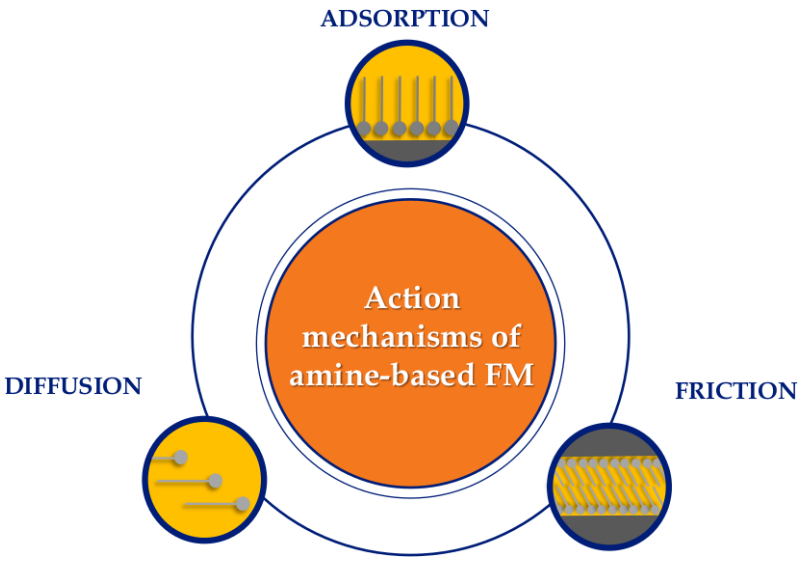

Figure 1.7 – OFM simulation studies covered in this manuscript.

1.2.1 Diffusion study

Thorough research has been undertaken to investigate the adsorption and tribological performance of OFM as a function of their molecular structure (*e.g.*, head group chemistry; hydrocarbon tail length, branching and unsaturation), the nature and roughness of the solid substrate, as well as a function of other important variables (temperature, pressure, shear rate, etc.). For comparative purposes and owing to methodology concerns, most of these fundamental academic studies have explored each of these factors in isolation and under controlled conditions, and also considering, for example, lubricant models consisting in a binary solution of a single OFM dissolved in a given solvent. However, commercial engine oils are formulated with an additive package containing several polar molecules (*e.g.*, anti-oxidants, dispersants, detergents) and surface-active compounds (*e.g.*, extreme pressure and AW agents, corrosion inhibitors and other FM), which may compete with OFM for metal surfaces, directly affecting the development of their protective BL film.[29,76,77] Yet, there seem to be fewer studies addressing the interaction and/or competition between OFM and other lubricant additives.

Relationship between competitive adsorption and diffusive behavior of OFM

Campen *et al.*[60] have investigated the competitive adsorption of OFM, and also their film removal and regeneration under shear, by determining the boundary friction of an additive (OFM A), before and after the addition of other compound into the solution (OFM B). It was found that, after adding the second OFM, the friction coefficient changes with the number of passes made over the surface. A schematic illustration of that experience is given in figure 1.8.[60]

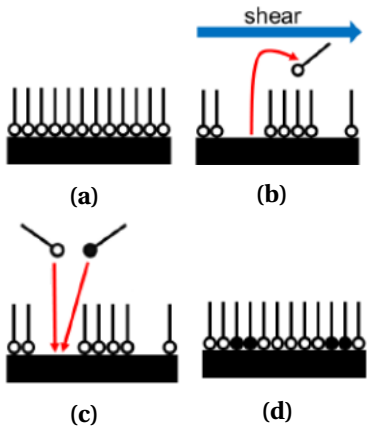

Figure 1.8 – *Langmuir-type model* used to describe the composition of the BL film during competitive adsorption: **(a)** initial monolayer film containing OFM A; **(b)** shear removal; **(c)** competitive adsorption between OFM A and B; **(d)** regenerated film containing both additives. (figure adapted from the indicated reference)[60]

Actually, that experimental study sheds light on the *dynamic behavior* of an OFM film (*i.e.*, formation, removal and regeneration during the sliding friction test), whose composition evolves with time, as a consequence of the competition among the numerous additives for the surface adsorption sites.

Besides, it has been shown that competitive adsorption may lead to a negative impact on the overall lubrication performance for mixed additive systems. Indeed, Loehlé *et al.*[46] have observed an *antagonistic effect* for the mixtures of saturated and unsaturated C_{18} fatty acids (stearic, oleic and linoleic acids, cf. figure 1.5, p. 7) blended in a synthetic poly-alpha-olefin BO (PAO 4). Their friction-reducing efficiency were tested on iron oxide surfaces under mixed boundary regime, and with different temperatures (323, 373 and 423 K).[46] Among these three studied OFM models, the single stearic acid — which is the saturated molecule — has shown the best tribological performance at 423 K, with a low friction coefficient and no visible wear.[46] However, that lubricating behavior was inhibited in the presence of unsaturated molecules (*i.e.*, oleic and linoleic acids), in particular at the highest probed temperature.[46]

To understand that antagonistic effect, MD simulations were then performed to evaluate the *diffusion coefficient* of the three fatty acids in a bulk liquid model of PAO 4. The obtained results showed that unsaturated molecules diffuse faster than the saturated one, for all of the studied temperatures, and they also indicate that the molecular diffusivity increases with temperature.[46] Thus, it has been suggested that, in mixtures of saturated and unsaturated acids, the unsaturated molecules reach the surface first and block it from saturated ones, to the detriment of low friction.[34,46] Most importantly, these results have pointed out the fact that the additive which exhibits the best friction-reducing effect may not necessarily be the one that reaches the surface first.[60]

Therefore, *diffusive* and *competitive behaviors* must not be overlooked on the performance evaluation of candidates for lubricating additives. In particular, the diffusion coefficient seems to be a suitable parameter to provide insights into the kinetic behavior of OFM within the bulk oil, and to help the interpretation of experimental data related to mixed additive systems.

Study of OFM diffusivity

Based on these findings, we have integrated in our MD simulation protocol a procedure to determine the OFM diffusivity in a given BO. Since it has been demonstrated that unsaturated fatty acids diffuse faster than saturated ones,[46] we further explored the link between the molecular structure and the diffusion coefficient, by investigating different features related not only to the OFM architecture (aside from the unsaturation degree present in their tail group), but also concerning the BO chemistry. In fact, the aim of this diffusion study was to better understand the influence of different structural parameters on OFM liquid dynamics, in an attempt to identify possible ways to enhance their diffusion rate, since we have assumed that *a faster molecule is likely to have a greater advantage during the adsorption process in presence of other competing additives*. That information might thus be useful for the design of OFM, intended to be incorporated into a fully formulated lubricant.

In practice, we have calculated the diffusion coefficient of various surfactant molecules, representing the OFM additives, and in different BO models, in order to compare them with each other and then to discern the effect of the following factors:

- *OFM head group chemistry*: other than the C_{18} primary amine, molecules containing different functional groups were selected, such as *carboxyl*, *hydroxyl*, *primary carboxylamide* and an *alkyl group*. In fact, the alkane molecule was utilized as a *reference model* of a C_{18} tail without a polar terminal group.
- Concerning *amine-based molecules*, three additional parameters were investigated:
  - *Number and nature of hydrogen substituents associated to nitrogen atom*: secondary and tertiary amines, with alkyl and ethoxylated groups (molecules with a C_{18} tail);
  - *Hydrocarbon tail length*: primary amines with C_6, C_{12}, C_{18} and C_{24} chains.
- *BO polarity nature*: molecules with different degrees of polarity were chosen to represent a nonpolar and a polar BO, being used as solvent model in the diffusivity calculation of all previously mentioned OFM models.

Moreover, we specify that only the *structural characteristics* associated with the lubricant constituents were varied and investigated in this study, and the physical conditions of *temperature* and *pressure* were maintained constants at 373 K and 1 atm, respectively. In addition, it should be indicated that all molecules considered here are described in the next chapter (cf. § 2.1, p. 18), and the diffusion study is fully detailed in chapter 3 (cf. p. 35).

1.2.2 Adsorption study

Following the track of additives dissolved within a lubricant solution, OFM diffuse into the base oil and they are then attracted by the polar surfaces of the thermal engine. To be effective in boundary contacts, they need to adsorb onto the lubricated components and form low-shear-strength films that keep the rubbing parts separated from each other. As a consequence, the friction-reducing properties of these adsorbed OFM films depend on the nature and the strength of their interfacial interactions with the solid substrates, as well as on the resulting film structure and density, which are directly linked to their *molecular surface coverage*[10] (Γ).[27,77]

Regarding our simulation protocol, and particularly the adsorption process of amine-based FM, it is not possible to elucidate their interaction nature with ferrous surfaces through classical MD simulations. Accordingly, the *adsorption mechanism* of primary amines on iron oxide substrates (*e.g.*, on hematite: α-Fe_2O_3) was studied using DFT calculations and XPS measurements. The results obtained from these alternative techniques have suggested a *chemisorption mechanism* for the considered OFM model. Further details are given in chapter 4, cf. § 4.1, p. 66). Then, the *adsorption energy* (E_{ads}) related specifically to the *(primary) amine-hematite interaction* was determined by DFT and used, as an energetic reference, to parameterize an *interfacial MD potential* required to describe the dynamic behavior of amine layers adsorbed on ferric oxide substrates. Lastly, a series of MD simulations was performed to investigate the structure and molecular organization of different SAM models, as a function of their surface coverage (cf. figure 1.9). This adsorption study is covered in chapter 4 (cf. p. 65).

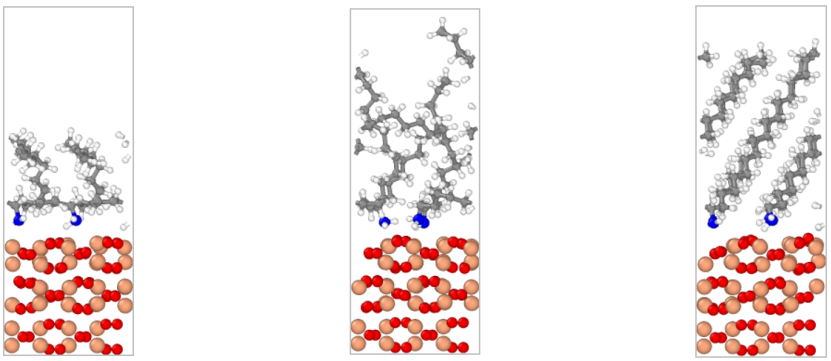

(a) Γ = **1.8 nm^{-2}** **(b)** Γ = **2.7 nm^{-2}** **(c)** Γ = **3.6 nm^{-2}**

Figure 1.9 – MD simulation snapshots representing the structure of ideal monolayers, made up of C_{18} primary amines adsorbed on an α-Fe_2O_3 slab. *Atomic color code: coral* - iron, *red* - oxygen, *white* - hydrogen, *gray* - carbon, *blue* - nitrogen.

[10] The *surface coverage*, Γ, is a quantitative indicator reflecting the density of adsorbed OFM films, being quantified as the number of OFM head groups per area of surface (possible Γ units: mol $\times$ m^{-2} and nm^{-2}).[57]

1.2.3 Friction study

After addressing the diffusion, the adsorption and the molecular assembly processes of OFM additives, a large-scale MD simulation was finally established to study their frictional behavior and response under ideal mechanical operating conditions. This simulation aims to mimic a model friction experiment at nanoscale, enabling the calculation of a "*computational friction coefficient*" (μ^*), which reflects the links between the OFM structure and their lubricating property, as a function of a specific range of tribological conditions (*e.g.*, applied normal load, molecular surface coverage, sliding velocity, etc.).

In fact, the systems investigated in the so-called *confined shearing simulations* are model contacts that basically represent single and smooth surface asperities, composed of two opposing and sliding hematite slabs, each one being covered by an adsorbed SAM of a given molecular density and formed by C_{18} primary amines (cf. figure 1.10). Some models also contain an intermediate BO-layer, confined between the opposing OFM films (cf. figure 1.10b). Besides, all systems are kept compressed by a high contact pressure and under a specific shear rate, in order to assess the OFM ability to lower the induced friction forces. The complete study is reported in chapter 5 (cf. p. 97).

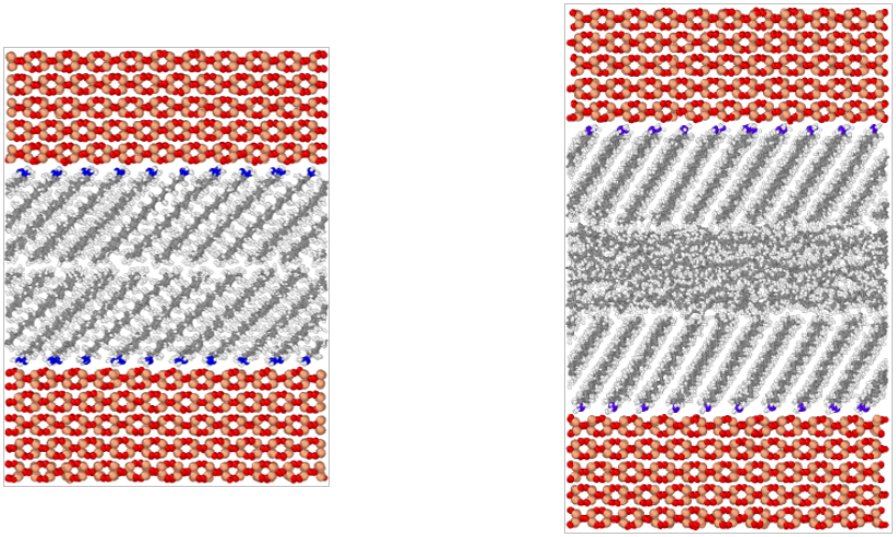

(a) Contact with SAM/SAM interface **(b) Contact with SAM/BO/SAM interface**

Figure 1.10 – Representative examples of the simulated systems used to model ideal nano-contacts formed by hematite slabs separated by adsorbed amine-based SAM (Γ = 3.6 nm^{-2}), with an interface: (**a**) *without confined BO molecules*; (**b**) *including a thin BO layer. Atomic color code: coral* - iron, *red* - oxygen, *white* - hydrogen, *gray* - carbon, *blue* - nitrogen.

To sum up, table 1.1 outlines the key features of the computational studies carried out to investigate the working mechanisms of an amine-based OFM model.

Table 1.1 – MD simulation protocol

Study	Investigation on
Diffusion	*Diffusion coefficient* (cf. chapter 3, p. 35), as a function of: • BO polarity • OFM polar head chemistry • hydrogen substituents (nature and number) • hydrocarbon tail length
Adsorption	*SAM structure: film density & molecular organization* (cf. chapter 4, p. 65), as a function of: • surface coverage
Friction	*Friction coefficient* (cf. chapter 5, p. 97), as a function of: • SAM surface coverage • interfacial film composition: presence (or not) of a BO-layer • sliding velocity

The remainder of this manuscript is organized as follows: chapter 2 provides a brief review of the materials and the computational method used in this work (cf. p. 17); chapters 3, 4 and 5 describe the simulation studies related to OFM diffusion, absorption and friction-reducing behaviors, respectively (cf. p. 35, 65 and 97, respectively); and ultimately, the main achievements of this doctoral project, as well as its perspectives, are summarized in chapter 6 (cf. p. 143).

2

Materials and Methods

For the successful development of lubricant additives that enhance engine efficiency and improve fuel economy, it is essential to obtain a better understanding of the microscopic phenomena governing their macroscopic properties. In this context, molecular dynamics simulations were used to investigate the OFM behavior at nanoscale, and to potentially gain insights into their action mechanisms that would be difficult to obtain experimentally.

The current chapter specifies the lubricant and substrate models considered in our computational studies (cf. § 2.1, p. 18), and it also provides a few basic principles of the MD method and some details of the employed classical force fields (cf. § 2.2, p. 23).

2.1 Materials

2.1.1 Lubricant model

For the diffusion study, an engine oil was defined as a *binary solution* comprising a single OFM (*i.e.*, the *solute*, whose concentration is fixed at 1 wt.%) and a given BO (*i.e.*, the *solvent*). Based on the broad expertise in both lubricant composition and additive chemistry of our industrial partner, two molecules with different degrees of polarity were selected to model a *non-polar BO*, representing the oils of the group IV[1] (*poly-alpha-olefin model*, PAO), and a *polar BO* characterizing the polyethers of group V (*poly-alkylene glycol model*, PAG). Both molecules are illustrated in figure 2.1.

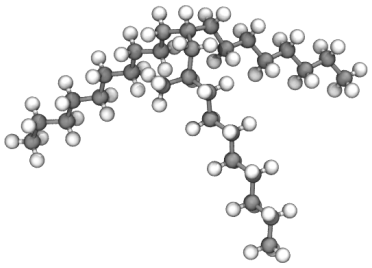

(a) PAO model ($C_{30}H_{62}$)

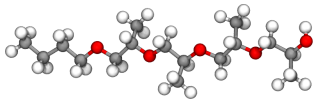

(b) PAG model$^{(*)}$ ($C_{29}H_{60}O_6$)

Figure 2.1 – Molecular structure of BO models used to represent synthetic oils with a kinematic viscosity of 4 $mm^2 \cdot s^{-1}$ at 373 K (PAO 4 and PAG 4). *Atomic color code: gray* - carbon, *white* - hydrogen and *red* - oxygen. $^{(*)}$ Notice that the PAG molecule illustrated here corresponds to a general structure of *polyalkylene glycols*, since the one used in our simulations cannot be displayed in this manuscript because of confidential reasons. However, the indicated molecular formula corresponds to the real molecule used to model the PAG base oil.

Concerning the OFM models, eleven *amphiphilic saturated molecules* were chosen to represent these additives in our MD simulations, in particular for the calculation of their diffusion coefficient. Also, a *linear alkane* was considered as a reference model of a molecule without polar head group. Their structures are shown in figure 2.2 (cf. p. 19) and supplementary information is given in table 2.1 (cf. p. 20).

[1] According to API base oil categories (*e.g.*, groups I – V).[29] For further information: `http://www.api.org/`.

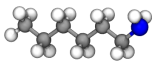

(a) C_6 primary amine [*n-hexylamine*; $C_6H_{15}N$]

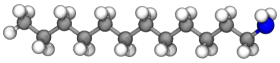

(b) C_{12} primary amine [*n-dodecylamine*; $C_{12}H_{27}N$]

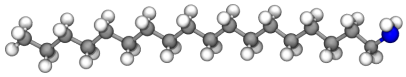

(c) C_{18} primary amine [*n-octadecylamine*; $C_{18}H_{39}N$]

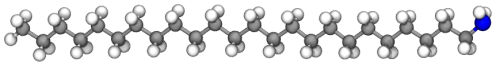

(d) C_{24} primary amine [*n-tetracosanamine*; $C_{24}H_{51}N$]

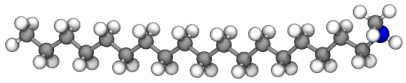

(e) C_{18} secondary alkyl-amine [*n-methyl-1-octadecylamine*; $C_{19}H_{41}N$]

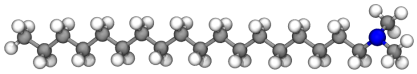

(f) C_{18} tertiary alkyl-amine [*n,n-dimethyl-1-octadecylamine*; $C_{20}H_{43}N$]

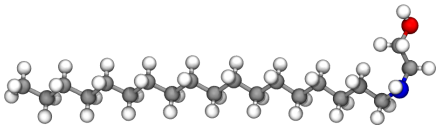

(g) C_{18} secondary ethoxylated-amine [*2-(octadecylamino)ethanol*; $C_{20}H_{43}NO$]

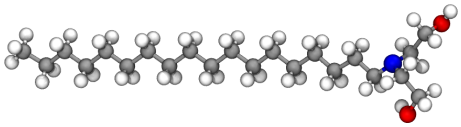

(h) C_{18} tertiary ethoxylated-amine [*2,2'-(octadecylimino)diethanol*; $C_{22}H_{47}NO_2$]

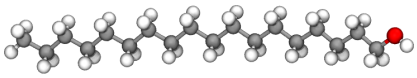

(i) C_{18} alcohol [*1-ocdecanol*; $C_{18}H_{38}O$]

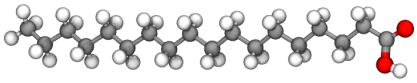

(j) C_{18} carboxylic acid [*n-octadecanoic acid*; $C_{18}H_{36}O_2$]

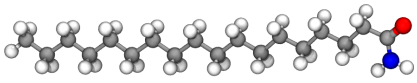

(k) C_{18} primary amide [*n-octadecanamide*; $C_{18}H_{37}NO$]

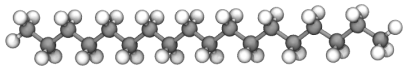

(l) C_{18} alkane [*n-octadecane*; $C_{18}H_{38}$]

Figure 2.2 – Molecular structure of the investigated OFM models.
Atomic color code: gray - carbon, *white* - hydrogen, *blue* - nitrogen, *red*: oxygen.

Table 2.1 – Molecular data related to OFM and BO models

Molecular ID	Hydrocarbon tail length	Polar head functional group	Molecular formula	Molar mass (g/mol)
OFM-A	C_6	amine	$C_6H_{15}N$	101.19
OFM-B	C_{12}	amine	$C_{12}H_{27}N$	185.36
OFM-C	**C_{18}**	**amine**	**$C_{18}H_{39}N$**	**269.52**
OFM-D	C_{24}	amine	$C_{24}H_{51}N$	353.68
OFM-E	C_{18}	amine	$C_{19}H_{41}N$	283.54
OFM-F	C_{18}	amine	$C_{20}H_{43}N$	297.57
OFM-G	C_{18}	amine	$C_{20}H_{43}NO$	313.57
OFM-H	C_{18}	amine	$C_{22}H_{47}NO_2$	357.62
OFM-I	C_{18}	alcohol	$C_{18}H_{38}O$	270.50
OFM-J	C_{18}	acid	$C_{18}H_{36}O_2$	284.48
OFM-K	C_{18}	amide	$C_{18}H_{37}NO$	283.50
OFM-L	C_{18}	alkane [(*)]	$C_{18}H_{38}$	254.50
BO-PAO	–	–	$C_{30}H_{62}$	422.83
BO-PAG	–	–	$C_{29}H_{60}O_6$	504.79

[(*)] *The C_{18} alkane does not have any polar group and it is not employed as a FM additive. Even though, this compound was chosen as a nonpolar molecule in order to allow comparisons with surfactant molecules to be drawn (e.g., OFM-A, I, K and K), possibly unveiling the effect of head group chemistry on OFM diffusivity.*

As explained in the introduction, *octadecylamine* (*OFM C*, cf. table 2.1) was used as an OFM model in all of the three MD studies composing our simulation protocol. The other molecules were only employed in the *diffusion study*, in order to evaluate the influence of a certain number of molecular parameters on OFM diffusivity, namely:

- *effect of hydrocarbon tail group*: models A, B, C & D (primary amines with C_6, C_{12}, C_{18} and C_{24} chains, respectively);
- *effect of number and nature of hydrogen substituents associated to nitrogen atom*: models C, E, F, G & H (primary, secondary and tertiary amines with a C_{18} tail);
- *effect of head group chemistry*: models C, I, J, K & L (primary amine, alcohol, carboxylic acid, primary amide and alkane with a C_{18} tail, respectively).

Note that the methyl (CH_3-) and ethoxyl (C_2H_5O-) groups were considered as the hydrogen substituents in the composition of the C_{18} secondary and tertiary amines. These molecules are termed here as *alkyl* and *ethoxylated amines*, respectively.

2.1.2 Surface model

The chemical composition of a native oxide layer on a steel surface was experimentally studied by Olla *et al.*,[78] using *angle-resolved XPS* measurements. As results, intermixed layers of different compounds were found throughout the substrate, with a depth profile ranging from *iron hydroxide* (FeOOH) to *iron oxides* [Fe(III) and Fe(II)], before reaching a bulk of *pure iron*. Therefore, depending on the severity levels prevailing in a tribological contact, we can expect different compositions of the rubbing surfaces, such as iron oxides for mild conditions, and pure iron for more severe ones.

Concerning the substrate model required to mimic the components of a mechanical system in the *adsorption* and *friction studies*, a *hematite surface* (α-Fe_2O_3) was chosen to represent an *oxidized steel surface*, which is a material of important academic and industrial interest.[31,46,47,52,55–58,64,65,79–82] Besides, a more comprehensive understanding of the OFM action mechanism as a function of the surface chemistry would be an interesting research target of future MD simulations, but it is beyond the scope of this PhD thesis. Additionally, a $(0\ 1\ \bar{1}\ 2)$ slab of this ferric oxide was utilized (cf. figure 2.3), since this surface plane is the most thermodynamically stable orientation exhibiting both iron- and oxygen-terminations in the outermost atomic layer.[80]

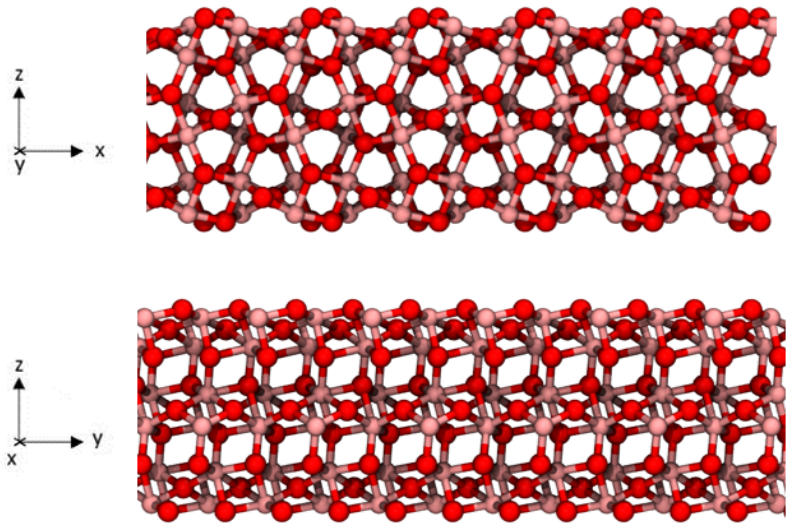

Figure 2.3 – Side views of an α-iron(III) oxide $(0\ 1\ \bar{1}\ 2)$ slab, which represents a surface of (3×3) unit cells, with an DFT-optimized geometry.
Atomic color code: coral - iron and *red* - oxygen.

Actually, this structure was especially taken account to study the adsorption mechanism of a primary amine on hematite via DFT calculation (cf. § 4.1, p. 66), because both Fe and O atoms are accessible as adsorption site centers to a potential interaction with the molecular amino group of the OFM models (cf. figure 2.3, p. 21). By doing that, no particular interaction involving the model OFM molecule and the substrate was favored, and the *ab initio* analysis was thus able to reveal the real nature of their interaction without any steric effect bias condition.

Moreover, the α-Fe_2O_3 geometry configuration employed in our MD simulations was obtained from the mentioned DFT calculations. For information, the methodology used to relax the surface model from the bulk structure can be found elsewhere.[80] In fact, special care was taken in order to ensure an accurate description of the electronic and magnetic properties of the hematite. The dimensions (*xyz*) of the *unit simulation cell* representing the relaxed surface slab is approximately of 10 Å × 11 Å × 10 Å, which corresponds to three elementary Fe_2O_3 layers (cf. figure 2.3, p. 21), where each one contains 40 atoms: 16 Fe and 24 O, with a Fe/O ratio remaining at 2:3.

2.2 Computational method

Owing to the advances of computing power and numerical algorithms, *molecular dynamics simulations* have emerged as a powerful tool to complement the traditional divisions of experimental and theoretical sciences, including the *tribology field*. In this section, we have no intention to extensively explain this technique, nor do we attempt to provide a comprehensive review of the MD-based research done to investigate tribological systems, since such information is available in excellent textbooks[83–85] and other scientific publications.[63,86–92] In the interest of brevity, we thus highlight only the key aspects of this method that are relevant to the simulation protocol employed in the current work. Besides, further computational details are given in each simulation study presented in the following chapters.

2.2.1 Brief outline of MD method

Molecular dynamics simulations describe the temporal evolution of a *many-body system*, comprising N interacting atoms, by integrating the *classical equations of motion* that are based on *Newton's second law*:[93]

$$m_i \cdot \frac{d^2\mathbf{r}_i}{dt^2} = \mathbf{F}_i(\mathbf{r}_1,\ldots,\mathbf{r}_N) \tag{2.1}$$

or,

$$m_i \cdot \frac{d\mathbf{v}_i}{dt} = \mathbf{F}_i(\mathbf{r}_1,\ldots,\mathbf{r}_N); \qquad \frac{d\mathbf{r}_i}{dt} = \mathbf{v}_i \tag{2.2}$$

where, m_i, $\mathbf{r}_i$ and $\mathbf{v}_i$ are the mass, position and velocity of the i^{th} atom (with $i = 1, \ldots, N$), respectively, and $\mathbf{F}_i$ is the net force acting on that atom i, being expressed as:[93]

$$\mathbf{F}_i(\mathbf{r}_1,\ldots,\mathbf{r}_N) = -\frac{\partial U(\mathbf{r}_1,\ldots,\mathbf{r}_N)}{\partial \mathbf{r}_i} \tag{2.3}$$

in which, the *potential energy function* U describes the atomic interactions that govern the physics and the properties of the simulated system.

In MD, these interactions are usually defined by *classical force fields*, whose parameters are derived from empirical data and/or quantum mechanical methods (*e.g.*, DFT).[83,91,94] Therefore, it is worth emphasizing that the reliability of the MD simulation results depends considerably upon the accuracy of the force fields used to model the investigated systems, under the conditions of interest. Concerning the force fields employed in our studies, their *functional form* and *parameters* are described in § 2.2.2 (cf. p. 26).

With regard to the simulated *system size*, only (relatively) small samples of atoms are currently accessible by MD, which generally range from thousands to hundreds of thousands of atoms, representing *nanometer-sized systems*.[63,84,91] Nevertheless, *periodic boundary conditions* (PBC) are usually applied to overcome that (intrinsic) size limitation, and also to minimize the edge effects induced by the use of a *finite simulated system* (*i.e.*, the so-called *simulation box* or *cell*).[85] Actually, PBC create an infinite lattice of periodically replicated cells that fill all space, according to the spacial dimensions chosen to be covered by these boundary conditions (*e.g.*, *x*, *y* and/or *z* directions, cf. figure 2.4).[63] Indeed, if a molecule leaves the cell though one boundary, it is reintroduced with the same velocity at the same point of departure through the opposite face of the cell.[63] Therefore, this strategy allows MD simulations to study bulk and confined systems in a computationally efficient approach.

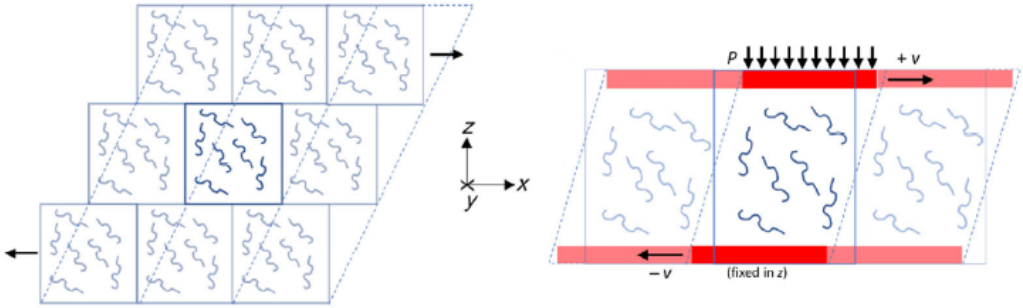

Figure 2.4 – Schematics representing simulated cells of bulk (*left*) and confined (*right*) fluid systems under shearing conditions. Note that translucent regions show the periodic images of the simulation cell from the imposed PBC. For the bulk fluid (*left*), PBC is applied in all dimensions, whereas for the confined system (*right*), only *x* and *y* directions are covered. (figure retrieved and adapted from the indicated reference)[63]

Once the geometry of the system and the boundary conditions are specified, the force fields are defined, and the initial position and velocity of each atom are assigned, *numerical integration* can be carried out.[86,91] In our MD simulations, we used the *velocity Verlet algorithm* to integrate the equations of motion (cf. equations 2.1-2.3).[83] This algorithm uses the position and the velocity of each atom i at time t — $\mathbf{r}_i(t)$ and $\mathbf{v}_i(t)$ — to predict the same respective variables at time $(t+\Delta t)$:[83]

$$\mathbf{r}_i(t+\Delta t) = \mathbf{r}_i(t) + \mathbf{v}_i(t)\cdot\Delta t + \frac{\mathbf{F}_i(t)}{2\cdot m_i}\cdot\Delta t^2 \tag{2.4}$$

$$\mathbf{v}_i(t+\Delta t) = \mathbf{v}_i(t) + \frac{\mathbf{F}_i(t+\Delta t) + \mathbf{F}_i(t)}{2\cdot m_i}\cdot\Delta t \tag{2.5}$$

where Δt is the *time step* used for integration, which depends on the *largest vibrational frequency* associated with the chemical functional groups found within the system.[86,91] Besides, since the treatment of time is iterative, a *smaller time step* yields a more exact solution, thereby ensuring that the total energy remains constant, on average, for the simulation of *equilibrium processes* (*i.e.*, when any external force or constraint is imposed on the system).[85] Considering these factors, a Δt value of a femtosecond was used in our work (*i.e.*, 1 fs $\equiv$ 10^{-15} s). As a consequence, the simulation runs were limited to nanosecond timescales ($\leq$ 20 ns), which correspond to billions of time steps. In addition, it must be specified that the classical MD code *LAMMPS*[95] (*version:* November 17$^{\text{th}}$ 2016) was employed to perform all of the simulations reported hereafter.

Therefore, by repeatedly solving the equations of motion, the trajectories of each interacting atom can be obtained, and then linked to *thermodynamic*, *structural* and *transport properties* of the simulated system using the principles of *statistical mechanics*.[83,85,91] For instance, the *temperature* can be calculated from the ensemble average kinetic energy, which is derived from the atomic momenta generated at every simulation time step.[83]

Furthermore, it should be noted that it is also possible to numerically adjust the system temperature and/or pressure — by means of a *thermostat* and/or a *barostat*, respectively — in order to reproduce the desired physical conditions of equilibrium and non-equilibrium processes.[96–99] In our case, different temperature and pressure control methods were applied in order to equilibrate the systems investigated within the *diffusion* and *adsorption studies*, which are described, respectively, by a (bulk) liquid OFM/BO mixture and an OFM-based SAM adsorbed on an α-Fe_2O_3 slab. For the confined shearing simulations of the *friction study*, in which two opposing adsorbed SAM are confined between hematite substrates and subjected to a given shear rate, a thermostat was used to prevent a potential rise in internal energy of the system, and thus in its temperature, which is induced by the applied (external) sliding force.

2.2.2 Classical MD force fields

A *force field* provides the energy functions and the associated parameter sets used to compute the interatomic forces required in a MD simulation.[94] The general form of the *total potential energy* is typically expressed as a sum of individual terms, which correspond to *covalent* and *noncovalent contributions* (U_{bonded} and $U_{\text{nonbonded}}$, respectively), as follows:

$$U_{\text{total}} = \sum U_{\text{bonded}} + \sum U_{\text{nonbonded}} \tag{2.6}$$

In our work, *bonded interactions* consist of *bond stretching*, *angle bending* and *torsion interactions*, which are related to the *intramolecular (covalent) forces* prevailing in OFM and BO molecules, while *nonbonded interactions* concern *vdW* and *electrostatic forces* and are associated with all atoms of the modeled systems (hematite solid surface and liquid organic molecules).

In the following, the employed interatomic potentials are detailed according to the nature of the concerned materials, whose interactions were described by individual energetic contributions, referred to here as $U^{\text{lubricant}}$ (for the lubricant molecules), U^{surface} (for the α-Fe_2O_3 slabs), and $U^{\text{interface}}$ (for the interfacial OFM-substrate interactions). In this specific framework, the total potential energy is alternatively defined as:

$$U_{\text{total}} = U^{\text{lubricant}} + U^{\text{surface}} + U^{\text{interface}} \tag{2.7}$$

2.2.2.1 Lubricant molecules

The atomic interactions involving OFM and BO molecules were modeled with *OPLS all atom potentials* (OPLS-AA), which are especially adapted to reproduce the thermodynamic properties of organic compounds in liquid state.[100–106] Actually, we have chosen a force field that describes explicitly all carbon and hydrogen atoms because recent MD simulations performed by Ewen *et al.*[58] have shown that an *all-atom representation*, compared to an *united-atom* one, is essential to provide an accurate flow and friction behaviors for lubricant constituents subjected to confinement.[107] Then, the original *OPLS-AA parameterization*[108] was selected, since it contains the parameters of all chemical functional groups found in our systems.

In practice, $U^{\text{lubricant}}$ is defined by the OPLS-AA functional form expressed as:[100]

$$\begin{aligned} U^{\text{lubricant}} = & \sum_{bonds} k_r \cdot (r - r_{eq})^2 \quad + \quad \sum_{angles} k_\theta \cdot (\theta - \theta_{eq})^2 \quad + \\ & \sum_{dihedrals} \left[\frac{V_1}{2} \cdot (1 + \cos\phi) + \frac{V_2}{2} \cdot (1 - \cos 2\phi) + \frac{V_3}{2} \cdot (1 + \cos 3\phi) + \frac{V_4}{2} \cdot (1 - \cos 4\phi) \right] + \\ & \sum_i \sum_{j>i} \left\{ \frac{q_i \cdot q_j}{r_{ij}} + 4\epsilon_{ij} \cdot \left[\left(\frac{\sigma_{ij}}{r_{ij}} \right)^{12} - \left(\frac{\sigma_{ij}}{r_{ij}} \right)^{6} \right] \right\} \cdot f_{ij} \end{aligned} \tag{2.8}$$

in which, the intramolecular bond stretching and angle bending energies are represented by harmonic terms — where the subscript "*eq*" denotes the equilibrium bond length r and angle θ —, and k are their force constants.[109] Additionally, the torsion term is expressed by a truncated Fourier series that sums over all dihedral angles ϕ, and where V_{1-4} are the Fourier coefficients. Besides, the energy associated with nonbonded interactions are defined by the sums over Coulomb and Lennard-Jones (LJ) 12-6 potential terms, covering pairwise interactions between the atomic sites — denoted i and j —, which are separated by a distance r_{ij}, and where q_i indicates the partial atomic charge of atom i in Coulomb potential. The LJ length and energy parameters for each ij pair (σ_{ij} and ϵ_{ij}, respectively) are obtained from a geometric combining rule (*i.e.*, $\sigma_{ij} = \sqrt{\sigma_{ii} \cdot \sigma_{jj}}$ and $\epsilon_{ij} = \sqrt{\epsilon_{ii} \cdot \epsilon_{jj}}$). Finally, it must be noted that the nonbonded energy term is computed using a scaling factor, termed as f_{ij}, for all intramolecular interactions between atoms separated by more than two bonds. For convention $f_{ij} = 1.0$, except for intramolecular "1-4 interactions" (*i.e.*, for atoms that are forth neighbors in the molecule), when $f_{ij} = 0.5$.

Regarding the parameters of the OPLS-AA force field, tables 2.2 – 2.5 (cf. p. 28 – 30) provide a compilation of all values used to described the nonbonded and bonded interactions of the modeled OFM and BO molecules.[2] Moreover, in order to access the accuracy of this interatomic potential in reproducing the liquid properties of our systems, we calculated the (bulk) liquid density of the pure BO models (PAO and PAG) at different temperatures, as the first step of our *diffusion study* — more details are given in chapter 3, § 3.2, p. 40). In this context, the obtained results were favorably compared with experimental data (cf. table 3.4, p. 51), and the original OPLS-AA force field was then integrated in our MD simulation protocol.

[2] For information, this data set was collected from the indicated reference.[108]

Table 2.2 – Parameters for nonbonded interactions (Coulomb and LJ potentials)

Element	Atom type i	Chemical Function/Group	σ_{ii}	ϵ_{ii}	Charge q_i
H	HC	alkane $H-C$	2.50	0.030	0.060
H	HC	diol & triol $H-COH$	2.50	0.030	0.060
H	HC	alkyl ether $H-COR$	2.50	0.030	0.030
H	HC	acyl $H-C-COX$	2.42	0.015	0.060
H	H	amine RNH_2	0.00	0.000	0.360
H	H	amine R_2NH	0.00	0.000	0.380
H	H	amide $-CO-NH_2$	0.00	0.000	0.380
H	HO	alcohol $-OH$	0.00	0.000	0.418
H	HO	carboxylic acid $-COOH$	0.00	0.000	0.450
C	CT	alkane CH_3-	3.50	0.066	-0.180
C	CT	alkane $-CH_2-$	3.50	0.066	-0.120
C	CT	alkane $>CH-$	3.50	0.066	-0.006
C	CT	amine CH_3-NHR	3.50	0.066	0.020
C	CT	amine CH_3-NR_2	3.50	0.066	0.030
C	CT	amine RCH_2-NH_2	3.50	0.066	0.060
C	CT	amine RCH_2-NHR	3.50	0.066	0.080
C	CT	amine RCH_2-NR_2	3.50	0.066	0.090
C	CT	alcohol CH_3OH & RCH_2OH	3.50	0.066	0.145
C	CT	alcohol R_2CHOH	3.50	0.066	0.205
C	CT	ethyl ether $-CH_2-OR$	3.50	0.066	0.140
C	CT	isopropyl ether $>CHOR$	3.50	0.066	0.170
C	C	carboxylic acid $-COOH$	3.75	0.105	0.520
C	C	amide $C=O$	3.75	0.105	0.500
N	NT	amine RNH_2	3.30	0.170	-0.900
N	NT	amine R_2NH	3.30	0.170	-0.780
N	NT	amine R_3N	3.30	0.170	-0.630
N	N	amide $-CO-NH_2$	3.25	0.170	-0.760
O	OH	alcohol $-OH$	3.12	0.170	-0.683
O	OH	carboxylic acid $-OH$	3.00	0.170	-0.530
O	OS	dialkyl ether $-O-$	2.90	0.140	-0.400
O	O	carboxylic acid $C=O$	2.96	0.210	-0.440
O	O	amide $C=O$	2.96	0.210	-0.500

Parameter σ_{ii} is expressed in Å, ϵ_{ii} in $kcal \cdot mol^{-1}$, and q_i in e *(elementary charge).*

Table 2.3 – Bond stretching parameters

Bond r	k_r (kcal · mol^{-1} · Å^{-2})	r_{eq} (Å)
$HC-CT$	340.0	1.090
$H-NT$	434.0	1.010
$HO-OH$	553.0	0.945
$CT-CT$	268.0	1.529
$CT-C$	317.0	1.522
$CT-NT$	382.0	1.448
$CT-OH$	320.0	1.410
$CT-OS$	320.0	1.410
$C-O$	570.0	1.229
$C-OH$	450.0	1.364
$C-N$	490.0	1.335
$N-H$	434.0	1.010

Table 2.4 – Angle bending parameters

Angle θ	k_θ (kcal · mol^{-1} · rad^{-2})	θ_{eq} (deg)
$HC-CT-HC$	33.00	107.80
$HC-CT-CT$	37.50	110.70
$CT-CT-CT$	58.35	112.70
$HC-CT-NT$	35.00	109.50
$CT-CT-NT$	56.20	109.47
$CT-NT-CT$	51.80	107.20
$CT-NT-H$	35.00	109.50
$H-NT-H$	43.60	106.40
$HC-CT-OH$	35.00	109.50
$CT-CT-OH$	50.00	109.50
$CT-OH-HO$	55.00	108.50
$HC-CT-OS$	35.00	109.50
$CT-CT-OS$	50.00	109.50
$CT-OS-CT$	60.00	109.50
$HC-CT-C$	35.00	109.50
$CT-CT-C$	63.00	111.10
$CT-C-O$	80.00	120.40
$C-OH-HO$	35.00	113.00
$O-C-OH$	80.00	121.00
$CT-C-N$	70.00	116.60
$C-N-H$	35.00	119.80

Table 2.5 – Torsional parameters (Fourier coefficients, kcal · mol^{-1})

Dihedral Angle ϕ	V_1	V_2	V_3	V_4
$HC-CT-CT-HC$	0.000	0.000	0.300	0.000
$HC-CT-CT-CT$	0.000	0.000	0.300	0.000
$CT-CT-CT-CT$	1.300	-0.050	0.200	0.000
$HC-CT-CT-OH$	0.000	0.000	0.468	0.000
$CT-CT-CT-OH$	-1.552	0.000	0.000	0.000
$HC-CT-OH-HO$	0.000	0.000	0.352	0.000
$CT-CT-OH-HO$	-0.356	-0.174	0.492	0.000
$HC-CT-CT-OS$	0.000	0.000	0.468	0.000
$CT-CT-CT-OS$	1.300	-0.050	0.200	0.000
$OH-CT-CT-OS$	4.319	0.000	0.000	0.000
$HC-CT-OS-CT$	-0.521	-2.018	1.996	0.000
$CT-CT-OS-CT$	0.650	-0.250	0.670	0.000
$OS-CT-CT-OS$	-0.550	0.000	0.000	0.000
$HC-CT-CT-NT$	-1.013	-0.709	0.473	0.000
$CT-CT-CT-NT$	2.392	-0.674	0.550	0.000
$OH-CT-CT-NT$	8.000	0.000	0.000	0.000
$HC-CT-NT-H$	0.000	0.000	0.400	0.000
$HC-CT-NT-CT$	0.000	0.000	0.560	0.000
$CT-CT-NT-H$	-0.190	-0.417	0.418	0.000
$CT-CT-NT-CT$	0.416	-0.128	0.695	0.000
$HC-CT-CT-C$	0.000	0.000	-0.100	0.000
$CT-CT-CT-C$	-2.060	-0.313	0.315	0.000
$HC-CT-C-O$	0.000	0.000	0.000	0.000
$CT-CT-C-O$	0.000	0.000	0.000	0.000
$HC-CT-C-OH$	0.000	0.000	0.000	0.000
$CT-CT-C-OH$	0.000	1.412	0.000	0.000
$CT-C-OH-HO$	1.500	5.500	0.000	0.000
$O-C-OH-HO$	0.000	5.000	0.000	0.000
$HC-CT-C-N$	0.000	0.000	0.000	0.000
$CT-CT-C-N$	1.173	0.189	-1.200	0.000
$CT-C-N-H$	0.000	4.900	0.000	0.000

2.2.2.2 Hematite substrate

The interactions prevailing in an α-Fe_2O_3 slab — a crystalline iono-covalent solid — was represented in the current work by the force field developed by Guillot *et al.*[110,111] to describe natural silicates made up of the geologically most abundant oxide components, which include the *hematite structure*. Thus, the interionic potential energy related to our ferric oxide surface model U^{surface} is defined as a sum of a Coulomb and a Buckingham-type potentials, which respectively model the electrostatic and vdW interactions between the ions i and j:

$$U^{\text{surface}} = \sum_i \sum_{j>i} \left(\frac{q_i \cdot q_j}{r_{ij}} + B_{ij} \cdot e^{-r_{ij}/\rho_{ij}} - \frac{C_{ij}}{r_{ij}^6} \right) \tag{2.9}$$

where r_{ij} is their relative distance, q_i is the charge associated with ion i, and B_{ij}, C_{ij} and ρ_{ij} are the energy and length parameters describing the repulsive and dispersive forces, respectively.[110] Besides, the pairwise parameter values are listed in table 2.6, and the ionic charges are $q_{Fe^{3+}} = 1.4175\ e$ and $q_{O^{2-}} = -0.0945\ e$.[110,111]

Table 2.6 – Pairwise parameters of Coulomb-Buckingham potential

Ion type i	Ion type j	B_{ij} (kcal · mol^{-1})	ρ_{ij} (Å)	C_{ij} (Å^6 · kcal · mol^{-1})
O^{2-}	O^{2-}	208 074.373	0.265	1 962.298
O^{2-}	Fe^{3+}	184 954.990	0.190	0.0
Fe^{3+}	Fe^{3+}	0.0	0.0	0.0

Note that only the ion pairs O - O and O - Fe are covered by the short-range Buckingham potential, whereas Fe - Fe interactions are exclusily described by Coulombic repulsive interactions.[110] *The parameters listed above were retrieved from the indicated reference.*[110]

For information, the choice of the Coulomb-Buckingham force field was validated for our substrate model based on the results of a MD calculation of the mechanical properties of an α-Fe_2O_3 crystal.[3] The agreement observed between the MD results and some reference data available in literature[112] have shown that this force field is effectively adapted to describe the considered iron oxide and its deformation under the high pressures applied in our simulations. However, that preliminary assessment simulation is not described in this manuscript for convenience.

[3] The computational procedure used to calculate the *elastic constant tensor* of the hematite crystal, and particularly its *bulk elastic modulus*, was adapted from a MD simulation example provided with LAMMPS package (*examples/ELASTIC*), which was developed by Aidan Thompson, being available at `https://github.com/lammps/lammps/blob/master/examples/ELASTIC/` (accessed: 20 June 2018).

2.2.2.3 OFM-surface interface

Finally, the last contribution to the total potential energy describing our systems concerns the interactions occurring at the interface of the solid substrate and the OFM molecules forming the protective boundary film, $U^{\text{interface}}$. Actually, in the *adsorption* and *friction studies*, amine-based SAM are adsorbed on α-Fe_2O_3 (0 1 $\bar{1}$ 2) slabs, with different molecular surface coverages (Γ). In these simulations, the interactions between the (primary) amine head groups and the iron oxide surface were represented by a sum of Coulomb and LJ (12-6) potential terms over all interacting sites *i* and *j*:

$$U^{\text{interface}} = \sum_i \sum_{j>i} \left\{ \frac{q_i \cdot q_j}{r_{ij}} + 4\epsilon_{ij} \cdot \left[\left(\frac{\sigma_{ij}}{r_{ij}} \right)^{12} - \left(\frac{\sigma_{ij}}{r_{ij}} \right)^{6} \right] \right\} \tag{2.10}$$

The pairwise LJ parameters required in our MD simulations to describe these interfacial interactions were fitted to reproduce both *adsorption energy* (E_{ads}) and *N-Fe equilibrium distance* ($d_{\text{N-Fe}}$) determined from DFT calculations (for full details, cf. chapter 4, § 4.1.3, p. 72). The fitted values of σ_{ij} and ϵ_{ij} are reported in table 2.7. Regarding the electrostatic interactions, the charges q_i and q_j correspond to the same values used to compute $U^{\text{lubricant}}$ and U^{surface} (cf. table 2.2 and § 2.2.2.2, respectively).

Table 2.7 – Pairwise parameters of LJ 12-6 potential for the amine-surface interface

Ion type *i*	Atom type *j*	σ_{ij} (Å)	ϵ_{ij} (kcal · mol^{-1})
O^{2-}	CT	4.21	0.145
O^{2-}	HC	3.4	0.096
O^{2-}	NT	2.5	0.35
O^{2-}	H	3.4	0.0
Fe^{3+}	CT	4.02	0.772
Fe^{3+}	HC	3.20	0.434
Fe^{3+}	NT	2.40	0.0
Fe^{3+}	H	3.20	0.16

The atom and ion types referred to here are the same used in table 2.2 and 2.6, respectively. As a reminder, **CT** *corresponds to carbon atoms present in CH_3-, -CH_2-, >CH- and RCH_2-NH_2 groups;* **HC** *indicates the hydrogen atoms associated with H-C alkane groups, whereas* **H** *represents those composing the amine group (RNH_2); lastly,* **NT** *describes the nitrogen atom of the primary amine molecule.*

To conclude this chapter, we draw attention to the fact that more information about the MD simulation procedures will be provided in each of the following studies related to the working mechanisms of OFM additives, namely:

- *diffusion* in chapter 3 (cf. § 3.2, p. 40);
- *adsorption* in chapter 4 (cf. § 4.2, p. 74);
- *friction* in chapter 5 (cf. § 5.2, p. 102).

3

Diffusion

Before adsorbing on an engine component and forming then a protective film, OFM molecules need to diffuse through the bulk oil and reach the lubricated contact surfaces. In addition, OFM have to spread faster than all other surfactant additives dissolved within the formulated lubricant in order to avoid competition for the surface adsorption sites (cf. § 1.2.1, p. 10). For these reasons, molecular diffusion cannot be disregarded in the performance evaluation of OFM, since their presence on the rubbing surfaces may be affected by their diffusive behavior and rate. Therefore, MD simulations were used to shed light on molecular interactions between lubricant oil and OFM, particularly to get insights into their dynamics in liquid phase.

This chapter is organized as follows: first, a concise review on computational methods that are usually used to determine diffusion coefficients is presented (cf. § 3.1, p. 36). Then, the simulation protocol employed to calculate the OFM diffusivities is detailed (cf. § 3.2, p. 40), followed by a description of the obtained results (cf. § 3.3, p. 51).

3.1 Background and literature review

In the current work, *molecular diffusion* — also termed in literature as intra, self or tracer diffusion[113–119] — refers to the translational movement of individual molecules, in a single or multicomponent solution, which is induced by the random thermal motion, the so-called *Brownian movement*.[1] This phenomenon is presented in a wide range of natural and industrial processes, and the knowledge of their diffusive transport properties is thus crucial for the design of a diverse number of practical applications, and specially for those where diffusion is a rate-limiting step.[115,119,127–132]

Several theoretical approaches have been developed to predict dynamic transport properties in liquids, particularly the *diffusion coefficient* ($\mathfrak{D}$), which is interchangeably termed as *diffusivity*.[121,132–135] Most of the models reported in literature are derived from the *kinetic*, *hydrodynamic* and *free volume theories*, as well as from *statistical mechanics*.[114,120,131,135–138] Also, diffusion coefficients can be obtained via experiments like *tracer-based techniques*, *nuclear magnetic resonance* (NMR) and *neutron scattering* measurements.[113,117,131,139,140] However, these experimental methods often present high cost and technical difficulties when complex systems are involved (*e.g.*, multicomponent solutions with polyatomic molecules, hazardous substances, challenging thermodynamic conditions, etc.).[115,127,132,138,139,141–143]

In this context, computational methods derived from statistical mechanics, and in particular from MD simulations, have been used as a low time- and resources-consuming alternative to determine diffusivities in single and multicomponent solutions.[115,121,127,132,142] Regarding the MD method, there are basically two conventional techniques available, based on either *equilibrium* (EMD) or *non-equilibrium* (NEMD) *algorithms*.[114,119,134,144,145] In NEMD, the simulated system is perturbed away from equilibrium by an external driving force, or a boundary or nonuniform initial condition, in order to create a mass flux within the system and then calculate the associated diffusion coefficient.[115,121,145] In contrast, EMD does not require any imposed perturbation and the diffusivities are computed from the molecular motion of a system at equilibrium.[115,121] Because of the similarity of NEMD simulations to physical experiments, this method has been treated as the most intuitive approach to obtain transport properties.[119,145] Nevertheless, EMD methods offer the advantage of calculating multiple system

[1] There is also another diffusion process named *inter-diffusion* — likewise known as bulk, collective, mutual or transport diffusion —, which describes the collective movement of molecules, resulting from a driving force, such as a concentration or a chemical potential gradient.[113,115,120] However, this process was not considered here. For detailed information on inter-diffusion process, the interested reader is referred to *appendix A* (cf. p. I), and also to some specific publications.[114–126]

properties in a single simulation without the need for exceptionally large driving forces.[115,127]

In addition to that, it must be pointed out that diffusion coefficients in liquids are function of *temperature*, *pressure* and *composition*.[120,121,132] In our case, we are interested only in a single thermodynamic state, namely a binary mixture of dilute OFM (1 wt.%) in a given BO, at 373 K and 1 atm (cf. § 2.1, p. 18). In the following, we thus focus attention on the prevalent EMD-based models commonly used to determine liquid diffusivities at uniform temperature and pressure conditions.

EMD methods to determine molecular diffusivity, $\mathfrak{D}$:

In practice, the diffusion coefficient of a component i in its *pure fluid state* (denoted by $\mathfrak{D}_i^0$) or in a *binary mixture* of components i and j (denoted by $\mathfrak{D}_{i,j}$) can be computed by analyzing the *mean-squared displacement* (MSD) of each molecule according to *Einstein relation* (cf. equation 3.1), or equivalently, from the *velocity autocorrelation function* (VACF) stated by *Green-Kubo expression* (cf. equation 3.2):[83,84,119,141,144]

$$\mathfrak{D} = \frac{1}{6 \cdot N_i} \lim_{m \to \infty} \frac{1}{m \cdot \Delta t} \left\langle \sum_{l=1}^{N_i} \left[\mathbf{r}_{l,i}(t + m \cdot \Delta t) - \mathbf{r}_{l,i}(t) \right]^2 \right\rangle \tag{3.1}$$

$$\mathfrak{D} = \frac{1}{3 \cdot N_i} \int_0^\infty dt' \left\langle \sum_{l=1}^{N_i} \left[\mathbf{v}_{l,i}(t) \cdot \mathbf{v}_{l,i}(t + t') \right] \right\rangle \tag{3.2}$$

where N_i is the total number of molecules of component i, m is the number of time steps, Δt is the time step, $\mathbf{r}_{l,i}(t)$ and $\mathbf{v}_{l,i}(t)$ are respectively the position and velocity vectors of the center-of-mass of the l^{th} molecule of type i at time t (both obtained from EMD simulations), and the angle brackets $\langle \cdots \rangle$ denote an ensemble average.[119,122,146]

Since equations 3.1 and 3.2 are valid for a compound i in single-component fluids ($\mathfrak{D}_i^0 = \mathfrak{D}$) as well as in mixtures i/j ($\mathfrak{D}_{i,j} = \mathfrak{D}$), the numerical values of diffusivity will differ in this two possible cases.[144,146] Besides, since diffusion coefficient in a mixture is itself composition-dependent, its value lies between its respective infinite dilution limits.[146] For example, for a binary mixture:

$$\mathfrak{D}_{1,2}^{x_1 \to 0} < \mathfrak{D}_{1,2} < \mathfrak{D}_{1,2}^{x_1 \to 1}$$

where x_i is the mole fraction for component i, and the subscripts *1* and *2* indicate the diffusing solute and solvent molecules, respectively.

Moreover, MSD and VACF approaches have extensively been employed to calculate diffusion coefficients in previous works, in which $\mathfrak{D}$ has widely been used to calibrate/assess the accuracy of molecular mechanical force fields, to interpret experimental data, as well as to better understand fluid dynamics and microscopic structure.[117,127,131,132,134,139,141–143,146–160] However, it should be mentioned that experimental and computational data on diffusivity of organic surfactant molecules applied as friction modifiers are scarce. To the best of our knowledge, diffusion coefficients of the regarded amine-based FM, BO and their resultant binary mixtures have not been studied and reported before, either by means of experiments or from molecular simulations. Therefore, by addressing this lack of empirical data, our work have intended to provide useful information for the design of more efficient additives.

After concisely reviewing the theoretical background for computing diffusivities, we remind that our purpose with this work does not rely on estimating a diffusion coefficient that accurately describes the mass flux occurring within a fully formulated lubricant employed in real engines (*e.g.*, ICE). As a matter of fact, the mass transfer processes involving lubricant additives in real-world applications are more complex, and they require a thorough modeling and investigation. Our study was actually an initial step to integrate a molecular diffusion analysis into the computational performance evaluation of OFM. Therefore, our primary aim here was to gain insights into interactions between additives and the lubricant oil, and to understand how chemical structure affects their liquid-state dynamics, but in relatively ideal conditions.

To that end, the MSD method was chosen because of its simplicity in computing $\mathfrak{D}_{OFM,BO}$ from the data collected from EMD simulations. Then, we have investigated the effect of different molecular structural parameters on diffusive behavior and rate of OFM and BO molecules, namely the *BO polarity* and the *OFM polar head chemistry*, as well as the *hydrocarbon chain length* (cf. table 3.1). For the compounds containing amine-based polar heads, we have also varied the *number* and *nature* of the *hydrogen substituents* associated to nitrogen atom — *number*: primary, secondary and tertiary amines; *nature*: alkyl and ethoxylated groups — to assess their influence on diffusivity. The computational methodology used to conduct this study and the corresponding diffusivity results are detailed in the following sections.

Table 3.1 – Molecular parameters investigated in the diffusion study

Components	**Structural factors**
Solvent (BO)	*Polarity* (*nonpolar:* PAO & *polar:* PAG; cf. § 3.3.1)
Solute (OFM)	*Polar head chemistry* (alkane, alcohol, acid, amine & amide; cf. § 3.3.2.1)
	Parameters concerning exclusively amine-based FM:
	Number of hydrogen substituents (1°, 2° & 3° amines; cf. § 3.3.2.2)
	Nature of hydrogen substituents (alkyl & ethoxylated amines; cf. § 3.3.2.2)
	Hydrocarbon tail length (chains with 6, 12, 18 & 24 carbons; cf. § 3.3.2.3)

3.2 Computational details

As mentioned earlier, the diffusion coefficients of OFM additives in a model BO were obtained using Einstein formalism. This method requires the generation of long-time trajectories via EMD simulations, and more specifically from a *NVE*[2] *ensemble simulation*, termed here as the *production* run. After the trajectory sampling phase, $\mathfrak{D}_{\mathrm{OFM,BO}}$ is calculated from the slope of MSD values, averaged over multiple trajectories of individual molecules as a function of time, within the diffusional regime:[83, 134, 141, 147]

$$\mathfrak{D}_{\mathrm{OFM,BO}} = \frac{1}{6} \lim_{t\to\infty} \frac{d}{dt} \langle \Delta \mathbf{r}^2 \rangle \tag{3.3}$$

To obtain the required molecular data, simulation cells representing the mixtures were initially designed (cf. § 3.2.1, p. 42), and then equilibrated at the desired pressure and temperature conditions. For both equilibration and production runs (cf. § 3.2.2 and § 3.2.3, p. 45 and 47, respectively), MD simulations were performed using the original OPLS-AA force field (cf. § 2.2.2, p. 26). Short-range nonbonded interactions were truncated at 15 Å, and analytical tail corrections[85] were used to estimate the long-range contributions of vdW interactions to energy and pressure. Electrostatic interactions were calculated applying the particle-particle particle-mesh (PPPM) solver,[161] with a desired relative error in forces of 1×10^{-6}. Besides, conventional periodic boundary conditions were used in all dimensions of the cubic simulation cells, and the standard velocity-Verlet algorithm[83] was applied to integrate Newton's equations of motion with a time step of 1 fs, employing *LAMMPS* package.[95]

Before going further on the description of this computational protocol, it is worth mentioning that there are generally four major factors impacting the accuracy of $\mathfrak{D}_{\mathrm{OFM,BO}}$ estimated from a MSD-time profile obtained via EMD simulations: the employed *force field*, the simulated *system size*, the *trajectory sampling procedure* and the *data post-treatment analysis*.[131, 134, 142, 151, 158, 162] So, it is important to make a clear statement on how these factors were addressed and then integrated in our work.

Firstly, it is well known that the models and the parameters of the applied *molecular potentials* do dictate the strength and the anisotropy of the intermolecular interactions involved within the simulated systems, and by consequence, their thermodynamic and transport properties.[91, 131, 134, 148] For example, the *density* of a dilute solution is mainly governed by the *solvent-solvent interactions*, and specifically by their vdW and electrostatic interactions.[58] Thus,

[2] *NVE* ensemble: constant number of particles, constant volume and constant energy.

the LJ and Coulomb potentials — which both describe these nonbonded interactions — affect not only the density and dynamics of the solvent but also the *solute diffusivity*, since an underestimated bulk density might result in an easier movement of the diffusing molecules, or conversely, an overestimated density might hinder the molecular motion.[131,132] Regarding the OPLS-AA potentials, it has been reported in previous works that the original force field can overestimate the density of linear long-chain alkanes at ambient conditions, owing to an overprediction of the melting point temperature, which ends up yielding unrealistic phase transitions.[58,147,153–155,158] In light of these findings, we have first determined the density and diffusivity of our pure BO models ($\rho_{\mathrm{BO}}(T)$ & $\mathfrak{D}^{0}_{\mathrm{BO}}(T)$), in order to assess the ability of the original OPLS-AA potentials in reproducing their liquid properties under the desired physical conditions. The obtained results are detailed later (cf. § 3.3.1, p. 51). Based on a comparison of the simulated densities with experimental data at different temperatures, we have indeed verified that the chosen force field provides numerical results that are in a very good agreement with experiments, specially at 373 K (cf. table 3.4, p. 51). Neither crystallization nor liquid-to-gel phase transition was observed during those test simulations. Therefore, the original OPLS-AA force field was validated, and then employed to model the molecular interactions of organic compounds throughout our investigation on action mechanisms of OFM, particularly in the current $\mathfrak{D}_{\mathrm{OFM,BO}}$ study.

Secondly, it has been proved that diffusion coefficient is sensitive to the simulated *system size*, mainly because of the numerical treatment of long-range interactions under periodic boundary conditions.[85,158] In fact, it has been found that regularly $\mathfrak{D}$ increases with increasing system size.[131,134,141,142,151,158,162–167] Accordingly, some analytical expressions have been proposed in the literature to correct diffusivities obtained with finite systems ($\mathfrak{D}^{\mathrm{PBC}}$), and thus to estimate infinite-system extrapolated values ($\mathfrak{D}^{\infty}$).[158,165,167] These corrections are useful when results from different simulations are compared, and more importantly, for comparison between simulations and experiments.[151,158] However, they require supplementary information about the solution constituent properties (*e.g.*, dynamic/shear viscosity of the solvent, η), which may lead to additional computational efforts and error propagation. For practical reasons, considering the multiplicity of binary mixtures investigated in this study, no additional correction of the system size was applied here. Although $\mathfrak{D}_{\mathrm{OFM,BO}}$ values presented hereafter are indeed coefficients calculated from a finite periodic system (*i.e.*, $\mathfrak{D}^{\mathrm{PBC}}_{\mathrm{OFM,BO}}$), we still believe they are a suitable reference to express and to quantify the effect of molecular structure on the diffusive properties of lubricant components. Nevertheless, in order to obtain comparable

$\mathfrak{D}_{\mathrm{OFM,BO}}$ values between the different systems, the simulation cells were designed with a similar number of solute and solvent molecules. In addition, each system was composed with more than twenty thousand atoms, as an attempt to mitigate the dependence on system-size of the calculated coefficients (cf. § 3.2.1, p. 42).

Finally, the *molecular trajectory sampling procedure* and the *MSD averaging technique* were also found to have a relevant impact on the accuracy associated to the calculated diffusivities. Actually, if the linear relation of the MSD-time profile does not hold, as it is expected in equation 3.3 (cf. p. 40), the predicted $\mathfrak{D}_{\mathrm{OFM,BO}}$ can be false.[131] So, extended simulation durations are required to achieve a linearity between MSD values and the simulation time.[83, 131, 146, 147, 154] Provided that long enough trajectories are sampled from the MD simulations, a MSD averaging over all diffusing molecules at multiple time origins can be applied for computational efficiency purposes, yielding enhanced statistical results (cf. § 3.2.4, p. 49).[134, 141] Besides, an average over several $\mathfrak{D}_{\mathrm{OFM,BO}}$ estimates obtained from independent simulations can also be implemented to improve statistical accuracy (cf. § 3.2.2, p. 45).[134, 141, 144, 160] Considering these numerical strategies, we initially performed a series of preliminary simulations to define and to optimize their required parameters (*e.g.*, number of simulations, trajectory time length, sampling interval, etc.), as well as the final MSD averaging technique, in order to establish an effective computational protocol likely to generate statistically reliable values of diffusivities. Therefore, the obtained simulation protocol is detailed in the following paragraphs.

3.2.1 System modeling

The input models were designed assuming that:

- the lubricant is represented by a *dilute binary mixture* of BO and OFM molecules, in which the solute concentration is approximately equal to 1 wt.%;
- the equilibrium thermodynamic state of interest implies a liquid solution, where all OFM are miscible in both BO, and the system temperature is higher than both OFM and BO melting point temperatures;
- electroneutrality is ensured for all molecules.

In total, twenty-six systems were investigated, comprising two models of pure BO — used to calculate $\rho_{\mathrm{BO}}(T)$ and $\mathfrak{D}^{0}_{\mathrm{BO}}(T)$ — and twenty-four models of OFM/BO mixtures — utilised to compute $\mathfrak{D}_{\mathrm{OFM,BO}}$. For every system, a large cubic simulation cell of edge length equal to 125 Å

was built using *Moltemplate* package.[3] Then, the solvent and solute molecules were placed uniformly inside the simulation cells. An example of the designed systems is illustrated in figure 3.1. For information, the number of molecules used in each case are specified in tables 3.2 and 3.3, as a function of the concerned BO (cf. p. 44).

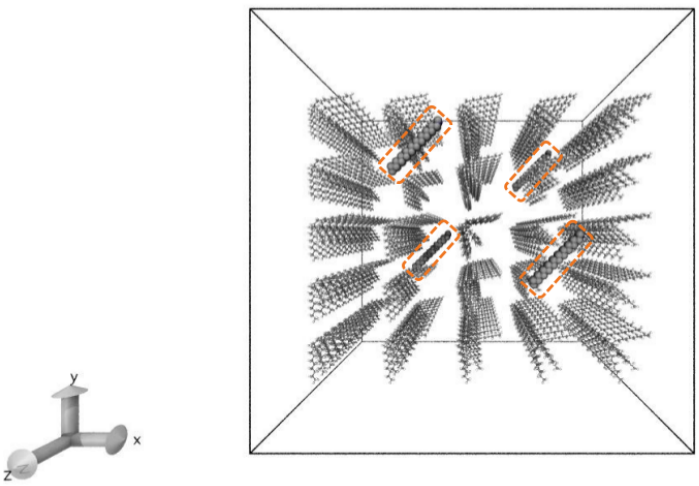

Figure 3.1 – Schematic illustration of an initial configuration that represents a solution containing C_{18} primary amine and PAO. The solute molecules are surrounded in *orange*. (N_{BO} = 254 and N_{OFM} = 4 molecules; n_{total} = 23 600 atoms)

After constructing the simulated cells, every system model was equilibrated through a series of *NVT*[4] and *NPT*[5] *ensemble* MD simulations (cf. § 3.2.2, p. 45), in which the Nosé-Hoover thermostat and barostat[96,97] were employed to control the temperature and pressure,[98] using damping constants of 0.1 and 1.0 ps, respectively.[6]

[3] *Moltemplate* package was used to build the input files used by LAMMPS (`http://www.moltemplate.org/`).

[4] NVT *ensemble:* constant number of particles, constant volume and constant temperature.

[5] NPT *ensemble:* constant number of particles, constant pressure and constant temperature.

[6] For information, in the *Nosé-Hoover thermostatting approach,*[96,97] a Hamiltonian with an extra degree of freedom for a heat reservoir is introduced in the algorithm, in conjunction with the MD equations of motion, in order to control the temperature of the simulated system. Besides, the Nosé-Hoover thermostat can be proven to generate the NVT ensemble under equilibrium conditions.[63] Concerning the pressure control, the Nosé-Hoover barostat,[96,97] which continuously alters the unit cell vectors and by consequence the cell volume, can be used to sample the NPT ensemble.[63]

Table 3.2 – Details of simulation cells with PAO as solvent model

Structural factor	OFM molecule	N_{OFM}	N_{PAO}	n_{total}
Pure solvent	-	0	220	20 240
Polar head chemistry	C_{18} *alkane*	4	240	22 304
	C_{18} *alcohol*	4	255	23 688
	C_{18} *acid*	4	269	24 972
	C_{18} *primary amine*	4	254	23 600
	C_{18} *primary amide*	4	268	24 884
Hydrogen atom substituents	C_{18} *primary amine*	4	254	23 600
	C_{18} *secondary alkyl-amine*	4	268	24 900
	C_{18} *tertiary alkyl-amine*	4	281	26 108
	C_{18} *secondary ethoxylated-amine*	3	222	20 619
	C_{18} *tertiary ethoxylated-amine*	3	253	23 492
Hydrocarbon tail length	C_6 *primary amine*	11	263	24 438
	C_{12} *primary amine*	6	263	24 436
	C_{18} *primary amine*	4	254	23 600
	C_{24} *primary amine*	3	250	23 228

N_{OFM} and N_{BO} indicate the number of OFM and BO molecules (PAO or PAG), respectively, which were placed into each simulation box during the design phase. Additionally, n_{total} refers to the total number of atoms representing the solution (i.e., solute and solvent atoms).

Table 3.3 – Details of simulation cells with PAG as solvent model

Structural factor	OFM molecule	N_{OFM}	N_{PAG}	n_{total}
Pure solvent	-	0	220	20 900
Polar head chemistry	C_{18} *alkane*	4	201	19 319
	C_{18} *alcohol*	4	214	20 558
	C_{18} *acid*	4	225	21 599
	C_{18} *primary amine*	4	213	20 467
	C_{18} *primary amide*	4	224	21 508
Hydrogen atom substituents	C_{18} *primary amine*	4	213	20 467
	C_{18} *secondary alkyl-amine*	4	224	21 524
	C_{18} *tertiary alkyl-amine*	4	235	22 581
	C_{18} *secondary ethoxylated-amine*	4	248	23 820
	C_{18} *tertiary ethoxylated-amine*	3	212	20 356
Hydrocarbon tail length	C_6 *primary amine*	11	220	21 142
	C_{12} *primary amine*	6	220	21 140
	C_{18} *primary amine*	4	213	20 467
	C_{24} *primary amine*	3	210	20 178

3.2.2 Equilibration

The equilibration phase was carried out in several stages, following a protocol inspired by procedures applied in earlier published works.[58, 141, 147, 155]

Considering the size of the simulation cell and the distance between molecules in the initial configurations (cf. figure 3.1, p. 43), the system models correspond to a gas rather than a liquid phase. Despite of this fact, they were firstly energy-minimized to remove any possible overlap between the represented molecules. Then, every model was submitted to a conventional NVT ensemble simulation at high temperature (773 K) to rapidly disorder the artificial molecular arrangement obtained during the system design. For information, the initial atomic velocities were assigned following a Maxwell-Boltzmann distribution.

After 2 ns (2 000 000 time steps of 1 fs), the molecules get random orientations and each simulation box was contracted from an edge length of 125 Å to around 60 Å ($\Delta V/V_0 \approx -50$ %), in order to reduce its large initial dimensions, and to obtain a more representative volume of the liquid state. This process was gradually done by means of several sequential volume reduction runs ($\Delta V/V = -2.5$ %), coupled with intermediate energy minimizations.

The compression stage was followed by a 3 ns NVT ensemble simulation (3 000 000 time steps), to bring the temperature of the contracted system into the desired value of 373 K. Additional replicated simulations were performed for the pure BO models in order to obtain their equilibrated systems also at 323 and 423 K.[7]

The subsequent equilibration step was a relaxation in the NPT ensemble, for 6 ns (6 000 000 time steps), and with the following physical conditions: *pressure* = 1 atm; *equilibrium temperatures*, T_{eq} = 323, 373 & 423 K for pure solvents, and 373 K for binary mixtures. For each system, the *equilibrium liquid density* predicted by the chosen force field was computed using the system volume averaged over the final 4 ns, when there was only negligible change in the simulation box.

After that first relaxation, the dimensions of the simulation cell that corresponds to the equilibrium density were fixed, and then the total linear momentum was set to zero in order to inhibit the effect of the flow that was probably created during the previous NPT run. Finally, a last relaxation process in NVT ensemble was performed at T_{eq} for a period of 2 ns (2 000 000 time steps).

[7] The analysis of the liquid densities $\rho_{BO}(T)$ reproduced by original OPLS-AA force field have taken into account three *equilibrium temperatures*, T_{eq}: 323, 373 and 423 K.

In summary, the equilibration procedure applied in this study has used long-time MD simulations[8] (13 ns, in total) in order to ensure that any phase transition of the BO matrix would not occur under the thermodynamic states of interest. Besides, the final thirty equilibrated systems are represented by cubic boxes with an edge length ranging from 54 to 64 Å (for an example, cf. figure 3.2).

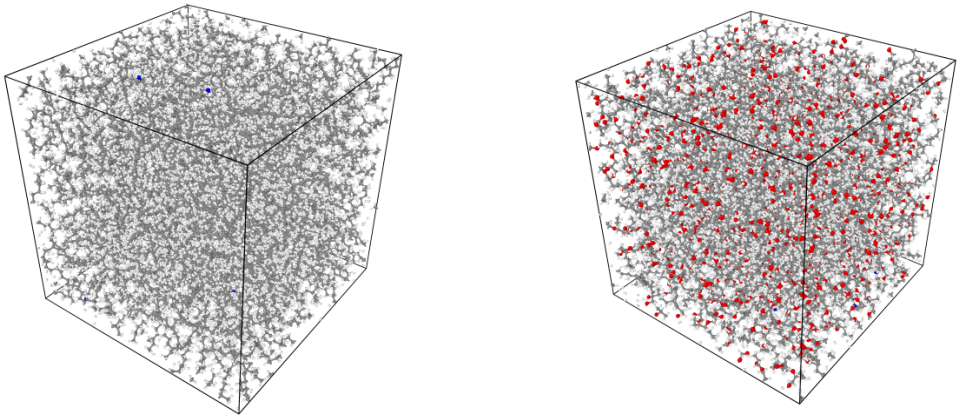

(a) **(b)**

Figure 3.2 – Examples of equilibrated systems at 373 K:
solution model of C_{18} primary amine in: **(a)** PAO & **(b)** PAG.
Atomic color code: white - hydrogen, *gray* - carbon, *blue* - nitrogen, *red* - oxygen.

In order to estimate the uncertainty related to the computational method utilised to obtain $\mathfrak{D}$, we decided to run five independent production runs, and to calculate their statistics from this set of simulations (*i.e.*, *mean* and *standard deviation*). To do that, each one of the five production runs requires a different initial configuration of each system, but the equilibration process previously described provides only a single equilibrated structure (cf. § 3.2.2, p. 45). Thus, four other independent configurations (referred to as #2, #3, #4 & #5) were obtained via sequential *heat-cooling cycles* (cf. figure 3.3, p. 47), and derived from the first equilibrated model (#1).

[8] For information, equilibration simulations were performed on a 16-cores processor (Dell C6320; Intel Xeon E5-2640 v3 2.60GHz) during 15 days, on average.

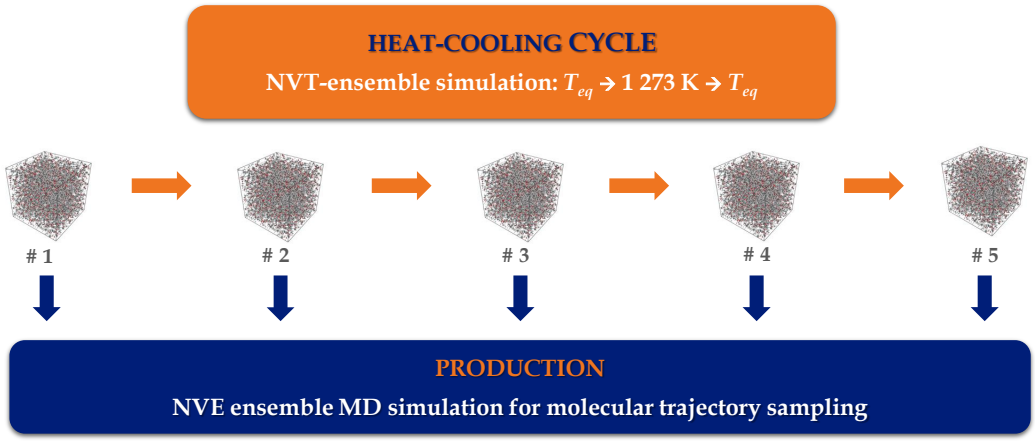

Figure 3.3 – Schematic illustration of the *heating-cooling cycles*, used to generate the four additional equilibrated structures (for each investigated system model), which were used as input configurations for the production simulations and trajectory sampling.

A heat-cooling cycle consists in increasing the temperature of a precedent equilibrated configuration, from T_{eq} to 1 273 K, in order to quickly reorient the molecular structure and obtain a new independent configuration, after decreasing the temperature from 1 273 K to the desired T_{eq}. Indeed, each initial equilibrated structure was heated up assigning the velocities of the molecules according to a Maxwell-Boltzmann distribution at 1 473 K, and then running a 2 ns NVT ensemble simulation (2 000 000 time steps of 1 fs) at 1 273 K. All other parameters concerning these NVT runs are identical to those performed during the first equilibration phase (cf. § 3.2.2, p. 45). After that, every system was cooled back to the targeted T_{eq}, for a period of 4 ns (4 000 000 time steps). Then, the total momentum was zeroed and each system was further equilibrated maintaining the temperature constant at T_{eq} for more 2 ns (2 000 000 time steps). In the end, each equilibrated configuration was used both to run a production simulation, as well as to run a new heat-cooling cycle. In total, four cycles were performed to obtain the five replicated production runs needed to estimate the statistics related to the calculated diffusivities.

3.2.3 Production

Once the equilibrated systems were obtained, production simulations were performed in order to sample the molecular trajectories required to determine the MSD averages ($\langle \Delta \mathbf{r}^2 \rangle$) and then, the diffusion coefficients ($\mathfrak{D}^0_{\mathrm{BO}}$ & $\mathfrak{D}_{\mathrm{OFM,BO}}$). This production phase was carried out in a NVE ensemble, without the application of any artificial thermostat in order to avoid introduc-

ing perturbations into the system dynamics. As a matter of fact, the temperature control in a NVT ensemble simulation is conducted by scaling the molecular velocities, which may negatively affect the molecular motion, and ultimately, the diffusivitiy estimates.[147]

Each production simulation was run for 20.25 ns[9] (20 250 000 time steps of 1 fs). Judging from the quite steady evolution of temperature and total energy with time (for an example, cf. figure 3.4), every system reaches equilibrium during the first 0.25 ns (or equivalently, 250 ps). Therefore, the unfolded positions ($\mathbf{r}_{l,i}(t)$) of the center-of-mass of all regarded diffusing molecules were stored every 100 time steps (0.1 ps), during the final 20 ns, resulting in a total of 200 000 configurations per molecule and per production run.

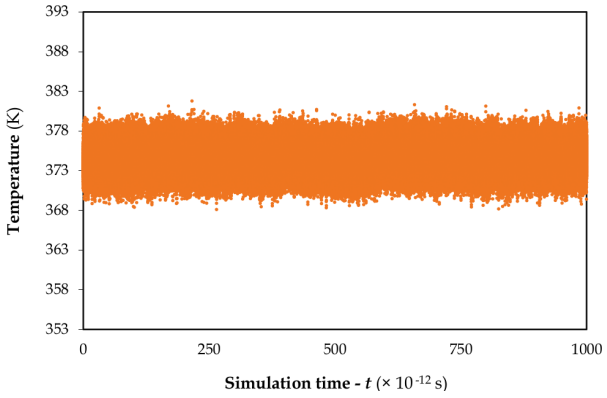

(a) Temperature

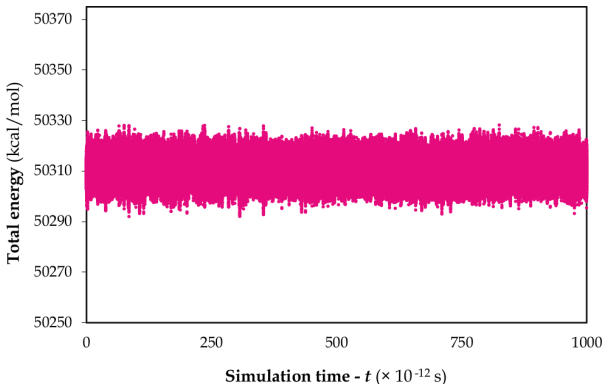

(b) Total energy

Figure 3.4 – Time evolution of: **(a)** *temperature* and **(b)** *total energy*, during the first 1 ns of the production simulation for a solution of C_{18} primary amine in PAO.
(*Related statistics:* temperature = 374.6 ± 1.4 K & total energy = 50311 ± 4 kcal·mol^{-1})

[9] For information, each production simulation required approximately 20 days of computing time.

3.2.4 MSD analysis

After the molecular data sampling, the mean-squared displacements were calculated and averaged, not only over all diffusing molecules but also over multiple calculations based on different time origins. In fact, the position samples were overlapped following a numerical strategy that provides extra MSD results, in order to improve their statistical accuracy.[84,141]

In practice, a single MSD value ($\Delta\mathbf{r}^2_{l,\tau_n}$) describes the position deviation of the center-of-mass of the l^{th} molecule of type i, with respect to a fixed origin (τ_n), at time t:[84,141]

$$\Delta\mathbf{r}^2_{l,\tau_n} = [\mathbf{r}_{l,i}(\tau_n + t) - \mathbf{r}_{l,i}(\tau_n)]^2 \tag{3.4}$$

Considering an overlapped data approach, the global trajectory generated in a production run is divided into multiple parts or blocks of equal time length (cf. figure 3.5). These blocks are obtained by shifting the reference position along each trajectory according to an evenly spaced time interval. As a result, each block associated with a specific origin provides molecular positions for an individual calculation of $\Delta\mathbf{r}^2_{l,\tau_n}$. Therefore, an average over all individual values is needed. In order to achieve that, MSD is first averaged over all molecules of type i present in the simulation cell (N_i):[141]

$$\langle\Delta\mathbf{r}^2\rangle_{\tau_n} = \frac{1}{N_i}\cdot\sum_{l=1}^{N_i}\Delta\mathbf{r}^2_{l,\tau_n} \tag{3.5}$$

Then, the final MSD average is taken over all overlapping blocks of equal time length (N_{τ_n}):

$$\langle\Delta\mathbf{r}^2\rangle = \frac{1}{N_{\tau_n}}\cdot\sum_{n=1}^{N_{\tau_n}}\langle\Delta\mathbf{r}^2\rangle_{\tau_n} \tag{3.6}$$

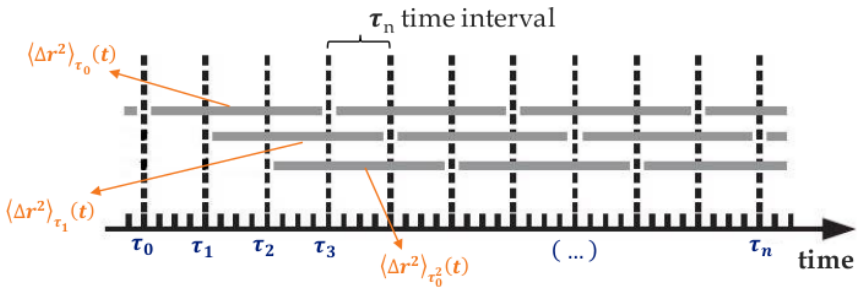

Figure 3.5 – Use of overlapped data to determine the final $\langle\Delta\mathbf{r}^2\rangle$: molecular positions obtained at any instant contribute to several MSD calculations. Trajectory blocks are shown as shaded lines, with dashed lines marking the different time origins (τ_n).[84]

Finally, the averaged MSD is plotted against the simulation time and the diffusion coefficient ($\mathfrak{D}^0_{\text{BO}}$ or $\mathfrak{D}_{\text{OFM,BO}}$) is estimated from the slope of the linear region of the MSD-time profile, as predicted by Einstein relation (cf. equation 3.3, p. 40).

In our case, each production run has provided a trajectory containing 200 000 positions for each molecule. In total, 2 000 time origins (N_{τ_n}) were taken as reference, every 5 000 times steps (τ_n time interval = 5 ps). Thus, each trajectory was divided in 2 000 overlapping blocks, each one containing a maximum number of 100 000 positions, which represents a maximal time length of 10 ns. As a reminder, the total number of diffusing molecules present in each system (N_i) are listed in tables 3.2 and 3.3 (cf. p. 44). Besides, some examples of MSD-time profiles obtained from the explained averaging technique are given in figure 3.6.

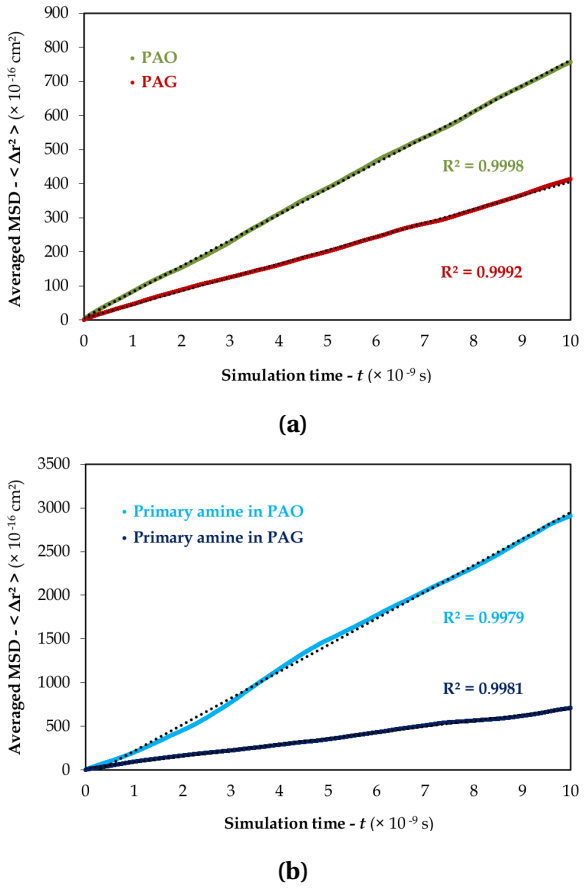

Figure 3.6 – MSD-time profiles determined from a trajectory sampled during a production run at T_{eq} = 373 K: **(a)** *pure BO models, PAO* (*moss green*) & *PAG* (*ruby*); **(b)** *solution of* C_{18} *primary amine in PAO* (*light blue*) and in *PAG* (*dark blue*).

Indeed, a high linearity between the averaged MSD and the simulation time was achieved for the investigated systems, as it is indicated by the values of the *correlation coefficient square* R^2, which were calculated via a least-square fitting of $\langle \Delta \mathbf{r}^2 \rangle$ data. These results suggest that the trajectory sampling and the MSD averaging procedures employed in this work effectively offer a suitable methodology for estimating diffusion coefficients involving OFM and BO molecules.

3.3 Results and discussion

The current study aims to better understand the effect of the molecular structure on interactions involving lubricant components in a liquid solution, and particularly on their diffusive behavior expressed by the diffusion coefficient. This section reports the results obtained through the foregoing computational protocol, focusing first on properties of the pure BO — when lubricant model fluids are free of any additive —, and then on those of OFM/BO mixtures. For each system model, the reported diffusivity and its associated uncertainty are the *mean* and the *standard deviation*, $\mathfrak{D}$ and σ_{SD}, respectively, which were obtained from the five independent production runs. Besides, $\mathfrak{D}$ is expressed in 10^{-6} $cm^2 \cdot s^{-1}$ and σ_{SD} is represented by error bars in the depicted histograms.

3.3.1 Pure BO properties

Since density is the most significant thermodynamic property of the regarded BO whose experimental data was available, we have considered this property as reference to evaluate the force field chosen to describe the interactions between organic compounds in our work. As discussed earlier, it is important to accurately reproduce the solvent density through the molecular simulations, because the ensuing prediction of the solute diffusivity strongly depends on the potential energy models (cf. § 3.2, p. 40).[126, 131, 132] In this context, the simulated and experimental BO densities are compared below, as a function of the equilibrium temperature.

Table 3.4 – Density of model base oils ($kg \cdot m^{-3}$) at T_{eq} and 1 atm

Base oil	T_{eq}	Experimental ρ_{BO} [(a)]	Simulated ρ_{BO} [(b)]	Deviation
	323 K	792	793	0.2 %
PAO	373 K	760	756	0.5 %
	423 K	728	721	1.0 %
	323 K	895	894	0.1 %
PAG	*373 K*	859	853	0.7 %
	423 K	822	813	1.1 %

[(a)] *Experimental data was provided by Total Marketing & Services (Solaize, France).* [(b)] *Simulated density values correspond to the averaged density calculated after the NPT ensemble run, during the equilibration phase (cf. § 3.2.2, p. 45).*

As can be seen from table 3.4 (cf. p. 51), the simulated densities substantially agree with experiments, for both BO and for all of the probed temperatures. In addition, no transition phase was detected in any MD simulation. Those results thus indicate that intermolecular interactions defining the BO liquid-state are accurately reproduced by the original OPLS-AA force field. Therefore, the following analyses of diffusion coefficient have relied on the assumption that the chosen force field is indeed suitable to correctly model the interactions prevailing in dilute mixtures made up of the considered OFM and BO model molecules.

Furthermore, the BO diffusivities $\mathfrak{D}^0_{\mathrm{BO}}(T)$ were computed to gain a preliminary understanding of the neat solvent dynamics in different temperatures (cf. figure 3.7), and also as an attempt to evaluate the computational protocol employed here to estimate $\mathfrak{D}$.

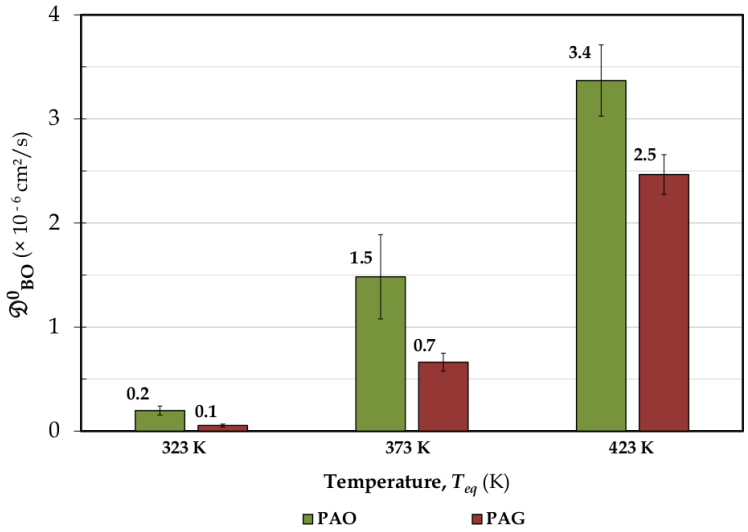

Figure 3.7 – Results of $\mathfrak{D}^0_{\mathrm{BO}}$ for the pure BO models (*PAO* in *moss green* and *PAG* in *ruby*), as a function of equilibrium temperature.

Regarding the accuracy of these results, the calculated coefficients have been found to be consistent with the diffusivities that are typically reported for liquids,[113,120] which are around 10^{-5} cm^2·s^{-1}. The obtained values are somewhat lower than those measured for the most studied solvents (*e.g.*, water, hexane, benzene, etc.),[113] mainly because of the relatively higher *molecular size* (or weight) of the investigated BO (*molar mass*, M: M_{PAO} = 422.83 g/mol & M_{PAG} = 504.79 g·mol^{-1}). Indeed, a mass dependence is indirectly observed for the diffusion rate of compounds exhibiting comparable chemical structure.[139,143,156,157,168–172] This correlation implies that, at a given and constant temperature, the relatively smaller molecules have a higher kinetic energy, which increases their thermal motion and eventually their diffu-

sivity. For that reason, it expected that, for example, PAO ($C_{30}H_{62}$) diffuses with a lower rate than a shorter alkane like hexane (C_6H_{14}).

Unfortunately, it was not possible to directly compare the calculated coefficients with experimental measurements, because of the lack of such data for the studied BO. Nevertheless, experimental diffusivities determined in similar physical conditions were found in the literature for n-*triacontane* and *squalane*, which are isomers of PAO (cf. figure 3.8).[170, 172] Their coefficient are reproduced in table 3.5, in order to allow a comparison with the calculated $\mathfrak{D}_{\mathrm{PAO}}^{0,\mathrm{PBC}}$ to be drawn.

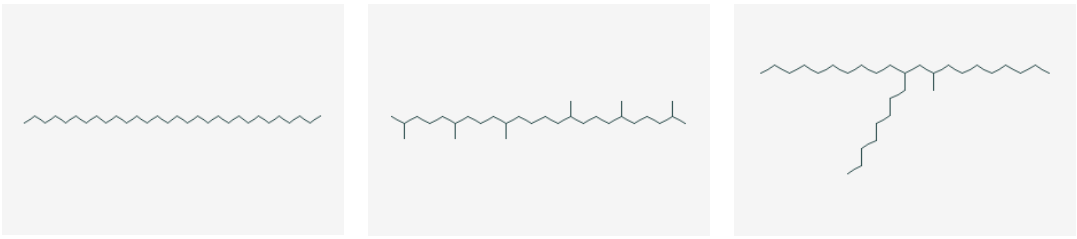

(a) *n*-Triacontane **(b) Squalane** **(c) PAO**

Figure 3.8 – Schematic structure of $C_{30}H_{62}$ isomers: **(a)** n-*triacontane* ; **(b)** *Squalane* (2,6,10,15,19,23-hexamethyl-tetracosane); **(c)** *PAO* (9-methyl-11-octyl-henicosane). These three medium-size alkanes have an equal molar mass but different molecular structures: n-*triacontane* is linear; *squalane* has a quasi-linear hydrocarbon chain, with six methyl branches symmetrically placed along a C_{24} backbone and finally; *PAO* is branched, with a methyl and an octyl groups branched at a C_{21} backbone.

Table 3.5 – Diffusion coefficient of pure $C_{30}H_{62}$ isomers (10^{-6} cm^2·s^{-1})

Isomer	Method	$\mathfrak{D}^0$ [(a)]	T	P	Reference
***n*-Triacontane**	*Experimental* [(b)]	3.9 (2)	376 K	0.99 atm	Vardag *et al.*[170]
Squalane	*Experimental* [(c)]	2.6 (3)	372 K	1.0 atm	Mondello *et al.*[172]
PAO	*MD simulation*	1.5 (4)	373 K	1.0 atm	-

[(a)] *The number in parentheses indicates the statistical uncertainty in the last given digit, related to the method of measurement or calculation of the diffusion coefficients.* [(b)] Pulsed-field gradient (PFG) NMR, *combined with Fourier transform.* [(c)] *PFG spin-echo NMR.*

Despite the fact that no system-size correction was used in our simulation study, we observe that the PAO diffusivity is in a fairly good agreement with those measured for its isomers. At least, their values are in the same order of magnitude, and more importantly, the effect of molecular branching on alkane dynamics was qualitatively described, which imposes that, for

similar size molecules, those with a branched structure usually move slower than the linear ones.[171,172] So, PAO molecules may diffuse in a lower rate than its isomers, as predicted by our simulations.

Concerning the diffusive behavior of PAO and PAG described in figure 3.7 (cf. p. 52), we can discern a clear difference between their diffusivities at any temperature ($\mathfrak{D}^0_{\mathrm{PAG}} < \mathfrak{D}^0_{\mathrm{PAO}}$). That dissimilarity cannot be explained solely on the basis of their molar mass ($M_{\mathrm{PAG}} > M_{\mathrm{PAO}}$), but also in terms of their *chemical structure*, which defines the intermolecular forces governing their properties. Actually, PAO is a nonpolar compound and PAG possesses several polar functional groups (*e.g.*, ether and hydroxyl), which have the ability to form *hydrogen bonds*. Indeed, the forces that hold together PAG molecules at the liquid state are stronger and more attractive than the ones encountered in a PAO solution. Thus, the spread of polar molecules through random thermal motion is, to a certain extent, slowed down by the resultant molecular cohesion, which eventually reduces their diffusion coefficient. That is why $\mathfrak{D}^0_{\mathrm{PAO}}$ are higher than $\mathfrak{D}^0_{\mathrm{PAG}}$.

It is also interesting to notice that the temperature dependence of BO diffusivities is rather well represented by an *Arrhenius-type equation* in the relatively small considered range of temperature (cf. figure 3.9). In fact, Arrhenius equation for molecular diffusion can be expressed as:[173]

$$\mathfrak{D}^0_{\mathrm{BO}} = \mathfrak{D}_0 \cdot \exp\left(\frac{-E^a}{k_b \cdot T}\right) \tag{3.7}$$

where $\mathfrak{D}_0$ is the diffusion prefactor, E^a is the diffusional energy barrier, k_b is the Boltzmann constant, and T is the absolute temperature.[173]

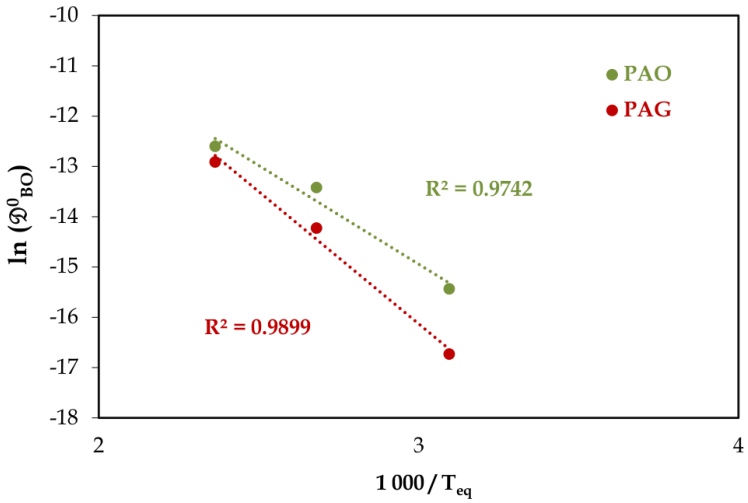

Figure 3.9 – Plot of Arrhenius-type fit of $\mathfrak{D}^0_{\mathrm{BO}}$ data (*PAO* in *moss green*, and *PAG* in *ruby*).

From a least-square fitting of the obtained $\mathfrak{D}^0_{BO}$ values, we calculated the energy barrier (E^a_{BO}) related to the diffusion of each BO model, yielding $E^a_{PAO} = 7.8 \pm 0.3$ kcal·mol^{-1} and $E^a_{PAG} = 10.5 \pm 0.6$ kcal·mol^{-1}.[10] In our case, E^a can be interpreted as a *deformation energy*, required to create a configurational space within the fluid medium, and enabling the thermally-induced molecular displacement to occur.[139] Thus, the obtained values of E^a_{BO} confirm the previously mentioned difference in diffusive behavior between PAO and PAG, indicating that a PAG molecule demands more energy to move, probably due to its need for "breaking" the surrounding hydrogen-bonding network, in comparison to the thermal motion of a PAO molecule in its own nonpolar matrix.

Therefore, the results obtained for the pure BO have provided useful information about the solvent liquid properties, and they constitute an important reference point to study the dynamics of OFM/BO mixtures, which was the next step of our investigation (cf. § 3.3.2). They have also suggested that the computational protocol used here to determine the diffusion coefficient is sufficiently accurate and effective to discern the influence of chemical structure on diffusive properties of lubricant components.

3.3.2 OFM/BO mixture properties

The liquid densities obtained for the binary solutions are presented in *appendix B* (cf. p. V). In the following, $\mathfrak{D}_{OFM,BO}$ results are reported according to the investigated structural factor (cf. table 3.1, p. 39). First, we studied the effect of OFM polar head for a given hydrocarbon chain (C_{18} tail), starting with an analysis of different chemical functional groups (cf. § 3.3.2.1, p. 56), and then focusing on characteristics of amine-based additives (*i.e.*, number and nature of hydrogen substituents; cf. § 3.3.2.2, p. 60). Afterwards, the influence of OFM tail length is described for a fixed primary amine polar head (cf. § 3.3.2.3, p. 62). Finally, the influence of BO polarity is addressed in each analysis related to OFM structure.

[10] For a comparative purpose, note that the *energy barrier* for squalane — determined from PFG NMR measurements performed by Mondello *et al.*,[171] — is approximately 6.23 kcal·mol^{-1}.

3.3.2.1 Effect of head group chemistry

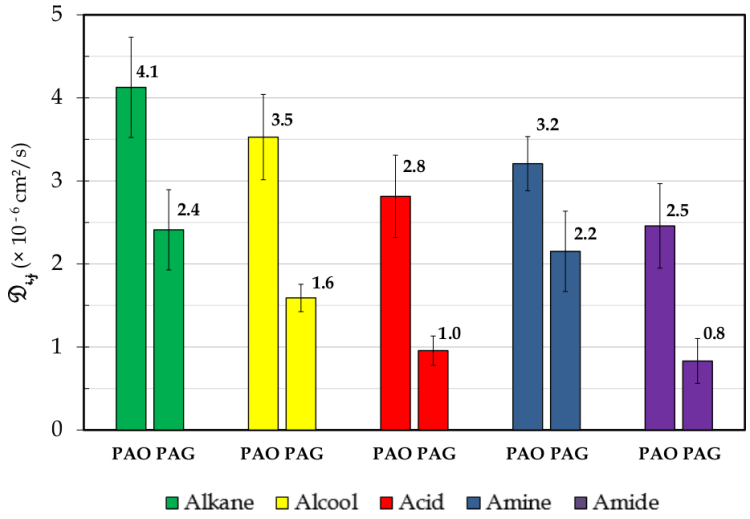

(a) $\mathfrak{D}_{i,j}$ data arranged by "head group chemistry" ordering

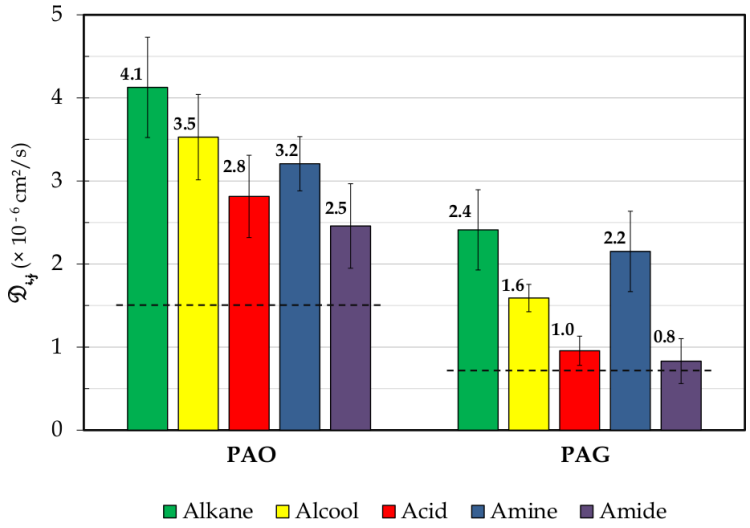

(b) $\mathfrak{D}_{i,j}$ data arranged by "BO polarity" ordering

Figure 3.10 – $\mathfrak{D}_{i,j}$ for liquid solutions of an OFM (*i*; 1 wt.%) in a BO (*j*: *PAO* – bars on left – or *PAG* – bars on right) at 373 K. Additive models are constituted with a C_{18} tail and a terminal group of a specific chemical function (groups: alkyl in *green*, hydroxyl in *yellow*, carboxyl in *red*, primary amine in *blue*, primary carboxamide in *purple*). Note that the alkane molecule is not an OFM model, but it is used here to assess the influence of additive head chemistry on diffusive behavior. For a comparison purpose, the mean value of pure BO diffusivities are indicated by dashed lines ($\mathfrak{D}^0_{PAO} = 1.5 \pm 0.4$ and $\mathfrak{D}^0_{PAG} = 0.7 \pm 0.1 \times 10^{-6}$ cm^2·s^{-1}).

First of all, it can be seen from results described in figure 3.10a a significant difference between the diffusivities of the investigated additive chemistries, which considerably depends on the solvent polarity. Actually, the alkane molecule and all studied OFM models (alcohol, carboxylic acid, primary amine and amide) diffuse faster in the nonpolar BO than in the polar

one. According to the Brownian motion, molecules move randomly because of their frequent collisions, where resultant molecular diffusion is enhanced by thermal energy.[131] Considering that the thermal energy comes from collisions between all of the solution components, when solvent molecules move faster more solute/solvent collisions occur and then, more thermal energy is generated to propel the solute molecules. In our mixtures, given that PAO propagates relatively faster than PAG (*i.e.*, $\mathfrak{D}^0_{\text{PAO}} > \mathfrak{D}^0_{\text{PAG}}$ at a specific temperature), OFM thus exhibit a boosted diffusion rate within PAO, in comparison with the one determined in a PAG-based solution.

That effect of solvent polarity on solute diffusive behavior can be confirmed by the experimental diffusivities determined by Park *et al.*,[139] who have studied the diffusion process of *methyl yellow* (MY: $C_{14}H_{15}N_3$, 4-dimethylaminoazobenzene), in several *n*-alkanes and *n*-alcohols solvents. Their main results are summarized in figure 3.11, which also presents a schematic structure of a MY molecule (cf. bottom left-hand corner in figure 3.11).

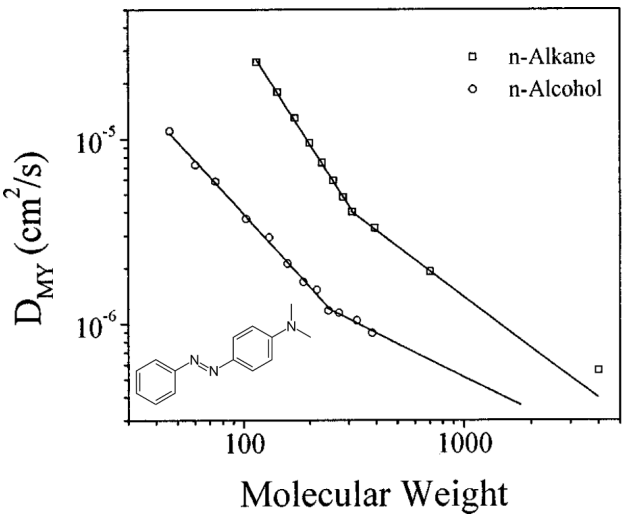

Figure 3.11 – MY diffusivity (D_{MY}) in *n*-alkanes and *n*-alcohols (plotted according to solvent molecular weight), obtained by forced Rayleigh scattering (FRS) at 318 K. For information, the *n*-alkanes studied were *n*-octane (C_8H_{18}), *n*-decane ($C_{10}H_{22}$), *n*-dodecane ($C_{12}H_{26}$), *n*-tetradecane ($C_{14}H_{30}$), *n*-hexadecane ($C_{16}H_{34}$), *n*-octadecane ($C_{18}H_{38}$), *n*-eicosane ($C_{20}H_{42}$), *n*-docosane ($C_{22}H_{46}$), *n*-octacosane ($C_{28}H_{58}$), *n*-pentacontane ($C_{50}H_{102}$), polyethylene (M_W : 4 000). The *n*-alcohols were ethanol (C_2H_5OH), 1-propanol (C_3H_7OH), 1-butanol (C_4H_9OH), 1-hexanol ($C_6H_{13}OH$), 1-octanol ($C_8H_{17}OH$), 1-decanol ($C_{10}H_{21}OH$), 1-dodecanol ($C_{12}H_{25}OH$), 1-tetradecanol ($C_{14}H_{29}OH$), 1-hexadecanol ($C_{16}H_{33}OH$), 1-octadecanol ($C_{18}H_{37}OH$), 1-docosanol ($C_{22}H_{45}OH$), and 1-hexacosanol ($C_{26}H_{53}OH$).
(figure retrieved from the original paper)[139]

As can be observed, $\mathfrak{D}_{\text{MY}}$ values are higher in the nonpolar solvents (alkanes) than in the polar ones (alcohols), certainly as a result of the resistance to motion induced by the strong in-

termolecular forces existing between the polar compounds, and particular involving the solute molecules, which also contain polar functional groups (*i.e.*, azo/diimide and tertiary amino groups). In addition, their study highlights the impact of the molecular weight of the solvent on the solute diffusivity, showing that MY diffusion coefficient decreases with increasing solvent mass, regardless of the considered solvent chemistry. To sum-up, we can generally conclude that a slower solvent leads to a slower solute, provided that both compounds exhibit comparable molecular weight.

The $\mathfrak{D}_{\text{OFM, BO}}$ results also suggest that the head group chemistry of OFM affects their diffusive behavior, but to different extents, depending on the solvent polarity (cf. figure 3.10b, p. 56). We observe that the investigated polar heads (hydroxyl, carboxyl, primary amine and carboxyamide) do slow down the OFM motion in both BO, making their molecules "stickier" in comparison with an alkyl group, which is the nonpolar terminal group used here as reference. Indeed, each one of the four studied polar end groups possesses a hydrogen atom attached to an electronegative element (*e.g.*, nitrogen or oxygen atoms), thereby being able to make hydrogen bonds with solute and/or polar solvent molecules (cf. figure 3.12). That attractive interaction most likely explains the observed relative decrease in OFM diffusion rate, especially in PAG-based solutions.

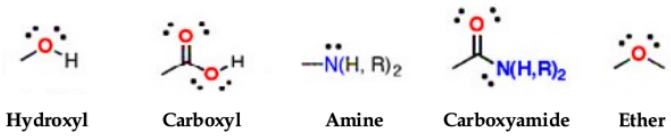

Figure 3.12 – Polar functional groups present in the composition of the lubricant components investigated in the present simulation study (*i.e.*, OFM & BO models). (*Reference [online]:* masterorganicchemistry.files.wordpress.com)

However, since statistical uncertainties (σ_{SD}) related to $\mathfrak{D}$ are rather scattered (cf. figure 3.10, p. 56), it is not possible to establish a rigorous ranking of the OFM diffusivities as a function of their polar head chemistry, and that mainly for those determined in PAO solutions. Nevertheless, the mean values of $\mathfrak{D}_{\text{OFM, BO}}$ still provide some interesting trends about the solute/-solvent and solute/solute interactions with the OFM/BO mixtures. For example, the relatively high diffusion coefficient of the primary amine in PAG seems to indicate that its polar head may have a weaker bonding network compared to the other OFM chemistries (*i.e.*, alcohol, acid and primary amide). Additionally, each one of the acid and primary amide molecules has two electronegative atoms, which may strengthen their solute/solvent interactions and then

hinder their motion in a PAG matrix. For a PAO-based solution, the relatively low diffusivity observed for the acid and the primary amide may result from a *self-association process*, which is an usual phenomenon related to surfactant compounds.[29, 34, 77, 118, 127, 140, 143, 148, 174–177] The formation of clusters/aggregates of these additives (*e.g*, dimers, reverse micelles, etc.) — most likely due to attractive solute/solute interactions — can be confirmed by an analysis of the *radial distribution functions* (RDF – $g_{p,p}(r)$), obtained for the OFM/PAO mixtures (cf. figure 3.13).[83, 85] In the figure below, it is important to note that $g_{p,p}$ axis length varies depending on OFM functional group.

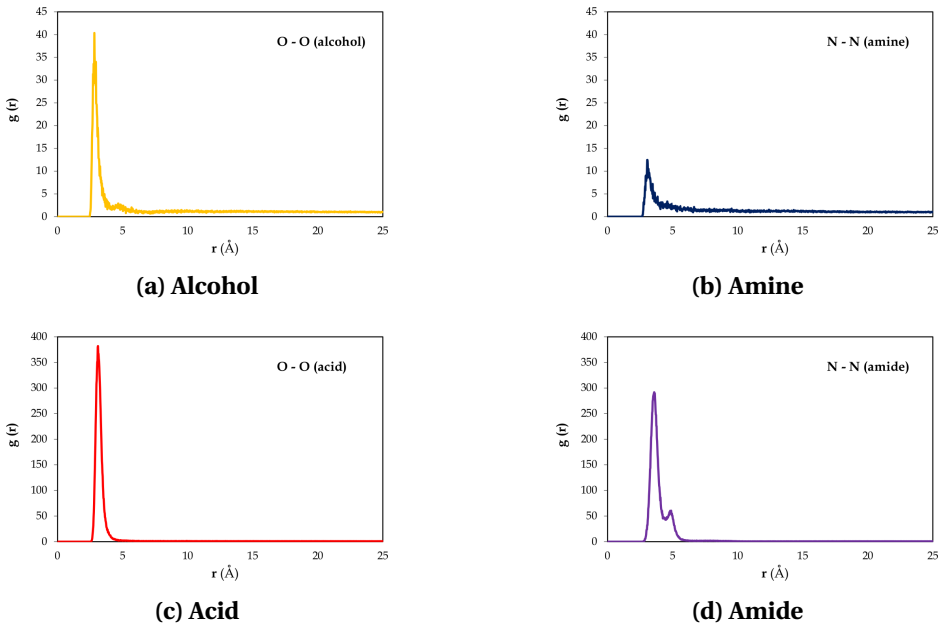

(a) Alcohol **(b) Amine**

(c) Acid **(d) Amide**

Figure 3.13 – *Radial distribution functions* $g_{p,p}(r)$ between the most negative charged atom (p) of each polar, in *PAO-based solutions*: **(a)** hydroxyl ($g_{O,O}$); **(b)** primary amine ($g_{N,N}$); **(c)** carboxyl ($g_{O,O}$; where the oxygen atom belongs to the hydroxyl group); **(d)** primary carboxylamide ($g_{N,N}$).

Actually, $g_{p,p}(r)$ provides the spherically averaged distribution of interatomic distance between the pair groups *p-p*, shedding light on the *local microstructure* of the regarded liquid solutions. In our PAO solutions, the analyses of the pair RDF indicate that the OFM molecules do interact with each other during their molecular diffusion, given that at least a sharp main peak can be identified in a short nearest-neighbor distance from the polar head (< 4 Å), for all additive models. Yet, based on a comparison in terms of the peak heights of the four polar chemistries, it seems that the acid and the primary amide tend to form more "time stable" clusters compared to those of alcohol and primary amine, which explains their diminished molecular diffusion rate.

3.3.2.2 Effect of number and nature of hydrogen substituents

After studying different polar head chemistries, we focused on the diffusive behavior of the amine-based FM, extending the investigation to the structures of their hydrogen substituents, notably their *number* and *chemical nature*. Thus, figure 3.14 shows the diffusion coefficients of C_{18} secondary and tertiary amines, with alkyl and ethoxyl groups, in PAO and PAG.

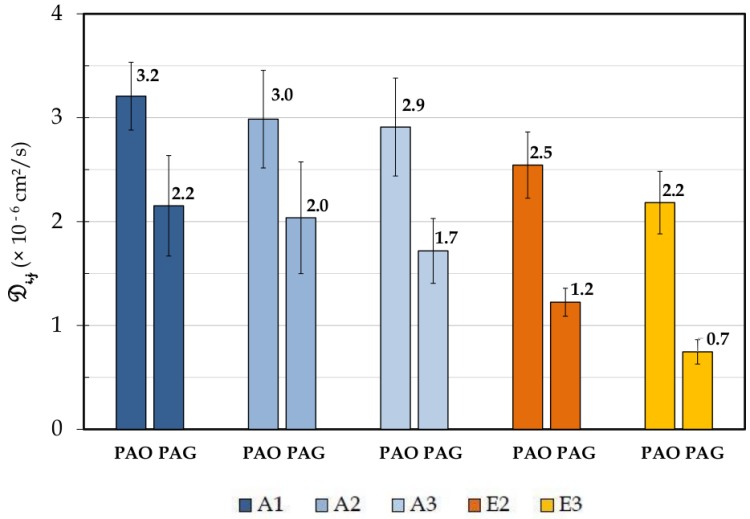

(a) $\mathfrak{D}_{i,j}$ data arranged by "amine-type head group" ordering

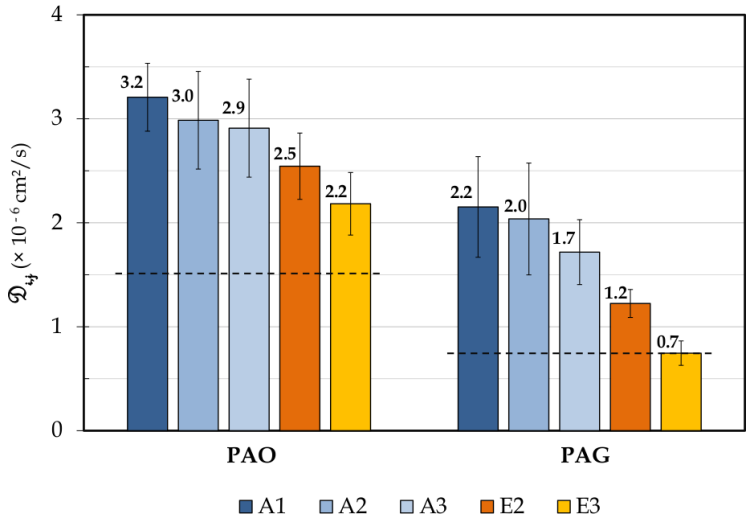

(b) $\mathfrak{D}_{i,j}$ data arranged by "BO polarity" ordering

Figure 3.14 – $\mathfrak{D}_{i,j}$ for liquid solutions of an amine-based FM (*i*; 1 wt.%) in a BO (*j*: *PAO* – bars on left – or *PAG* – bars on right) at 373 K. OFM are constituted with a C_{18} tail and an amine polar head: the number of hydrogen substituents are expressed in the legend (*1*: *primary*, *2*: *secondary* and *3*: *tertiary*) and their nature are indicated by different colors (*alkyl* – *A* in *light blue*, *ethoxyl* – *E* in *orange*). For a comparison purpose, the mean value of pure BO diffusivities are indicated by dashed lines ($\mathfrak{D}^0_{PAO} = 1.5 \pm 0.4$ and $\mathfrak{D}^0_{PAG} = 0.7 \pm 0.1 \times 10^{-6}$ cm^2·s^{-1}).

Concerning the BO polarity effect, all amine molecules diffuse faster in the nonpolar solvent, as the first results for the primary amine have already pointed out (cf. figure 3.10a, p. 56). Besides, we can observe that the diffusion rate is less sensitive to the structure of the amine polar head in a PAO compared to that in a PAG solution.

Despite the wider scattered results (cf. figure 3.14, p. 60), $\mathfrak{D}$ mean values seem to indicate that amine diffusivity decreases with increasing number and polarity of the hydrogen substituents:

- $\mathfrak{D}_{\text{tertiary}} < \mathfrak{D}_{\text{secondary}} < \mathfrak{D}_{\text{primary}}$;
- $\mathfrak{D}_{\text{ethoxyl}} < \mathfrak{D}_{\text{alkyl}}$ (note that for the ethoxylated substituents, which contain a hydroxyl group, another electronegative atom is added to the OFM molecular structure).

Thus, we can conclude that a broader (or heavier) and more polar substituent group renders the amine molecule slower, from a relative point of view.

3.3.2.3 Effect of hydrocarbon chain length

Lastly, the influence of the alkyl tail length was studied, and the diffusivity of primary amines ($\mathfrak{D}_{\mathrm{BO,\,A1}}$) containing 6, 12 and 24 carbon atoms were also calculated. Their values are presented in figure 3.15, along with those of the already mentioned C_{18} primary amine.

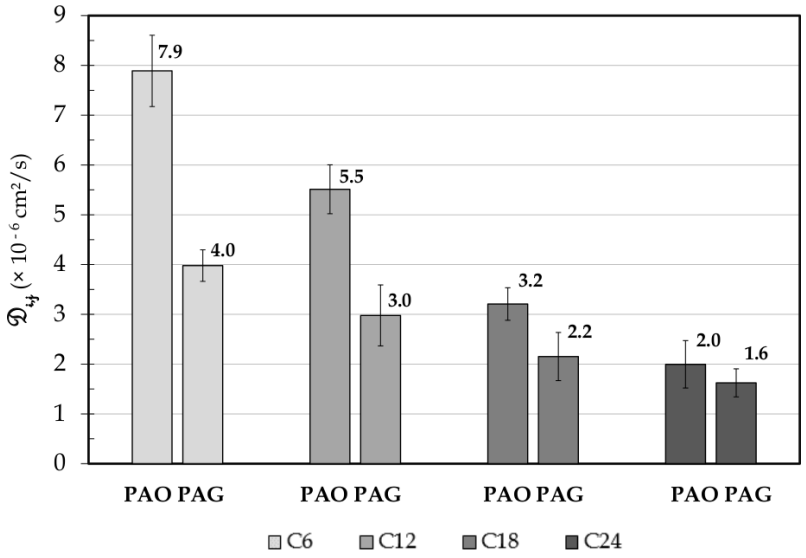

(a) $\mathfrak{D}_{i,j}$ data arranged by "hydrocarbon tail length" ordering

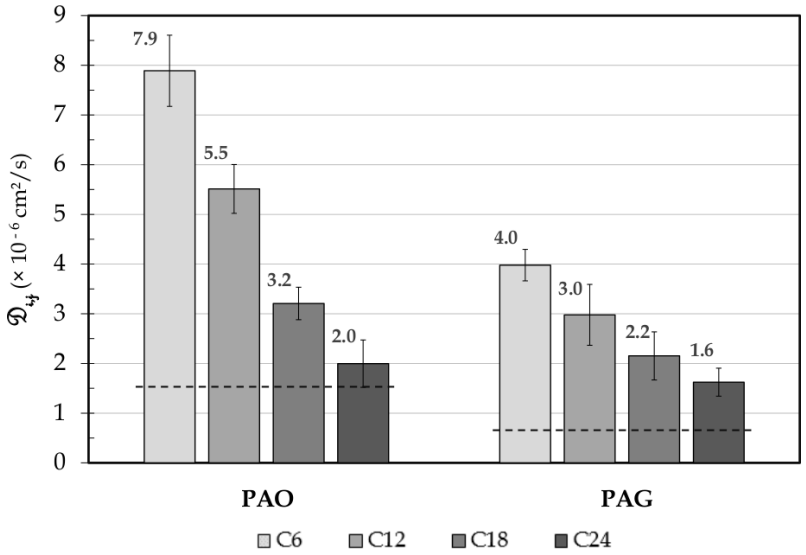

(b) $\mathfrak{D}_{i,j}$ data arranged by "BO polarity" ordering

Figure 3.15 – $\mathfrak{D}_{i,j}$ for liquid solutions of an amine-based FM (*i*; 1 wt.%) in a BO (*j*; *PAO* – bars on left – or *PAG* – bars on right) at 373 K. OFM are constituted with a primary amine polar head and a hydrocarbon tail of a given length, which is indicated in the legend: chains with C_6, C_{12}, C_{18} and C_{24}. For a comparison purpose, the mean value of pure BO diffusivities are indicated by dashed lines ($\mathfrak{D}^0_{\mathrm{PAO}} = 1.5 \pm 0.4$ and $\mathfrak{D}^0_{\mathrm{PAG}} = 0.7 \pm 0.1 \times 10^{-6}$ cm^2·s^{-1}).

As one would expected, the molecular diffusion rate of the investigated primary amines is enhanced by the reduction of their hydrocarbon chain, which is equivalent to a decrease in their molecular weight (cf. figure 3.16). In short, relatively smaller (or lighter) molecules diffuse faster in both nonpolar and polar BO, *i.e.*, $\mathfrak{D}_{C6\text{-}A1} > \mathfrak{D}_{C12\text{-}A1} > \mathfrak{D}_{C18\text{-}A1} > \mathfrak{D}_{C24\text{-}A1}$.

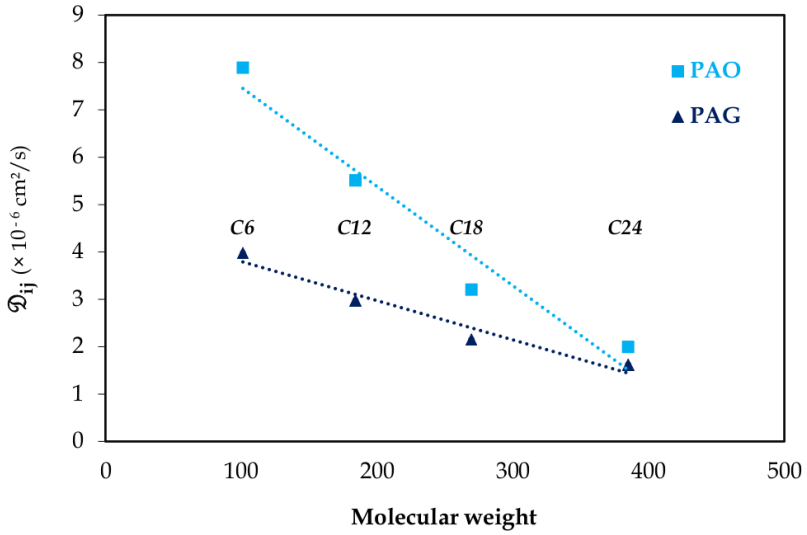

Figure 3.16 – Plot of $\mathfrak{D}_{A1,BO}$ as a function of amine molecular weights. $\mathfrak{D}_{A1,PAO}$ are represented in light blue and $\mathfrak{D}_{A1,PAG}$ in dark blue.

Moreover, we can observe that the effect of the tail length on $\mathfrak{D}_{A1,BO}$ greatly differs as a function of the BO polarity, being intensified in the nonpolar solvent. That effect is clear highlighted by the different slopes of the linear relation between $\mathfrak{D}_{A1,BO}$ and OFM molecular weight, as a function of the BO (cf. figure 3.16). For instance, the difference in terms of diffusivity between C_6 and C_{24} amines is twice greater in PAO than in a PAG solution.

3.4 Summary

The diffusion study covered in this chapter is based on analyses of OFM/BO diffusivities calculated from averaged MSD-time profiles, which were in turn obtained from EMD simulations. The computational procedure established in our work seems to provide a suitable framework for elucidating how the chemical structure related to BO and OFM molecules affects their liquid-state dynamics. In particular, this study has permitted the validation of the original OPLS-AA force field as a proper interaction model to investigate organic compounds.

Moreover, our results have indicated that the OFM diffusion coefficient is greatly controlled by the BO features (*i.e.*, polarity and mass), but it is also impacted, to a lesser extent, by their own molecular structure (*i.e.*, polar head chemistry and alkyl tail length). Briefly, it has been shown that *strong intermolecular interactions* involving the polar functional groups, as well as the increase in molecular weight, indeed act to impede and slow down their thermal-induced motion. Therefore, in order to improve the diffusion rate of OFM, and possibly their competitive ability for adsorption , we can conclude that it is better to use a nonpolar BO (*e.g.*, PAO) and a surfactant molecule that has the smallest possible structure, with a terminal polar group exhibiting a relatively low polarity.

However, the additive diffusivity must be in balance with other required attributes, such as its adsorption activity (or chemical reactivity) with solid surfaces, and also its oil solubility.[178] In fact, an effective OFM must have a head group that interacts sufficiently strongly with the engineering parts, and also a long enough aliphatic tail to ensure its solubility in the BO and to form close-packed structures that protect and separate the rubbing surfaces.[27,34,42,60,179] Considering this set of performance indicators along with the obtained values of $\mathfrak{D}_{\mathrm{OFM,\,PAO}}$, the molecules of C_{18} *primary amine* ($C_{18}H_{39}N$, octadecylamine) and *PAO* were selected as the lubricant constituent models for the following computational studies treating the adsorptive and frictional behaviors of OFM additives (cf. chapters 4 and 5, p. 65 and 97, respectively).

4

Adsorption

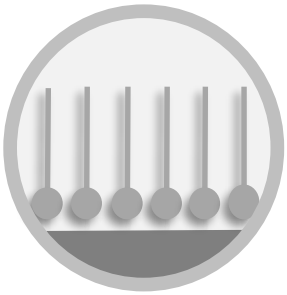

After investigating the molecular diffusion of OFM within the lubricant solution, we turned attention toward their activity at the interface with engine components. These surface-acting additives adsorb spontaneously on solid substrates, forming ordered monolayers capable of reducing the negative effects induced by friction and wear. Therefore, OFM effectiveness is strictly linked to phenomena related to their adsorption and self-assembly processes. Besides, considering that classical MD cannot describe electronic structure, alternative methods are thus necessary to better understand the adsorption mechanism of fatty amines on ferrous surfaces.

In this context, quantum-level calculations were carried out to obtain the interaction information needed to parameterize an interfacial force field required in our MD protocol. Once the $U^{\text{interface}}$ parameters were determined, a series of equilibrium MD simulations were performed in order to analyse the molecular organization of adsorbed amine monolayers, as a function of their surface coverage. The objectives were twofold: firstly, to validate the fitted potential, and secondly, to select the most relevant SAM densities used to design the subsequent friction simulations, and finally to investigate their lubricating behavior. Thus, the present chapter first reports the preliminary DFT and XPS analyses, probing amine adsorption mechanism, as well as the parameterization of the amine-hematite potential (cf. § 4.1, p. 66), and then, the structural study of the model adsorbed films is fully described (cf. § 4.2, p. 74).

4.1 Amine adsorption mechanism on iron oxide

The friction-reducing properties of OFM in a boundary contact arise from their ability to adsorb on solid substrates and to form organized thin films that are difficult to compress and easy to be sheared off (cf. figure 1.4, p. 5).[27,34,28,180] By consequence, *adsorption process* is a key step in their lubricating action, which is in turn influenced by the amount of the adsorbed additives, by the structure of the resulting molecular layer, and in particular, by the nature and strength of the interactions involving OFM functional groups and sliding surfaces.[46,55–57,65,77,181,182] These interfacial interactions can actually be of chemical or physical nature, where a *physisorption* concerns intermolecular forces such as vdW and hydrogen bonding, and a *chemisorption* implies a chemical reaction, where valence electrons are shared by the adsorbate and the surface.[27,31,35] Hence, a chemically adsorbed OFM exhibits a stronger binding interaction with the substrate compared to the one involving a physically adsorbed additive, which may be beneficial for protecting OFM film against the rubbing effects, thereby extending the engine durability.[6,29,31]

Concerning the interactions between aliphatic primary amines and iron-based surfaces, different adsorption mechanisms have been reported in the literature, as a function of the substrate nature.[30,45,183,184] Some works suggest a chemisorption through the nitrogen lone pair electrons from the amine molecule and the iron oxides,[45,183,184] whereas other studies pointed out a physisorption mechanism via hydrogen bonding between the amino polar head and hydroxyl terminal groups present on an iron hydroxide surface.[30,50] Incidentally, those findings highlight the fact that the adsorption process of a given surfactant-type molecule is greatly affected by the chemical nature of the substrate.[27] Besides, one can expect that multiple adsorption mechanisms coexist in real automotive engines since their steel component parts possess a heterogeneous microstructure and usually, they are covered by various iron oxides/hydroxides in addition to carbon contamination, depending on the considered environment (*e.g.*, presence of ambient oxygen and water) and on the rubbing/wear conditions.[27,31,78,185] However, as previously explained (cf. § 2.1.2, p. 21), we were specifically interested in studying the adsorption mechanism of primary alkyl amines on a model ferric oxide surface (α-Fe_2O_3).

To that end, DFT and XPS analyses were initially carried out by the members of LTDS in order to elucidate the *binding mechanism* prevailing in that system, and to possibly confirm the chemical adsorption found in literature. The obtained results are described in paragraphs 4.1.1 and 4.1.2 (cf. p. 67 and 71, respectively). Then, based on the adsorption energy and on the

geometry configuration determined from DFT, an interfacial potential $U^{\text{interface}}$ was derived to reproduce the (primary) amine-hematite interaction by means of classical MD simulations (cf. § 4.1.3, p. 72).

4.1.1 DFT calculations

As an *ab initio* quantum mechanical method, *density functional theory* is able to describe the electronic properties of matter, and consequently, to predict chemical reactivity.[75, 186] This method was thus employed to determine the *adsorption structure* and the corresponding *binding energy* (E_{ads}) of a primary amine on an α-Fe_2O_3 (0 1 $\bar{1}$ 2) slab.

Because of their high computational cost, DFT calculations describe static states and include system models limited to a few number of atoms.[81, 94] For these reasons and assuming that the OFM polar head is the *anchoring group* that directly interacts with the solid surfaces,[27, 33, 34] a single amine molecule containing a shorter alkyl tail was adopted to simplify the investigated system. This hypothesis is supported by previous computational works,[46, 65, 187] which have suggested that surfactant-surface interaction mechanism is not significantly sensitive either to the structure or to the length of the molecular tail group. Thus, a relaxed C_5 *primary amine* ($C_5H_{13}N$; 19 atoms) was employed here as input for the geometry optimizations, being vertically placed on the top of a hematite slab (120 atoms; cf. *unit surface cell* described in § 2.1.2, p. 21), with the aliphatic chain standing upright and the amino group oriented towards the substrate, as illustrated in figure 4.1.

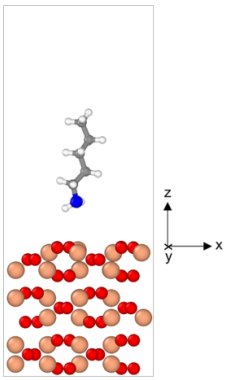

Figure 4.1 – Side view of the initial configuration used to study the adsorption of a $C_5H_{13}N$ molecule upon the α-Fe_2O_3 (0 1 $\bar{1}$ 2) slab via DFT. For information, the vacuum spacing in the *z* direction was fixed at 10 Å in order to avoid interaction between the repeated periodic simulation cells. *Atomic color code: coral* - iron, *red* - oxygen, *white* - hydrogen, *gray* - carbon, *blue* - nitrogen.

All computations were performed using *VASP* program (version 5.3.5),[188–193] which produces an iterative solution of the Kohn-Sham equations within a plane-wave basis for a system with periodic boundary conditions.[80,194] The performed calculations were spin-polarized and the exchange-correlation energy was determined with the generalized gradient approximation (GGA) of Perdew-Burke-Ernzerhof (PBE) functional.[195,196] In particular, the GGA+U method, such that formulated by Dudarev *et al.*,[197] was employed to correct the strong correlation of iron *3d*-electrons (U^{eff} = 5.0 eV). Besides,, a cutoff energy value of 500 eV was used for the plane-wave expansion, and a convergence criterion of 10^{-5} eV on the total energy was applied in the self-consistency cycle. During the relaxation phase, the atoms in the outermost layer of the hematite surface and the ones composing the adsorbate (*i.e.*, the C_5 amine molecule) were allowed to displace until residual forces reached 0.08 eV/Å, while the atoms in the remaining two layers of the surface were kept fixed.

Furthermore, different vertical adsorption configurations were investigated — with the C_5 hydrocarbon chain initially oriented perpendicular to the α-Fe_2O_3 slab — by varying the adsorption sites and the adsorbate-surface distance, and subsequently computing the total potential energy of the system in equilibrium . Then, the *adsorption energy* was calculated using the following expression for the amine-hematite interaction, E_{ads}:[198]

$$E_{ads} = E_{complex} - \left(E_{adsorbate} + E_{surface}\right) \tag{4.1}$$

in which, $E_{complex}$ is the energy of the optimized configuration associated to the adsorbed amine on the iron oxide surface, whereas $E_{adsorbate}$ and $E_{surface}$ refer to the energy of the relaxed configurations representing the isolated amine in gas phase and the bare hematite slab, respectively. It is important to note that a *negative adsorption energy* implies an *exothermic adsorption process*, and a relatively stronger interaction of the surfactant molecule on the oxidized surface in comparison with their separated states.[198]

From the results obtained for all of the analyzed upright configurations, the most energetically favorable and stable structure indicates that the nitrogen atom of the amine molecule adsorbs closely to the top site of a surface iron atom, with a resulting *N-Fe equilibrium distance* of $d_{N\text{-}Fe}$ = 2.16 Å (cf. figure 4.2, p. 69). In this configuration, the concerned iron is pulled outwards from its relaxed lattice position, by approximately 0.2 Å, in order to maximize its interaction with the adsorbate. Besides, the hydrogen atoms of the amino group are oriented away from the iron and towards the surrounding oxygens of the upper oxide layer, and the alkyl tail is tilted by most 45°, with respect to the surface normal.

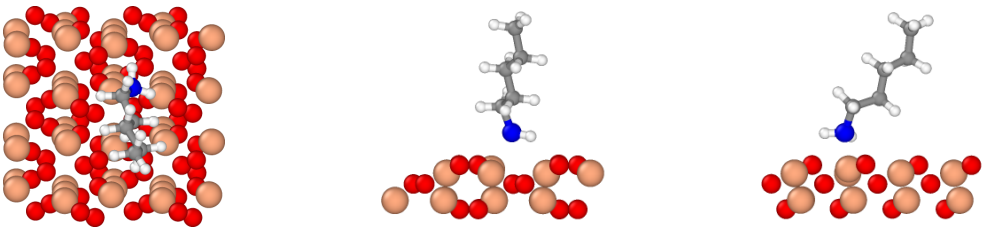

(a) ***xy*** **plane** **(b)** ***xz*** **plane** **(c)** ***yz*** **plane**

Figure 4.2 – Top (**a**) and side views (**b**, **c**) of the most stable adsorption geometry of a primary C_5 alkyl amine (upright position) on an α-Fe_2O_3 surface. *Atomic color code: coral* - iron, *red* - oxygen, *white* - hydrogen, *gray* - carbon, *blue* - nitrogen.

The corresponding *adsorption energy* calculated for that configuration is -17.48 kcal·mol^{-1} (or equivalently, $E_{ads} = -0.76$ eV), which can be considered as a relatively strong binding energy typical of chemical adsorptions ($|E_{chemisorption}| > 9-10$ kcal·mol^{-1}).[31,28,199,200] Moreover, in view of better characterizing the nature of the detected *N-Fe bonding interaction*, it is useful to analyze the charge redistribution occurring at the system interface, by comparing the *electronic charge density* (ϱ) of the adsorbed configuration with the ones of the amine and the hematite reference states ($\varrho_{complex}$, $\varrho_{adsorbate}$ and $\varrho_{surface}$)[194,201] In this regard, figure 4.3 shows the *charge density difference* ($\Delta\varrho$) defined as $\Delta\varrho = \varrho_{complex} - (\varrho_{adsorbate} + \varrho_{surface})$, where the blue and yellow isosurfaces respectively depict the regions of *electron accumulation* and *electron depletion* induced by the adsorption process.

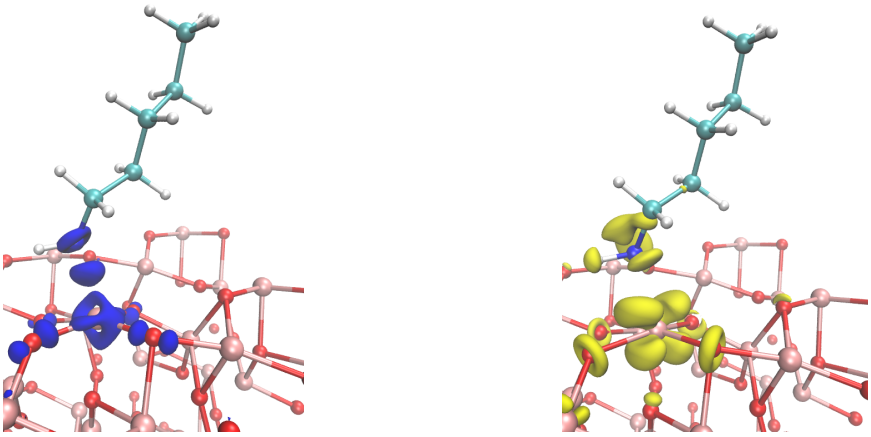

(a) Accumulation of charge **(b) Deficit of charge**

Figure 4.3 – Charge density difference ($\Delta\varrho$) of the primary C_5 alkyl amine on α-Fe_2O_3 (0 1 $\bar{1}$ 2) slab with $d_{N\text{-}Fe} = 2.16$ Å. The isosurface levels used to represent the electronic accumulation and depletion regions (in *blue* and in *yellow*, respectively) are 1.8×10^{-5} $e\cdot$Å^{-3} and -0.7×10^{-5} $e\cdot$Å^{-3}, respectively. Note that the boundaries of the simulation box are not represented here. *Atomic color code: pink* - iron, *red* - oxygen, *white* - hydrogen, *light blue* - carbon, *dark blue* - nitrogen.

The $\Delta\rho$ representation clearly reveals a significant charge rearrangement involving the main interacting species (cf. figure 4.3, p. 69). For example, charge deficit regions are observed around the nitrogen atom (cf. figure 4.3b), while a region of accumulation charge surrounds the concerned surface iron (cf. figure 4.3a). Most importantly, it shows the formation of a *N-Fe chemical bond*, which is indicated by the accumulation region of electron density that arises at the adsorbate-substrate interface, specifically situated in the middle of the axis extending from the iron to the nitrogen atom (cf. *blue elliptical isosurface*, located between the amine head group and the α-Fe_2O_3 slab, in figure 4.3a).

Besides, the observed chemical reaction is most likely due to the transfer of electronic charge from the nitrogen to the iron — through its lone pair electrons —, and predominantly forming a *covalent bond*, such as the results found in previous works.[45,202] Besides, the *Hirshelfd charge*[203] q^H, calculated for the nitrogen atom, allows the supposed charge transfer to be validated, since q^H_{N} = -0.224 e (before adsorption) and q^H_{N} = -0.162 e (after adsorption), confirming its electronic density depletion caused by the resulting adsorption process.

Therefore, the chemisorption of a short aliphatic primary amine on a hematite substrate was verified by DFT, where the obtained structure of minimum adsorption energy gives a N-Fe bond length of $d_{\text{N-Fe}}$ = 2.16 Å and a binding energy equal to $\mathrm{E_{ads}}$ = -17.48 kcal·mol^{-1}. These values were useful to derive an interfacial interaction potential $U^{\text{interface}}$ suitable to describe, through classical MD simulations, the adsorption of larger and denser systems like, for example, self-assembled monolayers composed of multiple C_{18} primary amines (cf. § 4.1.3, p. 72).

4.1.2 XPS analysis

Simultaneously with the quantum chemical computations, supplementary adsorption experiments were performed considering a system under gas phase (*i.e.*, without any solvent), in order to be as close as possible to the physical conditions applied in the foregoing DFT study. So, C_{18} primary amines was adsorbed onto an iron oxide surface within a vacuum chamber, followed by an in-situ *X-ray photoelectron spectroscopy* analysis. The obtained result from this experiment is compared with the one determined earlier for the pure octadecylamine powder in the figure below (cf. figures 4.4b and 4.4a, respectively). For clarity purposes, the experimental protocol and the complete XPS spectra of both systems are detailed in *appendix C* (cf. p. VII).

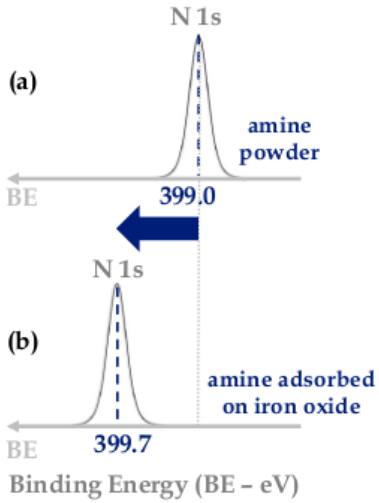

Figure 4.4 – Schematic of the main contributions of the N 1s spectra obtained from *in-situ* XPS analyses of the amine powder (*top spectrum*) and the adsorbed amine on the oxidized substrate (*bottom spectrum*).

The figure above shows the simplified *N 1s spectra* obtained from the amine powder (peak at 399 ± 0.1 eV), as well as from from the amine adsorbed on the oxidized surface (peak at 399.7 ± 0.1 eV). In each case, the N 1s spectrum was fitted with a single main contribution that was assigned to C-N bond. As can be seen, the peak for the adsorbed molecule was shifted by 0.7 eV to a higher binding energy, in comparison to the reference system (*i.e.*, the amine powder). That important shift indicates a strong interaction between the investigated amines and substrate, which can be explained by the formation of N-Fe bonds via the electron density donation from the nitrogens, by means of their lone pair electrons, to the iron-based surface.

This result is thus in agreement with the earlier DFT analysis (cf. § 4.1.1, p. 67), and also with the other experiments reported in literature,[45, 183, 184] thereby demonstrating that primary alkyl amines do chemisorb onto an iron oxide substrate.

4.1.3 Parameterization of an interfacial MD potential

After assessing the chemical nature and the strength associated with the adsorption process between primary alyphatic amines and a ferric oxide surface, we focused on obtaining an interfacial force field capable of reproducing their relatively strong interaction within the framework of large-scale MD simulations. Besides, it is worthwhile to remember here that our ultimately aim consisted in establishing a "computational tribotest" that enables us to investigate nanoscale sliding contacts. So, the friction simulations had to be designed in order to mimic the dynamic and lubricating properties of OFM-based SAM under different tribological conditions.

Considering these aspects, we chose to express the amine-hematite interactions by means of a pairwise atomic potential composed of nonbonded contributions, which is defined by the sum of *Lennard-Jones 12-6* and *Coulomb intermolecular models*, representing the potential energy involved in their vdW and electrostatic interactions, respectively (cf. $U^{\text{interface}}$, defined by equation 2.10 in § 2.2.2.3, p. 32). In spite of the fact that N-Fe bonds are created within the investigated system, *nonbonded potentials* were preferred to *bonded models*, because they theoretically allow an amine molecule to adsorb, to desorb and to dynamically migrate over the surface during the course of a MD simulation, provided that a proper set of parameters permits an effective description of the concerned interfacial interactions. Conversely, a classical intramolecular potential — modeling covalent bonds — cannot describe the dynamic behavior of adsorbed films in MD simulations, because it cannot reproduce the formation and breaking of chemical bonds, or in other words, the chemisorption and desorption of lubricant additives that might occur within boundary contacts in mechanical operation. That is why the LJ and Coulomb potentials were chosen to define our $U^{\text{interface}}$ force field.

Therefore, $U^{\text{interface}}$ parameters were adjusted to reproduce both adsorption energy and equilibrium configuration obtained from the aforementioned DFT analysis (cf. § 4.1.1, p. 68), using a *trial-and-error approach* similarly applied in other published works.[81,82,204] Moreover, in order to be consistent with all of the other MD potentials used to represent our systems — $U^{\text{lubricant}}$ and U^{surface} (cf. equations 2.8 and 2.9, p. 27 and 31, respectively) —, the values of the atomic/ionic charges used to determine the electrostatic interactions at the SAM/substrate interface were kept the same as those present in OPLS-AA force field[108] ($U^{\text{lubricant}}$), and in the interionic potential developed by Guillot *et al.*[110,111] (U^{surface}; cf. charges indicated in § 2.2.2.3, p. 32). Consequently, only the interfacial LJ pairwise parameters, ϵ_{ij} and σ_{ij}, were

derived from the results of the preliminary *ab initio* calculations. As a reminder, ϵ_{ij} and σ_{ij} respectively correspond to the *well-depth energy* and the *equilibrium distance* where the LJ term has its minimum energy value between each atom pair *ij*.[81]

In practice, the fitting of LJ parameters was carried out based on the calculation of the *adsorption energy* E_{ads}^{MD} involving a C_5 primary amine in contact with a hematite slab, where E_{ads}^{MD} is similarly defined as in equation 4.1 (cf. § 4.1.1, p. 68), but using the potential energies $E_{complex}$, $E_{adsorbate}$ and $E_{surface}$ determined from the three MD force fields employed in our computational protocol (cf. $U^{lubricant}$, $U^{surface}$ and $U^{interface}$ in § 2.2.2, p. 26). To do so, the configuration of the system considered in this parameterization process correspond to the DFT optimized geometry related to the adsorption model depicted in figure 4.2 (cf. p. 69, in which $d_{N\text{-}Fe}$ = 2.16 Å), but with a cell box containing a vacuum space in *z* direction of 100 Å.

Besides, all static calculations were performed with *LAMMPS* code.[95] Short-range non-bonded interactions were cut-off at 5 Å, and electrostatic interactions were calculated applying a slab implementation of the PPPM algorithm.[161,205] Periodic boundary conditions were applied only in *x* and *y* directions. Then, by tuning the LJ parameters of $U^{interface}$ potential, the E_{ads}^{MD} was repeatedly computed until a quantitative agreement with the adsorption energy determined from DFT was achieved, given that E_{ads}^{DFT} = -17.48 kcal·mol^{-1}.

After many iterative trials, a set of parameters comprising the ϵ_{ij} and σ_{ij} values of *eight different atomic pairs* was selected for a calculated adsorption energy of E_{ads}^{MD} = -16.72 kcal·mol^{-1}, which represents a relative deviation of 4%, compared to the DFT-derived data. As a reminder, the fitted pairwise parameters are listed in the table 2.7 of chapter 2 (cf. § 2.2.2, p. 26).

Despite both simplified *adsorption model* and *parameterization procedure* used here to establish the required $U^{interface}$, we have considered that this MD interfacial potential can ensure the *molecular anchoring* of aliphatic primary amines on iron adsorption sites of a hematite substrate, via their polar head group and with a proper attractive interaction strength. We have thereby assumed that the obtained $U^{interface}$ can indeed reproduce the dynamic evolution of adsorbed films made up of multiple and larger OFM molecules, such as C_{18} primary amines.

Accordingly, a series of equilibrium MD simulations was performed in order to investigate the molecular organization of amine-based SAM, as a function of their surface coverage, being this study an effective way of evaluating the reliability of the fitted interfacial LJ parameters. That structural investigation is presented in the next section (cf. § 4.2, p. 74).

4.2 MD study of adsorbed amine-based SAM

Other than the OFM adsorption onto solid substrates, their ensuing aggregation and self-organization into well-arranged molecular clusters are essential processes to effectively modify the chemistry and the shear stress of the interface formed between two opposing surfaces under BL conditions.[27,28,34,76,77,206,207] For instance, in a recent study made by Koshima *et al.*,[42] the control-friction performance of binary PAO-based solutions containing a wide range of OFM models were correlated with the vibrational spectral characteristics[1] of their self-assembled films on ferrous substrates, suggesting that the surfactant molecules that form an *ordered adlayer* on the rubbed surfaces exhibit a *superior friction-reducing efficiency*. Therefore, it is valuable to further explore how the morphology (*e.g.*, molecular packing, density, orientation, etc.) of these adsorbed OFM films affects their tribological properties.

As a matter of fact, although the head group dictates the initial driving force for the additive adsorption, it is the hydrocarbon tail that provides the stabilization required to form interfacial, low-shear-strenght films between rubbing surfaces, which reduce their experienced friction and prevent them from a direct solid-solid contact.[6,34,35,53,60,208,209] Then, it has been assumed that the adsorbed molecules align themselves parallel to each other in an upright configuration, covering the surface with a *self-assembled monolayer* (cf. *SAM model*, as shown in figure 4.5).[27,77,206,207,210,211] The integrity of the resulting protective film is derived from the *lateral vdW interactions* occurring between the methylene groups of neighbouring alky chains, which promote the collective molecular packing and contribute to the appearance of a well-defined slippage plane between the opposing moving boundaries.[6,34,54,76] Besides, these cohesive interactions also strengthen the mechanical robustness of the OFM adlayer, in order to support the normal load applied to the sliding contact.[29,34]

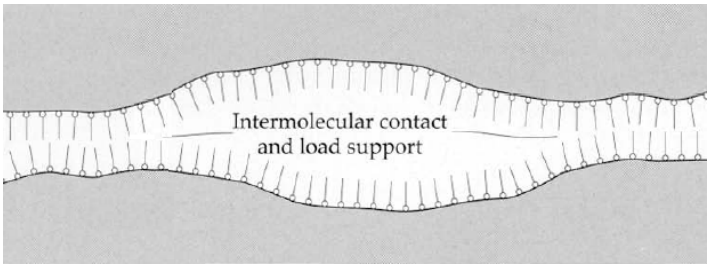

Figure 4.5 – Boundary contact model, composed of solid surfaces coated with OFM-based self-assembled monolayers. (figure adapted from the indicated reference)[27]

[1] Koshima *et al.* have used a surface-sensitive experimental technique, the *sum frequency generation* (SFG) spectroscopy, to analyze the molecular structures of the investigated additives adsorbed on metal surfaces.[42]

Several *ex-situ* and *in-situ* experimental techniques have been employed to probe the formation and the molecular organisation of organic thin films — and notably OFM-based SAM — adsorbed on solid substrates, whether within or not within rubbing contacts.[34, 211, 212] These include *scanning force microscopy* (SFM: AFM/LFM),[41, 53, 54, 213–233] *surface force apparatus* (SFA),[39, 234–237] *quartz crystal microbalance* (QCM),[36, 41, 50] *neutron reflectometry*[45, 182, 185, 238] and other *surface-specific vibrational spectroscopies*.[42, 45, 239–241] By means of these methods, it has been possible to reveal/confirm some interesting general facts about OFM assembly process, such as:

- Adsorbed surfactant additives do form ordered and closed-packed clusters, in which the molecules are vertically oriented and rather tilted from the surface normal, thereby aggregating in irregular shaped islands — with diameters varying from nanometers to micrometers — dispersed on a range of rubbed or not rubbed substrates.[6, 35, 41, 50, 53, 54, 231]
- The kinetic rate of OFM adsorption, as well as the resulting molecular surface coverage (or packing density), depend on and particularly increase with the additive bulk-solution concentration.[50, 53, 54, 60, 185]
- The natural formation of an adsorbed OFM monolayer from liquid solutions can be a relatively slow process (*e.g.*, timing periods up to several hours).[31, 39, 50, 53, 54, 61, 182, 207, 242] However, their molecular arrangement may be improved/accelerated by external factors, as well as by the operating conditions (*e.g.*, shear, load and temperature).[6, 31, 39, 77, 173, 182]
- Long alkyl tail groups increase the thickness of the adsorbed films and the lateral inter-adsorbate interactions.[68, 28, 77, 218, 219, 229]
- Straight molecular structures enhance the packing order and density of OFM adlayers. For instance, linear saturated hydrocarbon chains are preferred rather than the branched and unsaturated ones.[6, 34, 38, 39, 41, 44, 50, 61, 77, 181, 182]

As an example of these experimental studies, it is worth noting that *in-situ* liquid cell SFM analyses were carried out by the LTDS team, during our project, in order to investigate the morphology of self-assembled films formed by octadecylamine molecules ($C_{18}H_{39}N$) in a solution of PAO 4[2] and adsorbed on different surfaces, namely an atomically-smooth mica and an iron coated silicon substrate.[3] The experimental protocol used to perfom these scanning probe measurements is described in *appendix D* (cf. p. XIII).

[2] The octadecylamine concentration in PAO 4 used was of 1×10^{-3} M.
[3] The *root-mean-square roughness* (RMS) of the iron layer deposited on the silicon surface was of ca. 0.7 nm.

As a preliminary experiment, a surface of air-cleaved mica immersed into the studied solution was imaged using a *SFM contact mode*. After just a few minutes of scanning, the first topographical images indicated the formation of *rounded clusters*, with diameters of approximately 500 nm. Then, after four hours, a successive number of scans of the same area showed the aggregation and growth of *octadecylamine islands*, whose diameters achieved a steady value of 1 μm and a height of at least 1.3 nm (cf. figure 4.6), considering the employed experimental conditions (for further details, cf. *appendix D*, p. XIII). From those final images, a molecular coverage was estimated at around 48 – 63%, depending on the scanned area (50 μm × 50 μm). Incidentally, these results were found to be in good agreement with previous *in-situ* AFM experiments of octadecylamine adsorption on a mica surface immersed in binary solutions of dodecane and hexadecane.[54]

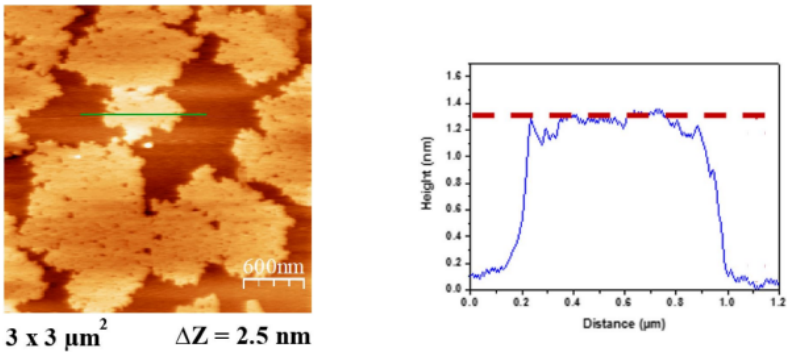

Figure 4.6 – *In-situ* contact mode AFM topographical image, with a scan size of 3 × 3 μm^2 (ΔZ = 2.5 nm), obtained from a mica sample immersed in a PAO 4 solution containing 10^{-3} M octadecylamine.

Later, in a second series of experiments, a silicon substrate coated with an iron layer, and thus containing a native iron oxide layer, was imaged using *lateral forces scanning* (LFM). In fact, it was very difficult to monitor via standard AFM topographical images the formation of amine islands for this specific system, owing to the significant roughness of the investigated ferrous surface (cf. figure 4.7a, p. 77). Thus, by recording the lateral force images during the trace and the retrace scanning, it was possible to detect relatively small areas exhibiting an important variation of frictional forces (cf. *green circled areas*, identified and numerated in figures 4.7b and 4.7c, p. 77). Besides, the cross-section profiles along the green lines of the corresponding LFM images also illustrate these force variations (cf. figures 4.7e and 4.7f, p. 77). Therefore, the observed areas — where a reversal contrast was noted between the trace and retrace scans — were attributed to the formation of small islands of adsorbed amine molecules, whose diam-

eters were estimated to be less than 25–30 nm. Concerning their height, it was difficult to precisely measure it because of the considered surface roughness. Yet, based on the cross-section height profile, measured along the green line in figure 4.7a, one can estimate the height of the octadecylamine islands to amount between 0.9 and 1.5 nm, considering the probed conditions.

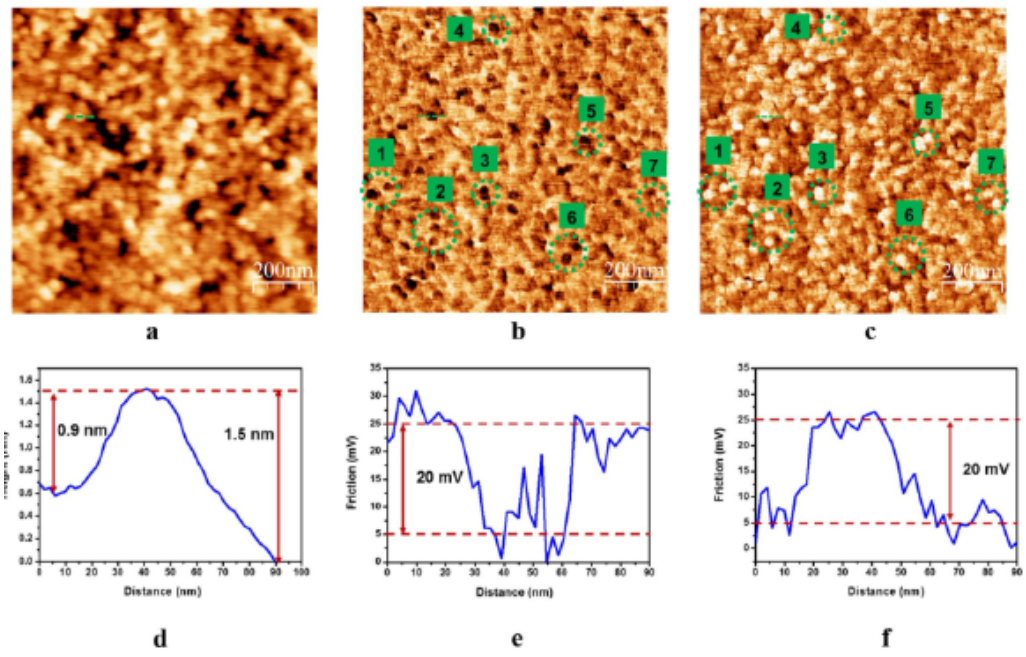

Figure 4.7 – *In-situ* contact mode AFM/LFM images, with a scan size of 1 × 1 μm^2, obtained from an iron sample immersed in PAO 4 solution containing 10^{-3} M octadecylamine: **(a)** *AFM topographical image*, $\Delta Z = 2$ nm; **(b)** *lateral force image*, obtained in the forward direction (*trace*), $\Delta V = 25$ mV; **(c)** *lateral force image*, obtained in the backward direction (*retrace*), $\Delta V = 25$ mV. Then, figures **(d)**, **(e)** and **(f)** correspond to the cross-section profiles of figures (a), (b) and (c), respectively.

Complementing the experimental work, computational tools like *MD simulations* have extensively been applied in recent years to study the molecular structure of organic assemblies on solids surfaces, providing useful information at atomic-scale that will long be unavailable from experiments.[34,46,47,52,55,57,63,86,88,91,210,211,243–257] However, since the adsorption of surfactants from a liquid solution and using realistic additive concentrations can be a relatively slow process[31,39,53,54,182,207] (cf. OFM diffusivities described in chapter 3, p. 56–63), the MD simulations reproducing the OFM self-assembly and the film formation — through an all-atom force fields and using very small time steps, which are required to accurately model the molecular motion — are still unattainable.[34,63] Nevertheless, given that experimental analyses have demonstrated that these additives do form close-packed films,[6,35,41,53,54,61,231] the MD simulations so far have generally been constructed with *pre-formed monolayers* — the so-called

self-assembled monolayer models, SAM [46, 47, 52, 55–59] — by placing the ordered OFM molecules with their head group close to the substrate at the beginning of the simulation. [34, 63] This system is actually similar to the *Langmuir-Blodgett experimental approach*, which is usually used to quickly form surfactant films with a controllable packing density over solid surfaces. [63, 180, 239]

Considering then that an "OFM film-forming simulation" still represents a technical challenge to the MD method, in terms of affordable time and length scales, we decided to investigate the morphology of equilibrated SAM composed of C_{18} primary amines directly adsorbed on a hematite slab, without integrating any BO molecule (*i.e.*, a simulation under "gas phase" and without a liquid solvent model). Besides, our chief motivations here were to evaluate the fitted $U^{\text{interface}}$ potential, and to select the most relevant molecular packing densities associated with the adsorbed films, in order to design their confined shearing simulations (cf. § 5.2, p. 102). This structural study is fully described in the following paragraphs.

4.2.1 Computational details

EMD simulations were performed to shed more light on the *microscopic structure* of adsorbed octadecylamine films, over a broad range of *surface coverages* and at a fixed temperature of 373 K. Thus, by varying the OFM density in the adlayer composition, a wide variety of structural information were obtained, including their collective molecular tilt angle and thickness, their mass-density, and their atomic-height probability profiles. In addition, the N-Fe interactions were particularly monitored via a two-dimensional spacial position distribution, in order to verify the $U^{\text{interface}}$ ability to reproduce the dynamic behavior of adsorbed molecular clusters onto ferric iron oxide.

4.2.1.1 System modeling

For the design of the input systems, some assumptions were made with the intention of obtaining low time- and resources-demanding calculations, namely:

- An (1 × 1) unit cell of the α-Fe_2O_3 (0 1 $\bar{1}$ 2) slab was used as the solid substrate model (120 atoms in total; cf. figure 2.3, p. 21), constituting a simulation box with dimensions approximately equal to 10 Å × 11 Å × 120 Å, which corresponds to a *superficial area* of around 112 $Å^2$ (plane *xy*). Also, it should be noted that the uppermost layer of the hematite surface exhibits *eight iron atoms* likely to equivalently act as *adsorption site centers* for the amino compounds (cf. figure 4.8, p. 80).
- The $C_{18}H_{37}NH_2$ molecules composing the investigated adlayers were considered to be in their *protonated form* (*i.e.*, electrically neutral structure, which should be favored in a low-polarity medium)[47, 52] and with an initial upright and straight configuration.
- The pre-formed SAM geometry was employed, and particularly at higher molecular densities. The individual amines were initially positioned with their polar groups pointing toward the substrate, and with their alkyl chains parallel to each other and perpendicular to the hematite slab, where the distance between the nitrogen atoms and the *xy* plane formed by the upper surface oxygens is less than 4 Å (cf. an example of adsorbed monolayer depicted in figure 4.9, p. 81).

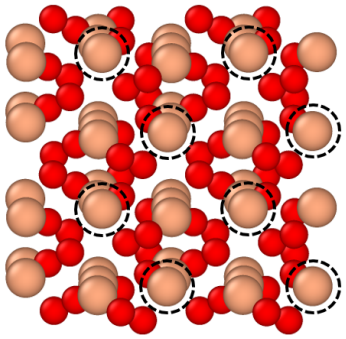

Figure 4.8 – Top view of the α-Fe_2O_3 (0 1 $\bar{1}$ 2) surface (*xy* plane).
The black dashed circles indicate the eight iron atoms present in the outermost atomic layer of the investigated hematite substrate model.
Atomic color code: coral - iron and *red* - oxygen.

Moreover, assuming that an octadecylamine can interact solely with one surface iron atom (and vice versa), a total number of eight simulation cells were constructed covering the entire range of possible molecular densities for our surface orientation model, the α-Fe_2O_3 (0 1 $\bar{1}$ 2) slab. About that, table 4.1 describes all of the investigated systems, listing the number of OFM additives considered in each simulation box and its respective surface coverage, where Γ is expressed in the different units (*e.g.*, $mol \cdot m^{-2}$ and nm^{-2}). In addition, figure 4.9 gives an example of the initial configuration of the system containing two molecules (Γ_2) adsorbed on the hematite substrate (cf. p. 81).

Table 4.1 – Details of simulation cells employed in the adsorbed amine SAM study

Simulation cell ID	Number of molecules	Coverage ratio (*)	Surface ($\mathbf{mol \cdot m^{-2}}$)	coverage – Γ ($\mathbf{nm^{-2}}$)
Γ_1	1	12.5 %	1.5×10^{-6}	0.9
Γ_2	2	25 %	3.0×10^{-6}	1.8
Γ_3	3	37.5 %	4.5×10^{-6}	2.7
Γ_4	4	50 %	5.9×10^{-6}	3.6
Γ_5	5	62.5 %	7.4×10^{-6}	4.5
Γ_6	6	75 %	8.9×10^{-6}	5.4
Γ_7	7	87.5 %	1.0×10^{-5}	6.3
Γ_8	8	100 %	1.2×10^{-5}	7.2

(*) *The* coverage ratio *is calculated as the number of amine molecules present into each simulation cell divided by the total number of iron atoms present in the uppermost layer of the (0 1 $\bar{1}$ 2) α-Fe_2O_3 slab, which amount to eight atoms. This parameter is expressed in percentage (%), and it reflects the fraction of potential adsorption sites occupied by the model OFM.*

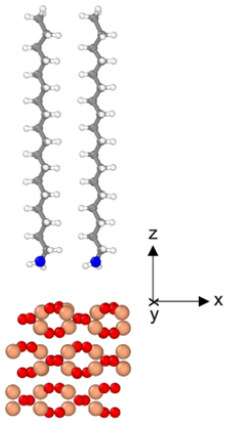

Figure 4.9 – Side view of the initial film model composed of two $C_{18}H_{39}N$ molecules adsorbed on α-Fe_2O_3 slab, which represents a coverage of $\Gamma_2 = 3 \times 10^{-6}$ mol·m^{-2} $\equiv$ 1.8 Å^{-2}. Note that the boundaries of the simulation cell are not represented here, but the cell dimensions are equal to 10 Å × 11 Å × 120 Å. *Atomic color code: coral* - iron, *red* - oxygen, *white* - hydrogen, *gray* - carbon, *blue* - nitrogen.

4.2.1.2 Equilibration

In order to equilibrate the MD simulation cells at the investigated temperature (373 K), and to simultaneously allow the adsorption and ensuing self-organization of the different OFM molecules onto the iron oxide substrate to be achieved, each system ($\Gamma_1 - \Gamma_8$) was first energy-minimized[4] using our three interatomic potentials, U^{surface}, $U^{\text{lubricant}}$ and $U^{\text{interface}}$ (cf. § 2.2.2, p. 26), by means of the LAMMPS simulator.[95] The short-range nonbonded interactions were cut-off at 5 Å, and the electrostatic interactions were evaluated applying a slab implementation of the PPPM algorithm,[161,205] in which the desired relative error in forces was set to 1×10^{-6}. Besides, periodic boundary conditions were imposed to *xy* plane.

Then, the initial atomic velocities were assigned according to the Maxwell-Boltzmann distribution for a target temperature of 373 K, followed by a 3 ns NVT ensemble calculation[5] (which represents 3 000 000 time steps of 1 fs), also at 373 K. The Nosé-Hoover thermostat[98] was employed to control the temperature of all amine molecules and the two topmost Fe_2O_3 layers of the hematite slab (cf. figure 4.9), using a damping constant equal to 100 fs. The remaining bottom Fe_2O_3 layer was kept fixed to simulate the oxide crystal bulk.

After that first equilibration step, an *annealing process* of each periodic SAM/surface system was conducted, comprising four stages of NVT ensemble runs, each one lasting 3 ns. In fact, this *heating-cooling cycle* consisted in increasing the system temperature from 373 K to

[4] The *quadratic line search algorithm* was used to perform the energy minimization of all initial configurations.
[5] As a reminder, the velocity Verlet integration algorithm[83] was employed to solve Newton's equation of motion.

473 K during 3 ns, then maintaining the temperature constant for 3 ns, followed by a decreasing of the temperature back to 373 K during 3 ns, and finally equilibrating the system at 373 K, for more 3 ns. The objective of this process was to confer enough thermal energy to the adsorbed octadecylamine molecule, in order to promote/facilitate their structural rearrangement, and maybe even their migration over the surface — through consecutive desorption and readsorption steps —, with the final perspective of obtaining a *lower-energy molecular organization*, where the film height is augmented and the packing density within the SAM is incresead, being these later configurations favored by the *interchain vdW interactions*.[54]

4.2.1.3 Production

Once the systems reached thermal equilibrium, they were later subjected to a NVE ensemble simulation, without thermostatting, for 3 ns (3 000 000 time steps of 1 fs). This final simulation was established to generate the trajectory data, and in particular the positions of each atom composing the amine molecules, needed to determine the structural average functions used to analyse the morphology of C_{18} primary amine adlayers as a function of their surface coverage.[6]

The obtained results are presented in detail in § 4.2.2 (cf. p. 83), but figure 4.10 already gives a glimpse into the effect of molecular density on the collective order of the adsorbed amine monolayers.

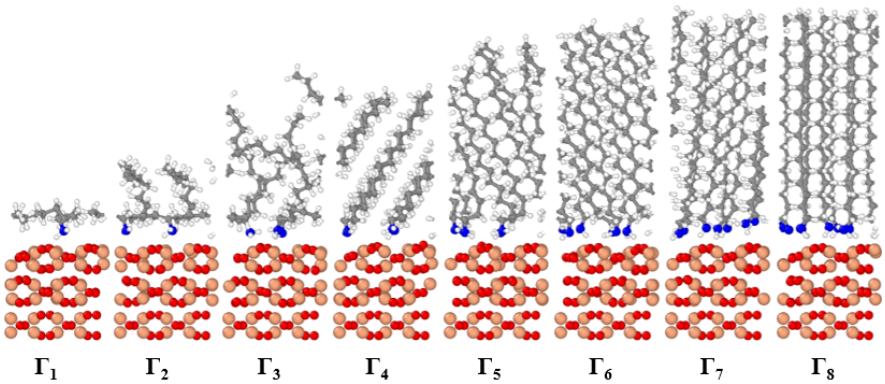

Figure 4.10 – Snapshots of the final production simulations, showing the SAM/surface structure of the eight investigated surface coverages (*side view, xz* plane).
The characteristics of each simulation cell Γ_{1-8} is detailed in table 4.1 (cf. p. 80).

[6] For information, the *equilibration* and *production* simulations were both performed on a 16-cores processor (Dell C6320; Intel Xeon E5-2640 v3 2.60GHz), during (total) time periods varying from 3 to 5 days, depending on the represented OFM surface coverage (cf. table 4.1, p. 80).

4.2.2 Results and discussion

The structure of (pre-formed) amine-based monolayers were studied at 373 K, for a large array of surface coverages, via EMD simulations, employing an interfacial force field specifically adjusted to reproduce quantum-level energetic data obtained from the octadecylamine/-hematite interaction. Actually, the atomic-scale information provided by these simulations were used to gain insights into OFM packing arrangement over the solid substrate model, which considerably affects their boundary lubricating action.

Thus, complementing the production simulation snapshots such that displayed in figure 4.10 (cf. p. 82), the morphology and self-organization of the eight SAM/surface systems (Γ_{1-8}) were investigated by analysing their:

- *amino-group mapping location upon the ferric oxide surface*, given by the projection of the N and Fe atomic coordinates into the interfacial *xy* plane (cf. figure 4.11, p. 84);
- *average N-C_9 tilt angle*, θ, defined as the angle between the vector extending from the nitrogen to the carbon situated halfway up in the alkyl chain (C_9) and the surface normal (cf. figure 4.12, p. 85);
- *atomic mass-density profiles of the adsorbed octadecylamines*, $\rho(z)$ (cf. figure 4.13, p. 86);
- *atomic position probability profiles*, $p(z)$, for the nitrogen atoms (N), the carbons present in the intermediary methylenes ($-CH_2-$ or C) and terminal methyl groups ($-CH_3$, C_{18} or CT; cf. figure 4.14, p. 87);
- *adsorbed monolayer thickness*, *L*, taken to be the average height from the surface, $h(z)$, associated to the terminal carbon atom of all represented amine molecules, (cf. *weighted arithmetic means*, and their respective *standard deviation*, calculated from $\rho_{1-8}^{CTT}(z)$ distributions and listed in table 4.2, p. 85).

It is important to specify that some of these structural properties are expressed as function of the distance from the surface (in z direction), which is represented through the plane formed by the outermost oxygen atoms of the α-Fe_2O_3 (0 1 $\bar{1}$ 2) slab, where it was placed the vertical system origin (*i.e.*, $z = 0$). In addition, the time-averaged values of these properties were calculated based on the data set obtained from all of 3 000 000 time steps constituting the production simulation (cf. § 4.2.1.3, p. 82).

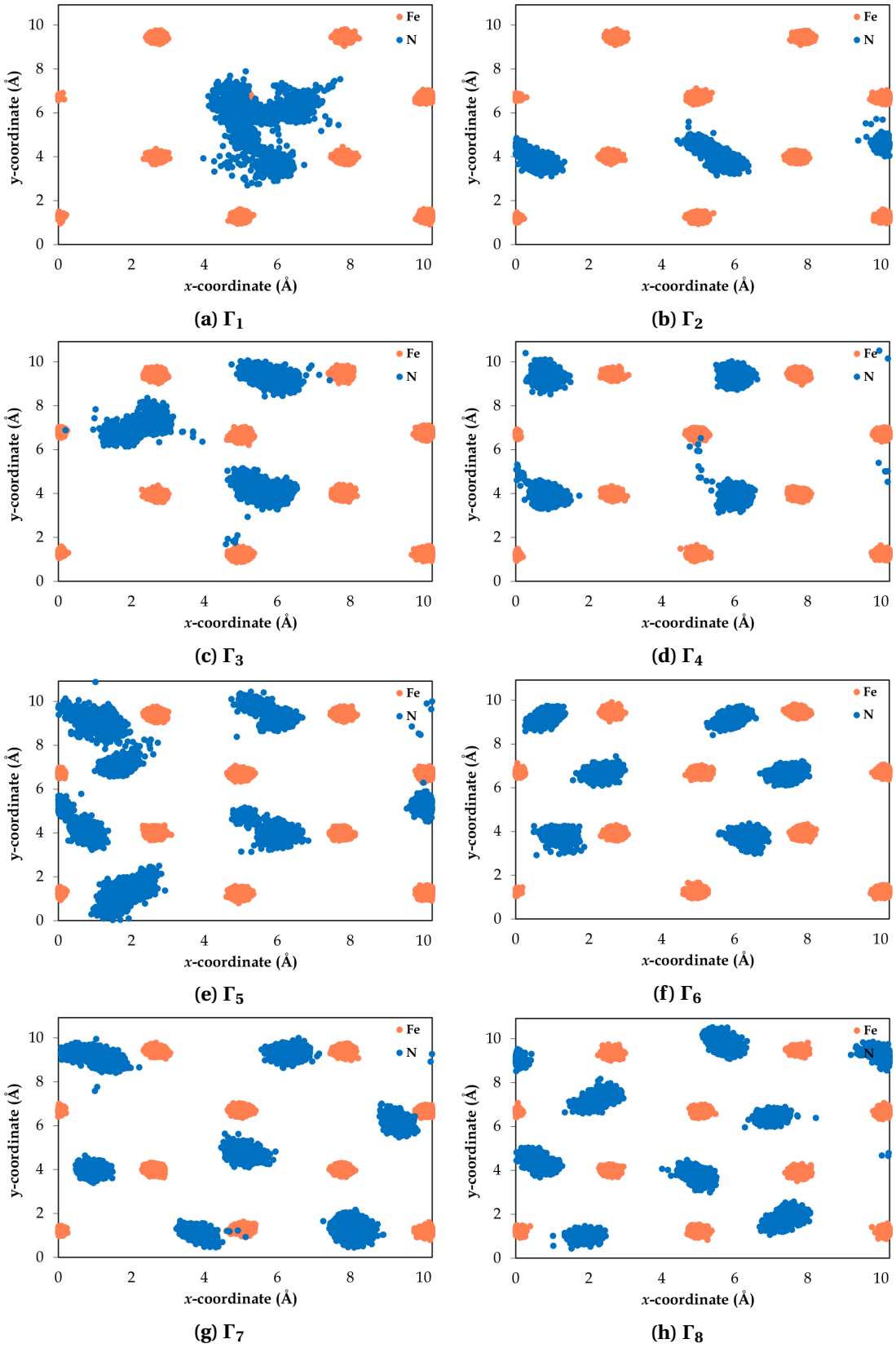

Figure 4.11 – Amino-group mapping location above the hematite surface for all investigated coverages. The different regions describe the projection of the *x* and *y* position coordinates (in Å), for the nitrogen and outermost iron atoms into the interfacial *xy* plane (in *blue* and *coral*, respectively), throughout the production simulation (3 ns). Actually, these schematics represent a simplified top view of the Γ_{1-8} systems.

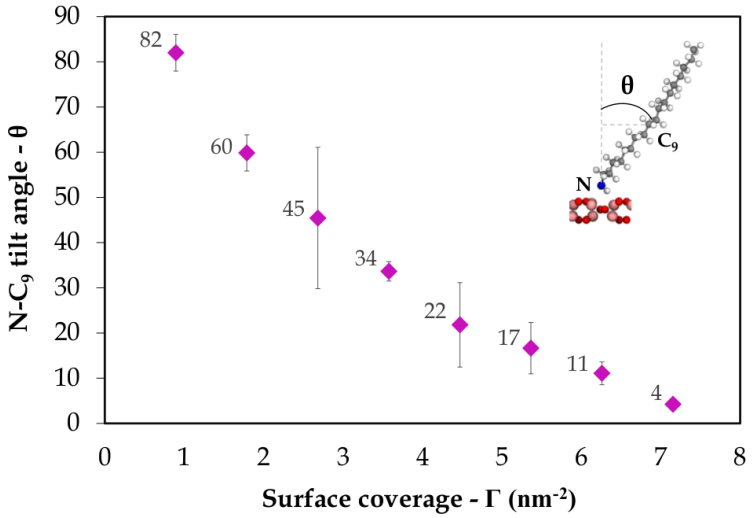

Figure 4.12 – Average N-C_9 tilt angle of the adsorbed octadecylamines (θ in degrees), as a function of the surface coverage, (Γ in nm^{-2}).
Note that a $\theta = 0°$ means that OFM molecules are pointing straight upwards, whereas a $\theta = 90°$ indicates that they are lying flat on the surface.

Table 4.2 – Thickness of the C_{18} primary amine films, *L*

Simulation cell ID	Coverage ratio	Γ (nm^{-2})	Thickness (Å)
Γ_1	12.5 %	0.9	3.6 ± 0.2
Γ_2	25 %	1.8	8.2 ± 0.8
Γ_3	37.5 %	2.7	13.9 ± 1.9
Γ_4	50 %	3.6	16.7 ± 0.6
Γ_5	62.5 %	4.5	20.9 ± 1.2
Γ_6	75 %	5.4	23.3 ± 0.7
Γ_7	87.5 %	6.3	24.8 ± 0.6
Γ_8	100 %	7.2	25.3 ± 0.1

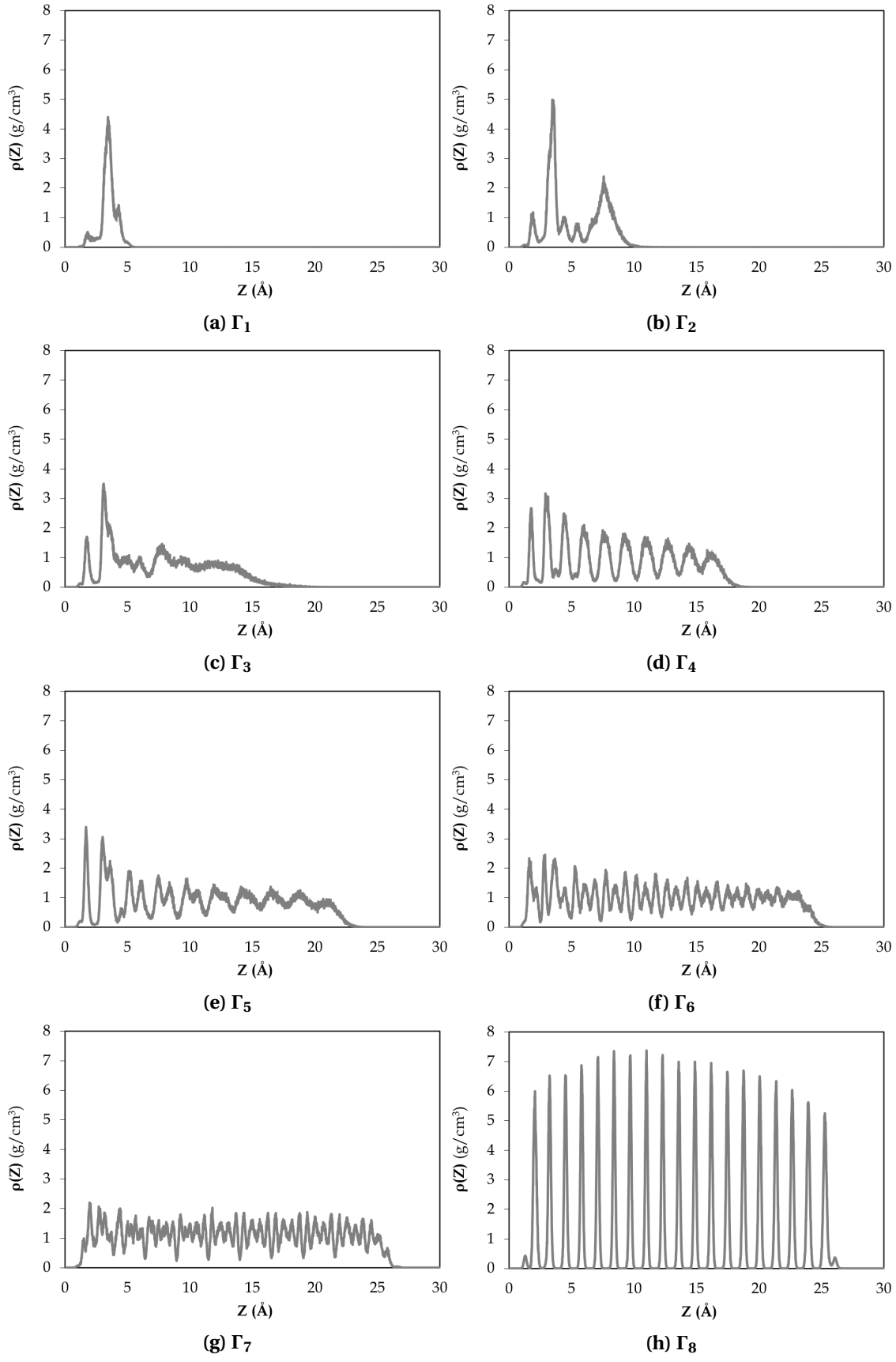

Figure 4.13 – Atomic mass density profiles in z, $\rho(z)$, of the adsorbed octadecylamines, as a function of the surface coverage (where ρ is expressed in g·cm^{-3}).

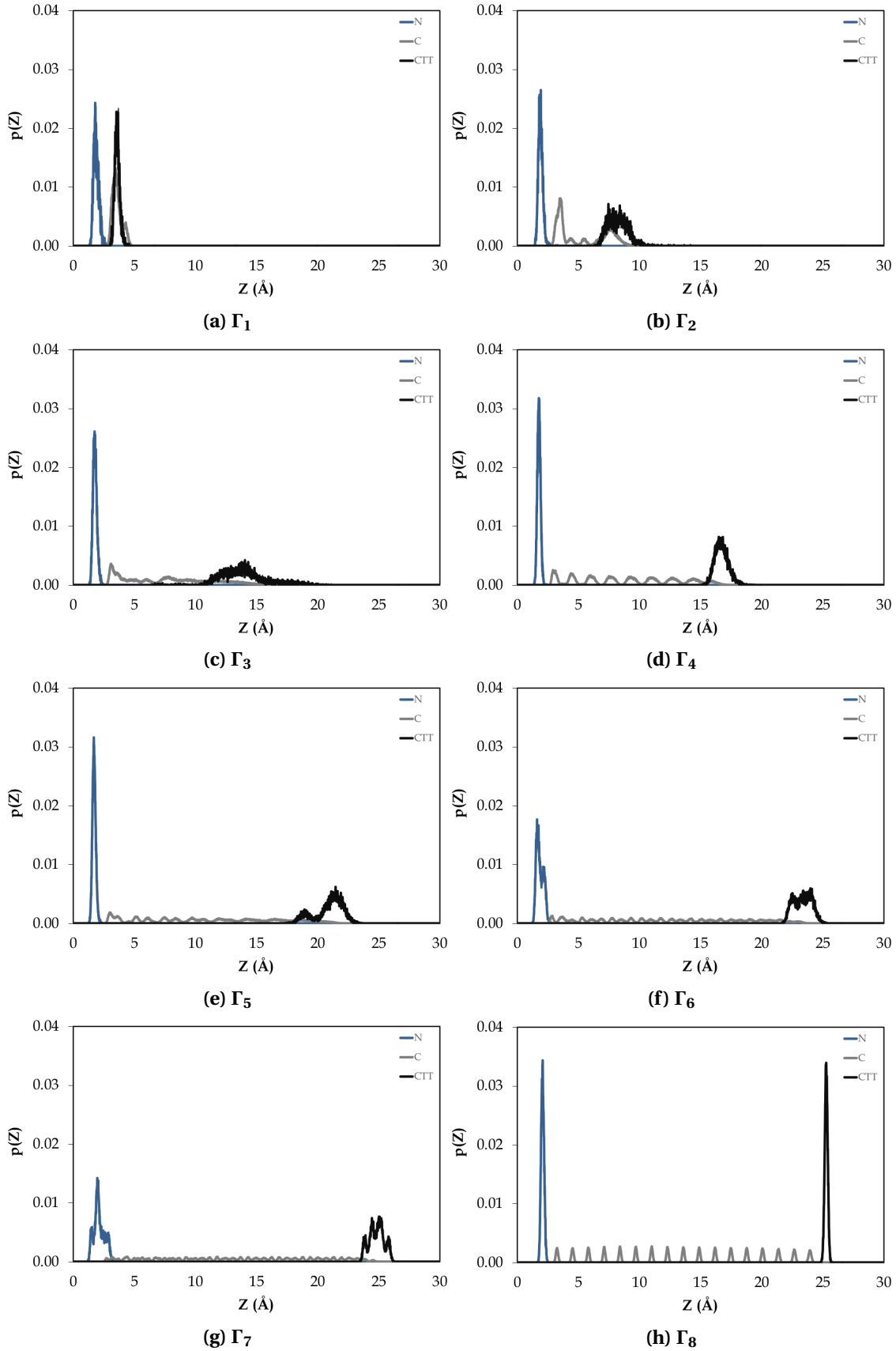

(a) Γ_1 **(b)** Γ_2

(c) Γ_3 **(d)** Γ_4

(e) Γ_5 **(f)** Γ_6

(g) Γ_7 **(h)** Γ_8

Figure 4.14 – Atomic position probability profiles in z, $p(z)$, for the nitrogens (N, in *blue*), and the carbon atoms in intermediate methylenes (C, in *gray*) and terminal tail groups (CTT, in *black*), as a function of the surface coverage, Γ.

First of all, regarding the interaction between the amino head groups and the iron oxide surface, there are clear indications that all C_{18} primary amine molecules effectively adsorb on the substrate, in the course of the equilibrium simulations carried out at 373 K. No evidence of partial or complete desorption was found, and this despite the performed annealing process, during which the systems were heated up to a maximum temperature of 423 K.

In fact, one can observe from figure 4.10 that all nitrogen atoms are closely positioned onto the surface (cf. *blue regions*, p. 82), holding the OFM molecules firmly tied to the solid slab, regardless of the considered surface coverage. That fact is likewise corroborated by the sharp peaks shown by the N atoms in $p_{1-8}(z)$ profiles, at short distances from the surface that range from 1.6 to 2.1 Å (cf. peaks in *blue*, in figure 4.14, p. 87).

Furthermore, by examining the figure 4.11 (cf. p. 84), which provides a "time-evolution representative top view" of the N and Fe atoms located at the SAM/substrate interface, it should be mentioned that the nitrogens are predominantly anchored near to the topmost surface irons, whose crystalline lattice structure probably dictate the *in-layer ordering* of the amine-based films. This long-range organization is consistent with other observations made in previous experimental and computational works.[6, 47, 52, 57]

Therefore, these outcomes have favorably suggested that the fitted $U^{\text{interface}}$ potential is indeed capable of reproducing the adsorption behavior of the octadecylamine/hematite system, as well as their N-Fe strong binding interaction, through dynamic simulations.

Concerning the effect of the surface coverage on OFM assembly, the post-processing results imply that the structure of the amine-adlayer changes substantially with its molecular density, and particularly for ratio coverages less or equal to 50%, which represent the Γ_1–Γ_4 systems.

Actually, for the simulation cell containing the *lowest coverage* ($\Gamma_1 = 0.9\,\text{Å}^{-2} \equiv 12.5\%$), the modeled octadecylamine molecule lies flat to the surface (cf. figure 4.15b), so that its terminal carbon is at a distance of around 3.6 Å, while N atom is at 1.8 Å (cf. CTT and N profiles in $p_1(z)$ distributions, as shown in figure 4.14a, p. 87). In addition, $\theta_1 \approx 82°$ and its $\rho_1(z)$ profile exhibits only a major broad peak at 3.4 Å (cf. figure 4.13a, p. 86).

It is also interesting to notice in figure 4.11a that the nitrogen coordinates evolve considerably around the ferrous adsorption site centers, during the production simulation (cf. p. 84). Since the surface coverage is quite low for this case ($\Gamma_1 = 1.5 \times 10^{-6}\ \text{mol}\cdot\text{m}^{-2}$), there is still enough volume available for the molecule to diffuse over the substrate (cf. figure 4.15a). Nevertheless, the adsorbed film may not be sufficiently thick either to claim an important reducing-friction effect or to effectively separate the opposing sliding surfaces ($L_1 = 3.6 \pm 0.2$ Å).

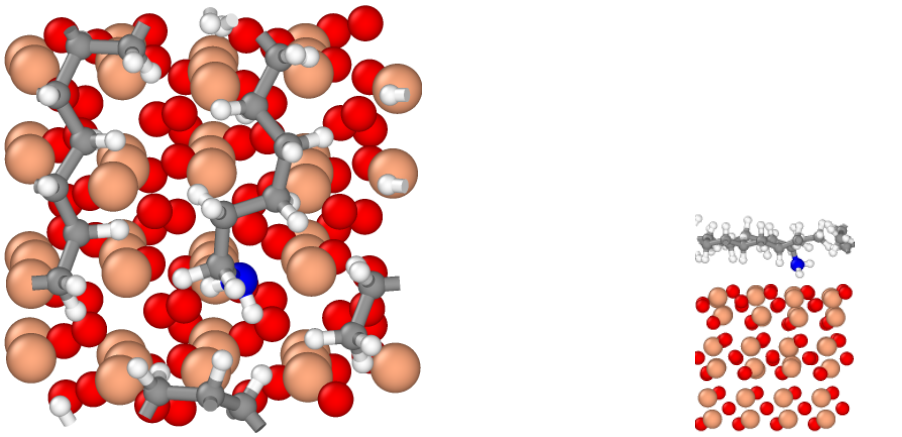

(a) Top view (*xy* plane) **(b) Side view (*yz* plane)**

Figure 4.15 – Snapshots of Γ_1 cell at the end of the production simulation. Note that the boundaries of the simulation box are not represented here. *Atomic color code: coral* - iron, *red* - oxygen, *white* - hydrogen, *gray* - carbon, *blue* - nitrogen.

At a coverage of 25% ($\Gamma_2 = 1.8\,\text{Å}^{-2}$), the direct "free volume" above the hematite decreases (cf. figure 4.16a) and, by consequence, the two represented molecules do begin closely assembling in a thin film ($L_2 = 8.2 \pm 0.8\,\text{Å}$), in which the hydrocarbon tails are slightly straightened upward ($\theta_2 \approx 60°$; cf. CTT $p_2(z)$ profile, shown in figure 4.14b, p. 87), and the amino head groups are stably fixed to specific surface sites (cf. N coordinates, depicted in figure 4.11b, p. 84).

However, considering their relatively low density ($\Gamma_2 = 3.0 \times 10^{-6}\,\text{mol}\cdot\text{m}^{-2}$), the molecules are still poorly organized, with their hydrocarbon backbone mostly orientate parallel to the surface, since this configuration is favored by the OFM-tail/surface vdW interactions.[65] As a matter of fact, it seems that the octadecylamines are bent in a shape similar to an "elongated S", with two different parts of their alkyl chain lying parallel to the surface (cf. figure 4.16b). As results, the obtained molecular arrangement leads somewhat to a layering of the adsorbed additives, which is explicitly indicated by the several peaks in $\rho_2(z)$ distribution (cf. figure 4.13b, p. 86), and also by the two intense peaks of the methylene $p_2(z)$ profile at 3.5 and 7.6 Å (cf. figure 4.14b, p. 87).

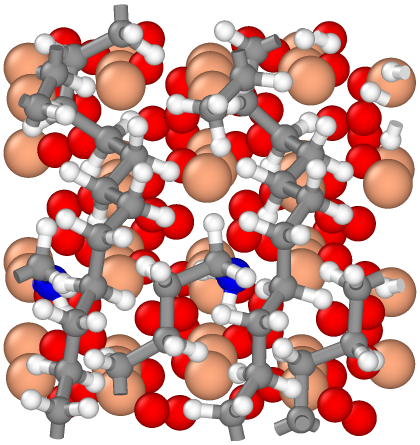

(a) Top view (*xy* plane)

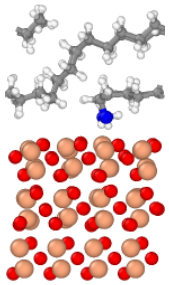

(b) Side view (*yz* plane)

Figure 4.16 – Snapshots of Γ_2 cell at the end of the production simulation. Note that the boundaries of the simulation box are not represented here. *Atomic color code: coral* - iron, *red* - oxygen, *white* - hydrogen, *gray* - carbon, *blue* - nitrogen.

As the molecular density was further increased for the Γ_3 cell ($\Gamma_3 = 4.5 \times 10^{-6}$ mol·m^{-2}), the steric interactions between the three adjacent amines were proportionally enhanced, forcing their hydrocarbon chains into more upright positions, thereby expanding the resulting monolayer thickness ($L_3 = 13.9 \pm 1.9$ Å). Besides, the amino groups are strongly anchored to the surface, according to a triangular arrangement that also contributes to vertically orientate the OFM additives (cf. N coordinates shown in figure 4.11c, p. 84).

Considering that the surface coverage is still not so high at $\Gamma_3 \equiv 37.5\%$, the packing constraints and the cohesive vdW interactions arising within the film are not strong enough to hinder the lateral movement of the C_{18} hydrocarbon tails (cf. figure 4.17b). Then, these alkyl groups still exhibit a significant conformational freedom to swing and to bend, keeping the disordered, entropically favoured, non-linear configurations.[47] That fact is highlighted by the scattered averaged N-C_9 tilt angle adopted by the three molecules, $\theta_3 = 45 \pm 16°$, as well as by the wider peak of the terminal carbons in $p_3(z)$ profile (cf. figure 4.14c, p. 87).

Additionally, it is worth comparing $\rho_2(z)$ and $\rho_3(z)$ distributions against each other (cf. figures 4.13b and 4.13c, respectively; p. 86), being $\rho_3(z)$ a more disordered and amorphous film than $\rho_2(z)$, in spite of the greater coverage for the Γ_3 system, which eventually presents a *liquid-like structure*.[35,54]

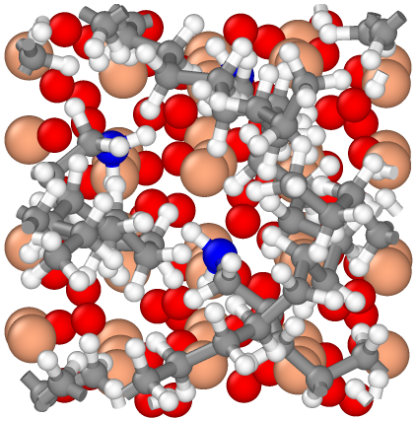

(a) Top view (*xy* plane)

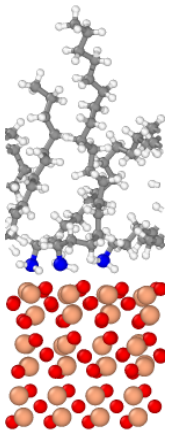

(b) Side view (*yz* plane)

Figure 4.17 – Snapshots of Γ_3 cell at the end of the production simulation. Note that the boundaries of the simulation box are not represented here. *Atomic color code: coral* - iron, *red* - oxygen, *white* - hydrogen, *gray* - carbon, *blue* - nitrogen.

Once the OFM ratio coverage achieved 50% ($\Gamma_4 = 3.6$ Å^{-2}, cf. figure 4.18), and even for greater values of Γ, such as those related to $\Gamma_5 - \Gamma_8$ systems ($\Gamma_{5-8} = 4.5$, 5.4, 6.3 and 7.2 Å^{-2}, respectively; cf. figures 4.19a–h, p. 93), the octadecylamine molecules are tightly aggregated on the hematite surface, forming densely packed and highly ordered monolayers (cf. regular and intense peaks in $\rho_{4-8}(z)$ profiles, described in figures 4.13d–h, p. 86), with the head groups strongly bound to the substrate (cf. figures 4.11d–h, p. 84), and the alkyl tails pointing away from the surface, predominantly in vertical positions (cf. CTT peaks at heights over 16 Å in $p_{4-8}(z)$ distributions, shown in figures 4.14d–h, p. 87). For instance, their collective molecular inclination range from $\theta_4 = 34 \pm 2°$ to $\theta_8 = 4 \pm 1°$ (cf. figure 4.12, p. 85).

In addition, amine-based OFM films get thicker with increasing surface coverage, owing to the stronger packing constraints prevailing within a more densely organized layer (cf. L_{4-8} values listed in table 4.2, p. 85). Indeed, excluded-volume intermolecular interactions favour an ordered arrangement of the molecules in extended linear conformations, since these configurations efficiently fill the space , eventually increasing the film thickness and enhacing its stability, which is also strengthened by the maximized vdW forces arising between the hydrocarbon chains.[6, 47, 52, 65, 91, 182]

Besides, one can observe that the average tilt angles and adlayer thicknesses for the Γ_5, Γ_6, Γ_7 and Γ_8 cells do not exhibit relatively striking dissimilarities (cf. figure 4.12 and table 4.2, respectively, p. 85). Moreover, based on the sharp and well-defined peaks featured by $\rho_4(z)$ and $\rho_8(z)$ profiles (cf. figures 4.13d and 4.13h, p. 86), it is interesting to note that Γ_4 and Γ_8 coverages especially yield a condensed layering, which can be compared to a *solid-like structure* for the Γ_4 film and a rigid crystalline phase for the Γ_8 SAM.[35, 54, 77]

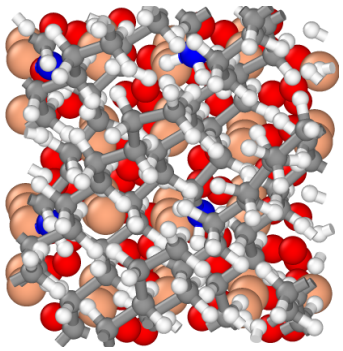

(a) Top view (*xy* plane)

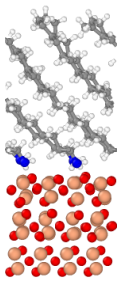

(b) Side view (*yz* plane)

Figure 4.18 – Snapshots of Γ_4 cell at the end of the production simulation. Note that the boundaries of the simulation box are not represented here. *Atomic color code: coral* - iron, *red* - oxygen, *white* - hydrogen, *gray* - carbon, *blue* - nitrogen.

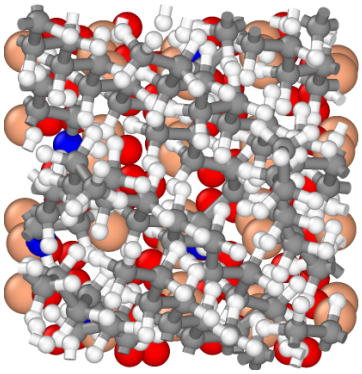

(a) Γ_5 – Top view (*xy* plane)

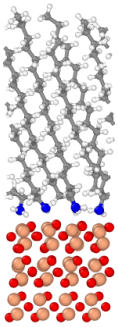

(b) Γ_5 – Side view (*yz* plane)

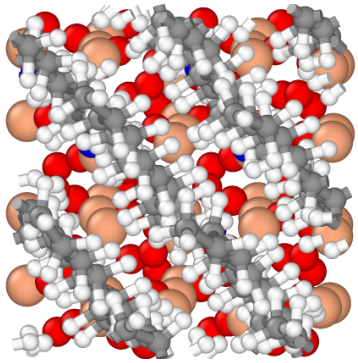

(c) Γ_6 – Top view (*xy* plane)

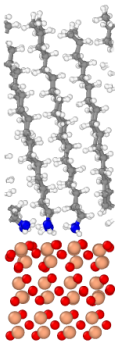

(d) Γ_6 – Side view (*yz* plane)

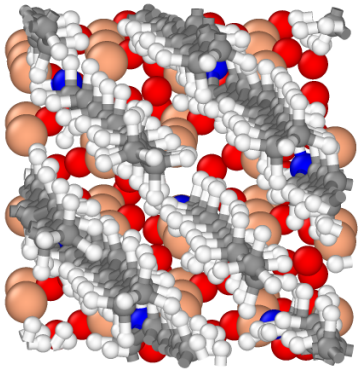

(e) Γ_7 – Top view (*xy* plane)

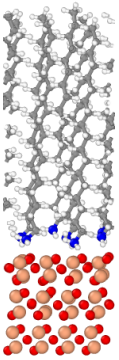

(f) Γ_7 – Side view (*yz* plane)

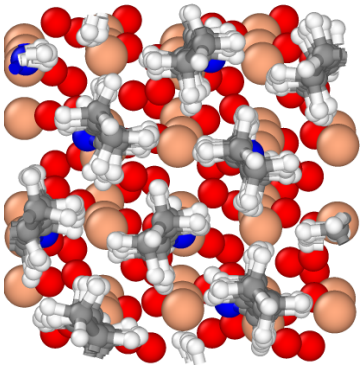

(g) Γ_8 – Top view (*xy* plane)

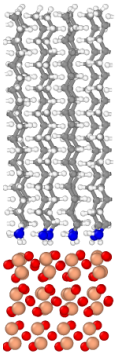

(h) Γ_8 – Side view (*yz* plane)

Figure 4.19 – Snapshots of Γ_5–Γ_8 cells at the end of the production simulation. Note that the boundaries of the simulation boxes are not represented here. *Atomic color code: coral* - iron, *red* - oxygen, *white* - hydrogen, *gray* - carbon, *blue* - nitrogen.

Furthermore, the obtained simulation results enabled us to consolidate the overall observation treating the assembly and the organization processes of amphiphilic compounds, which were particularly pointed out earlier by macroscopic experiments (cf. p. 75). Then, since our core motivation was to discern relationship(s) existing between the surfactant film morphology and their lubricating properties, we selected the most suitable structures to design the computer test allowing the investigation of OFM-based SAM under confinement and shearing conditions to be conducted. Incidentally, three simulated coverages have stood out from our findings, namely: Γ_2 , Γ_3 and Γ_4, which were later referred to as Γ_{low}, Γ_{medium}, Γ_{high} self-assembled monolayers (cf. figure 4.20).

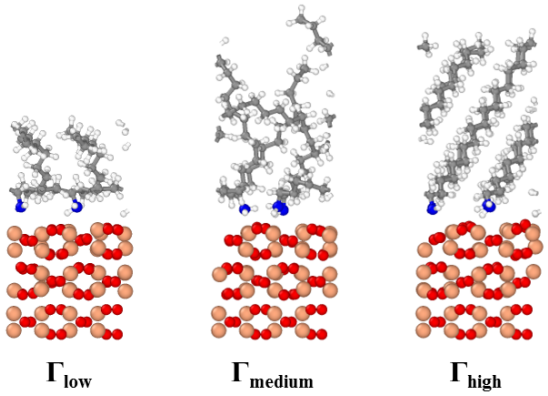

Figure 4.20 – Snapshots of the amine-films representing the surface coverages chosen to be probed in the confined shearing simulations (side view, *xz* plane).
For information, $\Gamma_{low} = 1.8\,nm^{-2}$, $\Gamma_{medium} = 2.7\,nm^{-2}$, $\Gamma_{high} = 3.6\,nm^{-2}$.
Note that the boundaries of the simulation boxes are not represented herein. *Atomic color code: coral* - iron, *red* - oxygen, *white* - hydrogen, *gray* - carbon, *blue* - nitrogen.

That choice was made considering not only the large range of structural characteristics represented by these specific films, but also based on the prior SFM measurements performed on a silicon substrate coated with a native iron oxide (cf. figure 4.7, p. 77). Indeed, the height of octadecylamine islands was empirically estimated to be between 9 and 15 Å for this system, which corresponds to the molecular thicknesses covered by Γ_{low}, Γ_{medium}, Γ_{high} SAM (cf. table 4.2, p. 85). Nevertheless, it must be stressed that *in-situ* liquid cell SFM experiments generally estimate a thinner thickness from organic films, owing to additional compression effect induced by the presence of a solvent, as well as by the use of a scanning tip cantilever. Besides, it is worthwhile to mention that the retained surface coverages are also in accordance with Γ values applied in other research works.[47, 52, 57]

4.3 Summary

A better understanding of the surface activity exhibited by surfactant additives and their microstructure developed over solid substrate is vital for determining the boundary lubrication role of organic friction modifiers. In this context, the presented adsorption study contributes experimental and computational information on the interaction mechanism and the layering morphology of C_{18} primary amine molecules adsorbed on an iron oxide surface.

In short, first-principle DFT calculations were employed to confirm the chemisorption of alkyl amines on hematite, providing enough data — about the N-Fe chemical bond — required to derive a classical MD potential able to reproduce their pairwise interaction, $U^{\text{interface}}$. Then, by using this interfacial force field, a series of EMD simulations were conducted to investigate the effect of the packing density on the structure of amine-based SAM, adsorbed onto an α-Fe_2O_3 substrate. Other than the validation of the fitted interatomic potential, the simulated octadecylamine films have shown that their packing order and their adlayer thickness increase with increasing surface coverage. Lastly, three surface coverages were selected — $\Gamma^{\text{SAM}}_{\text{low}} = 25\%$, $\Gamma^{\text{SAM}}_{\text{medium}} = 37.5\%$ and $\Gamma^{\text{SAM}}_{\text{high}} = 50\%$ — to be used as SAM models for the confined shearing simulations that compose the following friction study (cf. chapter 5, p. 97).

5

Friction

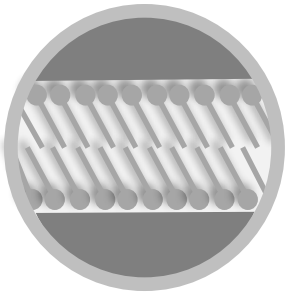

OFM are employed to minimize the energy losses induced by friction, as well as to mitigate detrimental effects of the ensuing wear. Besides, friction and wear phenomena especially arise within engineering systems subjected to BL conditions (*i.e.*, high pressure and low sliding velocity).[27] In practice, these additives form thin, densely packed layers over the engine components, which are difficult to compress but easy to shear off at the interface formed by the opposing aliphatic tails (cf. figure 1.4, p. 5).[28,210] Indeed, the repulsion between the contacting methyl and methylene groups contribute to decreasing the shear stresses at the rubbing interface, thereby diminishing the friction forces and then, the resistance of the moving parts to slide over another.[55] Also, it is interesting to note that the repulsion between OFM films occurs notably due to vdW and/or electrostatic forces.[29,34,55]

This chapter finally concerns the OFM tribological behavior, and notably those of C_{18} primary amine, under confinement and shear. In fact, it describes a NEMD simulation established to mimic a *computer tribometer experiment* at nanoscale, in order to explore the influence of several parameters (*e.g.*, interfacial film composition, SAM packing density, and sliding velocity) on the *computational friction coefficient*, μ^*. Thus, the following sections cover a brief outline of previous experimental studies dealing with amine-based FM (cf. § 5.1, p. 98), as well as the description of computational procedure, the obtained results, and the discussion about the probed friction properties (cf. § 5.2, 5.3 and 5.4, p. 102, 117 and 127, respectively).

5.1 Experimental background

5.1.1 Literature review on experiments with amine-based FM

Nitrogen-containing compounds have long held a prominent place within the engine oil industry, since they have largely been employed as corrosion/rust inhibitors,[34,202,258–265] friction modifiers,[6,30,42,45,49,50,52,54,61,236,237,242,266,267] and dispersants,[268–271] among other functional additives.[28,33] In particular, numerous patents have so far documented the employment of amine-based additives into commercial lubricant formulations.[272–285]

As tribo-improvers, linear molecules containing amino groups have been previously studied in order to examine their tribological performance at boundary and mixed lubrication regimes.[6,49,50,52,54,236,242,286] For example, it was found that octadecylamine can indeed reduce friction, but above a critical concentration (*e.g.*, between 10^{-6} and 10^{-3} M), depending on the probed temperature.[286] In addition, the degree of unsaturation related to their hydrocarbon tails seem also to affect their friction-control behavior. Actually, Campen *et al.*[54] have shown that a saturated C_{18} primary amine (*i.e.*, octadecylamine – $C_{18}H_{37}NH_2$) gives lower friction than its mono-unsaturated counterpart (*i.e.*, oleylamine – $C_{18}H_{35}NH_2$).

However, fatty amines and their derivatives have been found to yield an inferior performance, compared to additives possessing oxygen-based polar groups, such as fatty acids, alkyl esters, acylglycerols (or glycerides), and even fatty amides.[6,42,52,50,287–289] For example, Koshima *et al.*[42] have investigated the friction-reducing efficiency of binary PAO-based solutions containing different OFM models on ferrous substrates.[1] Their results have shown that the reduction in friction was approximately equal to 23% for oleylamine ($C_{18}H_{37}N$), whereas oleylamide ($C_{18}H_{35}NO$), glycerol monooleate ($C_{21}H_{42}O_4$), oleic acid ($C_{18}H_{34}O_2$) and stearic acid ($C_{18}H_{36}O_2$) exhibited a decrease of 33%, 35%, 45% and 54%, respectively. That fact is probably due to the lower binding energies of amino functional groups, in comparison with those of molecules containing carbonyl and carboxyl groups. Indeed, a stronger strength of the *interfacial surfactant-substrate interaction* allows OFM molecules to better struggle against the severe boundary operating conditions, thereby ensuring protection for the rubbing surfaces and eventually, mitigating the overall dynamic friction effects.[57,287,288] Nevertheless, it must be noticed that carboxylic acids exhibit a significant corrosive action on metallic surfaces, and also that primary amines may hinder the film-forming behavior of anti-wear tribofilms (in cer-

[1] Koshima *et al.* have used reciprocating friction tests at 373 K and under a load of 50 N, along with PAO solutions with 1 wt.% OFM.[42] Besides, the reduction of the measured friction coefficient was calculated using the reference value determined for a system lubricated by a *free-additive BO solution*, which is: $\mu_{PAO} = 0.197$.

tain conditions), as well as it may promote the degradation of elastomers.[34]

Furthermore, synergetic and boosting effects between amine-FM and inorganic-based additives, such as *zinc dialkyldithiophosphates* (ZDDP – AW agents)[48,49,61,242,270,289–297] and *molybdenum dithiocarbamates* (MoDTC – friction modifiers),[51,298] have also been referred to in the literature. For example, it has been observed that amines can change the composition, the morphology and/or the thickness of a ZDDP-derived tribofilm, whose beneficial effects impacting its final anti-wear performance depend on their amine/ZDDP molar ratio.[61] Yet, the various mechanisms likely to govern their interactions still remain unclear and open to debate.

In the following paragraph, experimental results from a series of tribological tests concerning the friction-reducing efficiency of different amines are summarized. They were carried out by Dr. Toni Massoud, within the framework of our project.

5.1.2 Tribological behavior of C_{18} amines in PAO

The boundary lubrication performance of four fatty amines — each one containing a C_{18}, linear and saturated hydrocarbon tail — was investigated in a steel-steel sliding contact, by means of a *reciprocating ball-on-flat tribometer* (*OFM models*: C, E, F and H; cf. table 2.1, p. 20).[61] The surfactants were blended at a concentration of 1 w.t.% to a PAO 4 base oil, and tested at 373 K, under a load of 2 N, which is equivalent to a maximum Hertzian pressure of approximately 504 MPa.[61] For clarity purposes, the experimental protocol is fully detailed in *appendix E* (cf. p. XV), and the obtained results of friction coefficient are listed below (cf. table 5.1).

Table 5.1 – Steady-state boundary friction coefficient (μ)

Amine	ID[(a)]	Formula	μ[(b)]	Reduction[(c)]
additive-free	—	—	0.134 ± 0.004	—
octadecylamine (1°)	OFM-C	$C_{18}H_{39}N$	0.078 ± 0.002	42%
n-methyl-1-octadecylamine (2°)	OFM-E	$C_{19}H_{41}N$	0.085 ± 0.001	37%
n,n-dimethyl-1-octadecylamine (3°)	OFM-F	$C_{20}H_{43}N$	0.094 ± 0.010	30%
2,2'-(octadecylimino)diethanol (3°)	OFM-H	$C_{22}H_{47}NO_2$	0.079 ± 0.001	41%

[(a)] *The* molecular IDs *used herein correspond to the same nomenclature referred to in table 2.1 (cf. p. 20).* [(b)] *The displayed values represent the* mean *and* standard deviation *calculated over the last 4 600 cycles, from a total of 9 600, which were performed with a stroke length of 3 mm.* [(c)] *The reduction in the friction coefficient produced by each OFM model is expressed in %, and it was calculated taking into account the reference value measured for a system lubricated by an additive-free PAO solution (μ = 0.134 ± 0.004).*

As one can observe, μ results indicates that all tested amines were able to reduce the average friction coefficient, from 0.134 to values between 0.078 and 0.094 (cf. table 5.1), which are in good agreement with previous published data.[30, 48, 291, 299] Besides, *primary alkyl amine* (*OFM-C*) showed the best tribological performance, whose obtained friction reduction amounts to approximately 42%.[61]

Those measurements have also revealed that the presence of methyl groups as hydrogen substituents — notably in the *secondary* and *tertiary alkyl amines* (*OFM-E* & *F*) — leads to an increase in the friction coefficient, relative to the one of octadecylamine, likely due to their relatively *lower binding energies*,[2] since:

$$E^{ads}_{A3} < E^{ads}_{A2} < E^{ads}_{A1} \quad \text{such that} \quad \mu_{PAO,\,A1} < \mu_{PAO,\,A2} < \mu_{PAO,\,A3}$$

[2] For more information on the *adsorption energies* (E^{ads}) of alkyl amines on iron-oxide, the interested reader is referred to *appendix F* (cf. XIX), which describes their values determined from DFT calculations.

and also, due to their likely lower surface coverages, which are a direct result of the steric effect brought on by their relatively larger terminal groups.[61]

In addition, it is worthwhile noting that, despite its two ethoxyl groups associated to the nitrogen atom that may inhibit the formation of highly dense SAM, the *tertiary ethoxylated amine* (*OFM-H*) shows a similar frictional behavior related to that of primary alkyl amine (cf. table 5.1, p. 100). That is probably owing to a superior molecular cohesion and robustness of the adsorbed films constituted of 2,2'-(octadecylimino)diethanol molecules, in comparison to those containing octadecylamines, which are probably caused by a *hydrogen-bonding interaction network* formed between the hydroxyl groups present in their ethoxylated polar head (cf. figure 2.2h, p. 19).[49,57,61]

After briefly reviewing the effective tribological behavior of some amine-based FM at macroscale, which has been observed through experimental techniques, our computational study treating the OFM lubricating properties at molecular level is addressed in the next sections (cf. § 5.2, 5.3 and 5.4, p. 102, 117 and 127, respectively).

5.2 Computational details

A non-equilibrium molecular dynamics (NEMD) simulation — termed hereafter as the *confined shearing simulation* — was developed in order to establish a model computer-based experiment that mimics a *boundary friction contact*. Besides, our computational protocol was inspired by other procedures applied in previous published works.[47, 52, 57–59, 64, 82, 107, 300, 301]

Actually, confined NEMD simulations have progressively proved a valuable tool with which to investigate the structure and the tribological properties of thin films of a wide range of fluids, on numerous surface chemistries and under different lubrication conditions (*e.g.*, BL, ML & HL regimes).[37, 57–59, 64, 79, 81, 82, 88, 91, 107, 176–179, 204, 210, 212, 215, 232, 246–249, 252, 253, 266, 300–369] Important advantages of those simulations include the fact that atomic-scale effects can directly be discerned, such those associated with *microstructure dynamics* (*e.g.*, density and viscosity inhomogeneities, phase transitions), as well as with *tribological phenomena* (*e.g.*, stick-slip, boundary slip and shear localization).[59, 63, 340, 370, 371] Another asset exhibited by the NEMD technique is the fact that the friction behavior of a given system emerges naturally from simulation, rather than being parameterized into the employed model.[107] Nevertheless, it must be remembered that the simulated microstructures, as well as their tribological properties, are still dependent on the accuracy of the used classical force fields, describing the interatomic interactions prevailing within the system of interest.

For a further overview on the historical evolution of confined NEMD simulations, and especially on those applied to *Tribology*, the interested reader is referred to more detailed reviews available in the literature.[63, 86, 87, 369, 372–374]

Concerning the current friction study, the *nanoscale contact* investigated within our confined shearing simulations consists in a *single-asperity model* composed of two *opposing iron oxyde surfaces* in relative motion, which are involved in a continuous and dynamic, rubbing process (cf. figure 5.1, p. 103). In addition, each surface is covered by an *adsorbed SAM composed of C_{18} primary amines* — with a specific surface coverage, Γ^{SAM} —, which are separated or not by an *intermediate PAO layer*, whose density is referred to as ρ^{PAO}.

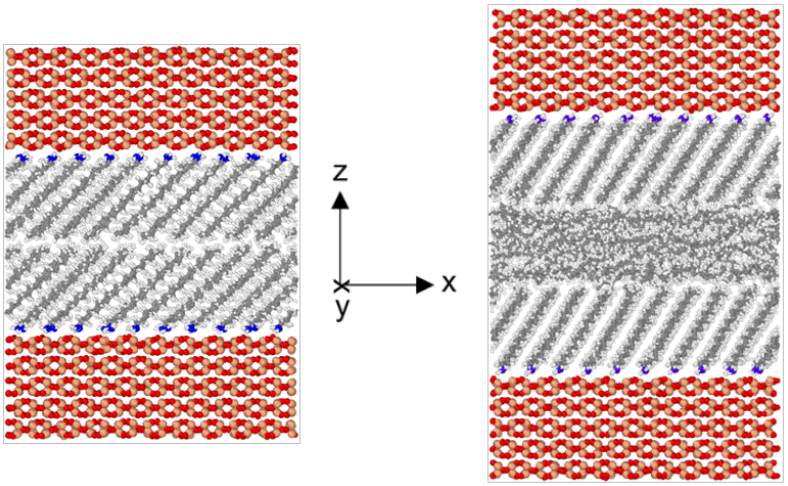

Figure 5.1 – Examples of model nano-contacts formed by hematite slabs and adsorbed amine-SAM, with: ***(i)*** *SAM/SAM interface*, without confined PAO molecules (*on the left*); ***(ii)*** *SAM/PAO/SAM interface*, including a thin BO layer (*on the right*). *Atomic color code: coral* - iron, *red* - oxygen, *white* - hydrogen, *gray* - carbon, *blue* - nitrogen.

In practice, the solid substrates are compressed one against another by an external *normal force or load* ($\mathbf{F}_N$), which is associated with a *normal pressure* (P_z), since $\mathbf{F}_N$ acts on a given *superficial contact area* (**A**). In our NEMD simulations, this constant force is applied on the *outermost* Fe_2O_3 *layer* of each slab (cf. the below referred to *"rigid layer"*, in figure 5.2), along *z* direction and perpendicular to hematite surfaces, which are in turn placed parallel to *xy* plane (cf. figure 5.1). Besides, $\mathbf{F}_N$ is high enough to ensure that OFM films are kept confined to length scales of a few nanometers, thereby setting up a *boundary-lubricated nanotribological system.*[353]

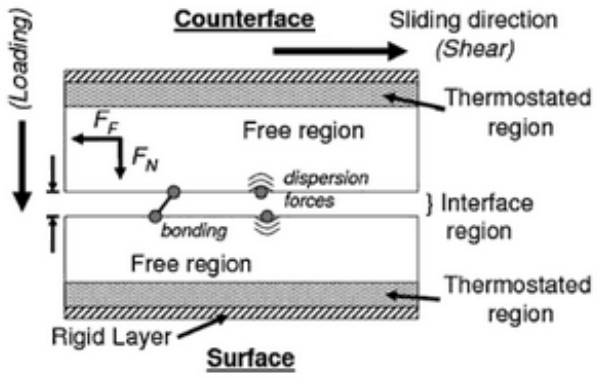

Figure 5.2 – Schematic diagram of a typical NEMD simulation of tribological experiment. (figure adapted from the indicated reference)[86]

Moreover, the *separating distance between the opposing rubbed substrates* (h^{film}) depends also on the composition and on the density of the interfacial film present between both substrates (cf. figure 5.1, p. 103). In our case, this *organic third-body* occasionally comprises BO model molecules, but it is predominantly formed by the adsorbed surfactant monolayers, whose inherent *shear strength* is lower than that exhibited by the bare iron oxide surfaces. This fact actually explains their functional usage as friction modifiers into liquid engine lubricants. For information, the systems that do not have any BO molecule in their interfacial film were called as the *nano-contact models with a SAM/SAM interface*, whose density was referred to as $\rho_{\emptyset}^{\text{PAO}}$. By contrast, the systems with intermediate PAO layers are named as the *nano-contact models with SAM/PAO/SAM interfaces*, which can possess two different densities: either $\rho_{\text{thin}}^{\text{PAO}}$ or $\rho_{\text{thick}}^{\text{PAO}}$.

Furthermore, the moving parts of real engineering systems are sheared off according to a given *shear rate* ($\dot{\gamma}$). Indeed, their motion is induced by an externally applied driving force — termed here as the *lateral force* ($\mathbf{F}_{\text{L}}$) —, which confers a specific *sliding velocity* (v^{s}) on the moving components (cf. figure 5.2, p. 103).[63, 375, 376] However, it must be noticed that, in our NEMD simulations, the sliding motion is originated through the movement of the solid surface boundaries — along x direction and in relatively opposite orientations (cf. figure 5.5, p. 114) — by imposing a constant sliding velocity to a given portion of iron and oxygen atoms constituting the *outermost layer* of both Fe_2O_3 slabs (cf. "rigid layer" in figure 5.2).[86, 348] Actually, it is not an external force that is computationally applied to the solid substrate models, but it is an *atomic sliding velocity* that is virtually imposed to a particular part of the system.

Hence, the magnitude of the resultant *friction force* ($\mathbf{F}_{\text{F}}$) experienced by each hematite slab corresponds to the total driving force required to maintain that targeted sliding velocity. In short, $\mathbf{F}_{\text{F}}$ is equal to the mentioned lateral force, but it points in the opposite direction:

$$\mathbf{F}_{\text{F}} = -\mathbf{F}_{\text{L}} \tag{5.1}$$

where the average value of $\mathbf{F}_{\text{L}}$ force can computationally be determined by means of the numerical outcome obtained from a specific technical operation called *fix setforce*,[3] which is applied to the surface subset termed as "rigid layer" (cf. figure 5.5, p. 114), during the production simulation timestepping in order to define a fixed and constant v_x^{s}.

[3] The programming command *fix set force* is available in the numerical solver *LAMMPS* (version: November 17th 2016). For further information on this command, the interested reader is referred to the following link *[online]* : `https://lammps.sandia.gov/doc/fix_setforce.html` (accessed January 10th 2019).

In addition, it has been assumed that the lateral forces, and consequently the frictional forces, are proportional to the intrinsic *sliding resistance* developed by the rubbing hematite surfaces. In particular, this resistance may reflect the influence of the *dynamics* and *interfacial structure* featured within the lubricated nano-contact (*e.g.*, h^{film}, Γ^{SAM}, ρ^{PAO}), as wells as the effect of the *operating conditions* (*e.g.*, total temperature, P_z, v_x^{s}). Therefore, we have considered as *OFM performance indicator* the dimensionless ratio between the aforementioned $\mathbf{F}_{\text{F}}$ and $\mathbf{F}_{\text{N}}$ forces, which was named hereafter as the *computational friction coefficient*, μ^*:

$$\mu^* \equiv \frac{\mathbf{F}_{\text{F}}}{\mathbf{F}_{\text{N}}} \tag{5.2}$$

As a matter of fact, μ^* was inspired by the first extension of the second *Amontons-Coulomb kinetic friction law*,[377,378] which states that the friction force is directly proportional to the applied normal load, at moderate constant sliding velocities.[301,353] Besides, it is interesting to recognize the existence in the literature of other extensions of that kinetic friction law, which includes a second term[303,379–381] into the *total lateral force model*, the *load-independent Derjaguin offset*[382] ($\mathbf{F}_0$), and even a third term, the *Bowden-Tabor friction term*[383] $\left(\tau \cdot \mathbf{A}_{\text{asp}}(\mathbf{F}_{\text{N}})\right)$ — where τ is the shear strength, and $\mathbf{A}_{\text{asp}}(\mathbf{F}_{\text{N}})$ the asperity contact area —, being both additional terms related to *adhesion-controled friction processes*.[353]

Nevertheless, the suggested *computational friction coefficient* (μ^*) has been taken as the reference lubricating descriptor in our simulation study since:

- our nano-contact model — containing a single asperity composed of atomically-smooth surfaces — is lubricated by a relatively thin organic film that cannot be squeezed out of the represented contact zone; thus presupposing that no direct contact between the iron oxide slabs would be allowed to occur (even at $\Gamma^{\text{SAM}}_{\text{low}}$ and $\rho^{\text{PAO}}_{\emptyset}$);
- only the dynamic friction process is emulated in the confined shearing simulations (*i.e.*, no static friction process is considered into the calculation of the proposed coefficient);
- a single and constant value of contact pressure was investigated ($P_z = 500$ MPa), which means that the ratio denominator depicted in equation 5.2 is maintained fixed ($\mathbf{F}_{\text{N}}$); thus, any variation measured in μ^* is a direct response of the lubricating properties related to the investigated system (and at the considered operating conditions), which are embodied by the $\mathbf{F}_{\text{L}}$ forces, and then, by $\mathbf{F}_{\text{F}}$;
- high sliding velocities were applied to solid substrates during the performed NEMD simulations ($v_x^{\text{s}} > 1.0\ \text{m}\cdot\text{s}^{-1}$);

- the breaking and reforming of chemical bonds can not be described by means of the classical MD force fields used in this work ($U^{\text{lubricant}}$, U^{surface}, $U^{\text{interface}}$; cf. § 2.2.2, p. 26);

thereby implying that no adhesion across the interface of the represented subsets was prone to be reproduced in such system, where a *subset* is defined as a single Fe_2O_3 slab coated with an octadecylamine SAM (cf. 5.5, p. 114).

Additionally, it is worth noting that some previous classical MD-based works have also used a similar definition of friction coefficient,[47,52,57,58] in comparison with μ^* (cf. equation 5.2), based on the extended Amontons-Coulomb kinetic friction law[353] subjected to a *high load approximation* (*i.e.*, when $\mathbf{F}_N >> 0$):

$$\frac{\mathbf{F}_L}{\mathbf{F}_N} = \frac{\mathbf{F}_0}{\mathbf{F}_N} + \frac{\left[\tau \cdot \mathbf{A}_{asp}(\mathbf{F}_N)\right]}{\mathbf{F}_N} + \mu \approx \mu \tag{5.3}$$

In fact, equation 5.3 clearly shows that, for relatively large values of contact loads ($\mathbf{F}_N$), both Derjaguin offset and Bowden-Tabor friction terms become negligible in comparison with the kinetic friction coefficient (μ), which can thus be simply calculated as the ratio between $\mathbf{F}_L$ and $\mathbf{F}_N$. Besides, the validity of such approximation (cf. equation 5.3) has been confirmed through confined NEMD simulations earlier performed by Ewen *et al.*,[57] using SAM models of stearic acid ($C_{18}H_{36}O_2$) and glycerol monooleate ($C_{21}H_{42}O_4$).[57] Indeed, they have used these two test cases to ensure that the linear fit of $\mathbf{F}_L$ as a function of $\mathbf{F}_N$ gives an insignificant value of $\mathbf{F}_0$, which indicates that the modeled OFM additives induce a low adhesion frictional contact.

Before describing the computational protocol developed to obtain the confined shearing simulations, it must also be highlighted some interesting aspects concerning certain limitations of the MD method. Actually, even if our modeled systems are intended to describe a BL contact (cf. 5.1, p. 103), it is still not possible to efficiently reproduce within a NEMD simulation the sliding velocities used to characterize this regime in macroscopic experiments, such as the ones applied in the friction tests described in section 5.1.2 (*e.g.*, $v^s = 8 \times 10^{-3}\ \text{m} \cdot \text{s}^{-1}$; cf. experimental conditions detailed in figure E.1b, appendix E, p. XVI).[61]

Therefore, in order to obtain a computational tribometer experiment exhibiting accessible system sizes and timescales through NEMD simulations, the investigated sliding velocities were greater than $1.0\ \text{m} \cdot \text{s}^{-1}$. However, a (virtual) *thermostatting technique* had thus to be employed, in order to control the large local temperature rises induced by such operating conditions within the established nanoscale model, as shown in figure 5.2 (cf. p. 103).[63,86] In-

deed, a "*thermostatted region*" was set up to offset the relatively high shear rates used in our NEMD simulations. Regarding this feature, the *Langevin thermostat*[99] was employed to dissipate the heat generated during the production sliding simulations (cf. § 5.2.2, p. 114), as it has been suggested by previous NEMD-based works[57, 58, 82, 107, 304, 336, 338] (further details are given in § 5.2.2, p. 114). Additionally, the "thermostatted region" was located in the middle of each hematite slab, as an attempt to prevent possible adverse interference effects caused by the applied thermostat in the interfacial dynamics of the confined organic molecules (*i.e.*, octadecylamines and PAO; cf. figure 5.5, p. 114).[86]

Moreover, it should be borne in mind that there has been no pretension in the current work of directly and quantitatively comparing the μ^* results, obtained from NEMD simulations (cf. tables 5.4, 5.5 and 5.6, p. 118), with the macroscale experimental results of μ (cf. table 5.1, p. 100). To do that, it would be necessary to obtain macroscopic tribological systems similar to the idealized models and conditions utilised within our confined shearing simulations (cf. figures 5.6, 5.7 and 5.8, p. 119), such as flat and smooth ferrous substrates, homogeneous and uniform surfactant self-assembled monolayers, as well as high sliding velocities, with relatively high confinement (*i.e.*, small h^{film}), and at controlled steady temperature.

Finally, the computational procedure established to assess the frictional behavior of OFM additives is fully detailed in the next paragraphs (cf. § 5.2.1 and 5.2.2, p. 108 and 114, respectively), followed by the sections describing and discussing the calculated μ^* results for systems containing octadecylamine and PAO molecules (cf. 5.3 and 5.4, p. 117 and 127, respectively).

5.2.1 System modeling and equilibration

In the current study, NEMD simulations were performed in order to gain molecular-scale insights into the properties of octadecylamine films adsorbed on hematite surfaces, under confinement and shear, and in particular, to investigate the influence of some specific parameters on the computational friction coefficient (μ^*). These parameters are related to :

- *Interfacial organic film structure:* surface coverage of amine-SAM ($\Gamma^{\text{SAM}}_{\text{low}}$, $\Gamma^{\text{SAM}}_{\text{medium}}$ & $\Gamma^{\text{SAM}}_{\text{high}}$), and intermediate PAO film density ($\rho^{\text{PAO}}_{\emptyset}$, $\rho^{\text{PAO}}_{\text{thin}}$ & $\rho^{\text{PAO}}_{\text{thick}}$);
- *Operating conditions:* sliding velocity (v^{s}_x).

To achieve that objective, nine different configurational models were thus required. Then, the *(1 × 1) unit cell* of each boundary-lubricated tribological system was designed according to the following characteristics and assumptions:

- A nanoscale contact is intended to describe a single-asperity model, containing two opposing substrates that are referred to as the *top* and *bottom surfaces/slabs*. Both substrates were placed — with their normal vector parallel to z direction — nearly to the extremities of the simulation cell (cf. figure 5.3, p. 110), whose dimensions are approximately equal to 10 Å × 11 Å × 120 Å (*superficial contact area*: $A_{xy} \approx 112$ Å^2; *distance between the innermost* Fe_2O_3 *layers:* $h^{\text{film}} \approx 80$ Å).
- Each hematite (0 1 $\bar{1}$ 2) slab exhibits a thickness of approximately 18 Å, which represents five elementary Fe_2O_3 layers (cf. figure 5.1, p. 103). This α-iron(III) oxide model was generated from the *basic unit cell*, obtained by DFT and described in § 2.1.2 (cf. figure 2.3, p. 21). Besides, each solid substrate is composed of 200 atoms (80 Fe & 120 O atoms).
- Octadecylamines and poly-alpha-olefins were considered in their *electrically neutral state*, which might be favored in a low-polarity medium.[47, 52]
- The $C_{18}H_{37}$–NH_2 molecules were incorporated into the cell volume situated between both ferrous surfaces, with their polar groups pointing toward the substrate, at a distance less than 4 Å, measured between the nitrogen atoms and the plane formed by the inner surface oxygens (cf. figure 5.3, p. 110). Additionally, their alkyl tails are initially configurated parallel to each other, and perpendicular to the solid substrates.
- The total number of primary alkyl amines introduced into each model cell were chosen to match the surface coverages selected from the analyses explained in chapter 4

(cf. § 4.2.2 and figure 4.20, p. 83 and 94, respectively), which are: $\Gamma^{\text{SAM}}_{\text{low}} = 1.8\ \text{nm}^{-2}$, $\Gamma^{\text{SAM}}_{\text{medium}} = 2.7\ \text{nm}^{-2}$, $\Gamma^{\text{SAM}}_{\text{high}} = 3.6\ \text{nm}^{-2}$, corresponding to 2, 3 and 4 molecules per unit cell, respectively, or in other words, a *coverage ratio* amounting to 25%, 37.5% and 50%, respectively.

- Concerning the BO molecules, six geometry models were constructed with an intermediate PAO layer, which are those possessing a *SAM/PAO/SAM interface* (cf. figures 5.3b and 5.3c, p. 110). For these systems, two different PAO film densities were utilized: $\rho^{\text{PAO}}_{\text{thin}}$ and $\rho^{\text{PAO}}_{\text{thick}}$, which correspond to 1 and 2 PAO molecules, respectively. These mono and bimolecular PAO layers were taken into account based on the previous NEMD simulation results that were recently obtained by Ewen *et al.*.[57] Actually, they performed a preliminary *squeeze-out simulation* in order to determine the lubricant film density — composed in their case of hexadecane molecules, $C_{16}H_{34}$ — that remains inside the contact volume, under confinement by two hematite slabs coveraged of adsorbed OFM monolayers (simulation conditions: $P_z = 500$ MPa and $T = 300$ K).[57] Their results showed that the *equilibrium lubricant thickness* is independent of the OFM coverage, and it corresponds to approximately two horizontally oriented molecular layers.[57] For this reason, we thus decided to explore the influence of ρ^{PAO} layer, in a range from 0 to 2 PAO molecules (cf. figure 5.3, p. 110).
- For that simulation cells comprising a SAM/PAO/SAM interface ($\rho^{\text{PAO}}_{\text{thin}}$ & $\rho^{\text{PAO}}_{\text{thick}}$), the BO molecules were located, following a horizontal orientation, in the middle of each system, according to a *sandwich configuration* between the amine molecules nearly placed to the opposing top and bottom hematite slabs (cf. figures 5.3b and 5.3c, p. 110).
- Lastly, it should be noted that the remaining three nano-contact models exhibiting a *SAM/SAM interface* ($\rho^{\text{PAO}}_{\emptyset}$) do not contain any PAO molecule into their nano-contact model (cf. figure 5.3a, p. 110).

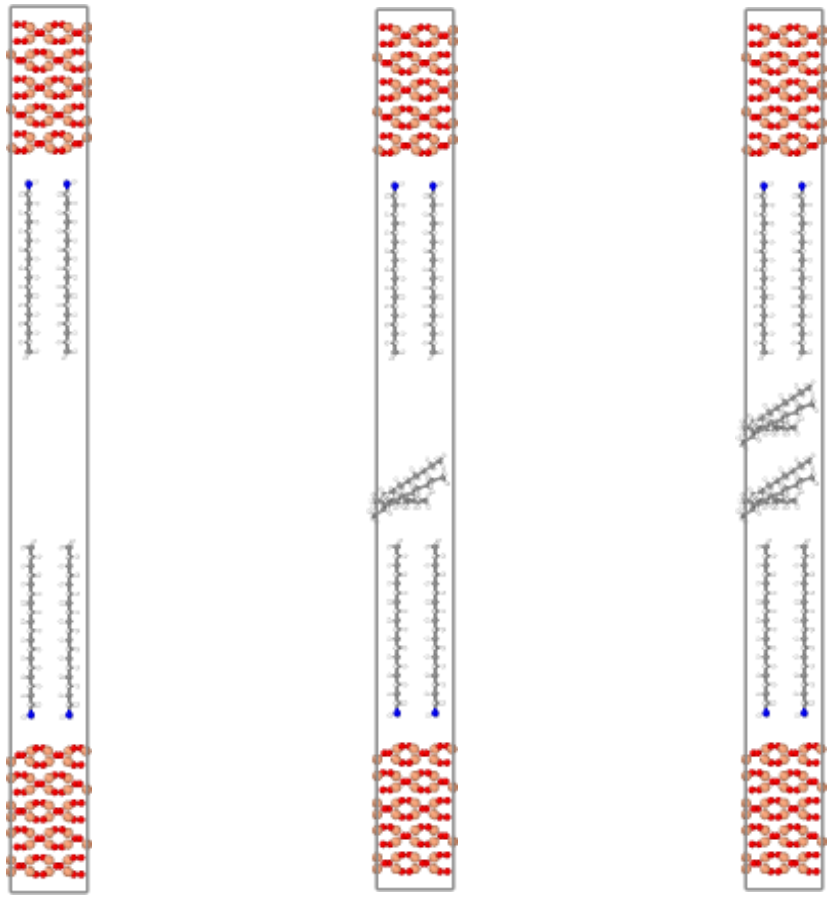

(a) $\rho_{\emptyset}^{\mathbf{PAO}}$ **(b)** $\rho_{\mathbf{thin}}^{\mathbf{PAO}}$ **(c)** $\rho_{\mathbf{thick}}^{\mathbf{PAO}}$

Figure 5.3 – Examples of initial configurations related to nano-contact models, depicted for a fixed surface coverage ($\Gamma_{\mathrm{low}}^{\mathrm{SAM}}$): **(a)** *SAM/SAM interface* ($\rho_{\emptyset}^{\mathrm{PAO}}$); **(b)** *SAM/PAO/SAM interface* ($\rho_{\mathrm{thin}}^{\mathrm{PAO}}$); **(c)** *SAM/PAO/SAM interface* ($\rho_{\mathrm{thick}}^{\mathrm{PAO}}$). Note that the unit cell dimensions are approximately equal to 10 Å × 11 Å × 120 Å. *Atomic color code: coral* - iron, *red* - oxygen, *white* - hydrogen, *gray* - carbon, *blue* - nitrogen.

Once the initial geometries of the nine required unit cells were built (cf. figure 5.3, p. 110), their equilibration was undertaken in order to establish the desired nano-contact models, consisting of a compressed couple of large hematite surfaces, coated by uniform octadecylamine self-assembled monolayers, which are separated or not by intermediate PAO layer(s) (for an example, cf. figure 5.5, p. 114). Therefore, an *equilibration phase* composed of four different steps was performed in order to obtained those configurations:

- *Step 1 – octadecylamine-SAM equilibration:* following a preliminary energy minimization[4] of each simulation cell, atomic velocities were assigned to all system atoms — according to a Maxwell-Boltzmann distribution for a temperature of 373 K —, except to those composing the BO molecules that were kept frozen, in order to assemble the amine molecules into a SAM-type ordering (cf. figure 5.4a, p. 112); after, a 3 ns NVT ensemble calculation[5] was performed (3 000 000 time steps of 1 fs), also at 373 K. Then, an annealing process was conducted in a similar way to that utilized to set up the SAM models investigated in chapter 4 (cf. § 4.2.1.2, p. 81), but at an intermediary temperature of 473 K and an ultimate temperature of 373 K. For information, this process totally lasted 12 ns, containing four intermediary 3 ns NVT ensemble simulations.
- *Step 2 – PAO-layer equilibration:* after organizing the different amine-SAM, the same simulation procedure used in *step 1* was applied to the intermediate BO model films — for the systems exhibiting a SAM/PAO/SAM interface (*i.e.*, $\rho^{\mathrm{PAO}} \neq 0$) —, maintaining in this turn the obtained SAM structures fixed (cf. figure 5.4b, p. 112). Thus, the PAO molecules were thermally reoriented at the targeted temperature of 373 K, but with an intermediary temperature of 673 K during the annealing process.
- *Step 3 – unit cell pressurization:* an external and constant normal force was applied to both top and bottom α-Fe_2O_3 $(0\ \ 1\ \ \bar{1}\ \ 2)$ slabs, during a 3 ns NVT ensemble simulation, in order to compress the system and obtain the model BL nano-contact (cf. figure 5.4c, p. 112). Besides, $P_z = 500$ MPa, acting on the outermost surfaces composing the hematite substrates (plane *xy*). In addition, the Langevin thermostat[99] was used with a time relaxation constant of 1.0 ps, in the directions perpendicular to the compression (*i.e.*, *x* and *y* directions) in order to allow the system to be equilibrated at 373 K (cf. figure 5.4d).

[4] The *quadratic line search algorithm* was used to performed the energy minimization of all initial configurations.

[5] All the NVT ensemble simulations performed in the aforementioned *steps 1* and *2* have used the *Nosé-Hoover thermostat*[98] to control the temperature of all mobile atoms, which are those that are not framed by a *green box* in figure 5.4 (cf. p. 112), and using a damping constant equal to 0.1 ps.

- *Step 4 – extended cell pressurization:* bigger simulation cells were constructed — by multiplying each of the previous squeezed and equilibrated unit cell by five, in x and y directions —, and submitted them to a further 1 ns NVT ensemble calculation at 373 K, using the same conditions described in *step 3*. For information, each of the obtained extended hematite slab exhibits 5 000 atoms and the dimensions of the final simulation cell are approximately equal to 51 Å × 55 Å × 120 Å, which represents a superficial contact area of $A_{xy} \approx 2\,796$ Å^2. Besides, the total number of organic atoms composing each of the nine simulation cells are listed in table 5.2 (cf. p. 113).

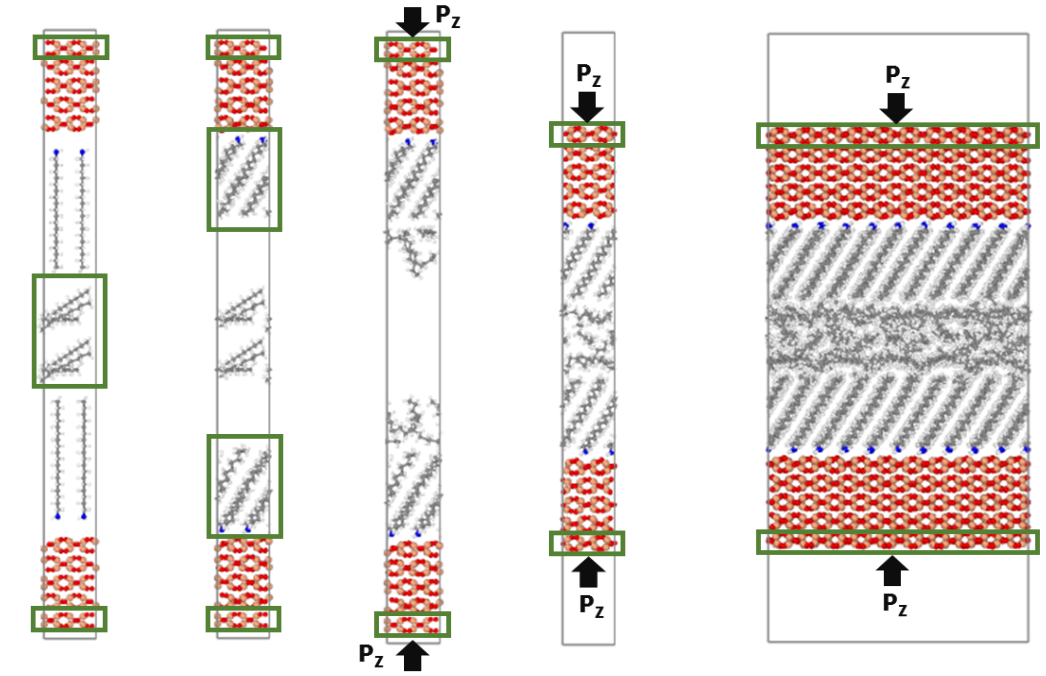

(a) Step 1 (initial cell) **(b) Step 2 (initial cell)** **(c) Step 3 (initial cell)** **(d) Step 3 (final cell)** **(e) Step 4 (final cell)**

Figure 5.4 – Schematics of the equilibration phase steps, showing their side views in xz plane: **(a)** initial configuration used in *step 1 – octadecylamine-SAM equilibration*; **(b)** initial configuration used in *step 2 – PAO-layer equilibration*; **(c)** initial configuration used in *step 3 – unit cell pressurization*; **(d)** final configuration obtained from *step 3 – unit cell pressurization*; **(e)** initial configuration used in *step 4 – extended cell pressurization*, with a *(5 × 5) unit cell*. For information, these examples particulary feature the simulation cells with a *SAM/PAO/SAM interface* at $\Gamma^{\mathrm{SAM}}_{\mathrm{high}}$ and $\rho^{\mathrm{PAO}}_{\mathrm{thick}}$. Note also that atoms framed by *green boxes* were kept fixed during the concerned MD simulations (in x, y for all steps, and in z dimensions only during steps 1 & 2). *Atomic color code: coral* - iron, *red* - oxygen, *white* - hydrogen, *gray* - carbon, *blue* - nitrogen.

Table 5.2 – Total number of organic atoms present into simulation cells, $N_{organic}$

Interface	Γ^{SAM}_{low}	Γ^{SAM}_{medium}	Γ^{SAM}_{high}
SAM/SAM ($\rho^{PAO}_{\emptyset}$)	5 800	8 700	11 600
SAM/PAO/SAM (ρ^{PAO}_{thin})	8 100	11 000	13 900
SAM/PAO/SAM (ρ^{PAO}_{thick})	10 400	13 300	16 200

For clarity purposes, it should be noted that, in all of the four equilibration steps, the classical MD simulations were carried out using the three selected energy potentials: $U^{surface}$, $U^{lubricant}$ and $U^{interface}$ (cf. § 2.2.2, p. 26). Besides, the standard velocity-Verlet algorithm[83] was applied to integrate Newton's equations of motion with a time step of 1 fs, applying *LAMMPS* program.[95] Moreover, short-range nonbonded interactions were cut-off at 15 Å, and the electrostatic interactions were evaluated employing a slab implementation of PPPM solver,[161,205] with a desired relative error in forces of 1×10^{-6}. Also, periodic boundary conditions were only imposed to *xy* plane.

5.2.2 Confined shearing simulation (production)

After obtaining squeezed and thermally equilibrated systems — whose confined organic film reached a (non-equilibrium) steady state, with a regular and stable thickness (h^{film}) —, the nine configurational models were then subjected to *compression* and *shear*, during the *production simulation phase*. For illustration purposes, a schematic representation of the *confined shearing simulation* is shown below.

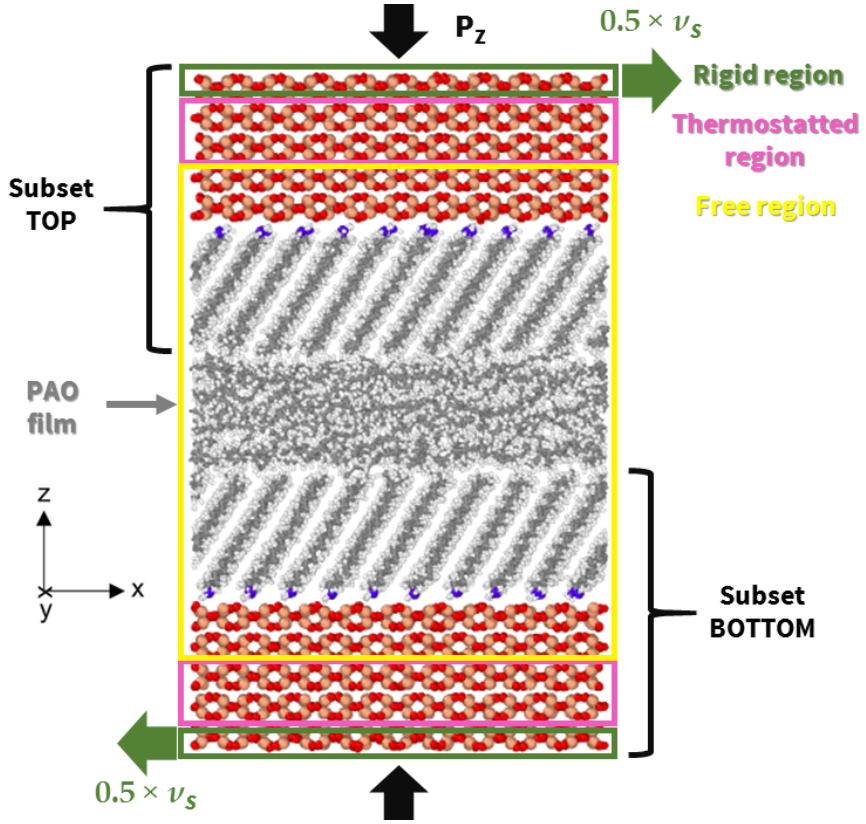

Figure 5.5 – Example of the *idealized boundary-lubricated nano-contact*, which was used as initial geometry in the confined shearing simulations. For information, this configuration has specifically $\Gamma^{\text{SAM}}_{\text{high}}$ and $\rho^{\text{PAO}}_{\text{thick}}$. Besides, note that the system contains three different functional zones: **(i)** *rigid region:* set of atoms where the normal force and a specific sliding velocity are imposed on $\left(\pm F_{N,z}\right.$ and $\left.\pm(1/2)\cdot v^{s}_{x}\right)$, respectively), in relatively opposite directions (*composition*: two Fe_2O_3 layers, in top & bottom slabs) ; **(ii)** *thermostatted region:* set of atoms controlled by Langevin thermostat, applied only in *y* direction (*composition*: four Fe_2O_3 layers, in top & bottom slabs) ; **(iii)** *free region:* set of atoms allowed to freely move according to the chosen MD force fields and the model constraints of shear and external load (*composition*: four Fe_2O_3 layers, in top & bottom slabs, and all organic atoms from octadecylamine and PAO molecules). Also, note that the nano-contact model is composed of two subsets — either in *top* or *bottom* position — which individually represents a surface covered by a SAM, being lubricated (or not) by a BO layer. Lastly, notice that simulation cell boundaries are not represented here, and periodic boundary conditions were applied only in *x* and *y* directions. *Atomic color code: coral* - iron, *red* - oxygen, *white* - hydrogen, *gray* - carbon, *blue* - nitrogen.

This final NEMD simulation was established to generate the atomic trajectory data related to the studied nano-contacts, and in particular the frictional forces arising on the iron and oxygen atoms composing the "rigid region" of both top and bottom hematite slabs (cf. figure 5.5, p. 114). These forces are a result of the resistance exhibited by the hematite surfaces to slide over another, which is in turn impacted by the interfacial film structure separating them, as well as by the applied operating conditions. Besides, that set of information is required to determine the structural average functions used to probe the microstructure formed by adsorbed octadecylamines and intermediate PAO molecules (whether present at SAM interface), and to calculate the resultant computational friction coefficient, as a function of the investigated parameters, namely: Γ^{SAM}, ρ^{PAO} and v_x^{s} (cf. results in section § 5.3, p. 117).

As a matter of fact, the system is forced out of equilibrium by imposing an external field to the solid substrates (*e.g.*, a shear rate), while maintaining a constant load on both surfaces. In practice, this was achieved by moving the concerned rigid atoms along the x direction, in order to obtained a constant total sliding velocity, which was varied from 1 to 5, and 10 $\mathrm{m \cdot s^{-1}}$. As one can observe from figure 5.5, the "rigid regions" are in relative motion, with an individual sliding velocity equal to $\left[+(1/2)\cdot v_x^{\mathrm{s}}\right]$ for the top slab, and $\left[-(1/2)\cdot v_x^{\mathrm{s}}\right]$ for the bottom one (cf. p. 114). Accordingly, twenty-seven simulations were conducted in the current friction study, thereby yielding twenty-seven different values of μ^*.

Concerning the duration of the confined shearing simulations, they are mainly dependent upon the investigated v_x^{s} values. For information, table 5.3 lists some of these computational details (cf. p. 116). Indeed, all simulations were conducted for a long enough time, in order to produce a sufficient relative *sliding distance* for the α-Fe_2O_3 slabs (e.g., $d_x^{\mathrm{s}} > 15$ nm).[6] In addition, relatively long-time simulations were considered (*i.e.*, for at least 6 ns), in an attempt to minimize the dependency of the calculated μ^* on the (single) initial configuration of each system model.

Therefore, after having ensured that all model systems attained a sliding and thermal steady state, the concerned normal and lateral forces were sampled, particularly to determine the representative average values of $\mathrm{F_{N},}_z$ and $\mathrm{F_{L},}_x$ needed to eventually calculate μ^* coefficients (cf. equation 5.2, p. 105).

[6] For information, the *equilibration* and *production* simulations were both performed on a 16-cores processor (Dell C6320; Intel Xeon E5-2640 v3 2.60GHz), during (total) time periods varying from approximately 36 to 76 days, depending on the structure and composition of the organic interfacial film, as well as on the substrate sliding velocity.

Table 5.3 – Details of the production simulation

Sliding velocity v_x^s ($m \cdot s^{-1}$)	Duration (ns)	Sliding displacement, d_x^s (nm)
1.0	15	15
5.0	9	45
10.0	6	60

Moreover, the basic computational characteristics related to the mentioned NEMD production simulations were the same as those used in "step 4" of the precedent equilibration phase (cf. § 5.2.1, p.113), except for the thermostatting approach. In this case, any heat induced by the relatively high shear rates was dissipated using a Langevin thermostat[99] applied to Fe and O atoms of the "thermostatted region", but solely in *y* direction (*i.e.*, the direction perpendicular to both compression and sliding movement). Besides, the time relaxation constant employed to control the temperature was set to 1.0 ps.

Regarding the obtained results, there are firstly and globally presented in § 5.3 (cf. p. 117), and then discussed in detail in § 5.4 (cf. p. 127).

5.3 Results

The nanoscale structure and the lubricating properties of organic layers — containing adsorbed octadecylamine films and intermediate PAO molecules — were investigated under relatively high shear rates and pressure ($P_z = 500$ MPa), for a rubbing contact equilibrated at T = 373 K (applied to "thermostatted region", cf. figure 5.5, p.114). In addition, the influence of the SAM coverage (Γ^{SAM}), the PAO layer density (ρ^{PAO}) and the substrate sliding velocity (v_x^s) on the proposed computational friction coefficient were studied through NEMD simulations, using a classical DFT-based potential specifically derived to reproduce N-Fe interactions.

In this context, the following results were determined from the atomic information generated during the last 3 ns of the production phase (3 000 000 time steps), which represents a non-equilibrium steady state of the confined shearing simulation (cf. § 5.2.2, p. 114). The obtained results are:

- *average computational friction coefficient*, μ^* (as function of Γ^{SAM}, ρ^{PAO} and v_x^s; cf. tables 5.4 – 5.6, p. 118);
- *separating distance between the opposing rubbed substrates*, h^{film} (at $v_x^s = 10\ m \cdot s^{-1}$, as function of Γ^{SAM} and ρ^{PAO}; cf. table 5.7, p. 119);
- *confined interfacial film density*, ρ^{film}, defined as the ratio between the total mass of organic components (OFM & BO models) and their volume occupied between opposing α-Fe_2O_3 slabs (at $v_x^s = 10\ m \cdot s^{-1}$, as function of Γ^{SAM} and ρ^{PAO}; cf. table 5.8, p. 119);
- *schematic snapshots* describing the final configurations of the simulated nano-contacts (at $v_x^s = 10\ m \cdot s^{-1}$, as function of Γ^{SAM} and ρ^{PAO}; cf. figures 5.6 – 5.8, p. 119 and 120);
- *atomic mass-density profiles of the organic films (SAM & BO)*, $\rho(z)$ (at $v_x^s = 10\ m \cdot s^{-1}$, as function of Γ^{SAM} and ρ^{PAO}; cf. figures 5.9 – 5.11, p. 121 – 123, respectively);
- *atomic position probability profiles related to the adsorbed amine monolayers*, $p^{SAM}(z)$, for the nitrogen atoms (N), the carbons present in the intermediate methylenes ($-CH_2-$ or C) and terminal methyl groups ($-CH_3$ or CTT; at $v_x^s = 10\ m \cdot s^{-1}$, as function of Γ^{SAM} and ρ^{PAO}; cf. figures 5.12 – 5.14, p. 124 – 126, respectively).

Note that $\rho(z)$ and $p^{SAM}(z)$ structural analyses are expressed as function of the distance from the surface (in z direction), which is in turn represented by a xy plane formed by the innermost oxygen atoms of the bottom hematite substrate, where it was placed the vertical system origin (*i.e.*, $z = 0$; cf. figure 5.5, p. 114).

Tribological behavior:

Table 5.4 – Computational friction coefficient (μ^*) at v_x^s = 1 m · s^{-1}

Interface	Γ^{SAM}_{low}	Γ^{SAM}_{medium}	Γ^{SAM}_{high}
SAM/SAM ($\rho^{PAO}_{\emptyset}$)	0.13	0.21	0.43
SAM/PAO/SAM (ρ^{PAO}_{thin})	0.14	0.13	0.11
SAM/PAO/SAM (ρ^{PAO}_{thick})	0.09	0.10	0.07

Table 5.5 – Computational friction coefficient (μ^*) at v_x^s = 5 m · s^{-1}

Interface	Γ^{SAM}_{low}	Γ^{SAM}_{medium}	Γ^{SAM}_{high}
SAM/SAM ($\rho^{PAO}_{\emptyset}$)	0.08	0.21	0.45
SAM/PAO/SAM (ρ^{PAO}_{thin})	0.16	0.18	0.11
SAM/PAO/SAM (ρ^{PAO}_{thick})	0.10	0.15	0.10

Table 5.6 – Computational friction coefficient (μ^*) at v_x^s = 10 m · s^{-1}

Interface	Γ^{SAM}_{low}	Γ^{SAM}_{medium}	Γ^{SAM}_{high}
SAM/SAM ($\rho^{PAO}_{\emptyset}$)	0.09	0.26	0.47
SAM/PAO/SAM (ρ^{PAO}_{thin})	0.17	0.18	0.11
SAM/PAO/SAM (ρ^{PAO}_{thick})	0.12	0.17	0.11

Structure of the confined interfacial organic films:[7]

Table 5.7 – Separating distance between the opposing hematite substrates, h^{film} (m)

Interface	$\Gamma^{\text{SAM}}_{\text{low}}$	$\Gamma^{\text{SAM}}_{\text{medium}}$	$\Gamma^{\text{SAM}}_{\text{high}}$
SAM/SAM ($\rho^{\text{PAO}}_{\emptyset}$)	19.0 ± 0.1	27.5 ± 0.1	33.7 ± 0.4
SAM/PAO/SAM ($\rho^{\text{PAO}}_{\text{thin}}$)	26.2 ± 0.1	34.7 ± 0.1	41.3 ± 0.1
SAM/PAO/SAM ($\rho^{\text{PAO}}_{\text{thick}}$)	32.7 ± 0.1	41.3 ± 0.1	48.0 ± 0.2

Table 5.8 – Confined interfacial film density, ρ^{film} ($\text{kg}\cdot\text{m}^{-3}$)

Interface	$\Gamma^{\text{SAM}}_{\text{low}}$	$\Gamma^{\text{SAM}}_{\text{medium}}$	$\Gamma^{\text{SAM}}_{\text{high}}$
SAM/SAM ($\rho^{\text{PAO}}_{\emptyset}$)	929 ± 9	920 ± 5	986 ± 11
SAM/PAO/SAM ($\rho^{\text{PAO}}_{\text{thin}}$)	903 ± 4	912 ± 3	958 ± 30
SAM/PAO/SAM ($\rho^{\text{PAO}}_{\text{thick}}$)	918 ± 5	916 ± 3	954 ± 3

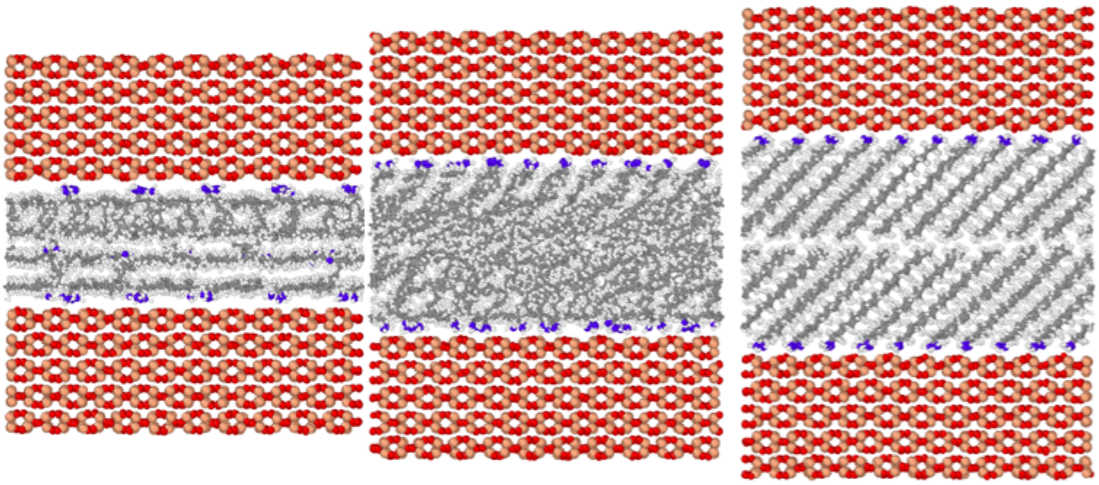

(a) $\Gamma^{\text{SAM}}_{\text{low}}$ **(b)** $\Gamma^{\text{SAM}}_{\text{medium}}$ **(c)** $\Gamma^{\text{SAM}}_{\text{high}}$

Figure 5.6 – Snapshots of *nano-contacts with SAM/SAM interface* ($\rho^{\text{PAO}}_{\emptyset}$) as function of the surface coverage. *Atomic color code: coral* - iron, *red* - oxygen, *white* - hydrogen, *gray* - carbon, *blue* - nitrogen.

[7] The *mean* and *standard deviation* of h^{film} and ρ^{film} were calculated from the atomic data obtained during the production simulations carried out at $v^{\text{s}}_{x} = 10\ \text{m}\cdot\text{s}^{-1}$.

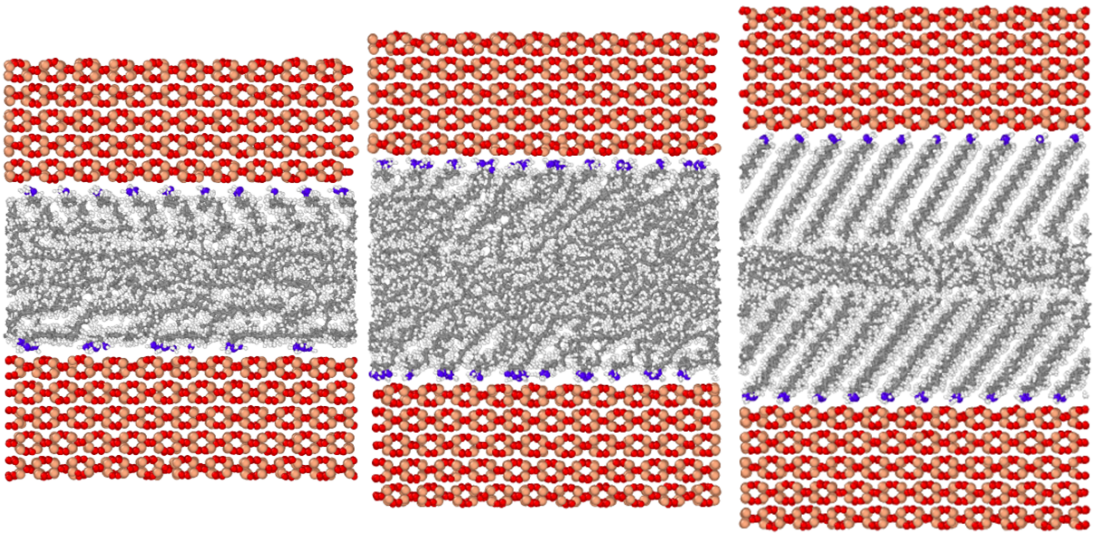

(a) $\Gamma^{\mathbf{SAM}}_{\mathbf{low}}$ **(b)** $\Gamma^{\mathbf{SAM}}_{\mathbf{medium}}$ **(c)** $\Gamma^{\mathbf{SAM}}_{\mathbf{high}}$

Figure 5.7 – Snapshots of *nano-contacts with SAM/PAO/SAM interface* ($\rho^{\mathrm{PAO}}_{\mathrm{thin}}$) as function of the surface coverage. *Atomic color code: coral* - iron, *red* - oxygen, *white* - hydrogen, *gray* - carbon, *blue* - nitrogen.

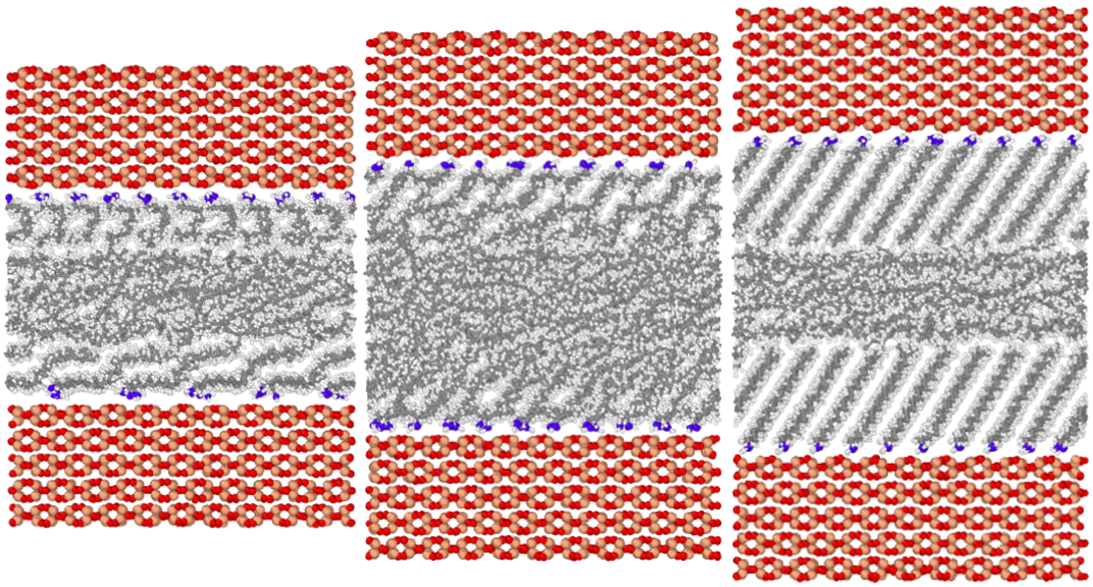

(a) $\Gamma^{\mathbf{SAM}}_{\mathbf{low}}$ **(b)** $\Gamma^{\mathbf{SAM}}_{\mathbf{medium}}$ **(c)** $\Gamma^{\mathbf{SAM}}_{\mathbf{high}}$

Figure 5.8 – Snapshots of *nano-contacts with SAM/PAO/SAM interface* ($\rho^{\mathrm{PAO}}_{\mathrm{thick}}$) as function of the surface coverage. *Atomic color code: coral* - iron, *red* - oxygen, *white* - hydrogen, *gray* - carbon, *blue* - nitrogen.

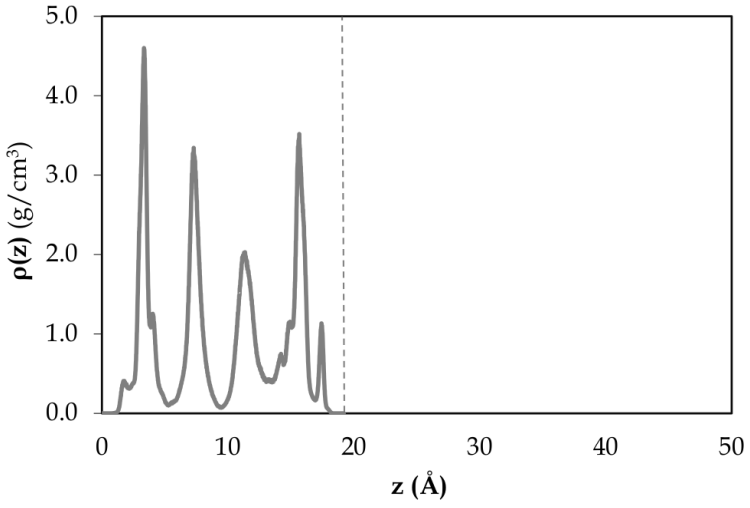

(a) $\Gamma^{\mathbf{SAM}}_{\mathbf{low}}$

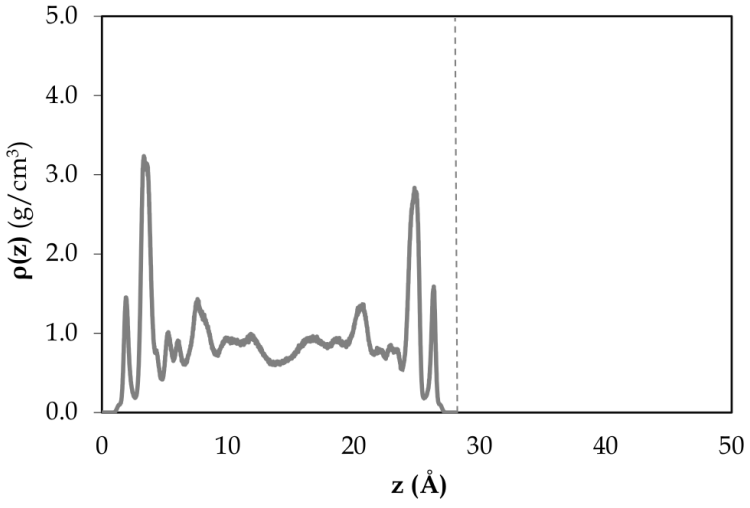

(b) $\Gamma^{\mathbf{SAM}}_{\mathbf{medium}}$

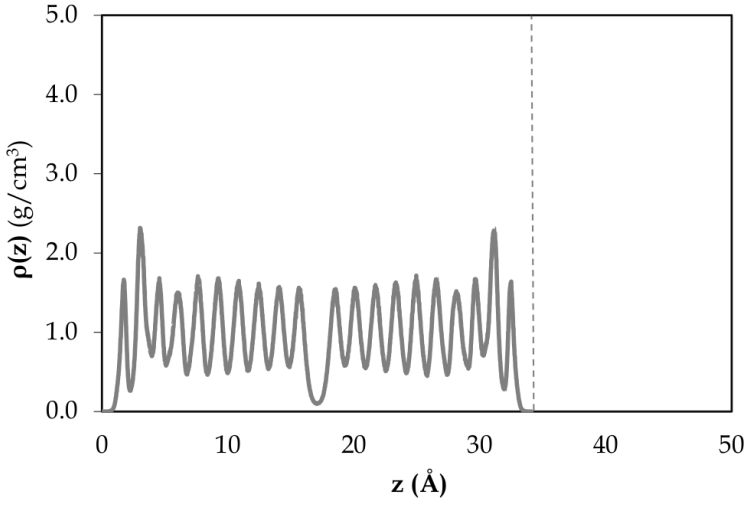

(c) $\Gamma^{\mathbf{SAM}}_{\mathbf{high}}$

Figure 5.9 – Atomic mass-density profiles, $\rho(z)$, of *nano-contacts with SAM/PAO/SAM interface* ($\rho^{\mathrm{PAO}}_{\phi}$) as function of the surface coverage. Note that the vertical dashed line approximately indicates the position of the innermost hematite surface of the top slab. *Color code: gray* - octadecylamine.

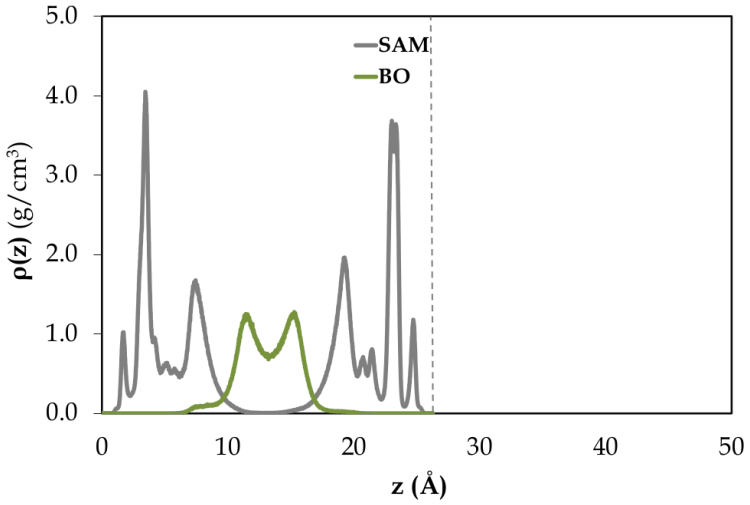

(a) $\Gamma^{\mathbf{SAM}}_{\mathbf{low}}$

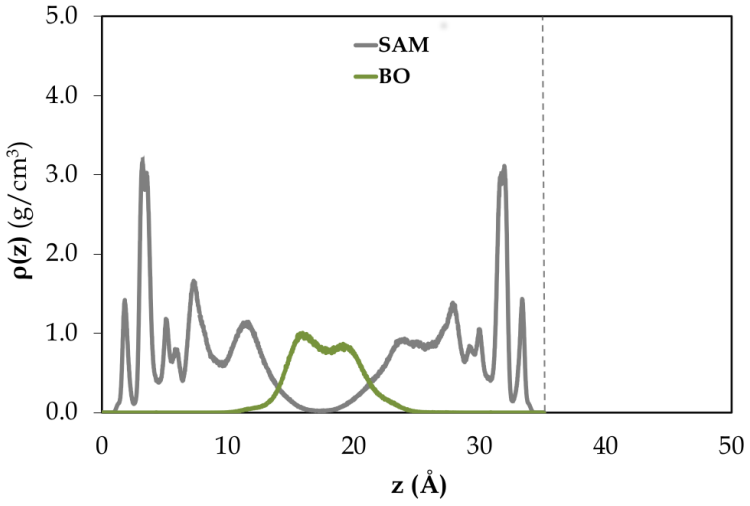

(b) $\Gamma^{\mathbf{SAM}}_{\mathbf{medium}}$

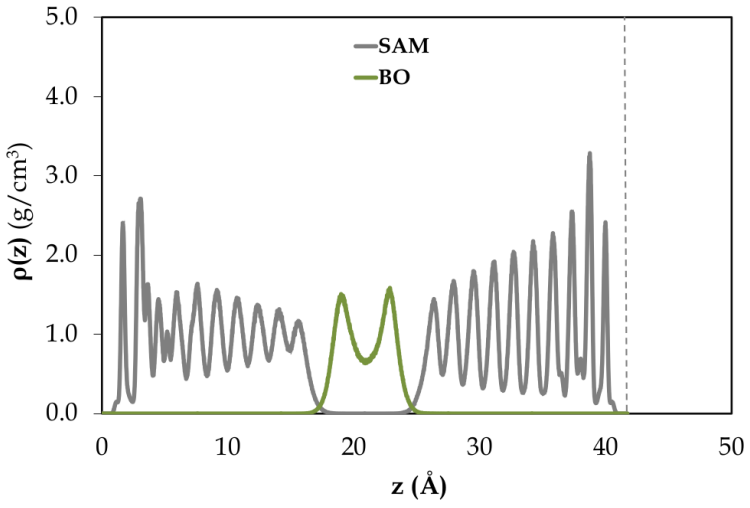

(c) $\Gamma^{\mathbf{SAM}}_{\mathbf{high}}$

Figure 5.10 – Atomic mass-density profiles, $\rho(z)$, of *nano-contacts with SAM/PAO/SAM interface* ($\rho^{\mathrm{PAO}}_{\mathrm{thin}}$) as function of the surface coverage. Note that the vertical dashed line approximately indicates the position of the innermost hematite surface of the top slab. *Color code: gray* - octadecylamine; *moss green* - PAO.

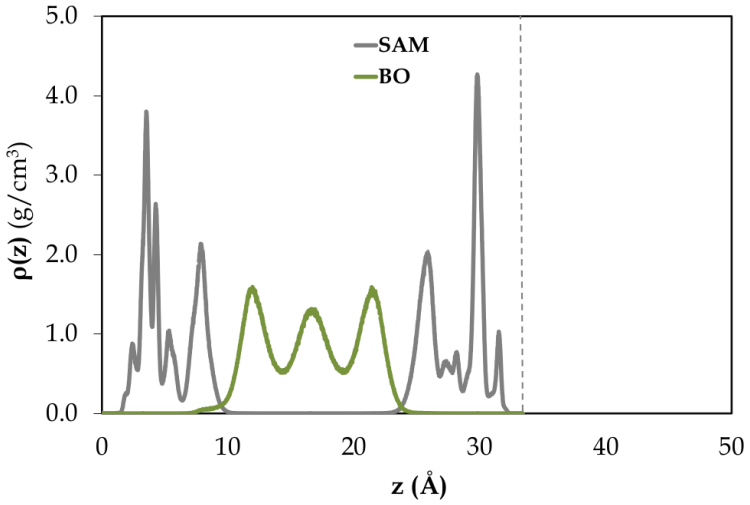

(a) $\Gamma^{\mathbf{SAM}}_{\mathbf{low}}$

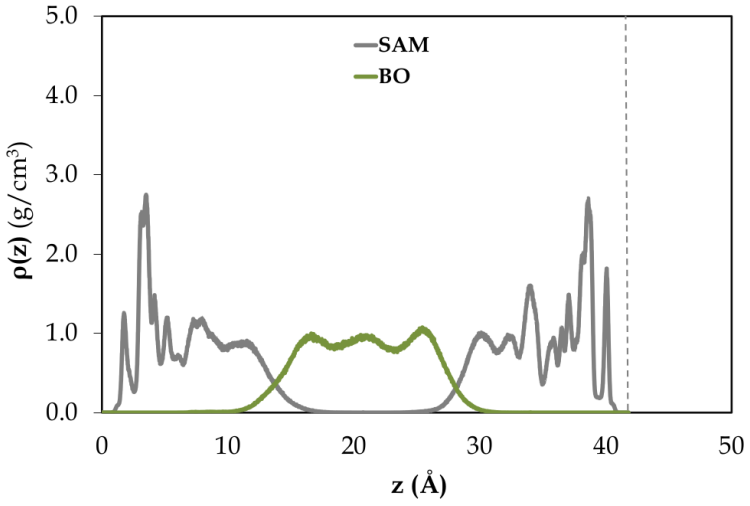

(b) $\Gamma^{\mathbf{SAM}}_{\mathbf{medium}}$

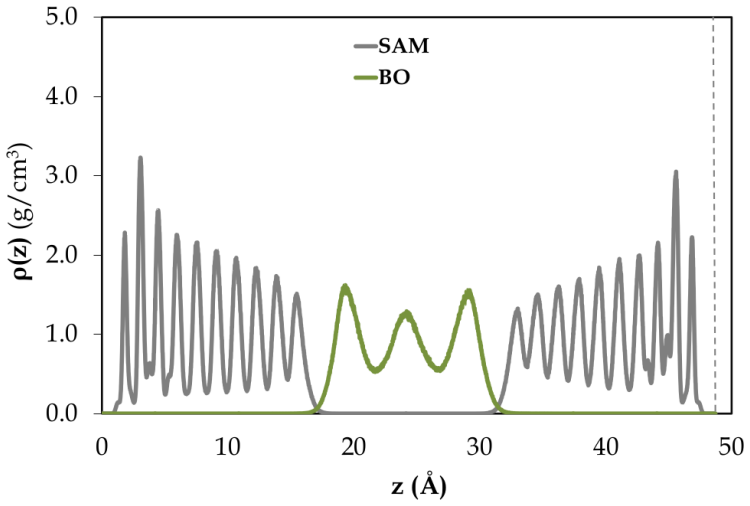

(c) $\Gamma^{\mathbf{SAM}}_{\mathbf{high}}$

Figure 5.11 – Atomic mass-density profiles, $\rho(z)$, of *nano-contacts with SAM/PAO/SAM interface* ($\rho^{\mathrm{PAO}}_{\mathrm{thick}}$) as function of the surface coverage. Note that the vertical dashed line approximately indicates the position of the innermost hematite surface of the top slab. *Color code: gray* - octadecylamine; *moss green* - PAO.

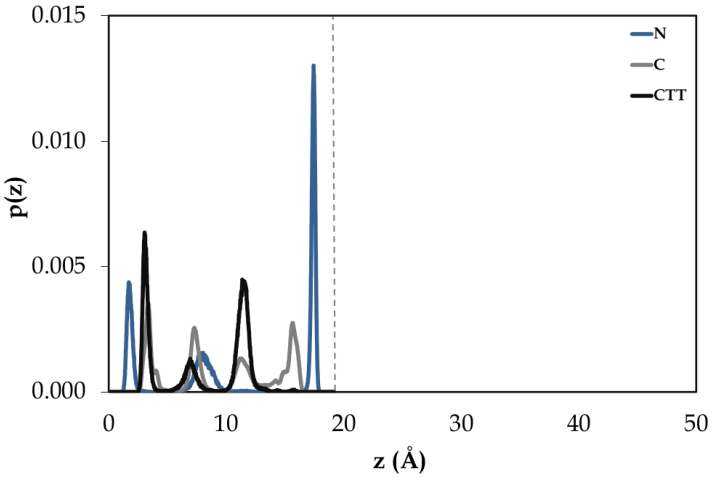

(a) $\Gamma^{\mathbf{SAM}}_{\mathbf{low}}$

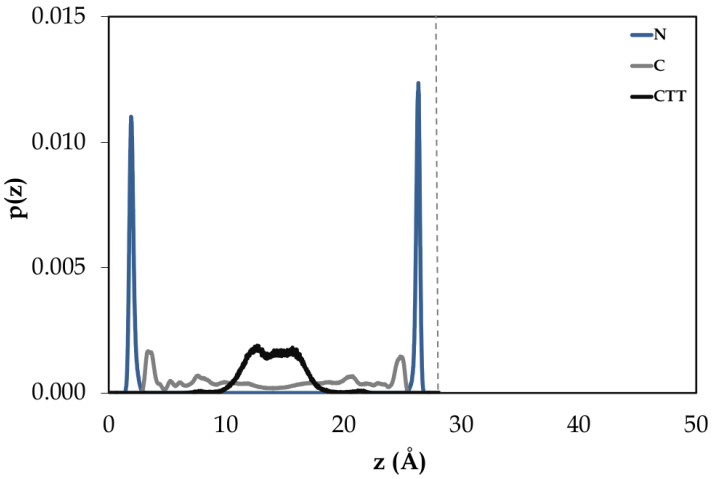

(b) $\Gamma^{\mathbf{SAM}}_{\mathbf{medium}}$

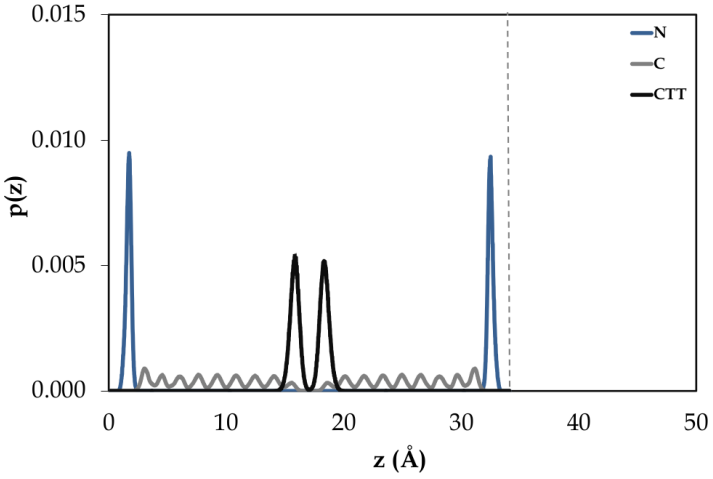

(c) $\Gamma^{\mathbf{SAM}}_{\mathbf{high}}$

Figure 5.12 – Atomic position probability profiles in z, $p^{\mathrm{SAM}}(z)$, of amine molecules in *nano-contacts with SAM/SAM interface* ($\rho^{\mathrm{PAO}}_{\emptyset}$), as function of the surface coverage. Note that the vertical dashed line approximately indicates the position of the innermost hematite surface of the top slab. *Color code: blue* - nitrogens (N); *gray* - carbon atoms in intermediate methylenes (C); *black* - terminal tail groups (CTT).

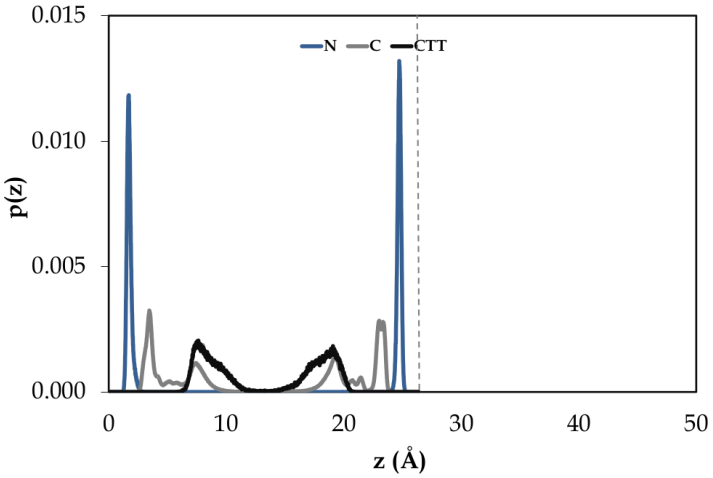

(a) $\Gamma^{\mathbf{SAM}}_{\mathbf{low}}$

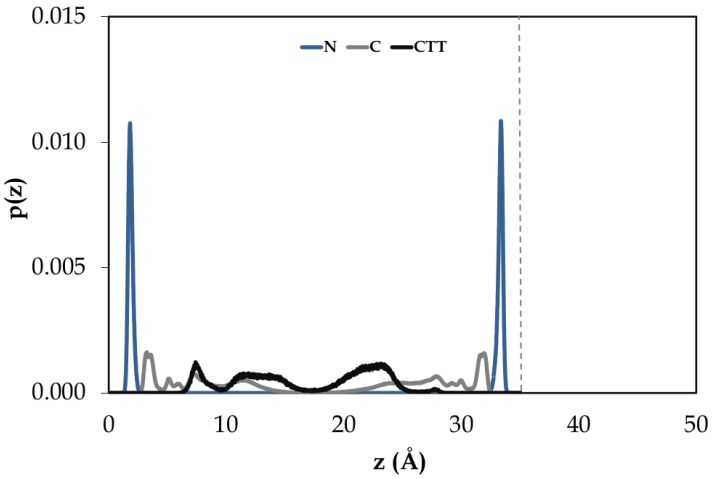

(b) $\Gamma^{\mathbf{SAM}}_{\mathbf{medium}}$

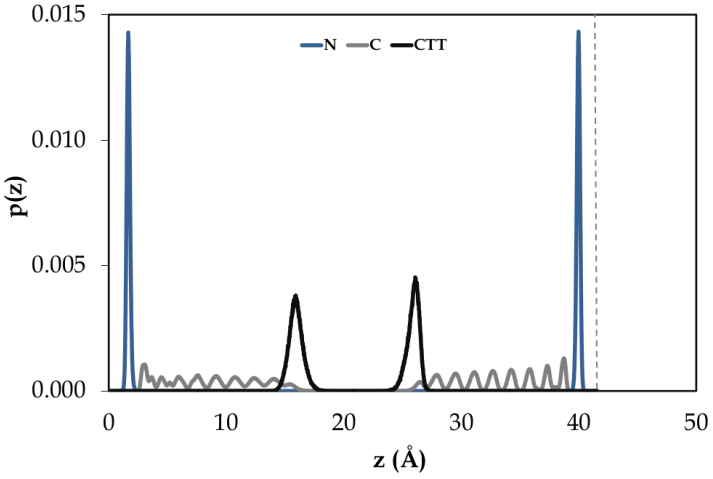

(c) $\Gamma^{\mathbf{SAM}}_{\mathbf{high}}$

Figure 5.13 – Atomic position probability profiles in z, $p^{\mathrm{SAM}}(z)$, of amine molecules in *nano-contacts with SAM/PAO/SAM interface* ($\rho^{\mathrm{PAO}}_{\mathrm{thin}}$), as function of the surface coverage. Note that the vertical dashed line approximately indicates the position of the innermost hematite surface of the top slab. *Color code: blue* - nitrogens (N); *gray* - carbon atoms in intermediate methylenes (C); *black* - terminal tail groups (CTT).

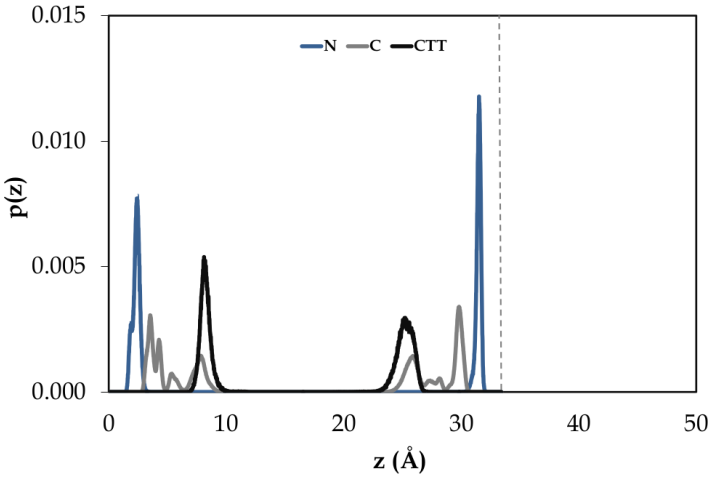

(a) $\Gamma^{\mathbf{SAM}}_{\mathbf{low}}$

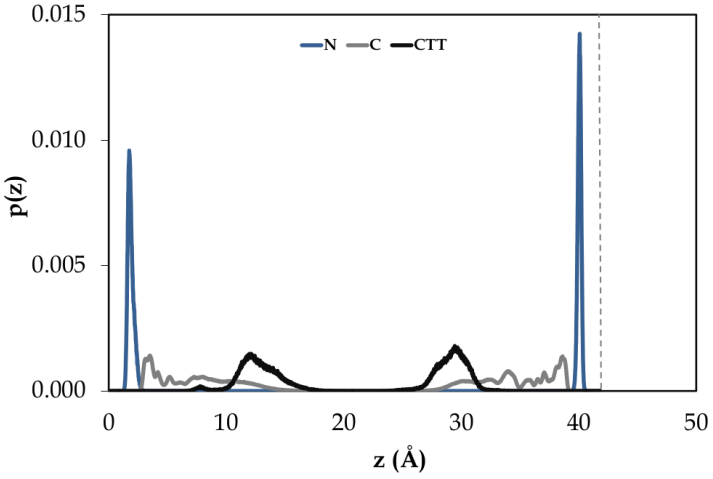

(b) $\Gamma^{\mathbf{SAM}}_{\mathbf{medium}}$

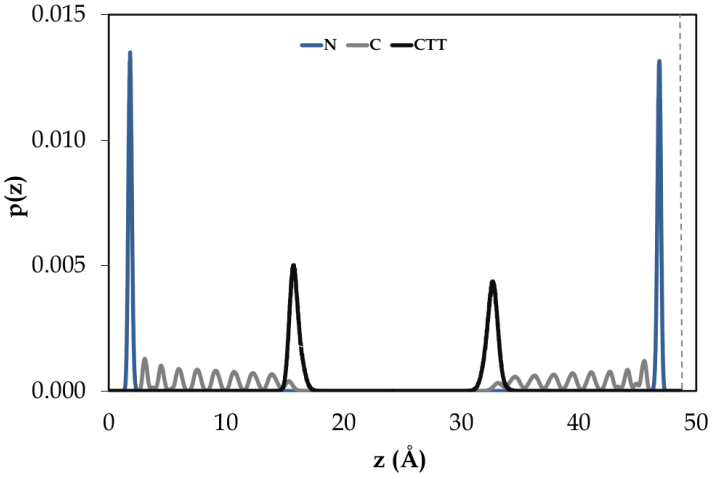

(c) $\Gamma^{\mathbf{SAM}}_{\mathbf{high}}$

Figure 5.14 – Atomic position probability profiles in z, $p^{\mathrm{SAM}}(z)$, of amine molecules in *nano-contacts with SAM/PAO/SAM interface* ($\rho^{\mathrm{PAO}}_{\mathrm{thick}}$), as function of the surface coverage. Note that the vertical dashed line approximately indicates the position of the innermost hematite surface of the top slab. *Color code: blue* - nitrogens (N); *gray* - carbon atoms in intermediate methylenes (C); *black* - terminal tail groups (CTT).

5.4 Discussion

Before beginning a detailed analysis on the influence of the investigated parameters (Γ^{SAM}, ρ^{PAO} and v_x^{s}) over the frictional behavior of our boundary lubricated model systems, it is important to remember and stress some intrinsic aspects associated with our *friction study*:

- the currently simulated nano-contacts have better be interpreted as *computational study cases* — whose layouts were tailored following idealized structures and conditions —, rather than an attempt to genuinely reproduce macroscopic tribological systems;
- no direct comparison, nor any data extrapolation has been made in the current work, in order to link our nanoscale systems with complex phenomena occurring in a real internal combustion engine;
- the trends and the conclusions drawn from the observed results are not chiefly intended either to input or to validate any particular theoretical or phenomenological model suggested in literature;
- ultimately, despite all technical care taken into account to establish a reliable confined shearing simulation with the available computer resources, the obtained results are still dependent on the employed MD interatomic potentials, on the assumptions made to design the numerical procedures, as well as on the statistically limited sample of configurational models used to calculate each μ^* value.

With this perspective in mind, the previously outlined computational results, and mainly those related to μ^* (cf. § 5.3, p. 117), are further discussed according to the following scheme:

- *nano-contacts with SAM/SAM interface* ($\rho_{\emptyset}^{\mathrm{PAO}}$; cf. § 5.4.1, p. 128);
- *nano-contacts with SAM/PAO/SAM interface* ($\rho_{\mathrm{thin}}^{\mathrm{PAO}}$ & $\rho_{\mathrm{thick}}^{\mathrm{PAO}}$) cf. § 5.4.2, p. 134);

where the effects of the three investigated parameters were eventually discerned, namely:

- octadecylamine-SAM surface coverage, Γ^{SAM};
- presence of an intermediate PAO layer, ρ^{PAO};
- sliding velocity, v_x^{s}.

Additionally, it must be highlighted that this discussion is mainly based on the results obtained from the NEMD simulations run at $v_x^{\mathrm{s}} = 10\ \mathrm{m \cdot s^{-1}}$, which are those exhibiting the largest *total sliding displacement* ($d_x^{\mathrm{s}} = 60\ \mathrm{nm}$).

5.4.1 Contacts with SAM/SAM interface ($\rho_{\emptyset}^{\mathbf{PAO}}$)

The confined shearing simulations performed with structural geometries consisting only in hematite substrates covered by octadecylamine-SAM, and without any lubricating PAO-layer, are particularly discussed in this subsection. Their results are referred to as *"SAM/SAM ($\rho_{\emptyset}^{PAO}$)"* in tables 5.4–5.8 (cf. p. 118–119, respectively), and they are also described in figures 5.6, 5.9 and 5.12 (cf. p. 119, 121 and 124, respectively).

First of all, examining attentively the final snapshots for the nine simulated structures (cf. figures 5.6–5.8, p. 119–120), it can be observed that the first system *"SAM/SAM ($\rho_{\emptyset}^{PAO}$) at Γ_{low}^{SAM}"* is the only one presenting desorbed amine molecules within its nano-contact model (cf. figure 5.6a, p. 119). Nevertheless, it must be specified that this irregular configuration was obtained from the equilibration phase, and it is not a result of the shear and pressure conditions that were concurrently applied throughout the production simulation. In fact, during *"step 1"* of the equilibration stage — when the amine molecules were freely relaxed within an unit cell in order to obtain a stable SAM configuration (cf. § 5.2.1, p.111) —, one molecule placed nearly to the bottom slab did not succeed to anchor its amino polar head at an adsorption site (*i.e.*, on an iron surface atom). By consequence, only a single amine molecule has effectively adsorbed on the bottom surface — with its C_{18} alkyl tail lying flat on the iron oxide substrate —, whereas the other molecule has lain down over the mentioned adsorbed OFM molecule. Moreover, as shown in figure 5.6a, two clear horizontal amine layers can be discerned over the bottom Fe_2O_3 slab. For the opposing top surface, both octadecylamines have conversely attained adsorption during the preliminary simulations. Although this nano-contact does not exhibit both solid substrates covered with equal OFM surface coverages (*i.e.*, $\Gamma_{\text{low}}^{\text{SAM,bottow-slab}} = 1/2 \cdot \Gamma_{\text{low}}^{\text{SAM,top-slab}}$), it was still used in a production simulation, and it was considered as a *special study case*, where the adsorbed SAM with low densities are lubricated by a thin intermediary layer that contains the same chemical compound that the one composing the surrounding OFM films.

In addition, it is interesting to note that, aside from the bottom subset of the nano-contact with SAM/SAM interface ($\rho_{\emptyset}^{\text{PAO}}$) at $\Gamma_{\text{low}}^{\text{SAM}}$, all other amine molecules were kept adsorbed during both equilibration and confined shearing simulations, and that despite the applied severe conditions in the later cases (*e.g.*, relatively high sliding velocity and contact load). Besides, no *boundary slip* — also termed in literature as *wall slip* — was observed during any production simulation. Therefore, the DFT-derived interaction potential obtained in this work has

proved to be efficient in ensuring OFM adsorption on the employed substrate model ($U^{\text{interface}}$, cf § 4.1.3, p. 72). Incidentally, that fact is evidenced by the intense, sharp peaks displayed by the nitrogen atoms in the position probability profiles (cf. *blue peaks* of $p_{\text{N}}^{\text{SAM}}(z)$, as shown in figures 5.12–5.14, p. 124–126).

With respect to the influence of Γ^{SAM} on SAM microstructures, one can observe that the distance between iron oxide slabs increases with increasing OFM surface coverage (cf. table 5.7, p. 119). That corroborates the OFM ability to protect rubbing surfaces subjected to BL conditions, from direct contact and against the ensuing wear effects. Besides, in order to better notice the evolution of SAM structural organization, it is worth carefully comparing $\rho^{\text{SAM}}(z)$ profiles in figures 5.9a–5.9c (cf. p. 121).

Another similar rising trend with Γ^{SAM} can be identified for the *computational friction coefficients* (cf. tables 5.4–5.6, p. 118). Indeed, figure 5.15 illustrates how μ^* evolves as a function of Γ^{SAM}, particularly for the simulations conducted at $v_x^{\text{s}} = 10$ m/s.

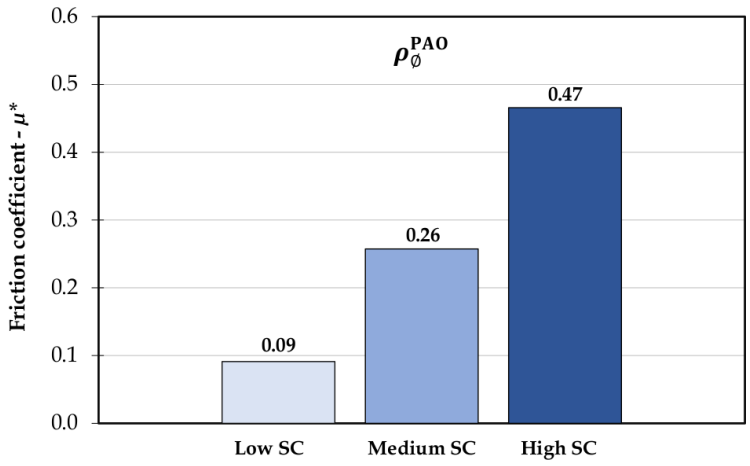

Figure 5.15 – Computational friction coefficient (μ^*) for the nano-contact with SAM/SAM interface ($\rho_{\emptyset}^{\text{PAO}}$), as a function of Γ^{SAM} (SC), at $v_x^{\text{s}} = 10$ m/s.

The above histogram clearly sheds light on an important information, pointed out by our NEMD simulations, that *a relatively higher molecular ordering/packing of the adsorbed SAM, which is brought about by a larger octadecylamine surface coverage, can induce a negative impact on their friction-reducing performance*:

$$\mu^*_{\Gamma^{\text{SAM}}_{\text{low}}} < \mu^*_{\Gamma^{\text{SAM}}_{\text{medium}}} < \mu^*_{\Gamma^{\text{SAM}}_{\text{high}}}, \qquad \text{where:} \quad \Gamma^{\text{SAM}}_{\text{low}} < \Gamma^{\text{SAM}}_{\text{medium}} < \Gamma^{\text{SAM}}_{\text{high}}$$

As a matter of fact, at $\Gamma^{\mathrm{SAM}}_{\mathrm{low}}$, a *well-defined slip plan* can be perceived between the top and the bottom subsets composing this specific nano-contact (cf. figure 5.16, p. 130), and notably at 9.8 Å (along z direction), in the concerned $\rho^{\mathrm{SAM}}(z)$ (cf. figure 5.9a, p. 121).

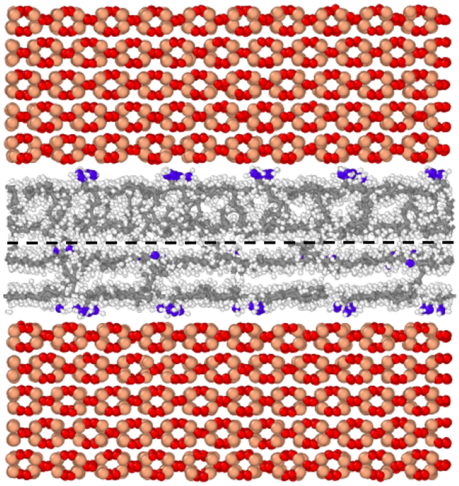

Figure 5.16 – Snapshot of the nano-contact with SAM/SAM interface ($\rho^{\mathrm{PAO}}_{\emptyset}$) at $\Gamma^{\mathrm{SAM}}_{\mathrm{low}}$, showing the resulting *slippage plan* — highlighted by a *black dashed line* — arising during the simulated sliding process.

In spite of the fact that a relatively small amount of primary amines is effectively adsorbed on the moving hematite slabs, their molecules assemble in a manner that yields relatively *closed-packed regions*, which easily slide past each other. Apropos of that, it must be noted that this specific system possesses a slightly higher average value of ρ^{film}, in comparison with the one exhibited by the similar model at $\Gamma^{\mathrm{SAM}}_{\mathrm{medium}}$ (cf. table 5.8, p. 119). This fact indicates that confined amine-SAM at $\Gamma^{\mathrm{SAM}}_{\mathrm{low}}$ are more tightly, densely arranged that those at $\Gamma^{\mathrm{SAM}}_{\mathrm{medium}}$, since $\Gamma^{\mathrm{SAM}}_{\mathrm{low}} < \Gamma^{\mathrm{SAM}}_{\mathrm{medium}}$ and $h^{\mathrm{film}}_{\Gamma^{\mathrm{SAM}}_{\mathrm{low}}} < h^{\mathrm{film}}_{\Gamma^{\mathrm{SAM}}_{\mathrm{medium}}}$ (at $\rho^{\mathrm{PAO}}_{\emptyset}$). This structural disparity is additionally supported by the differences in number and height of the peaks shown in their atomic mass density profiles (cf. $\rho^{\mathrm{SAM}}(z)$ in figures 5.6a–5.6b, p. 119).

Furthermore, that *slippage interface* — that can also be clearly identified from the well-separate peaks presented by the terminal methyl groups in figure 5.12a (cf. $p^{\mathrm{SAM}}_{\mathrm{CTT}}$ (z) indicated by a *black curve*, p. 124) — contributes to minimizing the sliding resistance of the moving subsets, to reducing the emerging frictional forces and eventually, to lowering its μ^{*}. Indeed, the nano-contact with SAM/SAM interface at $\Gamma^{\mathrm{SAM}}_{\mathrm{low}}$ has then yielded the best lubricating performance for all systems described through our NEMD simulations at $v^{\mathrm{s}}_{x} = 10\ \mathrm{m}\cdot\mathrm{s}^{-1}$: $\mu^{*}(\Gamma^{\mathrm{SAM}}_{\mathrm{low}}) = 0.09$ (cf. table 5.6, p. 118).

At $\Gamma^{\mathrm{SAM}}_{\mathrm{medium}}$, the confined SAM structure differs remarkably from that at $\Gamma^{\mathrm{SAM}}_{\mathrm{low}}$, and even from the one observed at $\Gamma^{\mathrm{SAM}}_{\mathrm{high}}$ (cf. figure 5.6, p. 119). In this case, both top and bottom octadecylamine monolayers are in an *intimate interfacial interaction*, thereby showing a substantial *molecular entanglement*. Thus, no apparent slip interface can be found out either in figure 5.6b or 5.9b (cf. p. 119 and 121, respectively), since a considerable *interdigitated region* is present in the center of the nano-contact model, involving the opposing OFM hydrocarbon tails. That can better be observed from the atomic position probability profile related to CH_3 end groups (CTT), as shown in the figure below (cf. $p^{\mathrm{SAM}}_{\mathrm{CTT}}(z)$ depicted by the *black curve* in figure 5.17, or in figure 5.12b, p. 124).

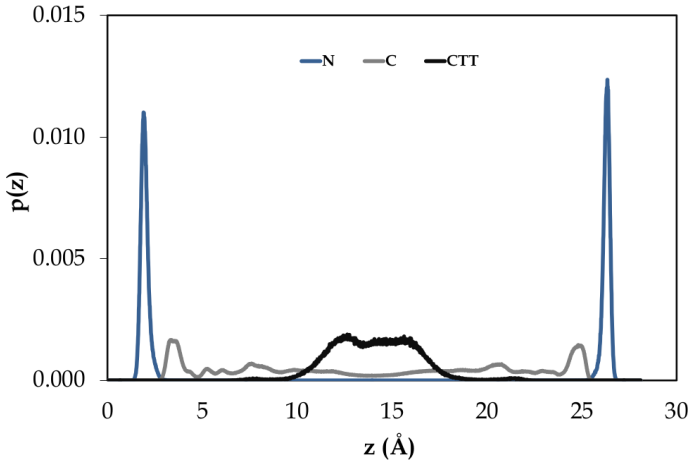

Figure 5.17 – Atomic position probability profiles in z, $p^{\mathrm{SAM}}(z)$, of amine molecules in nano-contacts with $\rho^{\mathrm{PAO}}_{\emptyset}$ and $\Gamma^{\mathrm{SAM}}_{\mathrm{medium}}$. *Color code: blue* - nitrogens (N); *gray* - carbon atoms in intermediate methylenes (C); *black* - terminal tail groups (CTT).

It should be added that, owing to the relatively high sliding velocities intrinsically imposed by the classical MD technique, the represented amine molecules do not have enough time to freely rearrange and then, to adjust their molecular structures in order to accomodate friction through a transient relaxation process and/or via dilatancy effects.[237] In fact, dynamic phenomena like friction, and even adhesion, are dependent on the *molecular relaxation time*, which defines the time needed for the interacting molecules — that are especially subjected to confinement and/or sliding conditions — to disentangle and then rearrange in a conformational fashion that produces low-shear-strength (interfacial) structures.[35, 237, 384–387]

As a result, this *molecular chain interdigitation* ends up enhancing the lateral forces that appear within the system, and consequently, it increases its computational friction coefficient: $\mu^{*}(\Gamma^{\mathrm{SAM}}_{\mathrm{medium}};\ v^{\mathrm{s}}_{x} = 10\,\mathrm{m}\cdot\mathrm{s}^{-1}) = 0.26$.

Finally, regarding the remaining contact with a SAM/SAM interface at $\Gamma^{\mathrm{SAM}}_{\mathrm{high}}$, high frictional forces do prevail in this system, such that: $\mu^{*}(v^{\mathrm{s}}_{x} = 10\ \mathrm{m\cdot s^{-1}}) = 0.47$, in spite of the fact that a visible and precise slip plane can be discerned between its bottom and top subsets, and with no substantial SAM interdigitation (cf. sharp, separate *black peaks* of $p^{\mathrm{SAM}}_{\mathrm{CTT}}(z)$, as shown in figure 5.12c, p. 124).

In fact, as previously noted in chapter 4 (cf. § 4.2.2, p. 92), when the surface coverage ratio related to an α-Fe_2O_3 (0 1 $\bar{1}$ 2) slab reaches 50% of the total number of available adsorption sites (*i.e.*, $\Gamma^{\mathrm{SAM}}_{\mathrm{high}} = 3.6\ \mathrm{nm^{-2}}$), *solid-like monolayers* are formed by the adsorbed octadecylamines (cf. $\rho^{\mathrm{SAM}}(z)$ in figure 5.9c, p. 121). Given that, and according to the results obtained during its confined shearing simulation, these relatively rigid, condensed surfactant films do slide past each other, following a *saw-tooth pattern* that is characteristic of a *stick-slip friction behavior* (cf. figure 5.18).[388]

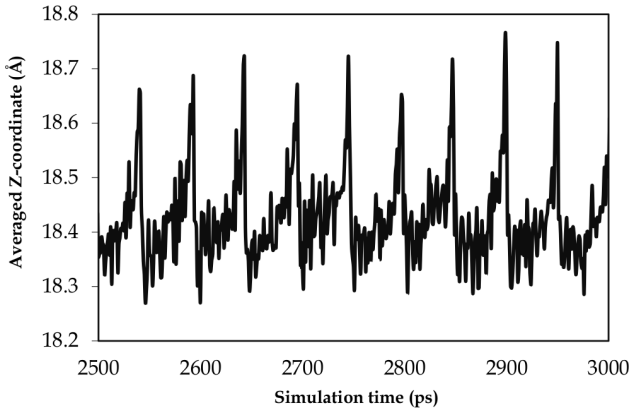

Figure 5.18 – Time evolution of z coordinate related to C atom of the terminal methyl groups (CTT), which are present in amine molecules adsorbed on the top hematite substrate, and composing the system with SAM/SAM interface ($\rho^{\mathrm{PAO}}_{\emptyset}$) and $\Gamma^{\mathrm{SAM}}_{\mathrm{high}}$. This figure illustrates a short time interval of the production phase conducted at $v^{\mathrm{s}}_{x} = 10\ \mathrm{m\cdot s^{-1}}$ (*simulation time:* between 2.5 and 3.0 ns).

Actually, stick-slip occurs when, instead of sliding over each other smoothly, the solid surfaces alternatively stick together and then slip past each other, in a *periodic* and *oscillatory motion*.[303] This phenomenon has been widely observed and described in the literature, from both experimental and computational investigative approaches.[301–303,305,313,351,364,374,388–400]

In our particular case, this stick-slip friction response has indeed been found, despite the presence of amine-based SAM with relatively high coverage at the interface between the hematite surfaces. That is likely due to the important commensurability of the concerned SAM/SAM interface, whose almost crystalline microstructure turns out to behave like an *elastic solid*. In

fact, from a computational point of view, a substantial energy is required to exceed the *massive movement activation barrier*, and to eventually overcome the *stick interaction phase*, thereby promoting the atomically-collective slip motion of both top and bottom subsets, which exhibit a highly organized interface (cf. figure 5.5, p. 114). That is why the simulated lateral forces, and consequently the arising friction forces, are so (relatively) high in this analyzed nano-contact model. However, it is assumed that the calculated computation friction coefficient, $\mu^*(\Gamma^{\mathrm{SAM}}_{\mathrm{high}}\ ;\ v^{\mathrm{s}}_x = 10\ \mathrm{m}\cdot\mathrm{s}^{-1})$, is still lower than the one associated with a hypothetical contact comprising only bare hematite surfaces. Nevertheless, this later $\mu^*(\Gamma^{\mathrm{SAM}}_{\emptyset};\rho^{\mathrm{PAO}}_{\emptyset})$ was not determined in our simulation study.

In addition, it is interesting to point out that previous NEMD simulations of surfactant monolayers in intimate contact have also shown high friction and a stick-slip behavior, owing to highly commensurable interfaces.[301,351] However, it has been found that the presence of a *thin, separating layer of a BO lubricating model* (*e.g.*, hexadecane) is capable of maintaining low friction.[57,301] For this reason, models with an intermediate PAO layer, which is our BO model in the current study, were included in our investigation. As already mentioned, two different densities of PAO film was probed: $\rho^{\mathrm{PAO}}_{\mathrm{thin}}$ and $\rho^{\mathrm{PAO}}_{\mathrm{thick}}$. Besides, their results are interpreted in the next subsection (cf. § 5.4.2, p. 134).

To conclude this part of the discussion, which was focused on results related to nano-contacts with SAM/SAM interfaces, it is worthwhile to note that no particular proportional relationship seems to exist between μ^* and the simulated sliding velocities for the systems with $\rho^{\mathrm{PAO}}_{\emptyset}$ (cf. figure 5.19 showing μ^* as a function of Γ^{SAM} at various v^{s}_x). In fact, a similar evolution of the computation friction coefficient was observed, regardless of the employed v^{s}_x value.

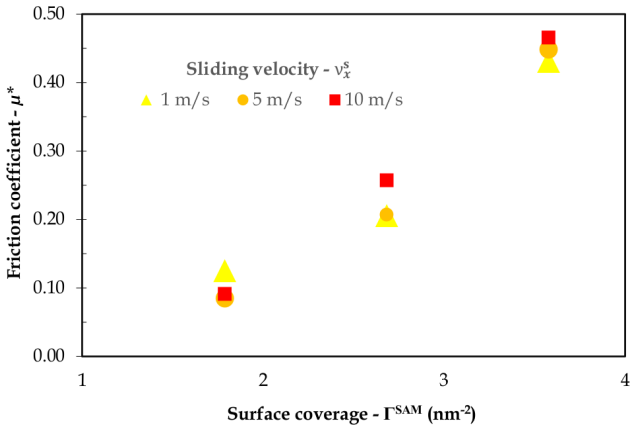

Figure 5.19 – Computational friction coefficient (μ^*) for the nano-contact with SAM/SAM interface ($\rho^{\mathrm{PAO}}_{\emptyset}$), as a function of Γ^{SAM} and v^{s}_x.

5.4.2 Contacts with SAM/PAO/SAM interface ($\rho^{\mathbf{PAO}}_{\mathbf{thin}}$ & $\rho^{\mathbf{PAO}}_{\mathbf{thick}}$)

After analyzing the influence on microstructure and lubricating properties of OFM coverage, in organic films composed exclusively of C_{18} primary amines, the following discussion brings light to the impact on tribological behavior of an additional BO-layer. Besides, it must be noticed that these PAO films were confined between pre-formed, model amine monolayers. By consequence, this initial configuration implies that homogeneous and uniform amine-based SAM were obtained, where relatively little interpenetration between the different organic molecules was effectively allowed to be achieved. At least, it was not possible to have any disrupted and heterogeneous octadecylamine monolayer, with molecular vacancies where PAO molecules would be able to directly interact with the simulated substrates, even at $\Gamma^{\mathrm{SAM}}_{\mathrm{low}}$.

Therefore, the results for those particular systems are referred to as *"SAM/PAO/SAM (ρ^{PAO}_{thin})"* and *"SAM/PAO/SAM (ρ^{PAO}_{thick})"* in tables 5.4–5.8 (cf. p. 118–119, respectively), as well as in figures 5.7, 5.10 and 5.13 for the thinner BO film (cf. p. 120, 122 and 125, respectively), and in figures 5.8, 5.11 and 5.14 for the thicker one (cf. p. 120, 123 and 126, respectively).

5.4.2.1 Effect of an intermediate PAO-layer

Based on an analysis of the representative snapshots shown in figures 5.7 and 5.8 (cf. p. 120), one can effortlessly conclude that the thickness of the confined organic films increases with increasing SAM coverage and PAO-layer density. The results of h^{film} and ρ^{film}, listed in tables 5.7 and 5.8 (cf. p. 119), clearly support that expected trend, which is profitable for the rubbed surfaces, since they are kept separated, thereby preventing possible detrimental wear effects.

It can also be observed that the intermediate PAO molecules organize themselves, between amine-SAM, according to a compacted, horizontally-oriented structure. This is additionally demonstrated by the atomic-density profiles obtained for the PAO layers, where distinguishable, regular peaks can be discerned in $\rho^{\mathrm{BO}}(z)$ (cf. *moss green curves*, in figures 5.10 and 5.11, p. 122 and 123, respectively).

Most importantly, it must be highlighted that this central lamellar film, at either $\rho^{\mathrm{PAO}}_{\mathrm{thin}}$ or $\rho^{\mathrm{PAO}}_{\mathrm{thick}}$, contribute to forming *well-defined slippage planes* between amine-monolayers, thus separating both top and bottom subsets. Besides, the shear strengths of SAM/PAO/SAM interfaces with $\Gamma^{\mathrm{SAM}}_{\mathrm{medium}}$ and $\Gamma^{\mathrm{SAM}}_{\mathrm{high}}$ are relatively lower than the ones exhibited by their equivalent SAM/SAM nano-contacts (cf. μ^* results in figures 5.20 and 5.21, p. 135, or in table 5.6, p. 118).

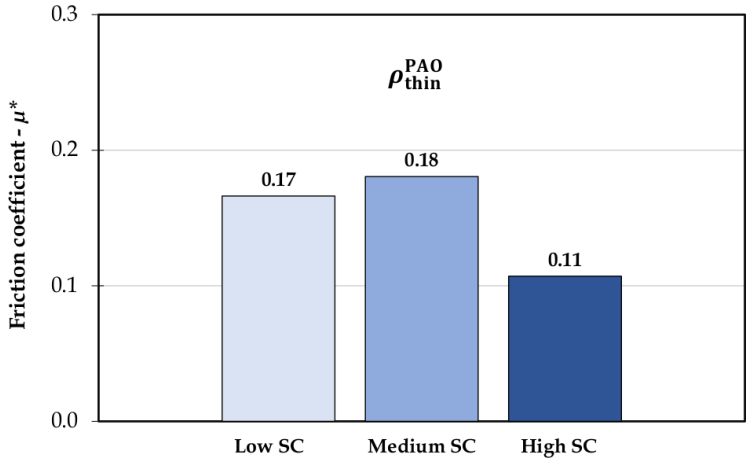

Figure 5.20 – Computation friction coefficient (μ^*) for the nano-contact with SAM/PAO/SAM interface and ρ^{PAO}_{thin}, as a function of Γ^{SAM} (SC), at $v^s_x = 10$ m/s.

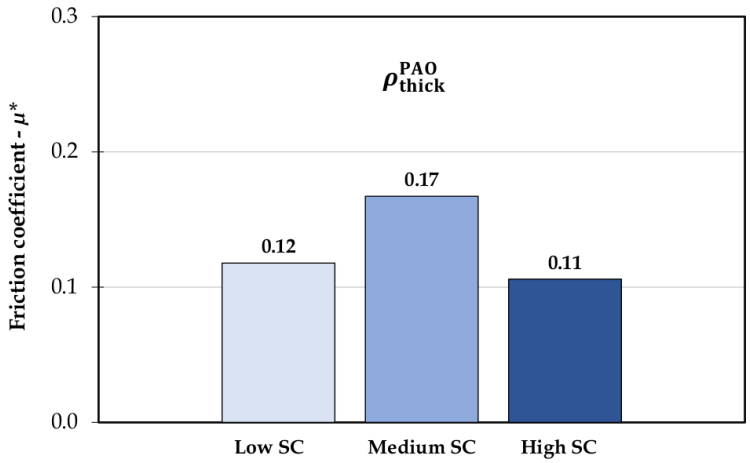

Figure 5.21 – Computational friction coefficient (μ^*) for the nano-contact with SAM/PAO/SAM interface and ρ^{PAO}_{thick}, as a function of Γ^{SAM} (SC), at $v^s_x = 10$ m/s.

As it has already been described in precedent published works,[57,301] the benefit of the presence of an intermediate BO film in the middle of a rubbing contact, was found in the current simulations to be especially greater for the systems composed of commensurate films, such as those with higher surface coverage. For example, a decrease in μ^*, by approximately 77 %, has been observed through the simple addition of either a thin or a thick PAO-layer between the Γ^{SAM}_{high} monolayers: $\mu^*(\rho^{PAO}_{\emptyset}) = 0.47 \longrightarrow \mu^*(\rho^{PAO}_{thin}/\rho^{PAO}_{thick}) = 0.11$, at $v^s_x = 10$ m/s. Actually, in these later cases (*i.e.*, nano-contact with a SAM/PAO/SAM interface at Γ^{SAM}_{high}), the BO molecules particularly work as a perturbing factor of the intermolecular interactions between highly ordered SAM, alternatively providing a relatively smoother, "sliding-friendly" interface, whose final computation friction coefficient is comparatively reduced.

However, an important remark have to be made concerning the employed BO in our NEMD simulations. In fact, the used *PAO 4 model* has a branched molecular architecture, as illustrated in figure 5.22. Although this lubricant oil might provide an optimal kinetic viscosity at HL regime, its molecular structure is more prone to intimately entangle with other BO species and/or OFM additives confined at a BL contact, in comparison with a linear hydrocarbon, and maybe even a surfactant molecule containing a straight aliphatic tail like the octadecylamine (cf. figures 5.6a and 5.7a, p. 119 and 120, respectively).

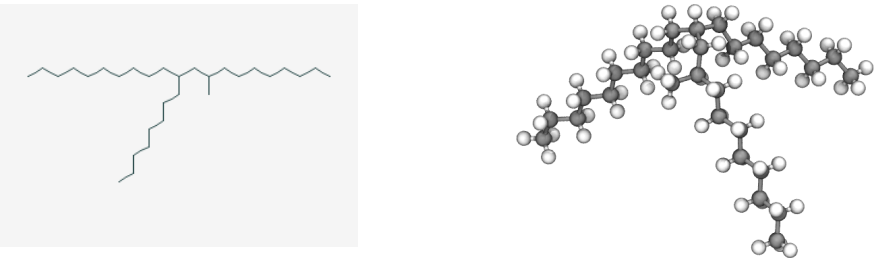

(a) **(b)**

Figure 5.22 – Schematics of PAO model structure ($C_{30}H_{62}$).

Indeed, the PAO-layers are likely to produce well-defined slip planes between OFM/SAM interface, but it cannot eliminate all the sliding resistance that appears within the lubricated contact due to their lateral molecular branches. That is why our first investigated system — the nano-contact with a SAM/SAM interface at Γ^{SAM}_{low} — yields a lower μ^* than those with an equivalent SAM coverage but containing lubricating PAO molecules (ρ^{PAO}_{thin} & ρ^{PAO}_{thick}). In this former *especial study case* (cf. 5.6a, p. 119), the slippage interfaces is defined between low-shear-strength, linear, C_{18} primary amines that have not succeed to adsorb onto the hematite slabs during the equilibration phase, and that eventually minimize the friction forces arising through the production simulation.

Therefore, the calculated computational friction coefficients have been found to be also controlled by the *molecular interdigitation level* exhibited by the different organic layers confined within the nano-contact model. This factor was not particularly quantified in the current analysis, but it can be captured by the *overlapped area extension* formed between the adjacent OFM and BO atomic density profiles (*i.e.*, the area below both interposed $\rho^{SAM}(z)$ and $\rho^{BO}(z)$ curves, as shown in figures 5.10 and 5.11, cf. p. 122 and 123). Then, those overlapping regions can particularly be used to rationalize the results of μ^* observed for the systems with SAM/-PAO/SAM at low and medium coverages (cf. an example given in figure 5.23, p. 137).

From this point of view, the $\rho^{SAM}(z)$ and $\rho^{BO}(z)$ profiles exhibiting broader molecular overlaps indeed show a deeper interdigitation, which accordingly leads to higher resulting friction forces and greater final μ^* values. Besides, these relatively *"higher frictional, interdigitated interfaces"* are specially linked to systems with Γ^{SAM}_{medium}, which have more amorphous structures and with lesser ordered layering, in comparison with either Γ^{SAM}_{low} or Γ^{SAM}_{high}. For example, $\mu^*(\rho^{PAO}_{thin}) = 0.18$ and $\mu^*(\rho^{PAO}_{thick}) = 0.17$, at Γ^{SAM}_{medium} and $v^s_x = 10$ m/s (cf. figures 5.10b and 5.11b, p. 122 and 123). Concerning the difference between μ^* values obtained for SAM/-PAO/SAM interfaces at Γ^{SAM}_{low}, with both thin and thick PAO-layers (0.17 and 0.12, respectively, at $v^s_x = 10$ m/s), they can likewise be elucidated by the greater interdigitation established by $\rho(z)$ overlapped areas (cf. figure 5.23). Lastly, one can also observe that thin PAO-layers are relatively more interdigitated with amine-SAM than the thick ones, thereby yielding greater μ^* results.

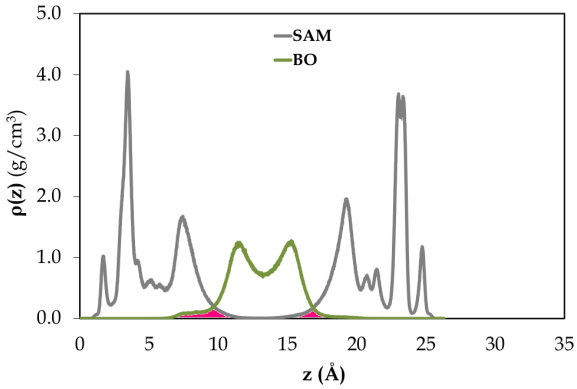

(a) ρ^{PAO}_{thin} — $\mu^* = 0.17$

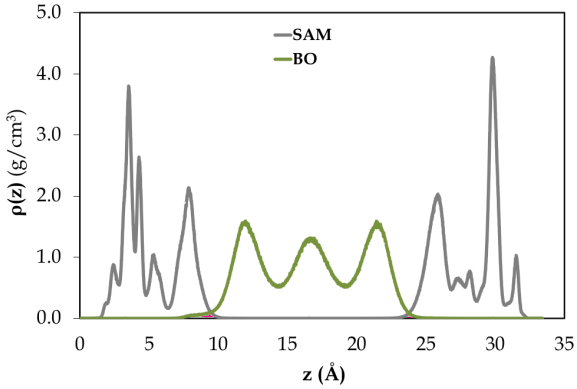

(b) ρ^{PAO}_{thick} — $\mu^* = 0.12$

Figure 5.23 – Atomic mass-density profiles, $\rho(z)$, of the two simulated nano-contacts with SAM/PAO/SAM interface at *low surface coverage* (Γ^{SAM}_{low}). Note that overlapped areas highlighted in *pink* indicate the observed molecular SAM/OFM interdigitation. *Color code: gray* - octadecylamine; *moss green* - PAO.

Finally, it is worthwhile to note that our outcomes are consistent with other comparable NEMD simulation results previously published in literature.[57,301] For example, Ewen *et al.*[57] have examined the atomistic structure and friction properties of commercially relevant OFM (*e.g.*, acid, amide, and glyceride OFMs, with saturated and Z-unsaturated hydrocarbon tail groups). Their assembled monolayers were adsorbed on iron oxide surfaces and lubricated by a separating layer of hexadecane, being also simulated at various surface coverages and sliding velocities. Their results have shown that:[57]

- at low and medium coverage ($\Gamma^{\mathrm{SAM}}_{\mathrm{low}} = 1.44\,\mathrm{nm}^{-2}$ and $\Gamma^{\mathrm{SAM}}_{\mathrm{medium}} = 2.88\,\mathrm{nm}^{-2}$, respectively), OFM formed liquid-like and amorphous monolayers, respectively, which were significantly interdigitated with the hexadecane lubricant, resulting in relatively high friction coefficients (cf. figure 5.24, p. 139);
- at high coverage ($\Gamma^{\mathrm{SAM}}_{\mathrm{high}} = 4.32\ \mathrm{nm}^{-2}$), solid-like monolayers were formed for all of the OFM, which, during sliding, resulted in slip planes between well-defined OFM and hexadecane layers, yielding a marked reduction in the friction coefficient (cf. figure 5.24, p. 139);
- OFM models, with saturated and Z-unsaturated hydrocarbon tails, were found to produce similar structure and friction behavior, when present at equal surface coverage;
- OFM with glyceride head groups yield significantly lower friction coefficients than amide and particularly carboxylic acid head groups;
- the molecular tilt angle[8] (θ) related to the simulated OFM monolayers appeared to be independent of both polar head and tail group types, suggesting that once the molecules were subjected to high pressure ($P_z = 500$ MPa), all of the molecules packed in a similar fashion regardless of the head group chemistry, or of the unsaturation degree related to hydrocarbon tails;
- the friction arising in confined NEMD simulations has been found to be independent of the orientation of the tilt angle, suggesting that a thin lubricant layer between the OFM films is critical in maintaining the consistent low friction observed in other previous NEMD simulations[301] and boundary friction experiments.[44]

[8] *Tilt angle*, θ, was defined as the angle between a vector from the carbonyl C atom to the C atom halfway up the OFM chain (C_9) and the surface normal.[57]

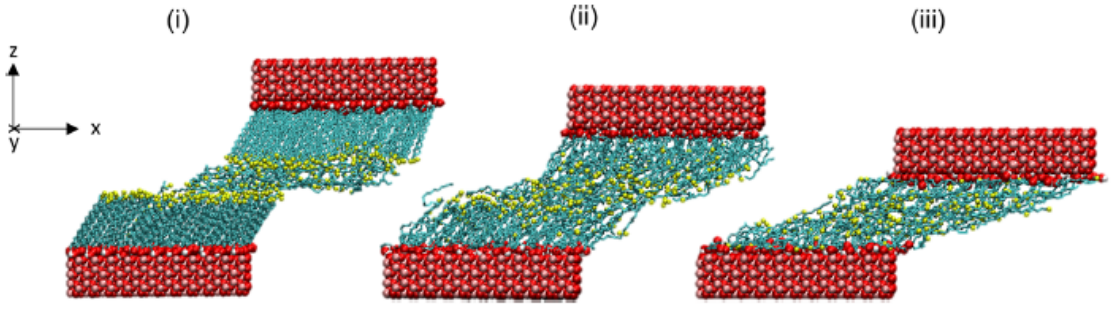

Figure 5.24 – Simulation snapshots of a representative OFM (*stearic acid*) of sliding at: **(i)** *high coverage*, **(ii)** *medium coverage*, and **(iii)** *low coverage*, with $P_z = 500$ MPa and $v_x^s = 10$ m/s. Oxygen atoms are shown in *red*; head group hydrogen atoms, in *white*; terminal carbon atoms, in *yellow*; the other tail group carbon atoms, in *cyan*; and iron atoms, in *pink*. Hydrogen atoms in the tail groups are omitted for clarity. Periodic images and boundaries are not shown here. (figure retrieved from the indicated reference) [57]

5.4.2.2 Effect of sliding velocity

Lastly, a comparative analysis of the calculated μ^* as a function of the three probed values of v_x^s imposed to hematite slabs (*e.g.*, $v_x^s = 1, 5, 10\ \mathrm{m \cdot s^{-1}}$) is providing in figure 5.25. The fitting curves describe a linearly increase of the *computational friction coefficient* with the *logarithm of sliding velocity* (cf. figure 5.25b), where the relative increasing gradients exhibited by μ^* are dependent on the OFM surface coverage ((Γ^{SAM}_{low}, Γ^{SAM}_{medium} & Γ^{SAM}_{high}).

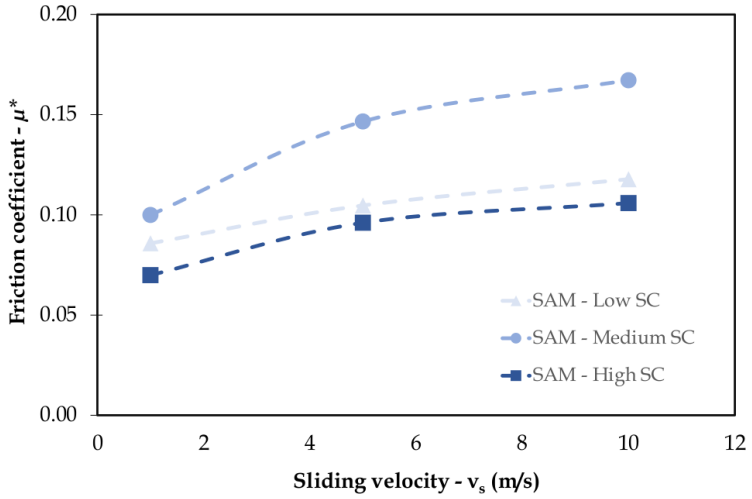

(a)

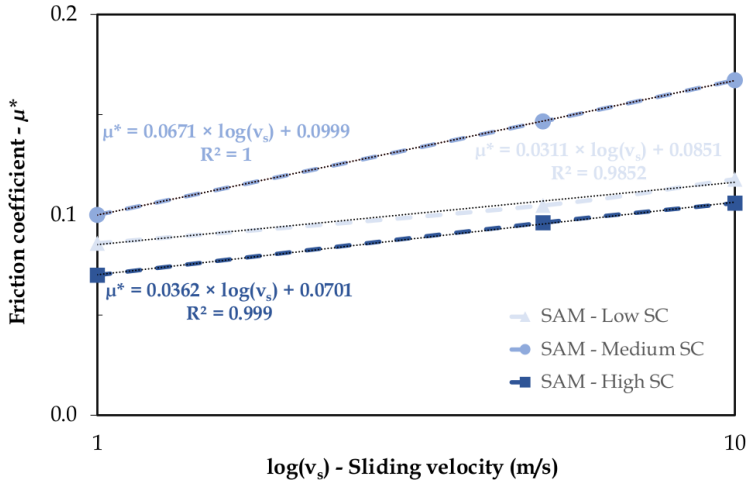

(b)

Figure 5.25 – Computational friction coefficient (μ^*) as a function of sliding velocity, for the nano-contacts with SAM/PAO/SAM interface of different surface coverages (SC).

Indeed, this depicted trend is in accordance with a similar one, identified for the evolution of the *kinetic friction coefficient* (μ) as a function of the sliding velocity. It was observed via NEMD simulations (simulated v_x^s : $1 - 20\ \mathrm{m \cdot s^{-1}}$),[57] as well as through macroscopic experiments (probed v^s : $5.62 \times 10^{-3} - 3.16 \times 10^{-7}\ \mathrm{m \cdot s^{-1}}$)[44,401] and from the stress-promoted thermal activation theory.[180]

Actually, Ewen *et al.* have interpreted their fitting curves of *"μ vs. $log(v_x^s)$"* in the following way: as two atoms approach in the interdigitated region, they experience a repulsive force.[57] At low values of v_x^s, the molecules can adjust their geometry by thermally induced translation, rotation and conformational changes in order to avoid increasing the repulsive force as the surfaces move past one another.[57,319] At high v_x^s, thermal molecular adjustment alone becomes too slow and must be increasingly augmented by shear-stress-promoted adjustments, so the shear stress and thus the friction coefficient increase with sliding velocity.[57,266]

Furthermore, it must be added that *stress-promoted thermal activation models*, such as the one observed in figure 5.25b, do yield a linear relationship between the logarithm of sliding velocity and the friction coefficient.[44,57,173,180] In fact, at $\Gamma_{\mathrm{high}}^{\mathrm{SAM}}$ and, to a relatively lesser extend at $\Gamma_{\mathrm{low}}^{\mathrm{SAM}}$, the barriers to interfacial sliding motion are small because there is very little interdigitation between the OFM monolayers and the intermediate PAO-film, inducing a low μ^*, which is indeed weakly affected by v_x^s. At $\Gamma_{\mathrm{medium}}^{\mathrm{SAM}}$, the amorphous and lesser packed SAM are more interdigitated with the BO model and their molecular rearrangement is relatively slow, owing to the fact that molecules are closely spaced. This means that activation barriers are both higher and more numerous for this latter case, leading to a high friction coefficient, which significantly varies with the sliding velocity.[57]

5.5 Summary

In the last study of our classical MD-based protocol, simulations were performed in order to shed light on structural and control-friction behavior of model OFM additives subjected to confinement and shear, and at the following constant operating conditions: $P_z = 500$ MPa and $T = 300$ K. In particular, the established NEMD simulation procedure have applied computationally feasible and reliably technical approaches to mimic a nano-scale BL system, composed of iron oxide slabs covered by octadecylamine monolayers, which were in turn separated or not by an intermediate, lamellar PAO-film. Moreover, it has allowed the investigation of the suggested *computational friction coefficient* (μ^*; cf. equation 5.2, p. 105) as a function of the surface coverage, the PAO-layer density and the sliding velocity.

In short, the obtained results have mainly shown that the effectiveness in reducing friction forces within the model nano-contact, associated with the probed organic films, is not strictly affected by the amount of adsorbed molecules on the rubbed substrates, but it relies on the ability of:

- OFM polar head to (relatively) strongly adsorbed on moving surfaces, ensuring its adhesion, even under severe sliding and compression conditions;
- OFM tail group to collectively assemble in a packed layering order;
- overall interfacial film to form well-defined slippage planes, with little molecular interdigitation.

6

Conclusion

In light of the fact that engine oils have progressively become thinner and that tribo-improvers have thus become a key lubricant constituent to control friction and to ensure engine protection under BL regime, this PhD project was carried out in order to further explore classical MD simulations as a probing tool of the lubricant additive performance. Additionally, the chief aim is to aid the development of more efficient friction modifiers and full organic formulations, which promote a greater reduction of CO_2 emissions generated by the thermal vehicles.

In this context, different EMD and NEMD simulations were developed to investigate the *diffusion*, *adsorption* and *friction-reducing behaviors of OFM additives*, and in particular those related to amine-based molecules. In the following, the different findings of our computational studies are summarized (cf. § 6.1, p. 144), and some research perspectives are pointed out in order to orient future work (cf. § 6.2, p. 147).

6.1 Summary

Following the general guidelines set by the work conducted by Loehlé *et al.*[46,55,56] — who have coupled computational and experimental methods to investigate the adsorption and tribological behavior of C_{18} fatty acids —, the numerical studies described in this manuscript have likewise confirmed the scientific interest of using atomistic simulations as a complementary technique to study lubricant additives. Indeed, MD simulations contribute to discerning the relationships between their molecular structure and their mechanisms of action, as well as to rationalizing macroscale experiments.

Besides, to the best of our knowledge, our classical MD-based simulation protocol is the first one to establish computational procedures integrating different performance indicators (*e.g.* $\mathfrak{D}_{\mathrm{OFM,BO}}$, Γ^{SAM} and μ^{*}), as well as treating both bulk liquid dynamics and liquid/solid interfacial behavior of surfactant additives, such as $C_{18}H_{39}N$, in particular under shear and confinement. Thus, the main outcomes of our work are briefly summarized in the next paragraphs.

Diffusion

Assuming that, in a multicomponent solution containing various surface-active agents, the surfactant molecules diffusing with a relatively higher rate are more prone to competitively adsorb on solid substrates, an EMD simulation was thus established to calculate the molecular diffusivity of BO and OFM models. In this context, the intra-diffusion coefficient were determined based on *Einstein formalism* and notably, on the *(time- and ensemble-averaged) MSD method* (cf. equations 3.1 and 3.3, p. 38 and 40, respectively), using the atomic information generated during the mentioned simulation.

In this context, the influence of different structural factors on liquid-state dynamics of the modeled lubricant constituents have been examined (cf. table 3.1, p. 39). The obtained diffusion coefficients of OFM were found to be greatly sensitive to the BO features (*e.g.*, *polarity* and *molar weight*), and to lesser extent, to their own molecular structure (*e.g.*, *polar head chemistry* and *alkyl tail length*; cf. § 3.3, p. 51).

Besides, owing to their relatively superior diffusivities ($\mathfrak{D}^{0}_{\mathrm{PAO}}$ and $\mathfrak{D}_{\mathrm{A1,PAO}}$, cf. figures 3.7 and 3.14, p. 52 and 60, respectively), the *octadecylamine* and the *PAO* were selected to represent the binary solution model of a lubricant in the subsequent computational studies, which have covered their absorptive and frictional behaviors (cf. chapters 4 and 5, p. 65 and 97).

Moreover, this study have also allowed the validation of the original OPLS-AA force field[108] as a pertinent energetic model, $U^{\text{lubricant}}$, to reproduce intra- and inter-molecular interactions related to the studied organic compounds (*e.g.*, PAO, PAG, and C_{18} alkyl and ethoxylated amines) at a temperature of 373 K. It has also be shown that, in a particular low-polarity medium such that represented by a PAO-based solution, the probed OFM models can indeed form aggregates (*e.g.*, dimers), whose diffusivity is lower then those of the individual species (cf. figure 3.13, p. 59).

Adsorption

Based on the results of a preliminary DFT-based study — carried out to discern the nature and the strength associated with the adsorptive interaction involving octadecylamines and an α-Fe_2O_3 $(0\ 1\ \bar{1}\ 2)$ surface (cf. § 4.1.1, p. 67) —, an interfacial pairwise potential was derived, $U^{\text{interface}}$, in order to reproduce the *chemisorption energy* (E_{ads}) and the resulting *equilibrium distance* ($d_{\text{N-Fe}}$) between the concerned *nitrogen* and *iron atoms* through a classical MD simulation (cf. § 4.1.3, p. 72).

Then, a series of EMD simulations were performed in order to validate the fitted force field, as well as to investigate the molecular structure of amine-based self-assembled monolayers, as a function of their surface coverage (Γ^{SAM}). The obtained results have successfully attested the $U^{\text{interface}}$ ability to model adsorbed octadecylamine films on a hematite substrate. Besides, they have also shown that a strong layering, combined with a long-range ordering, are indeed achieved when the amount of the model OFM increases over the investigated surface. Therefore, three OFM coverages were chosen — $\Gamma^{\text{SAM}}_{\text{low}} = 1.8\ \text{nm}^{-2}$, $\Gamma^{\text{SAM}}_{\text{medium}} = 2.7\ \text{nm}^{-2}$ and $\Gamma^{\text{SAM}}_{\text{high}} = 3.6\ \text{nm}^{-2}$ — to compose the range of SAM models used in the OFM frictional study (cf. chapter 5, p. 97).

Friction

A computer tribological test was set up through a *confined shearing NEMD simulation*, in order to describe an idealized BL contact at nanoscale, composed of sliding hematite slabs coated by pre-formed, octadecylamine-based SAM, which were separated or not by a PAO-layer (cf. figure 5.5, p.114). Besides, the structural and frictional properties of the employed OFM and BO models were assessed as a function of the SAM surface coverage, the intermediate

PAO-layer density, and the substrate sliding velocity.

As results, the performed simulations have shown that the effectiveness of C_{18} primary amines and PAO molecules in reducing adverse friction forces within the nano-contact model is strongly related to their ability to form *ordered, close-packed, confined organic films*, which exhibit *well-defined slip planes*, with *little molecular interdigitation*. In particular, these *low-shear-strength configurations* seem to be specially promoted at high and low SAM coverages (Γ^{SAM}_{high} & Γ^{SAM}_{low}, respectively), in presence of horizontally-oriented, intermediate films of PAO, or maybe even containing octadecylamines, as well as at (relatively) slower sliding velocities.

6.2 Perspectives

Throughout the described PhD project, many aspects were covered by the different established simulations, which are associated not only with the *molecular structure* of lubricant constituents (*e.g.*, range of BO polarity, OFM polar head chemistry, OFM tail length, SAM surface coverage, presence of an intermediate BO-layer), but also regarding some important *operating conditions* (*e.g.*, range of sliding velocity; at a temperature of 300 K; under a contact pressure of 500 MPa; at a mass concentration of 1 wt.%).

However, most of these classical MD simulations were designed assuming idealized conditions, as a first attempt to identified suitable indicators of the OFM working performance, which are indeed computationally calculable in an efficient way, without ignoring the intrinsic time- and length-scale limitations of the applied technique. Therefore, one of our main recommendations revolves around the configurational improvements on system models used as input of the EMD/NEMD simulations, in order to take into account more realistic and complex features, namely:

- commercial-relevant OFM additives (*e.g.*, amine salts, acylglycerols, esters, tartrate and citrate derivatives),[33,34,402,403] with multiple functional structures, including broader polar groups and unsaturated hydrocarbon tails;
- multicomponent solutions containing different lubricant constituents, such as tribo- and rheo-improvers along with maintainers additives, in order to gain insights into their aggregate phenomena, and their synergistic/antagonistic interaction effects;[29]
- other chemistries of solid substrates (*e.g.*, iron(II) hydroxide, phosphate glass representing a ZDDP tribofilm),[30,31,198,204] with rougher topography as already suggested in literature,[59,300,301,353,354,357,404] instead of the usual single-asperity model with atomically-smooth surface;
- adsorbed films exhibiting a heterogeneous composition, as well as a more irregular morphology than a simple SAM model (*e.g.*, various regions composed of vacancies, monolayers and multiple layers), in order to provide a more faithful representation of the protective additive films.

Another area of potential improvement is the *fitting method* employed to derived the interfacial MD force-field(s) required to reproduce the additive-substrate interactions. For instance, a wider range of molecular configurations and chemistries can be used within the reference

calculations, which can be performed by means of *ab initio* techniques. Besides, it can be included in these calculations the *lateral interactions* between adsorbed molecules affecting the stability of the adsorbed layer, as well as the *solvent effects* induced by the presence of a base oil. Alternatively, it must be said that *reactive force-fields* can also be employed to probe adsorptive and frictional properties of OFM additives, provided that their parameters are available for the systems of interest.[63, 86, 405–407]

Moreover, in order to further validate the developed computational protocol, experimental data could be obtained to set a comparative framework to our MD simulations. For example, liquid-based experiments can supply molecular diffusion coefficients of binary solutions containing amine and PAO molecules, such as those described in § 3.3.2 (cf. p. 55). Besides, since MD simulations of surfactant film formation from solution is still computationally prohibitive, it would be interesting to experimentally probe the friction behavior of a ternary solution whose constituents possess different diffusivities (*e.g.*, OFM-A/OFM-B/BO, like the one studied by Loehlé *et al.*;[46] cf. § 1.2.1, p. 10). In fact, that experiment may help a qualitative evaluation of the competitive adsorption effect on the lubricating action of different amine-based OFM chemistries. Furthermore, that experimental information might potentially support our assumption related to the importance of the thermal-induced molecular diffusion for the OFM adsorption onto solid surfaces in a context of a multicomponent mixture (*i.e.*, a fully formulated lubricant). Also, it would be useful to set up microscale tribological experiments that perform under conditions and configurations as similar as possible to our classical MD simulations, in order to obtain experimental friction coefficients that are comparable to the suggested μ^* (cf. equation 5.1, p. 104).

Finally, we expect that the current work contributes to boosting the deployment of molecular computational tools to study, and maybe even, to design novel lubricant additives that foster fuel economy and low-GHG emissions, in compliance with the principles of CO_2 neutrality and the other usual operational and cost-effectiveness standards.

Bibliography

[1] Intergovernmental Panel on Climate Change (IPCC), J. T. Houghton, G. J. Jenkins, and J. J. Ephraums, **1990**. *Climate change: the IPCC scientific assessment*. [https://www.ipcc.ch/site/assets/uploads/2018/03/ipcc_far_wg_I_full_report.pdf].

[2] Intergovernmental Panel on Climate Change (IPCC), R. K. Pachauri, and L. Mayer, **2015**. *Climate change 2014: synthesis report*. [https://www.ipcc.ch/site/assets/uploads/2018/02/SYR_AR5_FINAL_full.pdf].

[3] T. Klier and J. Linn, **2016**. *Comparing US and EU approaches to regulating automotive emissions and fuel economy*. Policy Brief — Resources for the Future, no. 16-03, [http://www.rff.org/files/document/file/RFF-PB-16-03.pdf].

[4] M. Urbakh, J. Klafter, D. Gourdon, and J. Israelachvili, **2004**. *The nonlinear nature of friction*. Nature, vol. 430 (6999), pp. 525–528, [http://www.nature.com/articles/nature02750].

[5] K. Holmberg, P. Andersson, and A. Erdemir, **2012**. *Global energy consumption due to friction in passenger cars*. Tribology International, vol. 47, pp. 221–234, [http://linkinghub.elsevier.com/retrieve/pii/S0301679X11003501].

[6] S. M. Campen, **2012**. *Fundamentals of organic friction modifier behaviour*. PhD thesis, Imperial College London, London, United Kingdom.

[7] K. Holmberg and A. Erdemir, **2017**. *Influence of tribology on global energy consumption, costs and emissions*. Friction, vol. 5 (3), pp. 263–284, [http://link.springer.com/10.1007/s40544-017-0183-5].

[8] P. Mock, **2017**. *2020-2030 CO_2 standards for new cars and light-commercial vehicles in the European Union*. International Council on Clean Transportation (ICCT), [https://www.theicct.org/publications/2020-2030-co2-standards-eu-cars-lcvs-20171026].

[9] P. Mock, **2018**. *The role of standards in reducing CO_2 emissions of passenger cars in the EU*. International Council on Clean Transportation (ICCT), [https://www.theicct.org/publications/role-standards-reducing-co2-emissions-passenger-cars-eu].

[10] Z. Yang and A. Bandivadekar, **2017**. *2017 Global Update — Light-duty ve-*

hicle greenhouse gas and fuel economy standards. International Council on Clean Transportation (ICCT), [https://www.theicct.org/publications/2017-global-update-LDV-GHG-FE-standards].

[11] E. Commission, ed., **2012**. *Energy roadmap 2050*. Publications Office of the European Union. ISBN: 978-92-79-21798-2. doi: 10.2833/10759.

[12] Intergovernmental Panel on Climate Change (IPCC) and O. Edenhofer, **2014**. *Climate change 2014: mitigation of climate change: Working Group III — contribution to the Fifth Assessment Report of the Intergovernmental Panel on Climate Change*. Cambridge University Press.

[13] D. Meszler, J. German, P. Mock, and A. Bandivadekar, **2016**. *CO_2 reduction technologies for the European car and van fleet: A 2025-2030 assessment*. International Council on Clean Transportation (ICCT), [https://www.theicct.org/sites/default/files/publications/EU-Cost-Curves_ICCT_nov2016.pdf].

[14] P. Mock, **2014**. *EU CO_2 standards for passenger cars and light-commercial vehicles*. International Council on Clean Transportation (ICCT), [https://www.theicct.org/publications/eu-co2-standards-passenger-cars-and-light-commercial-vehicles].

[15] ACEA, **2018**. *EU Parliament vote on CO_2 targets for cars and vans: auto industry voices concerns*. European Automobile Manufacturers' Association. [online] Available at: https://www.acea.be/press-releases/article/eu-parliament-vote-on-co2-targets-for-cars (accessed 20 December 2018).

[16] ACEA, **2018**. *Auto industry reacts to deal on CO_2 targets for cars and vans*. European Automobile Manufacturers' Association. [online] Available at: https://www.acea.be/press-releases/article/auto-industry-reacts-to-deal-on-co2-targets-for-cars-and-vans (accessed 20 December 2018).

[17] M. Şenzeybek, U. Tietge, and P. Mock, **2017**. *CO_2 emissions from new passenger cars in the EU: Car manufacturers' performance in 2016*. International Council on Clean Transportation (ICCT), [https://www.theicct.org/sites/default/files/publications/PV-EU-OEM_ICCT-Briefing_03072017_vF.pdf].

[18] N. Lutsey and A. Isenstadt, **2018**. *How will off-cycle credits impact U.S. 2025 efficiency standards?* International Council on Clean Transportation (ICCT), [https://www.theicct.org/publications/US-2025-off-cycle].

[19] P. Mock, **2016**. *2020-2030 CO_2 standards for new cars and light-commercial vehicles in the European Union*. International Council on Clean Transportation (ICCT), [https://www.theicct.org/sites/default/files/publications/ICCT_EU-CO2-stds_2020-30_brief_nov2016.pdf].

[20] N. Canter, **2015**. *GF-6, PC-11 and dexos1^{TM}: New engine oil specifications mean new*

additive challenges. Tribology and Lubrication Technology, vol. 71 (9), pp. 10–24, [http://digitaleditions.walsworthprintgroup.com/publication/index.php?i=269105&m=&l=&p=4&pre=&ver=html5#{%22page%22:12,%22issue_id%22:269105}].

[21] Infineum, **2018**. *Specification Updates*. Insight – Infineum International Limited. [online] Available at: http://www.infineuminsight.com/trends/specification-updates (accessed 15 May 2018).

[22] Lubrizol, **2018**. *ACEA - A Specification of Global Importance*. Lubrizol. [online] Available at: https://www.lubrizoladditives360.com/specifications/passenger-cars/acea/ (accessed 20 December 2018).

[23] ACEA, **2018**. *ACEA Oil Sequences 2016*. European Automobile Manufacturers' Association. [online] Available at: http://www.acea.be/news/article/acea-oil-sequences-2016 (accessed 15 May 2018).

[24] API, **2018**. *Oil Categories*. American Petroleum Institute (API). [online] Available at: http://www.api.org/products-and-services/engine-oil/eolcs-categories-and-classifications/oil-categories (accessed 15 May 2018).

[25] Lubrizol, **2018**. *ILSAC GF-6*. Lubrizol. [online] Available at: https://www.lubrizoladditives360.com/specifications/passenger-cars/ilsac/ (accessed 20 December 2018).

[26] Infineum, **2018**. *ILSAC GF-6*. Insight – Infineum International Limited. [online] Available at: http://www.infineuminsight.com/trends/ilsac-gf-6 (accessed 15 May 2018).

[27] G. W. Stachowiak and A. W. Batchelor, **2014**. *Engineering tribology*. Oxford: Elsevier/Butterworth-Heinemann, 4th edition ed. ISBN: 978-0-12-397047-3.

[28] L. R. Rudnick, ed., **2017**. *Lubricant additives: chemistry and applications*. Chemical industries, CRC Press, Taylor & Francis Group, 3rd ed. ISBN: 978-1-4987-3172-0.

[29] I. Minami, **2017**. *Molecular Science of Lubricant Additives*. Applied Sciences, vol. 7 (5), p. 445, [http://www.mdpi.com/2076-3417/7/5/445].

[30] M. Desanker, X. He, J. Lu, P. Liu, D. B. Pickens, M. Delferro, T. J. Marks, Y.-W. Chung, and Q. J. Wang, **2017**. *Alkyl-Cyclens as Effective Sulfur- and Phosphorus-Free Friction Modifiers for Boundary Lubrication*. ACS Applied Materials & Interfaces, vol. 9 (10), pp. 9118–9125, [http://pubs.acs.org/doi/10.1021/acsami.6b15608].

[31] S. Loehlé, **2014**. *Understanding of adsorption mechanisms and tribological behaviors of C18 fatty acids on iron-based surfaces: a molecular simulation approach*. PhD thesis, Ecole Centrale de Lyon, Lyon, France.

[32] S. Yazawa, I. Minami, and B. Prakash, **2014**. *Reducing Friction and Wear of Tribological*

Systems through Hybrid Tribofilm Consisting of Coating and Lubricants. Lubricants, vol. 2 (2), pp. 90–112, [http://www.mdpi.com/2075-4442/2/2/90].

[33] Z. Tang and S. Li, **2014**. *A review of recent developments of friction modifiers for liquid lubricants (2007–present)*. Current Opinion in Solid State and Materials Science, vol. 18 (3), pp. 119–139, [http://linkinghub.elsevier.com/retrieve/pii/S1359028614000059].

[34] H. Spikes, **2015**. *Friction Modifier Additives*. Tribology Letters, vol. 60 (1), [http://link.springer.com/10.1007/s11249-015-0589-z].

[35] S. Lundgren, **2008**. *Unsaturated Fatty Acids in Alkane Solution: Adsorption and Tribological Properties*. PhD thesis, Royal Institute of Technology, Stockholm, Sweden.

[36] S. Lundgren, K. Persson, B. Kronberg, and P. Claesson, **2006**. *Adsorption of fatty acids from alkane solution studied with quartz crystal microbalance*. Tribology Letters, vol. 22 (1), pp. 15–20, [http://link.springer.com/10.1007/s11249-005-9000-9].

[37] J.-H. Choo, A. K. Forrest, and H. A. Spikes, **2007**. *Influence of Organic Friction Modifier on Liquid Slip: A New Mechanism of Organic Friction Modifier Action*. Tribology Letters, vol. 27 (2), pp. 239–244, [http://link.springer.com/10.1007/s11249-007-9231-z].

[38] S. M. Lundgren, K. Persson, G. Mueller, B. Kronberg, J. Clarke, M. Chtaib, and P. M. Claesson, **2007**. *Unsaturated Fatty Acids in Alkane Solution: Adsorption to Steel Surfaces*. Langmuir, vol. 23 (21), pp. 10598–10602, [http://pubs.acs.org/doi/abs/10.1021/la700909v].

[39] S. Lundgren, M. Ruths, K. Danerlöv, and K. Persson, **2008**. *Effects of unsaturation on film structure and friction of fatty acids in a model base oil*. Journal of Colloid and Interface Science, vol. 326 (2), pp. 530–536, [http://linkinghub.elsevier.com/retrieve/pii/S0021979708006760].

[40] M. Ruths, S. Lundgren, K. Danerlöv, and K. Persson, **2008**. *Tribological Properties of Physisorbed, Unsaturated Fatty Acids*. ASME, pp. 47–48, [http://proceedings.asmedigitalcollection.asme.org/proceeding.aspx?articleid=1630273].

[41] M. Ruths, S. Lundgren, K. Danerlöv, and K. Persson, **2008**. *Friction of Fatty Acids in Nanometer-Sized Contacts of Different Adhesive Strength*. Langmuir, vol. 24 (4), pp. 1509–1516, [http://pubs.acs.org/doi/abs/10.1021/la7023633].

[42] H. Koshima, H. Kamano, Y. Hisaeda, H. Liu, and S. Ye, **2010**. *Analyses of the Adsorption Structures of Friction Modifiers by Means of Quantitative Structure-Property Relationship Method and Sum Frequency Generation Spectroscopy*. Tribology Online, vol. 5 (3), pp. 165–172, [http://joi.jlc.jst.go.jp/JST.JSTAGE/trol/5.165?from=CrossRef].

[43] S. M. Lundgren, K. Persson, J. Clarke, L. Nordstierna, and P. M. Claesson, **2011**. *The influence of water on the adsorption and the tribological properties of unsaturated fatty acids in*

alkane solution. Proceedings of the Institution of Mechanical Engineers, Part J: Journal of Engineering Tribology, vol. 225 (10), pp. 1048–1055, [http://journals.sagepub.com/doi/10.1177/1350650111411379].

[44] S. Campen, J. Green, G. Lamb, D. Atkinson, and H. Spikes, **2012**. *On the Increase in Boundary Friction with Sliding Speed*. Tribology Letters, vol. 48 (2), pp. 237–248, [http://link.springer.com/10.1007/s11249-012-0019-4].

[45] M. H. Wood, R. J. L. Welbourn, T. Charlton, A. Zarbakhsh, M. T. Casford, and S. M. Clarke, **2013**. *Hexadecylamine Adsorption at the Iron Oxide–Oil Interface*. Langmuir, vol. 29 (45), pp. 13735–13742, [http://pubs.acs.org/doi/10.1021/la4018147].

[46] S. Loehle, C. Matta, C. Minfray, T. Le Mogne, J.-M. Martin, R. Iovine, Y. Obara, R. Miura, and A. Miyamoto, **2014**. *Mixed Lubrication with C18 Fatty Acids: Effect of Unsaturation*. Tribology Letters, vol. 53 (1), pp. 319–328, [http://link.springer.com/10.1007/s11249-013-0270-3].

[47] M. Doig, C. P. Warrens, and P. J. Camp, **2014**. *Structure and Friction of Stearic Acid and Oleic Acid Films Adsorbed on Iron Oxide Surfaces in Squalane*. Langmuir, vol. 30 (1), pp. 186–195, [http://pubs.acs.org/doi/10.1021/la404024v].

[48] M. Ratoi, V. B. Niste, H. Alghawel, Y. F. Suen, and K. Nelson, **2014**. *The impact of organic friction modifiers on engine oil tribofilms*. RSC Adv., vol. 4 (9), pp. 4278–4285, [http://xlink.rsc.org/?DOI=C3RA46403B].

[49] K. Eriksson, **2014**. *Fatty amines as friction modifiers in engine oils: correlating adsorbed amount to friction and wear performance*. Master's thesis, Chalmers University of Technology, Gothenburg, Sweden.

[50] C. R. G. Lehner, **2015**. *Quartz crystal microbalance studies of friction modifiers for lubricant applications*. Master's thesis, Chemistry and Anthropology, University of Mary Washington, Virginia, USA.

[51] S. M. Lundgren, K. Eriksson, and B. Rossenaar, **2015**. *Boosting the Friction Performance of Amine Friction Modifiers with MoDTC*. SAE International Journal of Fuels and Lubricants, vol. 8 (1), pp. 27–30, [http://papers.sae.org/2015-01-0684/].

[52] M. Doig and P. J. Camp, **2015**. *The structures of hexadecylamine films adsorbed on iron-oxide surfaces in dodecane and hexadecane*. Physical Chemistry Chemical Physics, vol. 17 (7), pp. 5248–5255, [http://xlink.rsc.org/?DOI=C4CP05837B].

[53] S. Campen, J. H. Green, G. D. Lamb, and H. A. Spikes, **2015**. *In Situ Study of Model Organic Friction Modifiers Using Liquid Cell AFM; Saturated and Mono-unsaturated Carboxylic Acids*. Tribology Letters, vol. 57 (2), [http://link.springer.com/10.1007/s11249-015-0465-x].

[54] S. Campen, J. H. Green, G. D. Lamb, and H. A. Spikes, **2015**. *In Situ Study of Model Organic Friction Modifiers Using Liquid Cell AFM: Self-Assembly of Octadecylamine*. Tribology Letters, vol. 58 (3), [http://link.springer.com/10.1007/s11249-015-0514-5].

[55] S. Loehlé, C. Matta, C. Minfray, T. Mogne, R. Iovine, Y. Obara, A. Miyamoto, and J. Martin, **2015**. *Mixed lubrication of steel by C18 fatty acids revisited. Part I: Toward the formation of carboxylate*. Tribology International, vol. 82, pp. 218–227, [http://linkinghub.elsevier.com/retrieve/pii/S0301679X14003776].

[56] S. Loehlé, C. Matta, C. Minfray, T. Le Mogne, R. Iovine, Y. Obara, A. Miyamoto, and J. Martin, **2016**. *Mixed lubrication of steel by C18 fatty acids revisited. Part II: Influence of some key parameters*. Tribology International, vol. 94, pp. 207–216, [http://linkinghub.elsevier.com/retrieve/pii/S0301679X15003783].

[57] J. P. Ewen, C. Gattinoni, N. Morgan, H. A. Spikes, and D. Dini, **2016**. *Nonequilibrium Molecular Dynamics Simulations of Organic Friction Modifiers Adsorbed on Iron Oxide Surfaces*. Langmuir, vol. 32 (18), pp. 4450–4463, [http://pubs.acs.org/doi/abs/10.1021/acs.langmuir.6b00586].

[58] J. Ewen, C. Gattinoni, F. Thakkar, N. Morgan, H. Spikes, and D. Dini, **2016**. *A Comparison of Classical Force-Fields for Molecular Dynamics Simulations of Lubricants*. Materials, vol. 9 (8), p. 651, [http://www.mdpi.com/1996-1944/9/8/651].

[59] J. P. Ewen, S. Echeverri Restrepo, N. Morgan, and D. Dini, **2017**. *Nonequilibrium molecular dynamics simulations of stearic acid adsorbed on iron surfaces with nanoscale roughness*. Tribology International, vol. 107, pp. 264–273, [http://linkinghub.elsevier.com/retrieve/pii/S0301679X16304686].

[60] S. Campen, J. Wong, and H. Spikes, **2017**. *Boundary Film Formation and Competitive Adsorption*. 6th World Tribology Congress, Beijing, China, September 17 - 22, 2017, paper n° 494745 .

[61] T. Massoud, R. Pereira de Matos, T. Le Mogne, M. Cobián, M. Belin, P. David, B. Thiébaut, S. Loehlé, F. Dahlem, and C. Minfray, **2017**. *Tribological behavior and adsorption mechanism of fatty amines and derivatives*. 6th World Tribology Congress, Beijing, China, September 17th - 22th, 2017, paper n° 497461.

[62] A. Crespo, N. Morgado, D. Mazuyer, and J. Cayer-Barrioz, **2018**. *Effect of Unsaturation on the Adsorption and the Mechanical Behavior of Fatty Acid Layers*. Langmuir, vol. 34 (15), pp. 4560–4567, [http://pubs.acs.org/doi/10.1021/acs.langmuir.8b00491].

[63] J. P. Ewen, D. M. Heyes, and D. Dini, **2018**. *Advances in nonequilibrium molecular dynamics simulations of lubricants and additives*. Friction, [http://link.springer.com/10.1007/s40544-018-0207-9].

[64] J. P. Ewen, S. K. Kannam, B. D. Todd, and D. Dini, **2018**. *Slip of Alkanes Confined between Surfactant Monolayers Adsorbed on Solid Surfaces*. Langmuir, vol. 34 (13), pp. 3864–3873, [http://pubs.acs.org/doi/10.1021/acs.langmuir.8b00189].

[65] C. Gattinoni, J. P. Ewen, and D. Dini, **2018**. *Adsorption of Surfactants on α-Fe_2O_3 (0001): A Density Functional Theory Study*. The Journal of Physical Chemistry C, vol. 122 (36), pp. 20817–20826, [http://pubs.acs.org/doi/10.1021/acs.jpcc.8b05899].

[66] T. Kuwahara, P. A. Romero, S. Makowski, V. Weihnacht, G. Moras, and M. Moseler, **2019**. *Mechano-chemical decomposition of organic friction modifiers with multiple reactive centres induces superlubricity of ta-C*. Nature Communications, vol. 10 (1), [http://www.nature.com/articles/s41467-018-08042-8].

[67] W. A. Zisman, **1959**. *Friction, durability and wettability, properties of monomolecular films on solids*, in Friction and Wear (R. Davies, ed.), pp. 110–148, Elsevier, Amsterdam.

[68] S. Jahanmir, **1985**. *Chain length effects in boundary lubrication*. Wear, vol. 102 (4), pp. 331–349, [http://linkinghub.elsevier.com/retrieve/pii/0043164885901760].

[69] T. Hirayama, R. Kawamura, K. Fujino, T. Matsuoka, H. Komiya, and H. Onishi, **2017**. *Cross-Sectional Imaging of Boundary Lubrication Layer Formed by Fatty Acid by Means of Frequency-Modulation Atomic Force Microscopy*. Langmuir, vol. 33 (40), pp. 10492–10500, [http://pubs.acs.org/doi/10.1021/acs.langmuir.7b02528].

[70] W. B. Hardy and I. Doubleday, **1922**. *Boundary Lubrication. The Paraffin Series*. Proceedings of the Royal Society A: Mathematical, Physical and Engineering Sciences, vol. 100 (707), pp. 550–574, [http://rspa.royalsocietypublishing.org/cgi/doi/10.1098/rspa.1922.0017].

[71] W. B. Hardy, **1936**. *Collected Scientifc Papers*. Cambridge University Press: Cambridge, England.

[72] I. Szlufarska, M. Chandross, and R. W. Carpick, **2008**. *Recent advances in single-asperity nanotribology*. Journal of Physics D: Applied Physics, vol. 41 (12), p. 123001, [http://stacks.iop.org/0022-3727/41/i=12/a=123001?key=crossref.08fee99483809ad29df3fb04fb0c4b86].

[73] A. Stukowski, **2010**. *Visualization and analysis of atomistic simulation data with OVITO–the Open Visualization Tool*. Modelling and Simulation in Materials Science and Engineering, vol. 18, no. 1, p. 015012, [http://stacks.iop.org/0965-0393/18/i=1/a=015012?key=crossref.6895e2c3bb522d1563fb2e2fe9f22789].

[74] W. Humphrey, A. Dalke, and K. Schulten, **1996**. *VMD: visual molecular dynamics*. Journal of Molecular Graphics, vol. 14 (1), pp. 33–38, 27–28, [https://www.ncbi.nlm.nih.gov/pubmed/8744570].

[75] W. Kohn and L. J. Sham, **1965**. *Self-Consistent Equations Including Exchange and Correlation Effects*. Physical Review, vol. 140 (4A), pp. A1133–A1138, [https://link.aps.org/doi/10.1103/PhysRev.140.A1133].

[76] F. J. DeBlase, **2011**. *Improving Organic Antiwear and Friction Modifier Compounds for Automotive Applications*, in Surfactants in Tribology (G. Biresaw and K. L. Mittal, eds.), vol. 2, CRC Press.

[77] S. M. Hsu, **2004**. *Molecular basis of lubrication*. Tribology International, vol. 37 (7), pp. 553–559, [http://linkinghub.elsevier.com/retrieve/pii/

S0301679X03002342].

[78] M. Olla, G. Navarra, B. Elsener, and A. Rossi, **2006**. *Nondestructive in-depth composition profile of oxy-hydroxide nanolayers on iron surfaces from ARXPS measurement*. Surface and Interface Analysis, vol. 38 (5), pp. 964–974, [http://doi.wiley.com/10.1002/sia.2362].

[79] H. Berro, N. Fillot, and P. Vergne, **2010**. *Molecular dynamics simulation of surface energy and ZDDP effects on friction in nano-scale lubricated contacts*. Tribology International, vol. 43 (10), pp. 1811–1822, [http://linkinghub.elsevier.com/retrieve/pii/S0301679X10000575].

[80] N. Dzade, A. Roldan, and N. de Leeuw, **2014**. *A Density Functional Theory Study of the Adsorption of Benzene on Hematite (α-Fe_2O_3) Surfaces*. Minerals, vol. 4 (1), pp. 89–115, [http://www.mdpi.com/2075-163X/4/1/89].

[81] T. D. Ta, A. K. Tieu, H. Zhu, and B. Kosasih, **2015**. *Adsorption of Normal-Alkanes on Fe(110), FeO(110), and Fe_2O_3 (0001): Influence of Iron Oxide Surfaces*. The Journal of Physical Chemistry C, vol. 119 (23), pp. 12999–13010, [http://pubs.acs.org/doi/10.1021/acs.jpcc.5b01847].

[82] S. Tromp, L. Joly, M. Cobián, and N. Fillot, **2018**. *Chemical Physics at Interfaces within a Refrigerant-Lubricated Contact: From Electronic Structure to Large-Scale Molecular Dynamics Simulations*. The Journal of Physical Chemistry C, vol. 122 (10), pp. 5420–5429, [http://pubs.acs.org/doi/10.1021/acs.jpcc.7b11267].

[83] D. Frenkel and B. Smit, **2002**. *Understanding molecular simulation: from algorithms to applications*. Academic Press, 2nd ed. ISBN: 978-0-12-267351-1.

[84] D. C. Rapaport, **2004**. *The Art of Molecular Dynamics Simulation*. Cambridge: Cambridge University Press, 2nd ed. ISBN: 978-0-511-81658-1.

[85] M. P. Allen and D. J. Tildesley, **2017**. *Computer simulation of liquids*. Oxford, United Kingdom: Oxford University Press, 2nd ed. ISBN: 978-0-19-880319-5 978-0-19-880320-1.

[86] J. D. Schall, P. T. Mikulski, G. M. Chateauneuf, G. Gao, and J. A. Harrison, **2007**. *Molecular Dynamics Simulations of Tribology*, in Superlubricity, pp. 79–102, Elsevier.

[87] Y. Dong, Q. Li, and A. Martini, **2013**. *Molecular dynamics simulation of atomic friction: A review and guide*. Journal of Vacuum Science & Technology A: Vacuum, Surfaces, and Films, vol. 31 (3), no. 030801, [http://avs.scitation.org/doi/10.1116/1.4794357].

[88] J. A. Harrison, S. J. Stuart, and D. W. Brenne, **1999**. *Atomic-scale simulation of tribological and related phenomena*, in Handbook of micro/nanotribology (B. Bhushan, ed.), pp. 397–439, CRC Press, 2nd ed.

[89] M. Robbins and M. Müser, **2000**. *Computer Simulations of Friction, Lubrication, and Wear*, in Modern Tribology Handbook, vol. 5, CRC Press.

[90] S.-J. Heo, S. B. Sinnott, D. W. Brenner, and J. A. Harrison, **2005**. *Computational Modeling of Nanometer-Scale Tribology*, in Nanotribology and Nanomechanics (B. Bhushan, ed.), pp. 623–691, Springer-Verlag.

[91] J. A. Harrison, J. D. Schall, M. T. Knippenberg, G. Gao, and P. T. Mikulski, **2008**. *Elucidating atomic-scale friction using molecular dynamics and specialized analysis techniques*. Journal of Physics: Condensed Matter, vol. 20 (35), p. 354009, [http://iopscience.iop.org/article/10.1088/0953-8984/20/35/354009/meta].

[92] A. Vakis, V. Yastrebov, J. Scheibert, L. Nicola, D. Dini, C. Minfray, A. Almqvist, M. Paggi, S. Lee, G. Limbert, J. Molinari, G. Anciaux, R. Aghababaei, S. Echeverri Restrepo, A. Papangelo, A. Cammarata, P. Nicolini, C. Putignano, G. Carbone, S. Stupkiewicz, J. Lengiewicz, G. Costagliola, F. Bosia, R. Guarino, N. Pugno, M. Müser, and M. Ciavarella, **2018**. *Modeling and simulation in tribology across scales: An overview*. Tribology International, vol. 125, pp. 169–199, [https://linkinghub.elsevier.com/retrieve/pii/S0301679X18300756].

[93] G. E. Norman and V. V. Stegailov, **2013**. *Stochastic theory of the classical molecular dynamics method*. Mathematical Models and Computer Simulations, vol. 5 (4), pp. 305–333, [http://link.springer.com/10.1134/S2070048213040108].

[94] F. Jensen, **2017**. *Introduction to computational chemistry*. Chichester, UK ; Hoboken, NJ: John Wiley & Sons, 3rd ed. ISBN: 978-1-118-82599-0.

[95] S. Plimpton, **1995**. *Fast Parallel Algorithms for Short-Range Molecular Dynamics*. Journal of Computational Physics, vol. 117 (1), pp. 1–19, [http://linkinghub.elsevier.com/retrieve/pii/S002199918571039X].

[96] S. Nosé, **1984**. *A molecular dynamics method for simulations in the canonical ensemble*. Molecular Physics, vol. 52 (2), pp. 255–268, [http://www.tandfonline.com/doi/abs/10.1080/00268978400101201].

[97] W. G. Hoover, **1985**. *Canonical dynamics: Equilibrium phase-space distributions*. Physical Review A, vol. 31 (3), pp. 1695–1697, [https://link.aps.org/doi/10.1103/PhysRevA.31.1695].

[98] W. Shinoda, M. Shiga, and M. Mikami, **2004**. *Rapid estimation of elastic constants by molecular dynamics simulation under constant stress*. Physical Review B, vol. 69 (13), [https://link.aps.org/doi/10.1103/PhysRevB.69.134103].

[99] T. Schneider and E. Stoll, **1978**. *Molecular-dynamics study of a three-dimensional one-component model for distortive phase transitions*. Physical Review B, vol. 17 (3), pp. 1302–1322, [https://link.aps.org/doi/10.1103/PhysRevB.17.1302].

[100] W. L. Jorgensen, D. S. Maxwell, and J. Tirado-Rives, **1996**. *Development and Testing of the OPLS All-Atom Force Field on Conformational Energetics and Properties of Organic Liquids*. Journal of the American Chemical Society, vol. 118 (45), pp. 11225–11236, [http://pubs.acs.org/doi/abs/10.1021/ja9621760].

[101] W. Damm, A. Frontera, J. Tirado-Rives, and W. L. Jorgensen, **1997**. *OPLS all-atom force field for carbohydrates*. Journal of Computational Chemistry, vol. 18 (16), pp. 1955–1970, [http://doi.wiley.com/10.1002/%28SICI%291096-987X%28199712%2918%3A16%3C1955%3A%3AAID-JCC1%3E3.0.CO%3B2-L].

[102] W. L. Jorgensen and N. A. McDonald, **1998**. *Development of an all-atom force field for heterocycles. Properties of liquid pyridine and diazenes*. Journal of Molecular Structure: THEOCHEM, vol. 424 (1-2), pp. 145–155, [http://linkinghub.elsevier.com/retrieve/pii/S0166128097002376].

[103] N. A. McDonald and W. L. Jorgensen, **1998**. *Development of an All-Atom Force Field for Heterocycles. Properties of Liquid Pyrrole, Furan, Diazoles, and Oxazoles*. The Journal of Physical Chemistry B, vol. 102 (41), pp. 8049–8059, [http://pubs.acs.org/doi/abs/10.1021/jp981200o].

[104] R. C. Rizzo and W. L. Jorgensen, **1999**. *OPLS All-Atom Model for Amines: Resolution of the Amine Hydration Problem*. Journal of the American Chemical Society, vol. 121 (20), pp. 4827–4836, [http://pubs.acs.org/doi/abs/10.1021/ja984106u].

[105] E. K. Watkins and W. L. Jorgensen, **2001**. *Perfluoroalkanes: Conformational Analysis and Liquid-State Properties from ab Initio and Monte Carlo Calculations*. The Journal of Physical Chemistry A, vol. 105 (16), pp. 4118–4125, [http://pubs.acs.org/doi/abs/10.1021/jp004071w].

[106] M. L. P. Price, D. Ostrovsky, and W. L. Jorgensen, **2001**. *Gas-phase and liquid-state properties of esters, nitriles, and nitro compounds with the OPLS-AA force field*. Journal of Computational Chemistry, vol. 22 (13), pp. 1340–1352, [http://doi.wiley.com/10.1002/jcc.1092].

[107] J. P. Ewen, C. Gattinoni, J. Zhang, D. M. Heyes, H. A. Spikes, and D. Dini, **2017**. *On the effect of confined fluid molecular structure on nonequilibrium phase behaviour and friction*. Physical Chemistry Chemical Physics, vol. 19 (27), pp. 17883–17894, [http://xlink.rsc.org/?DOI=C7CP01895A].

[108] *OPLS All-Atom Parameters for Organic Molecules, Ions, Peptides & Nucleic Acids*, **2008**. Provided by W. L. Jorgensen, Yale University, [https://dasher.wustl.edu/tinker/distribution/params/oplsaa.prm].

[109] E. Harder, W. Damm, J. Maple, C. Wu, M. Reboul, J. Y. Xiang, L. Wang, D. Lupyan, M. K. Dahlgren, J. L. Knight, J. W. Kaus, D. S. Cerutti, G. Krilov, W. L. Jorgensen, R. Abel, and R. A. Friesner, **2016**. *OPLS3: A Force Field Providing Broad Coverage of Drug-like Small Molecules and Proteins*. Journal of Chemical Theory and Computation, vol. 12 (1), pp. 281–296, [http://pubs.acs.org/doi/10.1021/acs.jctc.5b00864].

[110] B. Guillot and N. Sator, **2007**. *A computer simulation study of natural silicate melts. Part I: Low pressure properties*. Geochimica et Cosmochimica Acta, vol. 71 (5), pp. 1249–1265, [http://linkinghub.elsevier.com/retrieve/pii/S0016703706021971].

[111] B. Guillot and N. Sator, **2007**. *A computer simulation study of natural silicate melts. Part II: High pressure properties*. Geochimica et Cosmochimica Acta, vol. 71 (18), pp. 4538–4556, [http://linkinghub.elsevier.com/retrieve/pii/S0016703707003936].

[112] D. Chicot, J. Mendoza, A. Zaoui, G. Louis, V. Lepingle, F. Roudet, and J. Lesage, **2011**. *Mechanical properties of magnetite (Fe_3O_4), hematite (α-Fe_2O_3) and goethite (α-FeO·OH) by instrumented indentation and molecular dynamics analysis*. Materials Chemistry and Physics, vol. 129 (3), pp. 862–870, [http://linkinghub.elsevier.com/retrieve/pii/S0254058411004627].

[113] O. Suárez-Iglesias, I. Medina, M. d. l. n. Sanz, C. Pizarro, and J. L. Bueno, **2015**. *Self-Diffusion in Molecular Fluids and Noble Gases: Available Data*. Journal of Chemical & Engineering Data, vol. 60 (10), pp. 2757–2817, [http://pubs.acs.org/doi/10.1021/acs.jced.5b00323].

[114] D. R. Wheeler and J. Newman, **2004**. *Molecular Dynamics Simulations of Multicomponent Diffusion. 1. Equilibrium Method*. The Journal of Physical Chemistry B, vol. 108 (47), pp. 18353–18361, [http://pubs.acs.org/doi/abs/10.1021/jp047850b].

[115] J. W. Nichols and D. R. Wheeler, **2015**. *Fourier Correlation Method for Simulating Mutual Diffusion Coefficients in Condensed Systems at Equilibrium*. Industrial & Engineering Chemistry Research, vol. 54 (48), pp. 12156–12164, [http://pubs.acs.org/doi/10.1021/acs.iecr.5b02849].

[116] P. C. Carman and L. H. Stein, **1956**. *Self-diffusion in mixtures. Part 1. Theory and its application to a nearly ideal binary liquid mixture*. Transactions of the Faraday Society, vol. 52, pp. 619–627, [http://xlink.rsc.org/?DOI=tf9565200619].

[117] A. Bardow, E. Kriesten, M. A. Voda, F. Casanova, B. Blümich, and W. Marquardt, **2009**. *Prediction of multicomponent mutual diffusion in liquids: Model discrimination using NMR data*. Fluid Phase Equilibria, vol. 278 (1-2), pp. 27–35, [http://linkinghub.elsevier.com/retrieve/pii/S0378381209000053].

[118] J. Li, H. Liu, and Y. Hu, **2001**. *A mutual-diffusion-coefficient model based on local composition*. Fluid Phase Equilibria, vol. 187-188, pp. 193–208, [http://linkinghub.elsevier.com/retrieve/pii/S0378381201005350].

[119] X. Liu, S. K. Schnell, J.-M. Simon, P. Krüger, D. Bedeaux, S. Kjelstrup, A. Bardow, and T. J. H. Vlugt, **2013**. *Diffusion Coefficients from Molecular Dynamics Simulations in Binary and Ternary Mixtures*. International Journal of Thermophysics, vol. 34 (7), pp. 1169–1196, [http://link.springer.com/10.1007/s10765-013-1482-3].

[120] R. Taylor and R. Krishna, **1993**. *Multicomponent mass transfer*. Wiley. ISBN: 978-0-471-57417-0.

[121] X. Liu, **2013**. *Diffusion in Liquids: Equilibrium Molecular Simulations and Predictive Engineering Models*. PhD thesis, Delft University of Technology, Delft, The Netherlands.

[122] X. Liu, T. J. Vlugt, and A. Bardow, **2011**. *Maxwell–Stefan diffusivities in liquid mix-*

tures: Using molecular dynamics for testing model predictions. Fluid Phase Equilibria, vol. 301 (1), pp. 110–117, [http://linkinghub.elsevier.com/retrieve/pii/S0378381210005856].

[123] X. Liu, A. Bardow, and T. J. H. Vlugt, **2011**. *Multicomponent Maxwell–Stefan Diffusivities at Infinite Dilution*. Industrial & Engineering Chemistry Research, vol. 50 (8), pp. 4776–4782, [http://pubs.acs.org/doi/abs/10.1021/ie102515w].

[124] X. Liu, T. J. Vlugt, and A. Bardow, **2011**. *Predictive Darken Equation for Maxwell-Stefan Diffusivities in Multicomponent Mixtures*. Industrial & Engineering Chemistry Research, vol. 50 (17), pp. 10350–10358, [http://pubs.acs.org/doi/abs/10.1021/ie201008a].

[125] X. Liu, T. J. H. Vlugt, and A. Bardow, **2011**. *Maxwell–Stefan Diffusivities in Binary Mixtures of Ionic Liquids with Dimethyl Sulfoxide (DMSO) and H_2O*. The Journal of Physical Chemistry B, vol. 115 (26), pp. 8506–8517, [http://pubs.acs.org/doi/abs/10.1021/jp203026c].

[126] X. Liu, S. K. Schnell, J.-M. Simon, D. Bedeaux, S. Kjelstrup, A. Bardow, and T. J. H. Vlugt, **2011**. *Fick Diffusion Coefficients of Liquid Mixtures Directly Obtained From Equilibrium Molecular Dynamics*. The Journal of Physical Chemistry B, vol. 115 (44), pp. 12921–12929, [http://pubs.acs.org/doi/abs/10.1021/jp208360s].

[127] G. Guevara-Carrion, T. Janzen, Y. M. Muñoz-Muñoz, and J. Vrabec, **2016**. *Mutual diffusion of binary liquid mixtures containing methanol, ethanol, acetone, benzene, cyclohexane, toluene, and carbon tetrachloride*. The Journal of Chemical Physics, vol. 144 (12), no. 124501, [http://scitation.aip.org/content/aip/journal/jcp/144/12/10.1063/1.4943395].

[128] S. Rehfeldt and J. Stichlmair, **2007**. *Measurement and calculation of multicomponent diffusion coefficients in liquids*. Fluid Phase Equilibria, vol. 256 (1-2), pp. 99–104, [http://linkinghub.elsevier.com/retrieve/pii/S0378381206004353].

[129] M. Winkelmann, L. Schneider, W. Gerlinger, B. Sachweh, R. Miller, and H. P. Schuchmann, **2012**. *Mass transport characteristics of alkyl amines in a water/n-decane system*. Journal of Colloid and Interface Science, vol. 372 (1), pp. 164–169, [http://linkinghub.elsevier.com/retrieve/pii/S0021979712000148].

[130] P. Wu and H. W. Siesler, **1999**. *The diffusion of alcohols and water in polyamide 11: A study by fourier-transform near-infrared spectroscopy*. Macromolecular Symposia, vol. 143 (1), pp. 323–336, [http://doi.wiley.com/10.1002/masy.19991430124].

[131] J. Wang and T. Hou, **2011**. *Application of molecular dynamics simulations in molecular property prediction II: Diffusion coefficient*. Journal of Computational Chemistry, vol. 32 (16), pp. 3505–3519, [http://doi.wiley.com/10.1002/jcc.21939].

[132] T. Fox and P. A. Kollman, **1998**. *Application of the RESP Methodology in the Parametrization of Organic Solvents*. The Journal of Physical Chemistry B, vol. 102 (41), pp. 8070–

8079, [http://pubs.acs.org/doi/abs/10.1021/jp9717655].

[133] C. R. Wilke and P. Chang, **1955**. *Correlation of diffusion coefficients in dilute solutions*. AIChE Journal, vol. 1 (2), pp. 264–270, [http://doi.wiley.com/10.1002/aic.690010222].

[134] C. G. Aimoli, E. J. Maginn, and C. R. A. Abreu, **2014**. *Transport properties of carbon dioxide and methane from molecular dynamics simulations*. The Journal of Chemical Physics, vol. 141 (13), no. 134101, [http://aip.scitation.org/doi/10.1063/1.4896538].

[135] H. J. V. Tyrrell and K. R. Harris, **1984**. *Diffusion in liquids: a theoretical and experimental study*. Butterworths. ISBN: 978-0-408-17591-3.

[136] J. Wesselingh and A. Bollen, **1997**. *Multicomponent Diffusivities from the Free Volume Theory*. Chemical Engineering Research and Design, vol. 75 (6), pp. 590–602, [http://linkinghub.elsevier.com/retrieve/pii/S0263876297715752].

[137] O. Suárez-Iglesias, I. Medina, C. Pizarro, and J. L. Bueno, **2008**. *On predicting self-diffusion coefficients in fluids*. Fluid Phase Equilibria, vol. 269 (1-2), pp. 80–92, [http://linkinghub.elsevier.com/retrieve/pii/S0378381208001829].

[138] O. Suárez-Iglesias, I. Medina, C. Pizarro, and J. L. Bueno, **2007**. *On predicting self-diffusion coefficients from viscosity in gases and liquids*. Chemical Engineering Science, vol. 62 (23), pp. 6499–6515, [http://linkinghub.elsevier.com/retrieve/pii/S0009250907005398].

[139] H. S. Park, T. Chang, and S. H. Lee, **2000**. *Diffusion of small probe molecule in oligomers*. The Journal of Chemical Physics, vol. 113 (13), no. 5502, [http://scitation.aip.org/content/aip/journal/jcp/113/13/10.1063/1.1289820].

[140] W. S. Price, H. Ide, and Y. Arata, **2003**. *Solution Dynamics in Aqueous Monohydric Alcohol Systems*. The Journal of Physical Chemistry A, vol. 107 (24), pp. 4784–4789, [http://pubs.acs.org/doi/abs/10.1021/jp027257z].

[141] N. D. Kondratyuk, G. E. Norman, and V. V. Stegailov, **2016**. *Self-consistent molecular dynamics calculation of diffusion in higher n -alkanes*. The Journal of Chemical Physics, vol. 145 (20), no. 204504, [http://aip.scitation.org/doi/10.1063/1.4967873].

[142] O. A. Moultos, Y. Zhang, I. N. Tsimpanogiannis, I. G. Economou, and E. J. Maginn, **2016**. *System-size corrections for self-diffusion coefficients calculated from molecular dynamics simulations: The case of CO_2 , n-alkanes, and poly(ethylene glycol) dimethyl ethers*. The Journal of Chemical Physics, vol. 145 (7), no. 074109, [http://aip.scitation.org/doi/10.1063/1.4960776].

[143] N. I. Anisa, N. A. Morad, Y. Iwai, and M. H. Shah Ismail, **2016**. *Molecular dynamics simulation for self-diffusion coefficients of ginger bioactive compounds in subcritical water with and without ethanol*. Fluid Phase Equilibria, vol. 407, pp. 197.e1–197.e10, [http://linkinghub.elsevier.com/retrieve/pii/S0378381215003374].

[144] D. J. Keffer, B. J. Edwards, and P. Adhangale, **2004**. *Determination of statistically reliable transport diffusivities from molecular dynamics simulation*. Journal of Non-Newtonian Fluid Mechanics, vol. 120 (1-3), pp. 41–53, [http://linkinghub.elsevier.com/retrieve/pii/S0377025704001053].

[145] D. R. Wheeler and J. Newman, **2004**. *Molecular Dynamics Simulations of Multicomponent Diffusion. 2. Nonequilibrium Method*. The Journal of Physical Chemistry B, vol. 108 (47), pp. 18362–18367, [http://pubs.acs.org/doi/abs/10.1021/jp047849c].

[146] R. Krishna and J. M. van Baten, **2005**. *The Darken Relation for Multicomponent Diffusion in Liquid Mixtures of Linear Alkanes: An Investigation Using Molecular Dynamics (MD) Simulations*. Industrial & Engineering Chemistry Research, vol. 44 (17), pp. 6939–6947, [http://pubs.acs.org/doi/abs/10.1021/ie050146c].

[147] Q. N. Vo, C. A. Hawkins, L. X. Dang, M. Nilsson, and H. D. Nguyen, **2015**. *Computational Study of Molecular Structure and Self-Association of Tri-n-butyl Phosphates in n-Dodecane*. The Journal of Physical Chemistry B, vol. 119 (4), pp. 1588–1597, [http://pubs.acs.org/doi/10.1021/jp510365c].

[148] C. Zhang and X. Yang, **2005**. *Molecular dynamics simulation of ethanol/water mixtures for structure and diffusion properties*. Fluid Phase Equilibria, vol. 231 (1), pp. 1–10, [http://linkinghub.elsevier.com/retrieve/pii/S037838120500066X].

[149] J. Brillo, A. I. Pommrich, and A. Meyer, **2011**. *Relation between Self-Diffusion and Viscosity in Dense Liquids: New Experimental Results from Electrostatic Levitation*. Physical Review Letters, vol. 107 (16), no. 165902, [https://link.aps.org/doi/10.1103/PhysRevLett.107.165902].

[150] V. A. Harmandaris, M. Doxastakis, V. G. Mavrantzas, and D. N. Theodorou, **2002**. *Detailed molecular dynamics simulation of the self-diffusion of n-alkane and cis-1,4 polyisoprene oligomer melts*. The Journal of Chemical Physics, vol. 116 (1), no. 436, [http://scitation.aip.org/content/aip/journal/jcp/116/1/10.1063/1.1416872].

[151] N. Ohtori and Y. Ishii, **2015**. *Explicit expressions of self-diffusion coefficient, shear viscosity, and the Stokes-Einstein relation for binary mixtures of Lennard-Jones liquids*. The Journal of Chemical Physics, vol. 143 (16), no. 164514, [http://aip.scitation.org/doi/10.1063/1.4934627].

[152] G. Guevara-Carrion, J. Vrabec, and H. Hasse, **2011**. *Prediction of self-diffusion coefficient and shear viscosity of water and its binary mixtures with methanol and ethanol by molecular simulation*. The Journal of Chemical Physics, vol. 134 (7), no. 074508, [http://aip.scitation.org/doi/10.1063/1.3515262].

[153] X. Ye, S. Cui, V. F. de Almeida, and B. Khomami, **2013**. *Effect of varying the 1–4 intramolecular scaling factor in atomistic simulations of long-chain n-alkanes with the OPLS-AA model*. Journal of Molecular Modeling, vol. 19 (3), pp. 1251–1258, [http://link.springer.com/10.1007/s00894-012-1651-5].

[154] S. W. I. Siu, K. Pluhackova, and R. A. Böckmann, **2012**. *Optimization of the OPLS-AA Force Field for Long Hydrocarbons*. Journal of Chemical Theory and Computation, vol. 8 (4), pp. 1459–1470, [http://pubs.acs.org/doi/abs/10.1021/ct200908r].

[155] K. Murzyn, M. Bratek, and M. Pasenkiewicz-Gierula, **2013**. *Refined OPLS All-Atom Force Field Parameters for n -Pentadecane, Methyl Acetate, and Dimethyl Phosphate*. The Journal of Physical Chemistry B, vol. 117 (51), pp. 16388–16396, [http://pubs.acs.org/doi/abs/10.1021/jp408162d].

[156] S.-H. Lee and T.-H. Chang, **2003**. *Viscosity and Diffusion Constants Calculation of n-Alkanes by Molecular Dynamics Simulations*. Bulletin of the Korean Chemical Society, vol. 24 (11), pp. 1590–1598, [http://koreascience.or.kr/journal/view.jsp?kj=JCGMCS&py=2003&vnc=v24n11&sp=1590].

[157] D. D. Li and M. L. Greenfield, **2014**. *Viscosity, relaxation time, and dynamics within a model asphalt of larger molecules*. The Journal of Chemical Physics, vol. 140 (03), no. 034507, [http://aip.scitation.org/doi/10.1063/1.4848736].

[158] I.-C. Yeh and G. Hummer, **2004**. *System-Size Dependence of Diffusion Coefficients and Viscosities from Molecular Dynamics Simulations with Periodic Boundary Conditions*. The Journal of Physical Chemistry B, vol. 108 (40), pp. 15873–15879, [http://pubs.acs.org/doi/abs/10.1021/jp0477147].

[159] N. Zhang, Z. Liu, X. Ruan, X. Yan, Y. Song, Z. Shen, X. Wu, and G. He, **2017**. *Molecular dynamics study of confined structure and diffusion of hydrated proton in Hyfion® perfluorosulfonic acid membranes*. Chemical Engineering Science, vol. 158, pp. 234–244, [http://linkinghub.elsevier.com/retrieve/pii/S0009250916305449].

[160] V. K. Michalis, O. A. Moultos, I. N. Tsimpanogiannis, and I. G. Economou, **2016**. *Molecular dynamics simulations of the diffusion coefficients of light n-alkanes in water over a wide range of temperature and pressure*. Fluid Phase Equilibria, vol. 407, pp. 236–242, [http://linkinghub.elsevier.com/retrieve/pii/S0378381215003118].

[161] R. W. Hockney and J. W. Eastwood, **1988**. *Computer simulation using particles*. A. Hilger, special student ed. ISBN: 978-0-85274-392-8.

[162] O. Gereben and L. Pusztai, **2011**. *System size and trajectory length dependence of the static structure factor and the diffusion coefficient as calculated from molecular dynamics simulations: The case of SPC/E water*. Journal of Molecular Liquids, vol. 161 (1), pp. 36–40, [http://linkinghub.elsevier.com/retrieve/pii/S0167732211001231].

[163] B. Dünweg and K. Kremer, **1991**. *Microscopic verification of dynamic scaling in dilute polymer solutions: A molecular-dynamics simulation*. Physical Review Letters, vol. 66 (23), pp. 2996–2999, [https://link.aps.org/doi/10.1103/PhysRevLett.66.2996].

[164] A. Wallqvist and O. Teleman, **1991**. *Properties of flexible water models*. Molecular Physics, vol. 74 (3), pp. 515–533, [http://www.tandfonline.com/doi/abs/10.1080/

00268979100102391].

[165] B. Dünweg, **1993**. *Molecular dynamics algorithms and hydrodynamic screening*. The Journal of Chemical Physics, vol. 99 (9), pp. 6977–6982, [http://aip.scitation.org/doi/10.1063/1.465444].

[166] I. M. Svishchev and P. G. Kusalik, **1994**. *Dynamics in liquid water, water-d2, and water-t2: a comparative simulation study*. The Journal of Physical Chemistry, vol. 98 (3), pp. 728–733, [http://pubs.acs.org/doi/abs/10.1021/j100054a002].

[167] D. M. Heyes, M. J. Cass, J. G. Powles, and W. A. B. Evans, **2007**. *Self-Diffusion Coefficient of the Hard-Sphere Fluid: System Size Dependence and Empirical Correlations*. The Journal of Physical Chemistry B, vol. 111 (6), pp. 1455–1464, [http://pubs.acs.org/doi/abs/10.1021/jp067373s].

[168] G. Guevara-Carrion, Y. Gaponenko, T. Janzen, J. Vrabec, and V. Shevtsova, **2016**. *Diffusion in Multicomponent Liquids: From Microscopic to Macroscopic Scales*. The Journal of Physical Chemistry B, vol. 120 (47), pp. 12193–12210, [http://pubs.acs.org/doi/10.1021/acs.jpcb.6b09810].

[169] T. Funazukuri, C. Y. Kong, and S. Kagei, **2006**. *Binary diffusion coefficients in supercritical fluids: Recent progress in measurements and correlations for binary diffusion coefficients*. The Journal of Supercritical Fluids, vol. 38 (2), pp. 201–210, [http://linkinghub.elsevier.com/retrieve/pii/S089684460600101X].

[170] T. Vardag, N. Karger, and H.-D. Lüdemann, **1991**. *Temperature and Pressure Dependence of Self Diffusion in Long Liquid n-Alkanes*. Berichte der Bunsengesellschaft für physikalische Chemie, vol. 95 (8), pp. 859–865, [http://doi.wiley.com/10.1002/bbpc.19910950803].

[171] M. Mondello and G. S. Grest, **1995**. *Molecular dynamics of linear and branched alkanes*. The Journal of Chemical Physics, vol. 103 (16), pp. 7156–7165, [http://aip.scitation.org/doi/10.1063/1.470344].

[172] M. Mondello, G. S. Grest, A. R. Garcia, and B. G. Silbernagel, **1996**. *Molecular dynamics of linear and branched alkanes: Simulations and nuclear magnetic resonance results*. The Journal of Chemical Physics, vol. 105 (12), pp. 5208–5215, [http://aip.scitation.org/doi/10.1063/1.472363].

[173] H. Spikes, **2018**. *Stress-augmented thermal activation: Tribology feels the force*. Friction, vol. 6 (1), pp. 1–31, [http://link.springer.com/10.1007/s40544-018-0201-2].

[174] L. Miller and P. C. Carman, **1959**. *Self-diffusion in mixtures. Part 2. — Simple binary liquid mixtures*. Trans. Faraday Soc., vol. 55 (0), pp. 1831–1837, [http://xlink.rsc.org/?DOI=TF9595501831].

[175] J. L. Bradley-Shaw, P. J. Camp, P. J. Dowding, and K. Lewtas, **2015**. *Glycerol Monooleate Reverse Micelles in Nonpolar Solvents: Computer Simulations and Small-Angle Neutron Scattering*. The Journal of Physical Chemistry B, vol. 119 (11), pp. 4321–4331, [http://

pubs.acs.org/doi/10.1021/acs.jpcb.5b00213].

[176] J. L. Bradley-Shaw, P. J. Camp, P. J. Dowding, and K. Lewtas, **2016**. *Molecular Dynamics Simulations of Glycerol Monooleate Confined between Mica Surfaces*. Langmuir, vol. 32 (31), pp. 7707–7718, [http://pubs.acs.org/doi/10.1021/acs.langmuir.6b00091].

[177] J. L. Bradley-Shaw, P. J. Camp, P. J. Dowding, and K. Lewtas, **2018**. *Self-assembly and friction of glycerol monooleate and its hydrolysis products in bulk and confined non-aqueous solvents*. Physical Chemistry Chemical Physics, vol. 20 (26), pp. 17648–17657, [http://xlink.rsc.org/?DOI=C8CP01785A].

[178] I. Minami and S. Mori, **2007**. *Concept of molecular design towards additive technology for advanced lubricants*. Lubrication Science, vol. 19 (2), pp. 127–149, [http://doi.wiley.com/10.1002/ls.37].

[179] S. Sambasivan, D. Fischer, S. Hsu, and S. Hsieh, **2008**. *Molecular Understanding of Nanofriction of Self-Assembled Monolayers on Silicon Using AFM*, in Surfactants in Tribology (G. Biresaw and K. Mittal, eds.), CRC Press.

[180] B. J. Briscoe and D. C. B. Evans, **1982**. *The Shear Properties of Langmuir-Blodgett Layers*. Proceedings of the Royal Society A: Mathematical, Physical and Engineering Sciences, vol. 380 (1779), pp. 389–407, [http://rspa.royalsocietypublishing.org/cgi/doi/10.1098/rspa.1982.0048].

[181] S. Jahanmir and M. Beltzer, **1986**. *An Adsorption Model for Friction in Boundary Lubrication*. ASLE Transactions, vol. 29 (3), pp. 423–430, [http://www.tandfonline.com/doi/abs/10.1080/05698198608981704].

[182] M. H. Wood, M. T. Casford, R. Steitz, A. Zarbakhsh, R. J. L. Welbourn, and S. M. Clarke, **2016**. *Comparative Adsorption of Saturated and Unsaturated Fatty Acids at the Iron Oxide/Oil Interface*. Langmuir, vol. 32 (2), pp. 534–540, [http://pubs.acs.org/doi/10.1021/acs.langmuir.5b04435].

[183] M. J. Incorvio, **1989**. *X-Ray Photoelectron Spectroscopic Studies of Metal/Inhibitor Systems: Structure and Bonding at the Iron/Amine Interface*. Journal of The Electrochemical Society, vol. 136 (9), pp. 2493–2498, [http://jes.ecsdl.org/cgi/doi/10.1149/1.2097443].

[184] J. Wielant, T. Hauffman, O. Blajiev, R. Hausbrand, and H. Terryn, **2007**. *Influence of the Iron Oxide Acid-Base Properties on the Chemisorption of Model Epoxy Compounds Studied by XPS*. The Journal of Physical Chemistry C, vol. 111 (35), pp. 13177–13184, [http://pubs.acs.org/doi/abs/10.1021/jp072354j].

[185] M. Campana, A. Teichert, S. Clarke, R. Steitz, J. R. P. Webster, and A. Zarbakhsh, **2011**. *Surfactant Adsorption at the Metal–Oil Interface*. Langmuir, vol. 27 (10), pp. 6085–6090, [http://pubs.acs.org/doi/abs/10.1021/la200670w].

[186] R. O. Jones, **2015**. *Density functional theory: Its origins, rise to prominence, and future*.

Reviews of Modern Physics, vol. 87 (3), pp. 897–923, [https://link.aps.org/doi/10.1103/RevModPhys.87.897].

[187] S. Rayne and K. Forest, **2010**. *Theoretical studies on the pKa values of perfluoroalkyl carboxylic acids*. Journal of Molecular Structure: THEOCHEM, vol. 949 (1-3), pp. 60–69, [http://linkinghub.elsevier.com/retrieve/pii/S0166128010001867].

[188] G. Kresse and J. Hafner, **1993**. *Ab initio molecular dynamics for liquid metals*. Physical Review B, vol. 47 (1), pp. 558–561, [https://link.aps.org/doi/10.1103/PhysRevB.47.558].

[189] G. Kresse and J. Hafner, **1994**. *Norm-conserving and ultrasoft pseudopotentials for first-row and transition elements*. Journal of Physics: Condensed Matter, vol. 6 (40), pp. 8245–8257, [http://stacks.iop.org/0953-8984/6/i=40/a=015?key=crossref.c873d42d314a5d78c0adf9bdfc34516c].

[190] G. Kresse and J. Hafner, **1994**. *Ab initio molecular-dynamics simulation of the liquid-metal — amorphous-semiconductor transition in germanium*. Physical Review B, vol. 49 (20), pp. 14251–14269, [https://link.aps.org/doi/10.1103/PhysRevB.49.14251].

[191] G. Kresse and J. Furthmüller, **1996**. *Efficient iterative schemes for ab initio total-energy calculations using a plane-wave basis set*. Physical Review B, vol. 54 (16), pp. 11169–11186, [https://link.aps.org/doi/10.1103/PhysRevB.54.11169].

[192] G. Kresse and J. Furthmüller, **1996**. *Efficiency of ab initio total energy calculations for metals and semiconductors using a plane-wave basis set*. Computational Materials Science, vol. 6 (1), pp. 15–50, [http://linkinghub.elsevier.com/retrieve/pii/0927025696000080].

[193] G. Kresse and D. Joubert, **1999**. *From ultrasoft pseudopotentials to the projector augmented-wave method*. Physical Review B, vol. 59 (3), pp. 1758–1775, [https://link.aps.org/doi/10.1103/PhysRevB.59.1758].

[194] P. O. Bedolla, G. Feldbauer, M. Wolloch, S. J. Eder, N. Dörr, P. Mohn, J. Redinger, and A. Vernes, **2014**. *Effects of van der Waals Interactions in the Adsorption of Isooctane and Ethanol on Fe(100) Surfaces*. The Journal of Physical Chemistry C, vol. 118 (31), pp. 17608–17615, [http://pubs.acs.org/doi/10.1021/jp503829c].

[195] J. P. Perdew, K. Burke, and M. Ernzerhof, **1996**. *Generalized Gradient Approximation Made Simple*. Physical Review Letters, vol. 77 (18), pp. 3865–3868, [https://link.aps.org/doi/10.1103/PhysRevLett.77.3865].

[196] J. P. Perdew, K. Burke, and M. Ernzerhof, **1997**. *Generalized Gradient Approximation Made Simple [Phys. Rev. Lett. 77, 3865 (1996)]*. Physical Review Letters, vol. 78 (7), pp. 1396–1396, [https://link.aps.org/doi/10.1103/PhysRevLett.78.1396].

[197] S. L. Dudarev, G. A. Botton, S. Y. Savrasov, C. J. Humphreys, and A. P. Sutton, **1998**. *Electron-energy-loss spectra and the structural stability of nickel oxide: An LSDA+U study*. Physical Review B, vol. 57 (3), pp. 1505–1509, [https://link.aps.org/doi/10.1103/

PhysRevB.57.1505].

[198] S. S. Rath, H. Sahoo, B. Das, and B. K. Mishra, **2014**. *Density functional calculations of amines on the (101) face of quartz*. Minerals Engineering, vol. 69, pp. 57–64, [http://linkinghub.elsevier.com/retrieve/pii/S0892687514002271].

[199] D. H. Buckley, **1981**. *Surface effects in adhesion, friction, wear, and lubrication*. No. 5 in Tribology series, Elsevier Scientific Pub. Co. ISBN: 978-0-444-41966-8.

[200] P. W. Atkins and J. De Paula, **2002**. *Physical chemistry*. W.H. Freeman, 7th ed. ISBN: 978-0-7167-3539-7.

[201] J.-G. Wang and A. Selloni, **2009**. *First Principles Study of Fatty Acid Monolayers on Au(111)†*. The Journal of Physical Chemistry C, vol. 113 (20), pp. 8895–8900, [http://pubs.acs.org/doi/abs/10.1021/jp901842p].

[202] Y.-F. Y. Yao, **1963**. *Heats of adsorption of amines, hydrocarbons, and water vapor on reduced and oxidized iron surfaces*. The Journal of Physical Chemistry, vol. 67 (10), pp. 2055–2061, [http://pubs.acs.org/doi/abs/10.1021/j100804a022].

[203] F. L. Hirshfeld, **1977**. *Bonded-atom fragments for describing molecular charge densities*. Theoretica Chimica Acta, vol. 44 (2), pp. 129–138, [http://link.springer.com/10.1007/BF00549096].

[204] T. D. Ta, A. K. Tieu, H. Zhu, Q. Zhu, P. B. Kosasih, J. Zhang, and G. Deng, **2016**. *Tribological Behavior of Aqueous Copolymer Lubricant in Mixed Lubrication Regime*. ACS Applied Materials & Interfaces, vol. 8 (8), pp. 5641–5652, [http://pubs.acs.org/doi/10.1021/acsami.5b10905].

[205] I.-C. Yeh and M. L. Berkowitz, **1999**. *Ewald summation for systems with slab geometry*. The Journal of Chemical Physics, vol. 111 (7), pp. 3155–3162, [http://aip.scitation.org/doi/10.1063/1.479595].

[206] C. Allen and E. Drauglis, **1969**. *Boundary layer lubrication: monolayer or multilayer*. Wear, vol. 14 (5), pp. 363–384, [http://linkinghub.elsevier.com/retrieve/pii/0043164869900179].

[207] D. K. Schwartz, **2001**. *Mechanisms and kinetics of self-assembled monolayer formation*. Annual Review of Physical Chemistry, vol. 52 (1), pp. 107–137, [http://www.annualreviews.org/doi/10.1146/annurev.physchem.52.1.107].

[208] L. Salem, **1962**. *Attractive Forces between Long Saturated Chains at Short Distances*. The Journal of Chemical Physics, vol. 37 (9), pp. 2100–2113, [http://aip.scitation.org/doi/10.1063/1.1733431].

[209] M. Beltzer and S. Jahanmir, **1987**. *Role of Dispersion Interactions Between Hydrocarbon Chains in Boundary Lubrication*. ASLE Transactions, vol. 30 (1), pp. 47–54, [http://www.tandfonline.com/doi/abs/10.1080/05698198708981729].

[210] P. T. Mikulski, G. Gao, G. M. Chateauneuf, and J. A. Harrison, **2005**. *Contact forces at the*

sliding interface: Mixed versus pure model alkane monolayers. The Journal of Chemical Physics, vol. 122 (2), p. 024701, [http://aip.scitation.org/doi/10.1063/1.1828035].

[211] M. Ferrari, **2012**. *Self-Assembly of Surfactants at Solid Surfaces*, in Supramolecular Chemistry (P. A. Gale and J. W. Steed, eds.), John Wiley & Sons, Ltd.

[212] D.-S. Kong, S.-L. Yuan, Y.-X. Sun, and Z.-Y. Yu, **2004**. *Self-assembled monolayer of o-aminothiophenol on Fe(110) surface: a combined study by electrochemistry, in situ STM, and molecular simulations*. Surface Science, vol. 573 (2), pp. 272–283, [http://linkinghub.elsevier.com/retrieve/pii/S0039602804012750].

[213] G. Binnig, C. F. Quate, and C. Gerber, **1986**. *Atomic Force Microscope*. Physical Review Letters, vol. 56 (9), pp. 930–933, [https://link.aps.org/doi/10.1103/PhysRevLett.56.930].

[214] C. G. Slough, H. Ohtani, M. P. Everson, and D. J. Melotik, **1998**. *The Effect of Friction Modifiers on the Low-Speed Friction Characteristics of Automatic Transmission Fluids Observed with Scanning Force Microscopy*. SAE Technical - Paper 981099, [http://papers.sae.org/981099/].

[215] E. Barrena, S. Kopta, D. F. Ogletree, D. H. Charych, and M. Salmeron, **1999**. *Relationship between Friction and Molecular Structure: Alkylsilane Lubricant Films under Pressure*. Physical Review Letters, vol. 82 (14), pp. 2880–2883, [https://link.aps.org/doi/10.1103/PhysRevLett.82.2880].

[216] S. Lee, Y.-S. Shon, R. Colorado, R. L. Guenard, T. R. Lee, and S. S. Perry, **2000**. *The Influence of Packing Densities and Surface Order on the Frictional Properties of Alkanethiol Self-Assembled Monolayers (SAMs) on Gold: A Comparison of SAMs Derived from Normal and Spiroalkanedithiols*. Langmuir, vol. 16 (5), pp. 2220–2224, [http://pubs.acs.org/doi/abs/10.1021/la9909345].

[217] B. D. Beake and G. J. Leggett, **2000**. *Variation of Frictional Forces in Air with the Compositions of Heterogeneous Organic Surfaces*. Langmuir, vol. 16 (2), pp. 735–739, [http://pubs.acs.org/doi/abs/10.1021/la990782d].

[218] E. W. van der Vegte, A. Subbotin, G. Hadziioannou, P. R. Ashton, and J. A. Preece, **2000**. *Nanotribological Properties of Unsymmetrical n -Dialkyl Sulfide Monolayers on Gold: Effect of Chain Length on Adhesion, Friction, and Imaging*. Langmuir, vol. 16 (7), pp. 3249–3256, [http://pubs.acs.org/doi/abs/10.1021/la990911q].

[219] N. J. Brewer, B. D. Beake, and G. J. Leggett, **2001**. *Friction Force Microscopy of Self-Assembled Monolayers: Influence of Adsorbate Alkyl Chain Length, Terminal Group Chemistry, and Scan Velocity*. Langmuir, vol. 17 (6), pp. 1970–1974, [http://pubs.acs.org/doi/abs/10.1021/la001568o].

[220] S. Lee, A. Puck, M. Graupe, R. Colorado, Y.-S. Shon, T. R. Lee, and S. S. Perry, **2001**. *Structure, Wettability, and Frictional Properties of Phenyl-Terminated Self-Assembled Mono-*

layers on Gold. Langmuir, vol. 17 (23), pp. 7364–7370, [http://pubs.acs.org/doi/abs/10.1021/la0111497].

[221] E. Barrena, C. Ocal, and M. Salmeron, **2001**. *A comparative AFM study of the structural and frictional properties of mixed and single component films of alkanethiols on Au(111)*. Surface Science, vol. 482-485, pp. 1216–1221, [http://linkinghub.elsevier.com/retrieve/pii/S003960280100869X].

[222] S. S. Perry, S. Lee, Y.-S. Shon, R. Colorado, and T. R. Lee, **2001**. *The relationships between interfacial friction and the conformational order of organic thin films*. Tribology Letters, vol. 10 (1-2), pp. 81–87, [https://link.springer.com/article/10.1023%2FA%3A1009022211823].

[223] M. Salmeron, **2001**. *Generation of defects in model lubricant monolayers and their contribution to energy dissipation in friction*. Tribology Letters, vol. 10 (1-2), pp. 69–79, [https://link.springer.com/article/10.1023%2FA%3A1009026312732].

[224] J. J. Benítez, S. Kopta, D. F. Ogletree, and M. Salmeron, **2002**. *Preparation and Characterization of Self-Assembled Monolayers of Octadecylamine on Mica Using Hydrophobic Solvents*. Langmuir, vol. 18 (16), pp. 6096–6100, [http://pubs.acs.org/doi/abs/10.1021/la011629y].

[225] J. J. Benítez, D. F. Ogletree, and M. Salmeron, **2003**. *Preparation and Characterization of Self-Assembled Multilayers of Octadecylamine on Mica from Ethanol Solutions*. Langmuir, vol. 19 (8), pp. 3276–3281, [http://pubs.acs.org/doi/abs/10.1021/la020325o].

[226] J. J. Benítez, S. Kopta, I. Díez-Pérez, F. Sanz, D. F. Ogletree, and M. Salmeron, **2003**. *Molecular Packing Changes of Octadecylamine Monolayers on Mica Induced by Pressure and Humidity*. Langmuir, vol. 19 (3), pp. 762–765, [https://pubs.acs.org/doi/10.1021/la020705%2B].

[227] N. J. Brewer and G. J. Leggett, **2004**. *Chemical Force Microscopy of Mixed Self-Assembled Monolayers of Alkanethiols on Gold: Evidence for Phase Separation*. Langmuir, vol. 20 (10), pp. 4109–4115, [http://pubs.acs.org/doi/abs/10.1021/la036301e].

[228] N. J. Brewer, T. T. Foster, G. J. Leggett, M. R. Alexander, and E. McAlpine, **2004**. *Comparative Investigations of the Packing and Ambient Stability of Self-Assembled Monolayers of Alkanethiols on Gold and Silver by Friction Force Microscopy*. The Journal of Physical Chemistry B, vol. 108 (15), pp. 4723–4728, [http://pubs.acs.org/doi/abs/10.1021/jp035492r].

[229] J. J. Benítez and M. Salmeron, **2006**. *The influence of chain length and ripening time on the self-assembly of alkylamines on mica*. The Journal of Chemical Physics, vol. 125 (4), p. 044708, [http://aip.scitation.org/doi/10.1063/1.2221692].

[230] J. J. Benítez, J. A. Heredia-Guerrero, and A. Heredia, **2007**. *Self-Assembly of Carboxylic Acids and Hydroxyl Derivatives on Mica. A Qualitative AFM Study*. The Journal of Physical Chemistry C, vol. 111 (26), pp. 9465–9470, [http://pubs.acs.org/doi/abs/10.1021/

jp070563y].

[231] J. J. Benítez, J. A. Heredia-Guerrero, and M. Salmeron, **2010**. *Steering the Self-Assembly of Octadecylamine Monolayers on Mica by Controlled Mechanical Energy Transfer from the AFM Tip*. The Journal of Physical Chemistry C, vol. 114 (29), pp. 12630–12634, [http://pubs.acs.org/doi/10.1021/jp102813s].

[232] H. Cheng and Y. Hu, **2012**. *Influence of chain ordering on frictional properties of self-assembled monolayers (SAMs) in nano-lubrication*. Advances in Colloid and Interface Science, vol. 171-172, pp. 53–65, [http://linkinghub.elsevier.com/retrieve/pii/S0001868612000061].

[233] H. Koshima, Y. Iyotani, Q. Peng, and S. Ye, **2016**. *Study of Friction-Reduction Properties of Fatty Acids and Adsorption Structures of their Langmuir-Blodgett Monolayers using Sum-Frequency Generation Spectroscopy and Atomic Force Microscopy*. Tribology Letters, vol. 64 (3), [http://link.springer.com/10.1007/s11249-016-0771-y].

[234] D. Tabor and R. H. S. Winterton, **1969**. *The Direct Measurement of Normal and Retarded van der Waals Forces*. Proceedings of the Royal Society A: Mathematical, Physical and Engineering Sciences, vol. 312 (1511), pp. 435–450, [http://rspa.royalsocietypublishing.org/cgi/doi/10.1098/rspa.1969.0169].

[235] J.-M. Georges, A. Tonck, and D. Mazuyer, **1994**. *Interfacial friction of wetted monolayers*. Wear, vol. 175 (1-2), pp. 59–62, [http://linkinghub.elsevier.com/retrieve/pii/0043164894901686].

[236] Y. Zhu, H. Ohtani, M. L. Greenfield, M. Ruths, and S. Granick, **2003**. *Modification of boundary lubrication by oil-soluble friction modifier additives*. Tribology Letters, vol. 15, p. 127–134, [https://link.springer.com/article/10.1023%2FA%3A1024405115736].

[237] D. Mazuyer, J. Cayer-Barrioz, A. Tonck, and F. Jarnias, **2008**. *Friction Dynamics of Confined Weakly Adhering Boundary Layers*. Langmuir, vol. 24 (8), pp. 3857–3866, [http://pubs.acs.org/doi/abs/10.1021/la703152q].

[238] T. Hirayama, T. Torii, Y. Konishi, M. Maeda, T. Matsuoka, K. Inoue, M. Hino, D. Yamazaki, and M. Takeda, **2012**. *Thickness and density of adsorbed additive layer on metal surface in lubricant by neutron reflectometry*. Tribology International, vol. 54, pp. 100–105, [http://linkinghub.elsevier.com/retrieve/pii/S0301679X12001296].

[239] M. T. L. Casford and P. B. Davies, **2009**. *The Structure of Oleamide Films at the Aluminum/Oil Interface and Aluminum/Air Interface Studied by Sum Frequency Generation (SFG) Vibrational Spectroscopy and Reflection Absorption Infrared Spectroscopy (RAIRS)*. ACS Applied Materials & Interfaces, vol. 1 (8), pp. 1672–1681, [http://pubs.acs.org/doi/10.1021/am900199f].

[240] J. J. Benítez, M. A. San-Miguel, S. Domínguez-Meister, J. A. Heredia-Guerrero, and M. Salmeron, **2011**. *Structure and Chemical State of Octadecylamine Self-Assembled*

Monolayers on Mica. The Journal of Physical Chemistry C, vol. 115 (40), pp. 19716–19723, [http://pubs.acs.org/doi/10.1021/jp203871g].

[241] K. Miyake, T. Kume, M. Nakano, A. Korenaga, K. Takiwatari, R. Tsuboi, and S. Sasaki, **2012**. *Effects of Surface Chemical Properties on the Frictional Properties of Self-Assembled Monolayers Lubricated with Oleic Acid*. Tribology Online, vol. 7 (4), pp. 218–224, [http://japanlinkcenter.org/DN/JST.JSTAGE/trol/7.218?lang=en&from=CrossRef&type=abstract].

[242] H. A. Spikes and A. Cameron, **1974**. *A Comparison of Adsorption and Boundary Lubricant Failure*. Proceedings of the Royal Society A: Mathematical, Physical and Engineering Sciences, vol. 336 (1607), pp. 407–419, [http://rspa.royalsocietypublishing.org/cgi/doi/10.1098/rspa.1974.0027].

[243] S. Loehlé and M. C. Righi, **2017**. *First principles study of organophosphorus additives in boundary lubrication conditions: Effects of hydrocarbon chain length*. Lubrication Science, vol. 29 (7), pp. 485–491, [http://doi.wiley.com/10.1002/ls.1382].

[244] M. A. Moller, D. J. Tildesley, K. S. Kim, and N. Quirke, **1991**. *Molecular dynamics simulation of a Langmuir-Blodgett film*. The Journal of Chemical Physics, vol. 94 (12), pp. 8390–8401, [http://aip.scitation.org/doi/10.1063/1.460071].

[245] S. Karaborni and G. Verbist, **1994**. *Effect of Chain Conformation on the Tilt Behaviour in Langmuir Monolayers*. Europhysics Letters (EPL), vol. 27 (6), pp. 467–472, [http://stacks.iop.org/0295-5075/27/i=6/a=010?key=crossref.3ebc590e385f8761a8657f5adaaefd79].

[246] M. L. Greenfield and H. Ohtani, **1999**. *Molecular dynamics simulation study of model friction modifier additives confined between two surfaces*. Tribology Letters, vol. 7 (2-3), pp. 137—-145, [https://link.springer.com/article/10.1023/A:1019133723193].

[247] Pradip and B. Rai, **2002**. *Design of tailor-made surfactants for industrial applications using a molecular modelling approach*. Colloids and Surfaces A: Physicochemical and Engineering Aspects, vol. 205 (1-2), pp. 139–148, [http://linkinghub.elsevier.com/retrieve/pii/S0927775701011530].

[248] B. Rai, Sathish P., C. P. Malhotra, Pradip, and K. G. Ayappa, **2004**. *Molecular Dynamic Simulations of Self-Assembled Alkylthiolate Monolayers on an Au(111) Surface*. Langmuir, vol. 20 (8), pp. 3138–3144, [http://pubs.acs.org/doi/abs/10.1021/la0357256].

[249] M. L. Greenfield and H. Ohtani, **2005**. *Packing of Simulated Friction Modifier Additives under Confinement*. Langmuir, vol. 21 (16), pp. 7568–7578, [http://pubs.acs.org/doi/abs/10.1021/la046862l].

[250] S. C. B. Mannsfeld and T. Fritz, **2006**. *Advanced modelling of epitaxial ordering of organic layers on crystalline surfaces*. Modern Physics Letters B, vol. 20 (11), pp. 585–605, [http://www.worldscientific.com/doi/abs/10.1142/S0217984906011189].

[251] J. Davidson, S. Hinchley, S. Harris, A. Parkin, S. Parsons, and P. Tasker, **2006**. *Molecular dynamics simulations to aid the rational design of organic friction modifiers*. Journal of Molecular Graphics and Modelling, vol. 25 (4), pp. 495–506, [http://linkinghub.elsevier.com/retrieve/pii/S1093326306000660].

[252] M. L. Klein and W. Shinoda, **2008**. *Large-Scale Molecular Dynamics Simulations of Self-Assembling Systems*. Science, vol. 321 (5890), pp. 798–800, [http://www.sciencemag.org/cgi/doi/10.1126/science.1157834].

[253] P. Clancy, **2011**. *Application of Molecular Simulation Techniques to the Study of Factors Affecting the Thin-Film Morphology of Small-Molecule Organic Semiconductors*. Chemistry of Materials, vol. 23 (3), pp. 522–543, [http://pubs.acs.org/doi/abs/10.1021/cm102231b].

[254] H. Feng, K. E. Becker, J. Zhou, and K. A. Fichthorn, **2012**. *Molecular Thin Films on Solid Surfaces: Mechanisms of Melting*. Langmuir, vol. 28 (19), pp. 7382–7392, [http://pubs.acs.org/doi/10.1021/la300826p].

[255] W. Shinoda, R. DeVane, and M. L. Klein, **2012**. *Computer simulation studies of self-assembling macromolecules*. Current Opinion in Structural Biology, vol. 22 (2), pp. 175–186, [http://linkinghub.elsevier.com/retrieve/pii/S0959440X12000292].

[256] J. Rodriguez, M. D. Elola, and D. Laria, **2015**. *Equilibrium and Dynamical Characteristics of Imidazole Langmuir Monolayers on Graphite Sheets*. The Journal of Physical Chemistry B, vol. 119 (29), pp. 9123–9128, [http://pubs.acs.org/doi/10.1021/jp508913w].

[257] B. Rai and Pradip, **2017**. *Modeling self-assembly of surfactants at interfaces*. Current Opinion in Chemical Engineering, vol. 15, pp. 84–94, [https://linkinghub.elsevier.com/retrieve/pii/S2211339817300011].

[258] T. Szauer and A. Brandt, **1983**. *Equilibria in solutions of amines and fatty acids with relevance to the corrosion inhibition of iron*. Corrosion Science, vol. 23 (12), pp. 1247–1257, [http://linkinghub.elsevier.com/retrieve/pii/0010938X83900756].

[259] T. Szauer and A. Brandt, **1983**. *The corrosion inhibition of iron by amines and fatty acids in neutral media*. Corrosion Science, vol. 23, pp. 473–480, [http://linkinghub.elsevier.com/retrieve/pii/0010938X83900975].

[260] T. Szauer, **1983**. *The corrosion inhibition of iron by amines and fatty acids placed in protective coatings*. Corrosion Science, vol. 23 (5), pp. 481–494, [http://linkinghub.elsevier.com/retrieve/pii/0010938X83900987].

[261] S. Raicheva, B. Aleksiev, and E. Sokolova, **1993**. *The effect of the chemical structure of some nitrogen- and sulphur-containing organic compounds on their corrosion inhibiting action*. Corrosion Science, vol. 34 (2), pp. 343–350, [http://linkinghub.elsevier.com/retrieve/pii/0010938X93900115].

[262] S. Ramachandran, B.-L. Tsai, M. Blanco, H. Chen, Y. Tang, and W. A. Goddard, **1996**. *Self-Assembled Monolayer Mechanism for Corrosion Inhibition of Iron by Imidazolines*.

Langmuir, vol. 12 (26), pp. 6419–6428, [http://pubs.acs.org/doi/abs/10.1021/la960646y].

[263] S. Ramachandran, B.-L. Tsai, M. Blanco, H. Chen, Y. Tang, and W. A. Goddard, **1997**. *Atomistic Simulations of Oleic Imidazolines Bound to Ferric Clusters*. The Journal of Physical Chemistry A, vol. 101 (1), pp. 83–89, [http://pubs.acs.org/doi/abs/10.1021/jp962041g].

[264] S. Xia, M. Qiu, L. Yu, F. Liu, and H. Zhao, **2008**. *Molecular dynamics and density functional theory study on relationship between structure of imidazoline derivatives and inhibition performance*. Corrosion Science, vol. 50 (7), pp. 2021–2029, [http://linkinghub.elsevier.com/retrieve/pii/S0010938X08001467].

[265] J. Zhang, J. Liu, W. Yu, Y. Yan, L. You, and L. Liu, **2010**. *Molecular modeling of the inhibition mechanism of 1-(2-aminoethyl)-2-alkyl-imidazoline*. Corrosion Science, vol. 52 (6), pp. 2059–2065, [http://linkinghub.elsevier.com/retrieve/pii/S0010938X10000776].

[266] Y. C. Kong and J. Alejandre, D. J. and Tildesley, **1997**. *The molecular dynamics simulation of boundary-layer lubrication*. Molecular Physics, vol. 92 (1), pp. 7–18, [https://www.tandfonline.com/doi/full/10.1080/002689797170554].

[267] L. Serreau, M. Beauvais, C. Heitz, and E. Barthel, **2009**. *Adsorption and onset of lubrication by a double-chained cationic surfactant on silica surfaces*. Journal of Colloid and Interface Science, vol. 332 (2), pp. 382–388, [http://linkinghub.elsevier.com/retrieve/pii/S0021979708017347].

[268] A. Tomlinson, T. N. Danks, D. M. Heyes, S. E. Taylor, and D. J. Moreton, **1997**. *Interfacial Characterization of Succinimide Surfactants*. Langmuir, vol. 13 (22), pp. 5881–5893, [http://pubs.acs.org/doi/abs/10.1021/la970550j].

[269] A. Tomlinson, B. Scherer, E. Karakosta, M. Oakey, T. Danks, D. Heyes, and S. Taylor, **2000**. *Adsorption properties of succinimide dispersants on carbonaceous substrates*. Carbon, vol. 38 (1), pp. 13–28, [http://linkinghub.elsevier.com/retrieve/pii/S0008622399000871].

[270] J. Zhang, E. Yamaguchi, and H. Spikes, **2014**. *The Antagonism between Succinimide Dispersants and a Secondary Zinc Dialkyl Dithiophosphate*. Tribology Transactions, vol. 57 (1), pp. 57–65, [http://www.tandfonline.com/doi/abs/10.1080/10402004.2013.845275].

[271] A. Kontou, M. Southby, N. Morgan, and H. A. Spikes, **2018**. *Influence of Dispersant and ZDDP on Soot Wear*. Tribology Letters, vol. 66 (4), [http://link.springer.com/10.1007/s11249-018-1115-x].

[272] H. Ohtani and R. J. Hartley, **1994**. *Friction modifier compositions and their use*. US 5441656A.

[273] H. Ohtani and R. J. Hartley, **1994**. *Automatic transmission fluids and additives therefor*.

US 5372735A.

[274] T. A. Tagliamonte, C. D. Tipton, and W. C. J. Ward, **2009**. *Method for lubricating a dual clutch transmission*. EP 1 499 701 B2.

[275] M. Ikeda, S. Hurley, W. D. Abraham, J. L. Sumiejski, and C. D. Tipton, **2010**. *Functional fluid*. US 2010/0144565 A1.

[276] Y. F. Suen, M. L. Lackie, and F. Parsinejad, **2012**. *Aminomethyl-substituted imidazole compounds for use as friction modifiers in lubricating oil compositions*. US 8268761B2.

[277] Y. F. Suen, **2012**. *Lubricating composition containing friction modifier blend*. WO/2012/071185.

[278] J. S. Vilardo, **2008**. *Fuel additives for use in high level alcohol-gasoline blends*. WO/2008/082916.

[279] J. S. Vilardo, **2009**. *Fuel additives for use in high level alcohol-gasoline blends*. US20090307965A1.

[280] J. S. Vilardo, **2010**. *Fuel additives for use in alcohol-fuels*. US 2010/0107484 A1.

[281] P. J. Dowding and C. J. Adams, **2009**. *Lubricating oil composition*. US 2009/0093385 A1.

[282] P. J. Dowding and C. J. Adams, **2009**. *Overbased metal sulphonate detergent*. US 2009/0093386 A1.

[283] B. J. Kaufman, J. R. Ketcham, and W. P. Acker, **2010**. *Fuel additives and fuel compositions and methods for making and using the same*. US 2010/0132253 A1.

[284] D. J. Saccomando, R. J. Vickerman, and S. M. Patterson, **2014**. *Amine Derivatives as Friction Modifiers in Lubricants*. US 8 778 858 B2.

[285] S. Lundgren, **2016**. *Fatty amine salts as friction modifiers for lubricants*. US 9 487 728.

[286] E. Yamaguchi, Z. Zhang, M. Kasrai, and G. Bancroft, **2003**. *Study of the Interaction of ZDDP and Dispersants Using X-ray Absorption Near Edge Structure Spectroscopy—Part 2: Tribochemical Reactions*. Tribology Letters, vol. 15 (4), pp. 385–394, [http://link.springer.com/10.1023/B:TRIL.0000003062.91646.8f].

[287] E. L. Cook and N. Hackerman, **1951**. *Adsorption of Polar Organic Compounds on Steel*. The Journal of Physical Chemistry, vol. 55 (4), pp. 549–557, [http://pubs.acs.org/doi/abs/10.1021/j150487a010].

[288] N. Hackerman and A. H. Roebuck, **1954**. *Adsorption of Polar Organic Compounds on Steel*. Industrial & Engineering Chemistry, vol. 46 (7), pp. 1481–1485, [http://pubs.acs.org/doi/abs/10.1021/ie50535a048].

[289] K. T. Miklozic, T. R. Forbus, and H. A. Spikes, **2007**. *Performance of Friction Modifiers on ZDDP-Generated Surfaces*. Tribology Transactions, vol. 50 (3), pp. 328–335, [http://www.tandfonline.com/doi/abs/10.1080/10402000701413505].

[290] S. Soltanahmadi, A. Morina, M. C. P. van Eijk, I. Nedelcu, and A. Neville, **2016**. *Investi-*

gation of the effect of a diamine-based friction modifier on micropitting and the properties of tribofilms in rolling-sliding contacts. Journal of Physics D: Applied Physics, vol. 49 (50), p. 505302, [http://stacks.iop.org/0022-3727/49/i=50/a=505302?key=crossref.b6dbba8b86cdad078a06777c35492be7].

[291] F. G. Rounds, **1978**. *Additive Interactions and Their Effect on the Performance of a Zinc Dialkyl Dithiophosphate*. ASLE Transactions, vol. 21 (2), pp. 91–101, [http://www.tandfonline.com/doi/abs/10.1080/05698197808982864].

[292] M. Shiomi, M. Tokashiki, H. Tomizawa, and T. Kuribayashi, **1989**. *Interaction between zinc dialkyldithiophosphate and amine*. Lubrication Science, vol. 1 (2), pp. 131–147, [http://doi.wiley.com/10.1002/ls.3010010203].

[293] H. Mansuy, P. Beccat, Y. Huiban, T. Palermo, and B. Desbat, **1995**. *Investigation of Interactions Between Antiwear and Dispersant Additives and Their Effect on Surface Activity of Zddp*, in Tribology Series, vol. 30, pp. 423–432, Elsevier.

[294] J. Martin, C. Grossiord, T. Le Mogne, and J. Igarashi, **2000**. *Role of nitrogen in tribochemical interaction between Zndtp and succinimide in boundary lubrication*. Tribology International, vol. 33 (7), pp. 453–459, [http://linkinghub.elsevier.com/retrieve/pii/S0301679X00000736].

[295] Z. Zhang, E. S. Yamaguchi, M. Kasrai, and G. M. Bancroft, **2004**. *Interaction of ZDDP with Borated Dispersant Using XANES and XPS*. Tribology Transactions, vol. 47 (4), pp. 527–536, [http://www.tandfonline.com/doi/abs/10.1080/05698190490500725].

[296] H. Fujita, R. P. Glovnea, and H. A. Spikes, **2005**. *Study of Zinc Dialkydithiophosphate Antiwear Film Formation and Removal Processes, Part I: Experimental*. Tribology Transactions, vol. 48 (4), pp. 558–566, [http://www.tandfonline.com/doi/abs/10.1080/05698190500385211].

[297] H. Fujita and H. A. Spikes, **2005**. *Study of Zinc Dialkyldithiophosphate Antiwear Film Formation and Removal Processes, Part II: Kinetic Model*. Tribology Transactions, vol. 48, pp. 567–575, [http://www.tandfonline.com/doi/abs/10.1080/05698190500385187].

[298] M. De Barros Bouchet, J. Martin, C. Oumahi, O. Gorbatchev, P. Afanasiev, C. Geantet, R. Iovine, B. Thiebaut, and C. Heau, **2018**. *Booster effect of fatty amine on friction reduction performance of Mo-based additives*. Tribology International, vol. 119, pp. 600–607, [https://linkinghub.elsevier.com/retrieve/pii/S0301679X17305534].

[299] B. J. Hamrock and D. Dowson, **1977**. *Isothermal Elastohydrodynamic Lubrication of Point Contacts: Part IV—Starvation Results*. Journal of Lubrication Technology, vol. 99 (1), p. 15, [http://Tribology.asmedigitalcollection.asme.org/article.aspx?articleid=1463531].

[300] S. Eder, A. Vernes, G. Vorlaufer, and G. Betz, **2011**. *Molecular dynamics simulations of mixed lubrication with smooth particle post-processing*. Journal of Physics: Condensed

Matter, vol. 23 (17), p. 175004, [http://stacks.iop.org/0953-8984/23/i=17/a=175004?key=crossref.41193f187bd46a055d2df07a0c608354].

[301] S. J. Eder, A. Vernes, and G. Betz, **2016**. *On the Derjaguin Offset in Boundary-Lubricated Nanotribological Systems*. Langmuir, vol. 29 (45), pp. 13760–13772, [http://pubs.acs.org/doi/abs/10.1021/la4026443].

[302] M. L. Gee, P. M. McGuiggan, J. N. Israelachvili, and A. M. Homola, **1990**. *Liquid to solidlike transitions of molecularly thin films under shear*. The Journal of Chemical Physics, vol. 93 (3), pp. 1895–1906, [http://aip.scitation.org/doi/10.1063/1.459067].

[303] P. A. Thompson and M. O. Robbins, **1990**. *Origin of Stick-Slip Motion in Boundary Lubrication*. Science, vol. 250 (4982), pp. 792–794, [http://www.sciencemag.org/cgi/doi/10.1126/science.250.4982.792].

[304] S. Y. Liem, D. Brown, and J. H. R. Clarke, **1992**. *Investigation of the homogeneous-shear nonequilibrium-molecular-dynamics method*. Physical Review A, vol. 45 (6), pp. 3706–3713, [https://link.aps.org/doi/10.1103/PhysRevA.45.3706].

[305] P. A. Thompson, G. S. Grest, and M. O. Robbins, **1992**. *Phase transitions and universal dynamics in confined films*. Physical Review Letters, vol. 68 (23), pp. 3448–3451, [https://link.aps.org/doi/10.1103/PhysRevLett.68.3448].

[306] J. N. Glosli and G. M. McClelland, **1993**. *Molecular dynamics study of sliding friction of ordered organic monolayers*. Physical Review Letters, vol. 70 (13), pp. 1960–1963, [https://link.aps.org/doi/10.1103/PhysRevLett.70.1960].

[307] M. Cieplak, E. D. Smith, and M. O. Robbins, **1994**. *Molecular Origins of Friction: The Force on Adsorbed Layers*. Science, vol. 265, no. 5176, pp. 1209–1212, [http://www.sciencemag.org/cgi/doi/10.1126/science.265.5176.1209].

[308] K. J. Tupper and D. W. Brenner, **1994**. *Molecular dynamics simulations of friction in self-assembled monolayers*. Thin Solid Films, vol. 253 (1-2), pp. 185–189, [http://linkinghub.elsevier.com/retrieve/pii/0040609094903174].

[309] A. Koike and M. Yoneya, **1996**. *Molecular dynamics simulations of sliding friction of Langmuir–Blodgett monolayers*. The Journal of Chemical Physics, vol. 105 (14), pp. 6060–6067, [http://aip.scitation.org/doi/10.1063/1.472442].

[310] S. A. Gupta, H. D. Cochran, and P. T. Cummings, **1997**. *Shear behavior of squalane and tetracosane under extreme confinement. III. Effect of confinement on viscosity*. The Journal of Chemical Physics, vol. 107 (23), pp. 10335–10343, [http://aip.scitation.org/doi/10.1063/1.474173].

[311] A. Koike and M. Yoneya, **1997**. *Effects of Molecular Structure on Frictional Properties of Langmuir–Blodgett Monolayers*. Langmuir, vol. 13 (6), pp. 1718–1722, [http://pubs.acs.org/doi/abs/10.1021/la9606557].

[312] P. A. Thompson and S. M. Troian, **1997**. *A general boundary condition for liquid flow*

at solid surfaces. Nature, vol. 389, no. 6649, pp. 360–362, [http://www.nature.com/articles/38686].

[313] J. Klein and E. Kumacheva, **1998**. *Simple liquids confined to molecularly thin layers. I. Confinement-induced liquid-to-solid phase transitions*. The Journal of Chemical Physics, vol. 108 (16), pp. 6996–7009, [http://aip.scitation.org/doi/10.1063/1.476114].

[314] L. I. Kioupis and E. J. Maginn, **1999**. *Molecular Simulation of Poly-α-olefin Synthetic Lubricants: Impact of Molecular Architecture on Performance Properties*. The Journal of Physical Chemistry B, vol. 103 (49), pp. 10781–10790, [http://pubs.acs.org/doi/abs/10.1021/jp992399n].

[315] Y. C. Kong and D. J. Tildesley, **1999**. *The Effect of Molecular Geometry on Boundary Layer Lubrication*. Molecular Simulation, vol. 22 (2), pp. 149–168, [http://www.tandfonline.com/doi/abs/10.1080/08927029908022092].

[316] J. Gao, W. D. Luedtke, and U. Landman, **2000**. *Structures, solvation forces and shear of molecular films in a rough nano-confinement*. Tribology Letters, vol. 9 (1-2), pp. 3–13, [https://doi.org/10.1023/A:1018840023845].

[317] A. Jabbarzadeh, J. Atkinson, and R. Tanner, **2000**. *Effect of the wall roughness on slip and rheological properties of hexadecane in molecular dynamics simulation of couette shear flow between two sinusoidal walls*. Physical Review. E, Statistical Physics, Plasmas, Fluids, and Related Interdisciplinary Topics, vol. 61 (1), pp. 690–699, [https://www.ncbi.nlm.nih.gov/pubmed/11046312].

[318] S. T. Cui, P. T. Cummings, and H. D. Cochran, **2001**. *Molecular simulation of the transition from liquidlike to solidlike behavior in complex fluids confined to nanoscale gaps*. The Journal of Chemical Physics, vol. 114 (16), pp. 7189–7195, [http://aip.scitation.org/doi/10.1063/1.1359736].

[319] G. He and M. O. Robbins, **2001**. *Simulations of the kinetic friction due to adsorbed surface layers*. Tribology Letters, vol. 10 (7), pp. 7–14, [https://link.springer.com/article/10.1023/A:1009030413641].

[320] S. Bair, C. McCabe, and P. T. Cummings, **2002**. *Comparison of Nonequilibrium Molecular Dynamics with Experimental Measurements in the Nonlinear Shear-Thinning Regime*. Physical Review Letters, vol. 88 (5), [https://link.aps.org/doi/10.1103/PhysRevLett.88.058302].

[321] M. Chandross, G. S. Grest, and M. J. Stevens, **2002**. *Friction between Alkylsilane Monolayers: Molecular Simulation of Ordered Monolayers*. Langmuir, vol. 18 (22), pp. 8392–8399, [http://pubs.acs.org/doi/abs/10.1021/la025598y].

[322] A. Jabbarzadeh, J. Atkinson, and R. Tanner, **2002**. *The effect of branching on slip and rheological properties of lubricants in molecular dynamics simulation of Couette shear flow*. Tribology International, vol. 35 (1), pp. 35–46, [http://linkinghub.elsevier.com/retrieve/pii/S0301679X01000895].

[323] J.-L. Barrat and F. Chiaruttini, **2003**. *Kapitza resistance at the liquid–solid interface*. Molecular Physics, vol. 101 (11), pp. 1605–1610, [http://www.tandfonline.com/doi/abs/10.1080/0026897031000068578].

[324] I. M. Sivebaek, V. N. Samoilov, and B. N. J. Persson, **2003**. *Squeezing molecular thin alkane lubrication films between curved solid surfaces with long-range elasticity: Layering transitions and wear*. The Journal of Chemical Physics, vol. 119 (4), pp. 2314–2321, [http://aip.scitation.org/doi/10.1063/1.1582835].

[325] L. Zhang, Y. Leng, and S. Jiang, **2003**. *Tip-Based Hybrid Simulation Study of Frictional Properties of Self-Assembled Monolayers: Effects of Chain Length, Terminal Group, Scan Direction, and Scan Velocity*. Langmuir, vol. 19 (23), pp. 9742–9747, [http://pubs.acs.org/doi/abs/10.1021/la034007g].

[326] M. Chandross, E. B. Webb, M. J. Stevens, G. S. Grest, and S. H. Garofalini, **2004**. *Systematic Study of the Effect of Disorder on Nanotribology of Self-Assembled Monolayers*. Physical Review Letters, vol. 93 (16), [https://link.aps.org/doi/10.1103/PhysRevLett.93.166103].

[327] A. Jabbarzadeh, P. Harrowell, and R. I. Tanner, **2005**. *Very Low Friction State of a Dodecane Film Confined between Mica Surfaces*. Physical Review Letters, vol. 94 (12), [https://link.aps.org/doi/10.1103/PhysRevLett.94.126103].

[328] C. D. Lorenz, M. Chandross, G. S. Grest, M. J. Stevens, and E. B. Webb, **2005**. *Tribological Properties of Alkylsilane Self-Assembled Monolayers*. Langmuir, vol. 21 (25), pp. 11744–11748, [http://pubs.acs.org/doi/abs/10.1021/la051741m].

[329] J. Chen, I. Ratera, J. Y. Park, and M. Salmeron, **2006**. *Velocity Dependence of Friction and Hydrogen Bonding Effects*. Physical Review Letters, vol. 96 (23), [https://link.aps.org/doi/10.1103/PhysRevLett.96.236102].

[330] A. Jabbarzadeh, P. Harrowell, and R. I. Tanner, **2006**. *Crystal Bridge Formation Marks the Transition to Rigidity in a Thin Lubrication Film*. Physical Review Letters, vol. 96 (20), [https://link.aps.org/doi/10.1103/PhysRevLett.96.206102].

[331] V. Kapila, P. A. Deymier, and S. Raghavan, **2006**. *Molecular dynamics simulations of friction between alkylsilane monolayers*. Modelling and Simulation in Materials Science and Engineering, vol. 14 (2), pp. 283–297, [http://stacks.iop.org/0965-0393/14/i=2/a=011?key=crossref.7c8e6412293efa29fe1341d828594571].

[332] A. Martini, Y. Liu, R. Snurr, and Q. J. Wang, **2006**. *Molecular dynamics characterization of thin film viscosity for EHL simulation*. Tribology Letters, vol. 21 (3), pp. 217–225, [http://link.springer.com/10.1007/s11249-006-9023-x].

[333] A. Jabbarzadeh, P. Harrowell, and R. I. Tanner, **2006**. *Low friction lubrication between amorphous walls: Unraveling the contributions of surface roughness and in-plane disorder*. The Journal of Chemical Physics, vol. 125 (3), p. 034703, [http://aip.scitation.org/doi/10.1063/1.2216695].

[334] A. Jabbarzadeh, P. Harrowell, and R. Tanner, **2007**. *The structural origin of the complex rheology in thin dodecane films: Three routes to low friction*. Tribology International, vol. 40 (10-12), pp. 1574–1586, [http://linkinghub.elsevier.com/retrieve/pii/S0301679X0600329X].

[335] D. M. Huang, C. Sendner, D. Horinek, R. R. Netz, and L. Bocquet, **2008**. *Water Slippage versus Contact Angle: A Quasiuniversal Relationship*. Physical Review Letters, vol. 101 (22), [https://link.aps.org/doi/10.1103/PhysRevLett.101.226101].

[336] A. Martini, H.-Y. Hsu, N. A. Patankar, and S. Lichter, **2008**. *Slip at High Shear Rates*. Physical Review Letters, vol. 100 (20), [https://link.aps.org/doi/10.1103/PhysRevLett.100.206001].

[337] A. Martini, A. Roxin, R. Q. Snurr, Q. Wang, and S. Lichter, **2008**. *Molecular mechanisms of liquid slip*. Journal of Fluid Mechanics, vol. 600, [http://www.journals.cambridge.org/abstract_S0022112008000475].

[338] S. Bernardi, B. D. Todd, and D. J. Searles, **2010**. *Thermostating highly confined fluids*. The Journal of Chemical Physics, vol. 132 (24), p. 244706, [http://aip.scitation.org/doi/10.1063/1.3450302].

[339] H. Berro, **2010**. *A molecular dynamics approach to nano-scale lubrication*. PhD thesis, Institut National des Sciences Appliquées de Lyon, Lyon, France.

[340] H. Docherty and P. T. Cummings, **2010**. *Direct evidence for fluid–solid transition of nanoconfined fluids*. Soft Matter, vol. 6 (8), p. 1640, [http://xlink.rsc.org/?DOI=c000821d].

[341] C. D. Lorenz, M. Chandross, J. M. D. Lane, and G. S. Grest, **2010**. *Nanotribology of water confined between hydrophilic alkylsilane self-assembled monolayers*. Modelling and Simulation in Materials Science and Engineering, vol. 18 (3), p. 034005, [http://stacks.iop.org/0965-0393/18/i=3/a=034005?key=crossref.67a1e0d9a066677967ecb01caba49a69].

[342] L. Pastewka, S. Moser, and M. Moseler, **2010**. *Atomistic Insights into the Running-in, Lubrication, and Failure of Hydrogenated Diamond-Like Carbon Coatings*. Tribology Letters, vol. 39 (1), pp. 49–61, [http://link.springer.com/10.1007/s11249-009-9566-8].

[343] H. Washizu and T. Ohmori, **2010**. *Molecular dynamics simulations of elastohydrodynamic lubrication oil film*. Lubrication Science, vol. 22 (8), pp. 323–340, [http://doi.wiley.com/10.1002/ls.126].

[344] H. Berro, N. Fillot, P. Vergne, T. Tokumasu, T. Ohara, and G. Kikugawa, **2011**. *Energy dissipation in non-isothermal molecular dynamics simulations of confined liquids under shear*. The Journal of Chemical Physics, vol. 135 (13), p. 134708, [http://aip.scitation.org/doi/10.1063/1.3644938].

[345] M. R. Farrow, A. Chremos, P. J. Camp, S. G. Harris, and R. F. Watts, **2011**. *Molecular Simula-*

tions of Kinetic-Friction Modification in Nanoscale Fluid Layers. Tribology Letters, vol. 42 (3), pp. 325–337, [http://link.springer.com/10.1007/s11249-011-9777-7].

[346] T. A. Ho, D. V. Papavassiliou, L. L. Lee, and A. Striolo, **2011**. *Liquid water can slip on a hydrophilic surface*. Proceedings of the National Academy of Sciences, vol. 108 (39), pp. 16170–16175, [http://www.pnas.org/cgi/doi/10.1073/pnas.1105189108].

[347] Q. Li, Y. Dong, D. Perez, A. Martini, and R. W. Carpick, **2011**. *Speed Dependence of Atomic Stick-Slip Friction in Optimally Matched Experiments and Molecular Dynamics Simulations*. Physical Review Letters, vol. 106 (12), [https://link.aps.org/doi/10.1103/PhysRevLett.106.126101].

[348] S. Bernardi, S. J. Brookes, D. J. Searles, and D. J. Evans, **2012**. *Response theory for confined systems*. The Journal of Chemical Physics, vol. 137, no. 7, p. 074114, [http://aip.scitation.org/doi/10.1063/1.4746121].

[349] K. Falk, F. Sedlmeier, L. Joly, R. R. Netz, and L. Bocquet, **2012**. *Ultralow Liquid/Solid Friction in Carbon Nanotubes: Comprehensive Theory for Alcohols, Alkanes, OMCTS, and Water*. Langmuir, vol. 28 (40), pp. 14261–14272, [http://pubs.acs.org/doi/10.1021/la3029403].

[350] J. B. Lewis, S. G. Vilt, J. L. Rivera, G. K. Jennings, and C. McCabe, **2012**. *Frictional Properties of Mixed Fluorocarbon/Hydrocarbon Silane Monolayers: A Simulation Study*. Langmuir, vol. 28, pp. 14218–14226, [http://pubs.acs.org/doi/10.1021/la3024315].

[351] L. Ramin and A. Jabbarzadeh. *Frictional properties of two alkanethiol self assembled monolayers in sliding contact: Odd-even effects*. The Journal of Chemical Physics, vol. 137 (17), p. 174706, [http://aip.scitation.org/doi/10.1063/1.4764301].

[352] D. Savio, N. Fillot, P. Vergne, and M. Zaccheddu, **2012**. *A Model for Wall Slip Prediction of Confined n-Alkanes: Effect of Wall-Fluid Interaction Versus Fluid Resistance*. Tribology Letters, vol. 46 (1), pp. 11–22, [http://link.springer.com/10.1007/s11249-011-9911-6].

[353] A. Vernes, S. Eder, G. Vorlaufer, and G. Betz, **2012**. *On the three-term kinetic friction law in nanotribological systems*. Faraday Discussions, vol. 156, p. 173, [http://xlink.rsc.org/?DOI=c2fd00120a].

[354] A. C. F. Mendonça, A. A. H. Pádua, and P. Malfreyt, **2013**. *Nonequilibrium Molecular Simulations of New Ionic Lubricants at Metallic Surfaces: Prediction of the Friction*. Journal of Chemical Theory and Computation, vol. 9 (3), pp. 1600–1610, [http://pubs.acs.org/doi/10.1021/ct3008827].

[355] L. Ramin and A. Jabbarzadeh, **2013**. *Effect of Water on Structural and Frictional Properties of Self Assembled Monolayers*. Langmuir, vol. 29 (44), pp. 13367–13378, [http://pubs.acs.org/doi/10.1021/la403321a].

[356] D. Savio, N. Fillot, and P. Vergne, **2013**. *A Molecular Dynamics Study of the Transition from Ultra-Thin Film Lubrication Toward Local Film Breakdown*. Tribology Letters, vol. 50 (2),

pp. 207–220, [http://link.springer.com/10.1007/s11249-013-0113-2].

[357] X. Zheng, H. Zhu, A. Kiet Tieu, and B. Kosasih, **2013**. *A molecular dynamics simulation of 3D rough lubricated contact*. Tribology International, vol. 67, pp. 217–221, [https://linkinghub.elsevier.com/retrieve/pii/S0301679X13002764].

[358] H. J. Castejón, T. J. Wynn, and Z. M. Marcin, **2014**. *Wetting and Tribological Properties of Ionic Liquids*. The Journal of Physical Chemistry B, vol. 118 (13), pp. 3661–3668, [http://pubs.acs.org/doi/10.1021/jp411765f].

[359] H. L. Adams, M. T. Garvey, U. S. Ramasamy, Z. Ye, A. Martini, and W. T. Tysoe. *Shear-Induced Mechanochemistry: Pushing Molecules Around*. The Journal of Physical Chemistry C, vol. 119 (13), pp. 7115–7123, [http://pubs.acs.org/doi/10.1021/jp5121146].

[360] J. E. Black, C. R. Iacovella, P. T. Cummings, and C. McCabe, **2015**. *Molecular Dynamics Study of Alkylsilane Monolayers on Realistic Amorphous Silica Surfaces*. Langmuir, vol. 31 (10), pp. 3086–3093, [http://pubs.acs.org/doi/10.1021/la5049858].

[361] N. Voeltzel, A. Giuliani, N. Fillot, P. Vergne, and L. Joly, **2015**. *Nanolubrication by ionic liquids: molecular dynamics simulations reveal an anomalous effective rheology*. Physical Chemistry Chemical Physics, vol. 17 (35), pp. 23226–23235, [http://xlink.rsc.org/?DOI=C5CP03134F].

[362] Z. Ye and A. Martini, **2015**. *Atomic friction at exposed and buried graphite step edges: experiments and simulations*. Applied Physics Letters, vol. 106 (23), p. 231603, [http://aip.scitation.org/doi/10.1063/1.4922485].

[363] G. Bahlakeh, M. Ghaffari, M. R. Saeb, B. Ramezanzadeh, F. De Proft, and H. Terryn, **2016**. *A Close-up of the Effect of Iron Oxide Type on the Interfacial Interaction between Epoxy and Carbon Steel: Combined Molecular Dynamics Simulations and Quantum Mechanics*. The Journal of Physical Chemistry C, vol. 120 (20), pp. 11014–11026, [http://pubs.acs.org/doi/10.1021/acs.jpcc.6b03133].

[364] S. Maćkowiak, D. M. Heyes, D. Dini, and A. C. Brańka, **2016**. *Non-equilibrium phase behavior and friction of confined molecular films under shear: A non-equilibrium molecular dynamics study*. The Journal of Chemical Physics, vol. 145 (16), p. 164704, [http://aip.scitation.org/doi/10.1063/1.4965829].

[365] L. Martinie and P. Vergne, **2016**. *Lubrication at Extreme Conditions: A Discussion About the Limiting Shear Stress Concept*. Tribology Letters, vol. 63 (2), [http://link.springer.com/10.1007/s11249-016-0709-4].

[366] D. Savio, L. Pastewka, and P. Gumbsch, **2016**. *Boundary lubrication of heterogeneous surfaces and the onset of cavitation in frictional contacts*. Science Advances, vol. 2 (3), p. e1501585, [http://advances.sciencemag.org/lookup/doi/10.1126/sciadv.1501585].

[367] A. Z. Summers, C. R. Iacovella, M. R. Billingsley, S. T. Arnold, P. T. Cummings, and

C. McCabe, **2016**. *Influence of Surface Morphology on the Shear-Induced Wear of Alkylsilane Monolayers: Molecular Dynamics Study*. Langmuir, vol. 32 (10), pp. 2348–2359, [http://pubs.acs.org/doi/10.1021/acs.langmuir.5b03862].

[368] A. Z. Summers, C. R. Iacovella, P. T. Cummings, and C. MCabe, **2017**. *Investigating Alkylsilane Monolayer Tribology at a Single-Asperity Contact with Molecular Dynamics Simulation*. Langmuir, vol. 33 (42), pp. 11270–11280, [http://pubs.acs.org/doi/10.1021/acs.langmuir.7b02479].

[369] B. D. Todd and P. J. Daivis, **2017**. *Nonequilibrium molecular dynamics: theory, algorithms and applications*. Cambridge University Press. ISBN: 978-0-521-19009-1.

[370] J. J. Magda, M. Tirrell, and H. T. Davis, **1985**. *Molecular dynamics of narrow, liquid-filled pores*. The Journal of Chemical Physics, vol. 83 (4), pp. 1888–1901, [http://aip.scitation.org/doi/10.1063/1.449375].

[371] K. P. Travis, B. D. Todd, and D. J. Evans, **1997**. *Departure from Navier-Stokes hydrodynamics in confined liquids*. Physical Review E, vol. 55 (4), pp. 4288–4295, [https://link.aps.org/doi/10.1103/PhysRevE.55.4288].

[372] D. J. Evans and G. P. Morriss, **1990**. *Statistical Mechanics of Nonequilibrium Liquids*. Elsevier. ISBN: 978-0-12-244090-8.

[373] G. Ciccotti, R. Kapral, and A. Sergi, **2005**. *Non-Equilibrium Molecular Dynamics*, in Handbook of Materials Modeling (S. Yip, ed.), pp. 745–761, Dordrecht: Springer Netherlands.

[374] A. Vanossi, N. Manini, M. Urbakh, S. Zapperi, and E. Tosatti, **2013**. *Colloquium : Modeling friction: From nanoscale to mesoscale*. Reviews of Modern Physics, vol. 85 (2), pp. 529–552, [https://link.aps.org/doi/10.1103/RevModPhys.85.529].

[375] I. Bitsanis, J. J. Magda, M. Tirrell, and H. T. Davis, **1987**. *Molecular dynamics of flow in micropores*. The Journal of Chemical Physics, vol. 87 (3), pp. 1733–1750, [http://aip.scitation.org/doi/10.1063/1.453240].

[376] W. T. Ashurst and W. G. Hoover, **1975**. *Dense-fluid shear viscosity via nonequilibrium molecular dynamics*. Physical Review A, vol. 11 (2), pp. 658–678, [https://link.aps.org/doi/10.1103/PhysRevA.11.658].

[377] G. Amontons, **1699**. *Mémoires de l'Académie Royale*. 257.

[378] C. A. Coulomb, **1785**. *Mémoires de mathématiques et de physique*. Paris, 161.

[379] A. M. Homola, J. N. Israelachvili, P. M. McGuiggan, and M. L. Gee, **1990**. *Fundamental experimental studies in tribology: The transition from "interfacial" friction of undamaged molecularly smooth surfaces to "normal" friction with wear*. Wear, vol. 136 (1), pp. 65–83, [http://linkinghub.elsevier.com/retrieve/pii/004316489090072I].

[380] P. A. Thompson and M. O. Robbins, **1990**. *Shear flow near solids: Epitaxial order and flow boundary conditions*. Physical Review A, vol. 41 (12), pp. 6830–6837, [https://link.aps.org/doi/10.1103/PhysRevA.41.6830].

[381] S. Yamada, K. A. Inomata, E. Kobayashi, T. Tanabe, and K. Kurihara, **2016**. *Effect of a Fatty Acid Additive on the Kinetic Friction and Stiction of Confined Liquid Lubricants*. Tribology Letters, vol. 64 (2), [http://link.springer.com/10.1007/s11249-016-0756-x].

[382] B. Derjaguin, **1934**. *Untersuchungen über die Reibung und Adhäsion, IV: Theorie des Anhaftens kleiner Teilchen*. Kolloid-Zeitschrift, vol. 69 (2), pp. 155–164, [http://link.springer.com/10.1007/BF01433225].

[383] F. P. Bowden and D. Tabor, **1950**. *The friction and lubrication of solids*. Clarendon Press ; Oxford University Press.

[384] Y. L. Chen, Z. Xu, and J. Israelachvili, **1992**. *Structure and interactions of surfactant-covered surfaces in nonaqueous (oil-surfactant-water) media*. Langmuir, vol. 8 (12), pp. 2966–2975, [http://pubs.acs.org/doi/abs/10.1021/la00048a020].

[385] H. Yoshizawa, Y. L. Chen, and J. Israelachvili, **1993**. *Fundamental mechanisms of interfacial friction. 1. Relation between adhesion and friction*. The Journal of Physical Chemistry, vol. 97 (16), pp. 4128–4140, [http://pubs.acs.org/doi/abs/10.1021/j100118a033].

[386] B. N. J. Persson, **2000**. *Sliding Friction*. Springer Berlin Heidelberg.

[387] M. Ruths, A. D. Berman, and J. N. Israelachvili, **2004**. *Surface Forces and Nanorheology of Molecularly Thin Films*, in Springer Handbook of Nanotechnology (B. Bhushan, ed.), pp. 543–603, Springer Berlin Heidelberg.

[388] J. N. Israelachvili, **2011**. *Intermolecular and Surface Forces*. Elsevier, 3rd ed.

[389] J. N. Israelachvili, P. M. Mcguiggan, and A. M. Homola, **1988**. *Dynamic Properties of Molecularly Thin Liquid Films*. Science, vol. 240 (4849), pp. 189–191, [http://www.sciencemag.org/cgi/doi/10.1126/science.240.4849.189].

[390] M. O. Robbins and P. A. Thompson, **1991**. *Critical Velocity of Stick-Slip Motion*. Science, vol. 253 (5022), pp. 916–916, [http://www.sciencemag.org/cgi/doi/10.1126/science.253.5022.916].

[391] H. Yoshizawa and J. Israelachvili, **1993**. *Fundamental mechanisms of interfacial friction. 2. Stick-slip friction of spherical and chain molecules*. The Journal of Physical Chemistry, vol. 97 (43), pp. 11300–11313, [http://pubs.acs.org/doi/abs/10.1021/j100145a031].

[392] G. Reiter, A. L. Demirel, and S. Granick, **1994**. *From Static to Kinetic Friction in Confined Liquid Films*. Science, vol. 263, no. 5154, pp. 1741–1744, [http://www.sciencemag.org/cgi/doi/10.1126/science.263.5154.1741].

[393] G. Reiter, A. L. Demirel, J. Peanasky, L. L. Cai, and S. Granick, **1994**. *Stick to slip transition and adhesion of lubricated surfaces in moving contact*. The Journal of Chemical Physics, vol. 101, no. 3, pp. 2606–2615, [http://aip.scitation.org/doi/10.1063/1.467633].

[394] J. Klein and E. Kumacheva, **1995**. *Confinement-Induced Phase Transitions in Simple Liquids*. Science, vol. 269, pp. 816–819, [http://www.sciencemag.org/cgi/doi/10.1126/science.269.5225.816].

[395] M. O. Robbins and E. D. Smith, **1996**. *Connecting Molecular-Scale and Macroscopic Tribology †*. Langmuir, vol. 12 (19), pp. 4543–4547, [http://pubs.acs.org/doi/abs/10.1021/la9505576].

[396] A. Dhinojwala, S. C. Bae, and S. Granick, **2000**. *Shear-induced dilation of confined liquid films*. Tribology Letters, vol. 9 (1-2), pp. 55–62, [https://link.springer.com/article/10.1023/A:1018852326571].

[397] Y. Leng and P. T. Cummings, **2005**. *Fluidity of Hydration Layers Nanoconfined between Mica Surfaces*. Physical Review Letters, vol. 94 (2), [https://link.aps.org/doi/10.1103/PhysRevLett.94.026101].

[398] Y. Lei and Y. Leng, **2011**. *Stick-Slip Friction and Energy Dissipation in Boundary Lubrication*. Physical Review Letters, vol. 107 (14), [https://link.aps.org/doi/10.1103/PhysRevLett.107.147801].

[399] I. Rosenhek-Goldian, N. Kampf, A. Yeredor, and J. Klein, **2015**. *On the question of whether lubricants fluidize in stick–slip friction*. Proceedings of the National Academy of Sciences, vol. 112 (23), pp. 7117–7122, [http://www.pnas.org/lookup/doi/10.1073/pnas.1505609112].

[400] A.-Y. Jee, K. Lou, and S. Granick, **2015**. *Scrutinizing evidence of no dilatancy upon stick–slip of confined fluids*. Proceedings of the National Academy of Sciences, vol. 112 (36), pp. E4972–E4972, [http://www.pnas.org/lookup/doi/10.1073/pnas.1511129112].

[401] M. Ingram, J. Noles, R. Watts, S. Harris, and H. A. Spikes, **2010**. *Frictional Properties of Automatic Transmission Fluids: Part I—Measurement of Friction–Sliding Speed Behavior*. Tribology Transactions, vol. 54 (1), pp. 145–153, [http://www.tandfonline.com/doi/abs/10.1080/10402004.2010.531888].

[402] J. Hiebert, C. N. Rowe, and L. R. Rudnick, **1994**. *Alkylated citric acid adducts as antiwear and friction modifying additives*. US 5 338 470 A.

[403] J. Kocsis, J. S. Vilardo, J. R. Brown, D. E. Barrer, R. J. Vickerman, and P. E. Mosier, **2012**. *Tartaric acid derivatives in fuel compositions*. US 8 133 290 B2.

[404] X. Zheng, H. Zhu, A. K. Tieu, and B. Kosasih, **2014**. *Roughness and Lubricant Effect on 3D Atomic Asperity Contact*. Tribology Letters, vol. 53 (1), pp. 215–223, [http://link.springer.com/10.1007/s11249-013-0259-y].

[405] A. C. T. van Duin, **2006**. *Reactive Force Fields Based on Quantum Mechanics for Applications to Materials at Extreme Conditions*. vol. 845, pp. 581–584, [http://aip.scitation.org/doi/abs/10.1063/1.2263389].

[406] T. Liang, Y. K. Shin, Y.-T. Cheng, D. E. Yilmaz, K. G. Vishnu, O. Verners, C. Zou, S. R. Phillpot, S. B. Sinnott, and A. C. van Duin, **2013**. *Reactive Potentials for Advanced Atomistic Simulations*. Annual Review of Materials Research, vol. 43 (1), pp. 109–129, [http://www.annualreviews.org/doi/10.1146/annurev-matsci-071312-121610].

[407] T. P. Senftle, S. Hong, M. M. Islam, S. B. Kylasa, Y. Zheng, Y. K. Shin, C. Junkermeier, R. Engel-Herbert, M. J. Janik, H. M. Aktulga, T. Verstraelen, A. Grama, and A. C. T. van Duin, **2016**. *The ReaxFF reactive force-field: development, applications and future directions*. npj Computational Materials, vol. 2 (1), [http://www.nature.com/articles/npjcompumats201511].

[408] H. A. Kooijman and R. Taylor, **1991**. *Estimation of diffusion coefficients in multicomponent liquid systems*. Industrial & Engineering Chemistry Research, vol. 30 (6), pp. 1217–1222, [http://pubs.acs.org/doi/abs/10.1021/ie00054a023].

[409] X. Liu, A. Martín-Calvo, E. McGarrity, S. K. Schnell, S. Calero, J.-M. Simon, D. Bedeaux, S. Kjelstrup, A. Bardow, and T. J. H. Vlugt, **2012**. *Fick Diffusion Coefficients in Ternary Liquid Systems from Equilibrium Molecular Dynamics Simulations*. Industrial & Engineering Chemistry Research, vol. 51 (30), pp. 10247–10258, [http://pubs.acs.org/doi/10.1021/ie301009v].

Appendix A
Literature review on inter-diffusivity

In the current MD-based simulation work, we have considered the *intra-diffusion coefficient* as a *reference molecular descriptor* in order to study the influence of difference structural factors, related to some lubricant constituents (OFM and BO models), on their dynamics and diffusive behavior within a liquid binary solution (cf. chapter 3, p. 35). However, it is also important to point out the existence of other diffusive process, the *inter-diffusion.*[113–119]

Whereas *intra-diffusion* defines the random translational movement of individual molecular species in a single or multicomponent solution due to the random thermal motion, the *inter-diffusion*[1] describes the collective movement of molecules resulting from a driving force, such as a *concentration* or a *chemical potential gradient.* Besides, it shoud be highlighted that it is the inter-diffusion process the effective responsible for the mass transfer phenomena occuring in multicomponent systems.[113,120]

Therefore, a brief literature review on *inter-diffusivity* is given in this appendix for a binary liquid solution, as a complement to that concerning the intra-diffusion coefficient (cf. § 3.1, p. 38).

Inter-diffusivities

The most commonly advocated approaches to model *inter-diffusion* in liquids are the generalized *Fick's law* and the *Maxwell-Stefan theory* (MS).[119,120,122–126,144,408] In both methods, an inter-diffusion coefficient relates a diffusive mass flux to a specific driving force, which is a concentration gradient in Fick's law (∇c_i) and a gradient of chemical potential in MS theory ($\nabla \mu_i$).

[1] *Inter-diffusion* is also known as *bulk, collective, mutual* or *transport diffusion.*

Considering the *molar-averaged reference velocity* [2] $\mathbf{u}$, the diffusive molar fluxes $\mathbf{J}_i$ are expressed as:[146]

$$\mathbf{J}_i = c_i \cdot (\mathbf{u}_i - \mathbf{u}) \equiv c \cdot x_i \cdot (\mathbf{u}_i - \mathbf{u}) \qquad \text{for } i = 1 \text{ or } 2 \tag{A.1}$$

in which,

$$\mathbf{u} = x_1 \cdot \mathbf{u}_1 + x_2 \cdot \mathbf{u}_2 \tag{A.2}$$

where $\mathbf{u}_i$ is the ensemble-averaged velocity of a given component ($\mathbf{u}_i = \langle \mathbf{v}_i \rangle$), c is the total molar concentration, and x_i is the mole fraction for component i.

In this reference frame, the *Fick inter-diffusion coefficients* ($D_{1,1}$ & $D_{2,2}$) are defined by the following constitutive relations obtained from the generalized *Fick's law*:[119,122]

$$\mathbf{J}_1 = -c \cdot D_{1,1} \cdot \nabla x_1 \tag{A.3}$$

$$\mathbf{J}_2 = -c \cdot D_{2,2} \cdot \nabla x_2 \tag{A.4}$$

Since the net flux of the system is zero, $\mathbf{J}_1 + \mathbf{J}_2 = 0$, and $x_1 + x_2 = 1$ for a binary mixture, thus $D_{1,1} = D_{2,2} \equiv D$.[119,128,146] So, only a *single Fick diffusivity* D is required to describe the diffusive mass transport in such case. Besides, D depends on concentration but not on the magnitude of concentration gradient (*i.e.*, the driving force), which is a quantity that can be measured experimentally.[119,168]

Another inter-diffusion coefficient can be defined from *MS theory*. This model is based on the assumption of an equilibrium between molecular friction and thermodynamic interaction, which implies that any deviation from this equilibrium leads to a diffusive flux.[128] In fact, for a non-electrolytic liquid mixture, the chemical potential gradient $\nabla \mu_i$ is considered to be the driving force d_i, which can be expressed as:[127,128,146,408,409]

$$d_i \equiv \frac{x_i}{R \cdot T} \cdot \nabla_{(T,P)}\, \mu_i \tag{A.5}$$

where R is the molar gas constant and T the absolute temperature. Consequently, d is counterbalanced by the *molecular friction force*, which is proportional to the mutual velocity between the solution components and their amount of mole fractions.[146,409] For example, for the solute:

$$d_1 = \frac{x_1 \cdot x_2}{Đ_{12}} \cdot (\mathbf{u}_2 - \mathbf{u}_1) \tag{A.6}$$

[2] Indeed, a frame of reference is required to express diffusive fluxes. The *molar-averaged reference* was used here to define Fick inter-diffusion coefficients, but other reference frames can alternatively be used (*e.g.*, the *volume-averaged reference*).[115,120,168] However, note that MS diffusivities do not demand any reference frame, but only Fick diffusivities depend on it.[126]

where $Đ_{12}$ is the *Maxwell-Stefan inter-diffusion coefficient*. Actually, this coefficient has the physical significance of an inverse drag coefficient describing the magnitude of friction between *i*-*j* components.[119, 146, 408]

MS diffusivities are symmetric (*i.e.*, $Đ_{12} = Đ_{21} \equiv Đ$), and usually depend less strongly on concentration than Fick diffusivities.[119, 120] On the other hand, it is not possible to determine Đ experimentally because chemical potential gradients cannot be measured directly.[119, 127] However, the MS inter-diffusion coefficient can be computed from EMD simulations by calculating *Onsager coefficients* $\Lambda_{i,j}$:[127, 146]

$$Đ = \frac{x_2}{x_1}\cdot\Lambda_{1,1} + \frac{x_1}{x_2}\cdot\Lambda_{2,2} - \Lambda_{1,2} - \Lambda_{2,1} \tag{A.7}$$

where $\Lambda_{i,j}$ are obtained from MSD or VAF data (cf. equations A.8 and A.9, respectively), but following a formalism based on the system correlation functions:[119, 146]

$$\Lambda_{i,j} = \frac{1}{6}\lim_{m\to\infty}\frac{1}{N}\cdot\frac{1}{m\cdot\Delta t}\cdot\left\langle\left\{\sum_{l=1}^{N_i}\left[\mathbf{r}_{l,i}(t+m\cdot\Delta t)-\mathbf{r}_{l,i}(t)\right]\right\}\cdot\left\{\sum_{k=1}^{N_j}\left[\mathbf{r}_{k,j}(t+m\cdot\Delta t)-\mathbf{r}_{k,j}(t)\right]\right\}\right\rangle \tag{A.8}$$

$$\Lambda_{i,j} = \frac{1}{3\cdot N}\int_0^\infty dt'\left\langle\left[\sum_{l=1}^{N_i}\mathbf{v}_{l,i}(t)\right]\cdot\left[\sum_{k=1}^{N_j}\mathbf{v}_{k,j}(t+t')\right]\right\rangle \tag{A.9}$$

Moreover, it must be highlighted that the driving force d_1 can be related to the mixture composition as follows:[128, 408]

$$d_1 = \Gamma\cdot\nabla x_2 \tag{A.10}$$

in which, Γ is the so-called *thermodynamic factor*, defined by:[115, 121, 127, 128, 146, 408]

$$\Gamma = 1 + x_1\cdot\left(\frac{\partial\ln\gamma_1}{\partial x_1}\right)_{T,p} = 1 + x_2\cdot\left(\frac{\partial\ln\gamma_2}{\partial x_2}\right)_{T,p} \tag{A.11}$$

where, γ_i is the activity coefficients of component *i*. The thermodynamic factor is usually extracted from experimental vapor-liquid equilibrium data or from excess enthalpy measurements, but it can also be obtained from molecular simulations, like grand-canonical Monte Carlo calculations.[121, 127, 168]

Furthermore, it is worth noting that MS approach accounts for thermodynamics and mass transfer separately, and only the latter contribution is characterized by Đ.[127] The thermodynamic contribution is actually expressed by Γ, which is also useful to couple Fick and MS inter-diffusivities as follows:[115, 117, 121, 127, 128, 146, 408, 409]

$$D = \Gamma\cdot Đ \tag{A.12}$$

Hence, MS inter-diffusion coefficient can be transformed to Fick inter-diffusivity and vice versa, provided that the thermodynamic factor is indeed known.[127] Nevertheless, the large uncertainty related to Γ calculation makes it difficult to obtain Đ from measurable D in practice.[121]

Equivalences between intra- ($\mathfrak{D}$) and inter-diffusivities (D & Đ):

In certain conditions, equivalence relations between the aforementioned diffusivities exist, namely:

- in binary mixtures, the Fick inter-diffusion coefficient (D) of a component becomes equal to its intra-diffusivity ($\mathfrak{D}$) in the limit of *infinite dilution*.[115, 116, 128, 145] For example, for the solute:

$$D^{x_1 \to 0} = \mathfrak{D}_{1,2}^{x_1 \to 0}$$

- since *ideality* is always approached in *dilute solutions* (*i.e.*, the factor $\frac{\partial \ln \gamma_i}{\partial x_i} \to 1$), the limiting values of MS and Fick inter-diffusivities are equivalent (D and Đ, respectively), along with the intra-diffusion coefficient ($\mathfrak{D}$) of the minor component, at each end of the composition range:[116]

$$\Gamma^{x_1 \to 0} = 1$$

$$Đ^{x_1 \to 0} = D^{x_1 \to 0} = \mathfrak{D}_{1,2}^{x_1 \to 0}$$

Since our work have intended to gain insights into the interactions between additives and lubricant oil models in order to and understand how chemical structure affects their liquid-state dynamics in relatively ideal conditions, we ended up choosing the *intra-diffusion process* as the framework of this study, along with the *MSD-time profile* to compute $\mathfrak{D}_{OFM,BO}$ (cf. *OFM* and *BO intra-diffusivity* results, as described in § 3.3, p. 51).

Appendix B
Simulated OFM/BO mixture densities

The *averaged densities* obtained after equilibration phase for the OFM/BO mixtures ($\rho_{OFM,BO}$) at T_{eq} = 373 K (cf. diffusion study — chapter 3, p. 35) are provided hereafter, along with their associated *deviations*, which were calculated in comparison to experimental pure BO densities (ρ^0_{BO}), since OFM concentration is relatively low (1.0 wt.%), implying a *dilute solution model*.

Table B.1 – Simulated densities for mixtures with PAO as solvent model
ρ^0_{PAO} (T_{eq} = 373 K) = 760.0 kg/m^3

Solute	Simulated $\rho_{OFM,BO}$ (kg/m^3)	Deviation
C_{18} *alkane*	756.1	0.5 %
C_{18} *alcohol*	757.0	0.4 %
C_{18} *acid*	757.0	0.4 %
C_{18} *primary amine*	756.5	0.5 %
C_{18} *primary amide*	757.3	0.4 %
C_6 *primary amine*	756.0	0.5 %
C_{12} *primary amine*	756.4	0.5 %
C_{18} *primary amine*	756.5	0.5 %
C_{24} *primary amine*	756.6	0.5 %
C_{18} *secondary alkyl-amine*	757.0	0.4 %
C_{18} *tertiary alkyl-amine*	757.0	0.4 %
C_{18} *secondary ethoxylated-amine*	757.0	0.4 %
C_{18} *tertiary ethoxylated-amine*	757.0	0.4 %

Table B.2 – Simulated densities for mixtures with PAG as solvent model
ρ^{0}_{PAG} (T_{eq} = 373 K) = 859.0 kg/m^3

Solute	Simulated $\rho_{OFM,BO}$ (kg/m^3)	Deviation
C_{18} *alkane*	851.8	0.8 %
C_{18} *alcohol*	852.3	0.8 %
C_{18} *acid*	853.2	0.7 %
C_{18} *primary amine*	852.6	0.8 %
C_{18} *primary amide*	853.6	0.6 %
C_6 *primary amine*	851.5	0.9 %
C_{12} *primary amine*	851.9	0.8 %
C_{18} *primary amine*	852.6	0.8 %
C_{24} *primary amine*	852.4	0.8 %
C_{18} *secondary alkyl-amine*	852.0	0.8 %
C_{18} *tertiary alkyl-amine*	852.5	0.8 %
C_{18} *secondary ethoxylated-amine*	852.2	0.8 %
C_{18} *tertiary ethoxylated-amine*	853.4	0.7 %

Appendix C
Adsorption experiments via *in-situ* XPS

Adsorption experiments in gas phase of *n*-octadecylamine ($C_{18}H_{39}N$) on native iron oxide were carried out in LTDS with the *ECAT apparatus* (cf. figure C.1, p. VIII). After the adsorption process, *in-situ* X-ray photoelectron spectrometry analyses were performed on the iron oxide surface. The goal of this experimental study was to further investigate the adsorption mechanism of octadecylamines on an iron oxide substrate (under gas phase), and also in order to complement the equivalent DFT study. The experimental protocol used in this procedures is described in the following.

ECAT details

The "UHV [3] preparation chamber" of ECAT was used to carry out the adsorption experiments (cf. figure C.1, p. VIII). After the introduction of the iron sample[4] in the UHV preparation chamber , the sample was slightly etched with an Ar^+ ion gun (250 V) in order to remove contamination present on surface. After, XPS analyses of this substrated were performed in order to control the fact that adventitious carbon has been removed from the native iron oxide. For that, the vacuum in the UHV preparation chamber was around 3×10^{-7} mbar at that step.

Then, the "cleaned" iron oxide sample was effectively exposed to octadecylamine vapor within the UHV chamber. To do so, an introduction system, made of UHV tubes and valves, was used and purged before introducing the amine vapor. The powder of octadecylamine (acquired from Sigma-Aldrich) was stored in a reservoir and heated up to 423 K to be evaporated.[5] The

[3] UHV: Ultra-high vacuum.
[4] Iron deposited on silicium, and covered by a native iron oxide.
[5] *Octadecylamine melting temperature:* 323 - 325 K, and *boiling temperature:* 622 K.

sample was then exposed to octadecylamine vapor for a time period of 7 min. At that step, the pressure in the chamber was varied from 3 to 9 $\times$ 10^{-6} mbar. After exposure, the chamber was pumped in order to get a pressure of 9×10^{-7} mbar, allowing the transfer of the sample to the XPS chamber.

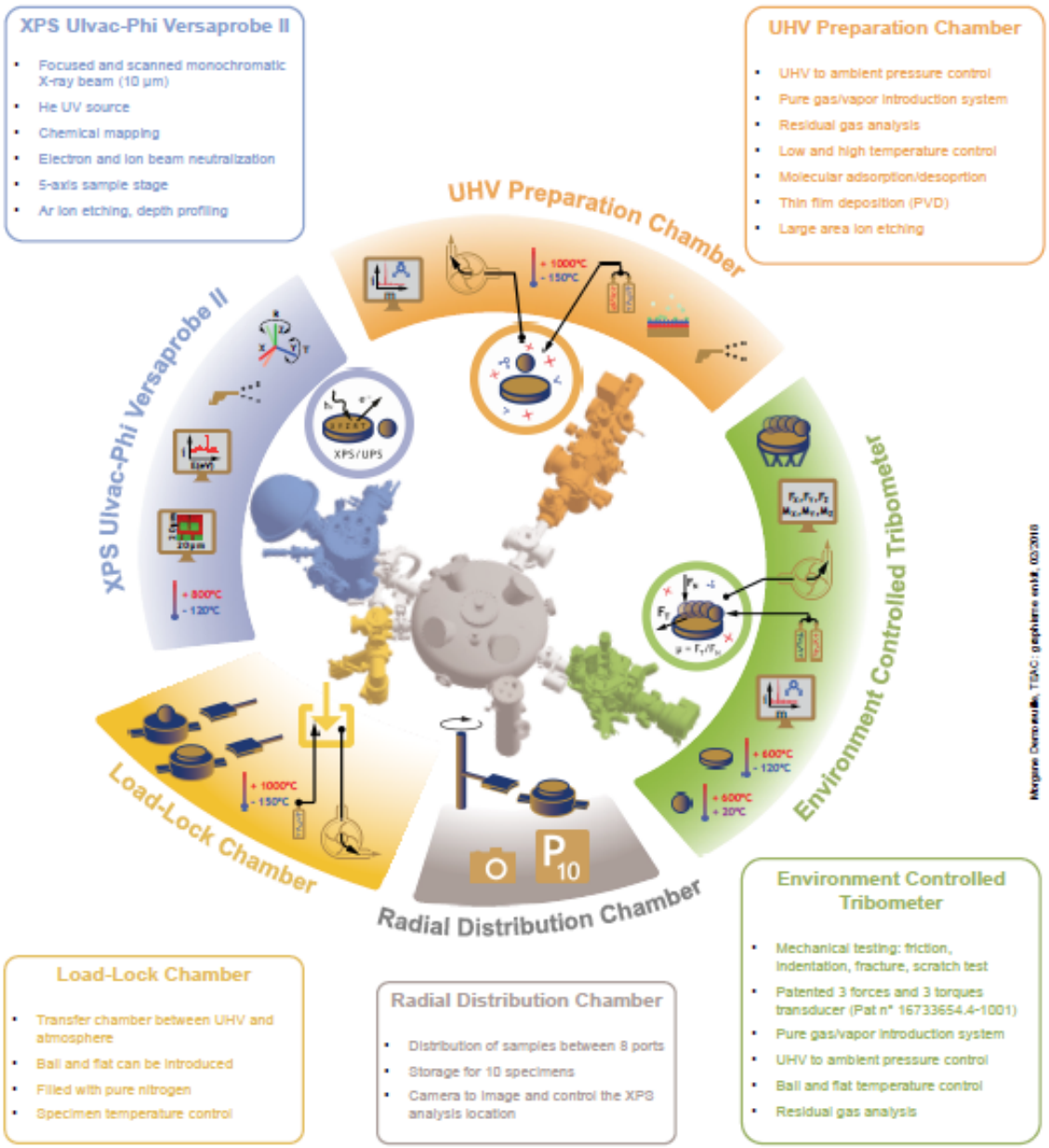

Figure C.1 – *Environmental Controlled Analytical Tribometer* (ECAT), developed at LTDS.

XPS details

XPS analyses were carried out using PHI 5000 VersaProbe II spectrometer, equipped with a monochromatic Al Kα source (1486.6 eV). The calibration of the binding energy scale was done by using as a reference the Au $4f_{5/2}$ and Au $4f_{7/2}$, with known binding energies at 84 and 87.7 eV, respectively.

The emitted electrons were collected at a 45° take-off angle, with respect to the substrate surface. A dual beam charge neutralization system was used to compensate the charging effect (*i.e.*, low energy electrons and Ar^+ ions). Besides, the aliphatic carbon binding energy was fixed at 284.8 eV.

Then, survey spectrum and high resolution spectra were recorded using an X-ray beam diameter equal to 50 μm. Survey spectra were recorded with a pass energy of 187.85 eV and a step size of 0.8 eV, while high resolution spectra were recorded with a pass energy of 23.5 eV and a step size of 0.2 eV.

Finally, data processing was performed using the PHI Multipack software. The spectra were fitted from the product of Gaussian and Lorentzian functions after subtracting a Shirley background. For information, only small variations in FWHM[6] of the peaks were permitted.

Results

The figure 4.4 presented in chapter 4 (cf. p. 71) gives a schematic representation of the N 1s spectra main contributions obtained for the amine powder (peak at 399 ± 0.1 eV), and for the adsorbed amine on the oxidized substrate (peak at 399.7 ± 0.1 eV). These peaks are both attributed to C-N bonds, but they are shifted by 0.7 eV, at a higher binding energy for the adsorbed molecule, in comparison with the standard molecule. As earlier discussed, this important energetic shift for the adsorbed molecule indicates a strong interaction between amines and the iron oxide surface. It could be explained by the formation of N-Fe bonds through the donation of electron density from the nitrogen atoms — via their lone pair electrons — to the irons present on the ferrous surface.

In what follows, the raw and fitted XPS data are reported in detail.

[6] FWHM: full widths at half-maximum.

- ***Octadecylamine powder*:**

Figure C.2 shows the fitted N 1s spectrum obtained for the octadecylamine powder. A main contribution has been found at 399 ± 0.1 eV, and it is attributed to C-N bonds. A smaller contribution at 400.9 ± 0.1 eV can be also detected and assigned to a small N-C=O contamination of the compound sample.

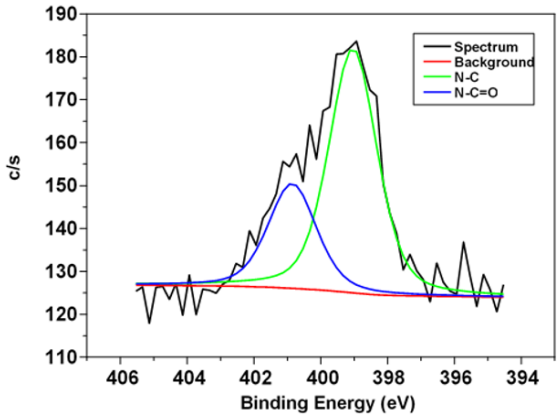

Figure C.2 – N 1s peak for octadecylamine standard compound, observed from an XPS experiment.

- ***Adsorbed octadecylamine on steel: adsorption experiments under gas phase in ECAT apparatus, followed by* in-situ *XPS analysis*:**

The fitted N 1s spectrum of the adsorbed amine on native iron oxide is shown in figure C.3. The main contributions (C-N bonds) is found at 399.7 ± 0.1 eV and shifted by 0.7 eV to higher binding energy compared to the standard molecule (cf. figure C.2).

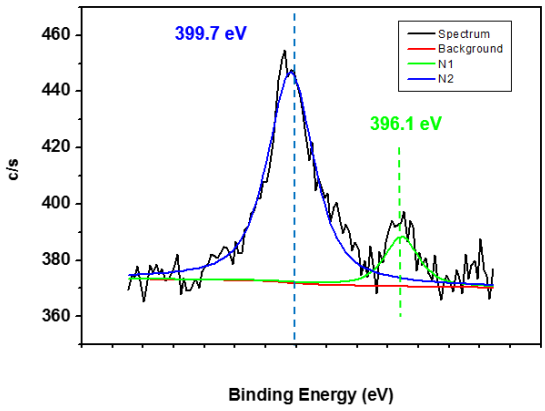

Figure C.3 – N 1s peak for octadecylamine compound adsorbed on iron oxide in ECAT apparatus, followed by *in-situ* XPS experiments.

As previously mentioned, this energy shift is an evidence of the formation of N-Fe bonds. A smaller contribution at 396.1 ± 0.1 eV was also found and it is attributed to the formation of *iron nitride*. In fact, during the cleaning process of the steel sample, we slightly etched the surface with Ar^+. During this process, we removed the adventitious carbon, keeping the native iron oxide (checked by XPS), but it was not possible to avoid the appearance of iron metal atoms at the surface. Actually, these iron atoms are considerably reactive with amines, thereby forming iron nitride.

- ***Adsorbed octadecylamine on steel: XPS analyses performed in the wear track after a tribotest under lubricated conditions*:**

XPS analyses were also performed in a wear track, after a reciprocating tribotest in a ball-on-flat configuration. The tribotest was performed at 373 K, under a maximum Hertz pressure of 500 MPa, and at a reciprocating speed of 8 mm/s. Besides, the octadecylamine was blended in PAO 4 at 1 wt.%. After the tribotest, the steel sample (AISI 52100) was cleaned in n-heptane. XPS was then performed in the wear track, yielding the fitted N 1s spectrum shown in figure C.4. The same shift of 0.7 eV can be found comparing the standard and the adsorbed octadecylamine, which confirms the chemisorption of primary amine molecules on the iron oxide, as it was observed in the first adsorption experiment, conducted under gas phase with ECAT apparatus.

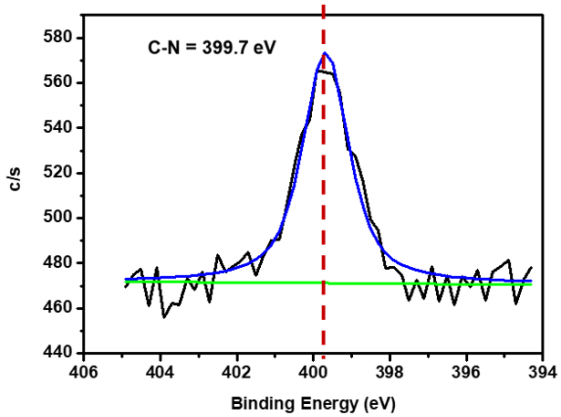

Figure C.4 – Results (N 1s peak) of the XPS analyses carried out on in a wear track after a lubricated tribotest with PAO 4 + 1 wt.% octadecylamine.

Appendix D
In-situ liquid cell SFM experiments

Samples

Muscovite mica substrates, acquired from Agar Scientific (RMS ≈ 0.1 nm), were first used as an atomically flat model surface. Then, iron coated silicon substrates, prepared in *Néel Institute* (RMS ≈ 0.6 nm) were used in order to be more representative of the steel sample chemistry, but exhibiting a lower RMS roughness.

SFM measurements

Scanning force microscopy measurements were carried out using either a *tapping mode* (*i.e.*, following an intermittent contact) or a *contact mode*, by means of a Veeco Dimension 3100 SPM and its Nanoscope V controller.

A soft contact mode was used for *in-situ* SFM measurements on smooth samples, which were fully immersed in the lubricant (*e.g.*, mica or iron layer deposited on silicone). The silicon nitride cantilever-tip was an ArrowCONT with a nominal spring constant of 0.2 N/m. Even if it may disturb the molecules, the contact mode was selected in order to probe the twist of the cantilever at each point, where the height data was recorded.

In addition, it is important to specify that, on flat surface samples, the obtained *lateral signal* reflects the change of friction coming from different surface properties. Actually, this simultaneous mapping, treating both *frictional forces* and *topography*, does allow a better detection of the additives present on a relatively rough surface.[7]

[7] For further information, the interested reader is referred to the indicated reference: https://www.parksystems.com/index.php/park-spm-modes/91-standard-imaging-mode/222-lateral-force-microscopy-lfm.

Appendix E
Boundary friction experiments

The current appendix covers the technical details related to the macroscopic BL experiments — carried out with a ball-on-flat tribometer —, in order to assess the friction-reducing performance of amine-based FM models. For information, the obtained results of friction coefficient are listed in table 5.1 (cf. chapter 5, p. 100).[61]

Samples

The ball and flat substrates used in the tribological tests are made up of AISI 52100 steel (RMS $\approx$ 10 – 15 nm), and they were purchased from *CIMAP* and *PCS Instruments*, respectively.[61]

Base oil and FM additives

The considered BO model was a poly-alpha-olefin (PAO 4) and the investigated OFM models have all a C_{18} alkyl tail, but with different hydrogen atom substituents: *number* — primary, secondary, tertiary amines; *nature* — alkyl and ethoxylated groups (cf. table E.1, p. XVI).[61]

Tribological tests

Figure E.1 (cf. p. XVI) gives a schematic representation of the mentioned tribometer, as well as some details of its operating conditions.[61]

In practice, few drops of the binary lubricating solution (100 μl) were applied in each tribotest, which was run during 9 600 cycles and with a stroke length of 3 nm (cf. figure E.2, p. XVII), at 373 K. The sliding speed was 8 mm/s and the normal load was 2 N, yielding a maximum Hertzian pressure of 504 MPa. Besides, those experiments were repeated, at least three times, for each tested OFM model.

Table E.1 – Base oil and tribo-improvers additives probed in the friction study[61]

Product	Supplier	Description
PAO (BO)	Total M&S	Physical properties at 373 K: • *Density*: 759.6 $kg \cdot m^{-3}$ • *Kinematic viscosity*: 4.0 $mm^2 \cdot s^{-1}$ • *Dynamic viscosity*: 3.04 × 10^{-3} $Pa \cdot s$ • *Pressure-viscosity coefficient*: 10.6 GPa^{-1}
OFM-C	Sigma Aldrich	1° amine; assay ≥ 99%
OFM-E	Sigma Aldrich	2° amine; assay ≥ 98%
OFM-F	AkzoNobel	3° amine; assay ≈ 98%
OFM-H	TCI Europe	3° amine; assay ≥ 98%

The molecular IDs used here correspond to the same nomenclature referred to in table 2.1 (cf. chapter 2, p. 20), indicating the probed OFM models: n-octadecylamine, n-methyl-1-octadecylamine, n,n-dimethyl-1-octadecylamine *and* 2,2'-(octadecylimino)diethanol *molecules, respectively.*

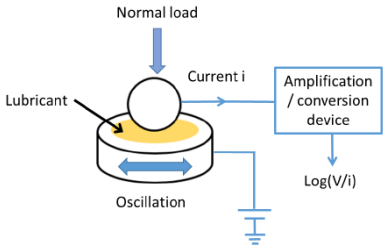

(a) Tribometer

Tribological Test Conditions	
Frequency (Hz)	1.33
Stroke length (mm)	3
Sliding speed (mm/s)	8
Normal load (N)	2
Test duration (s)	7200
Radius of the ball (mm)	6.35
Maximum pressure (MPa)	504
Average pressure (MPa)	336
Temperature (°C)	100

(b) Experimental conditions

Figure E.1 – Details on friction tests: **(a)** the employed *tribometer* — in the reciprocating sliding mode — in order to measure the evolution of friction coefficient as a function of the number of cycles; **(b)** *experimental conditions* used in the friction tests. (figure retrieved from the indicated reference)[61]

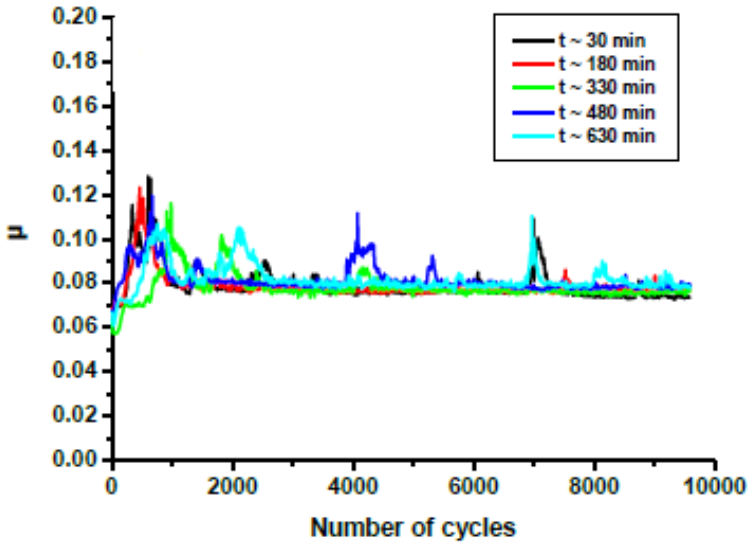

Figure E.2 – Example of the time evolution of the measured friction coefficient (μ), as a function of the number of cycles for a system lubricated by a solution composed of PAO 4 and *octadecylamine* (1 wt.%), at 373 K. (figure retrieved from the indicated reference)[61]

Appendix F
DFT calculations of adsorption energy

Although only the absorptive and frictional behaviors of *primary amines* have been covered in this manuscript, the adsorption mechanism of other molecules have also been examined through a DFT-based approach, within the framework of our project (cf. figure F.1). Thus, this appendix describes the results of the study on *surfactant-surface interaction* of different C_5 alkyl amines.

Method & Materials

In total, three molecules were investigated by means of DFT calculations, following the computational protocol detailed in section 4.1.1 (p. 67). Their molecular structures differ in the number of hydrogen substituents — represented by methyl groups (-CH_3) — since a *secondary* and a *tertiary* amine were compared against a *primary* one. Additionaly, it must be stressed that DFT calculations were carried out by Dr. Manuel Cobián, using VASP program (version 5.3.5).[188–193]

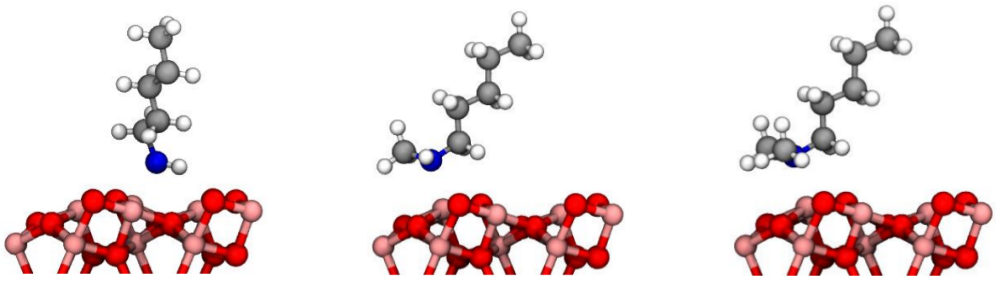

(a) A1 - $C_5H_{11}NH_2$ **(b) A2 - $C_5H_{11}NHCH_3$** **(c) A3 - $C_5H_{11}N(CH_3)_2$**

Figure F.1 – Schematic of C_5 alkyl amines: **(a)** *primary*; **(b)** *secondary*; **(c)** *tertiary*. *Atomic color code: coral* - iron, *red* - oxygen, *white* - hydrogen, *gray* - carbon, *blue* - nitrogen.

Results & Discussion

According to the obtained results (cf. table F.1), all of the probed amines do chemically react with an α-Fe_2O_3 $(0\ 1\ \bar{1}\ 2)$ surface. Besides, as it may be reasonably expected, a decrease of the *adsorption energy* along with an increase of the *length of the formed N-Fe bond* were observed with increasing number of hydrogen substituents:

$$d^{\mathrm{A1}}_{\mathrm{N\text{-}Fe}} < E^{\mathrm{A2}}_{\mathrm{N\text{-}Fe}} < E^{\mathrm{A3}}_{\mathrm{N\text{-}Fe}}$$

$$E^{\mathrm{ads}}_{\mathrm{A3}} < E^{\mathrm{ads}}_{\mathrm{A2}} < E^{\mathrm{ads}}_{\mathrm{A1}}$$

Therefore, these DFT results seem to be in line with the influence of the *head group polarity*, as well as with the *steric effects* related to the hydrogen substituents, on the *strength* of the *amine-hematite interaction*.

Table F.1 – DFT calculation results

C_5 alkyl amine	Length of N-Fe bond, $d_{n\text{-}Fe}$ (Å)	Adsorption energy, (kcal·mol^{-1})	E^{ads} (eV)
1°	2.16	17.48	0.76
2°	2.17	16.60	0.72
3°	2.26	14.04	0.61

AUTORISATION DE SOUTENANCE

Vu les dispositions de l'arrêté du 25 mai 2016,

Vu la demande du directeur de thèse

Madame C. MINFRAY

et les rapports de

M. N. FILLOT
Maître de Conférences HDR - Laboratoire de Mécanique des Contacts et des Structures (LaMCoS - UMR 5259) - INSA de Lyon - Bâtiment S. Germain, bureau 324404X
avenue Jean Capelle - 69100 Villeurbanne

et de

M. M. MOSELER
Professeur - Fraunhofer IWM - Physics Institute of the University of Freiburg - Wöhlerstr. 11
79108 Freiburg - Allemagne

Monsieur PEREIRA DE MATOS Rafael

est autorisé à soutenir une thèse pour l'obtention du grade de **DOCTEUR**

Ecole doctorale MATERIAUX

Fait à Ecully, le 16 avril 2019

P/Le directeur de l'E.C.L.
La directrice des Etudes

ÉCOLE CENTRALE DE LYON
Service Scolarité
ECULLY

M-A. GALLAND